Understanding the Emergence, Tunability, and Performance of Plasmonic Copper Selenide Semiconductor Nanoparticles

by

Xing Yee Gan

B.S. University of Washington, 2014

Submitted to the Graduate Faculty of the

Dietrich School of Arts and Sciences in partial fulfillment

of the requirements for the degree of

Doctor of Philosophy

University of Pittsburgh

2021

UNIVERSITY OF PITTSBURGH

DIETRICH SCHOOL OF ARTS AND SCIENCES

This dissertation was presented

by

Xing Yee Gan

It was defended on

March 25, 2021

and approved by

Committee Member: Dr. Nathaniel Rosi, Professor, Department of Chemistry

Committee Member: Dr. Haitao Liu, Professor, Department of Chemistry

Committee Member: Dr. Renee Frontiera, Professor, Department of Chemistry, University of Minnesota

Committee Chair: Dr. Jill Millstone, Associate Professor, Department of Chemistry

Understanding the Emergence, Tunability, and Performance of Plasmonic Copper Selenide Semiconductor Nanoparticles

Xing Yee Gan, PhD

University of Pittsburgh, 2021

The phenomena of localized surface plasmon resonances (LSPRs) has been broadly studied and is a property of nanomaterials that can be used to enhance or enable a wide variety of technologies including cancer treatment, light-driven catalysis, and ultrasensitive detection. Although plasmonic behavior is most widely-observed and studied in noble metal nanomaterials, there is significant interest in developing earth-abundant plasmonic materials. However, whether or not their performance can match or even surpass their noble metal counterparts remains to be established. An important first step in determining the extent of their versatility is to understand basic aspects of their plasmonic features. We first synthesize and demonstrate the LSPR energy tunability of air-stable degenerately doped copper selenide (Cu_2Se) NPs (**Chapter 2.0**). We quantitatively access the LSPR and correlate its spectral features with changes in the nanoparticle structure that can be controlled chemically. Analytical tools for analyzing the surface chemistry of Cu_2Se NPs are discussed next, which clarifies the site of potential catalytic behavior (**Chapter 3.0**). We then establish their molar extinction coefficient, which is an important readout for the LSPR intensity and showcases our ability to control such intensity with NP size (**Chapter 4.0**). Importantly, we determine that size-dependent increases in molar extinction coefficients behave much like their noble metal analogues, as the trend mimics the Mie theory predictions. Further, the LSPR extinction is an important figure of merit which can be used to improve $Cu_{2-x}Se$ NP

performance in sensing and catalytic applications. In **Chapter 5.0**, we demonstrate the first plasmon-driven chemical conversion on the surface of this new plasmonic material class. Finally, we establish a reaction-insensitive, material-specific design rule to prepare multicomponent nanostructures starting from Cu_2Se (**Chapter 6.0**). Taken together, these results give a promising outlook towards rational designs and implementations of technology-relevant and earth-abundant materials.

Table of Contents

List of Tables

List of Figures

List of Equations

Acknowledgements

I am very grateful to have had many amazing mentors in my life. First and foremost, I would like to thank my advisor, Prof. Jill Millstone, who has been the best mentor and inspiration I could have ever asked for. Her enthusiasm for the science and everything else in general has taught me to look everywhere for inspiration (even rocks), appreciate all hard work, and see the importance of effective communication at all levels. Above all, I thank her for her unwavering support for me, both professionally and personally. Completing a PhD is a challenging process as is, let alone doing it in the middle of a pandemic when your family is thousands of miles away. I want to express my gratitude to have her support and appreciate for her compassion and understanding in this difficult period. Prof. Millstone also pushed me to be the best and seeking opportunities outside of my comfort zone. I could not have asked for a better advisor and a long-term mentor.

Next, I would like to thank my committee members, Professors Renee Frontiera, Nathaniel Rosi, and Haitao Liu, whom provide essential guidance towards the completion of my PhD. Specifically, Prof. Liu’s guidance was integral in the earlier part of my graduate work, Prof. Rosi who is a constant collaborator throughout the years, and Prof. Frontiera, who is also a wonderful collaborator to work with while at the University of Minnesota. I want to also thank Prof. J. Karl Johnson for leading the multi-year, multi-university collaboration that I am extremely lucky to be a part of.

I want to also thank both the past and present members of the Millstone lab, as everyone has been essential in ensuring that we work productively together as a team while maintaining my overall sanity through various fun activities outside of work. In particular, I am grateful to my mentors, Lauren Marbella and Derrick Kaseman, whom I relied on for guidance during the earlier stage of my program. I thank Scott Crawford specifically for his friendship, guidance, and collaborative ideas. During the pandemic, I also have the pleasure of having a wonderful "pod" of friends that got me through the last year of my PhD, specifically Riti Sen, Karli Kunzler, and Jacob Smith. My student collaborators-turned-friends, Emily Keller, Tianyi Luo, and Chris Warkentin, are all also instrumental in helping me look at my research through different lenses and broaden my area of interests and expertise.

Additionally, I want to thank Alina Schimpf, who has been my close friend and long-term mentor since I was a first generation, immigrant, sophomore year undergraduate student seeking research experience at the University of Washington. Her guidance and patience when she was a senior graduate student have inspired me to pursue a PhD and a career in science. She also showed me the importance of having a good mentor in one's research career and inspired me to pay it forward by trying to be one for others.

Outside of work, I am grateful to my supportive friends, who ensure that I maintain a healthy work-life balance. In particular, I want to thank my support systems, Penny Poon and Jose Araujo in Seattle, Arai Kairalapova, Shreya Ghosh, Abena Botwe-Asamoah, and Leila Terrab in Pittsburgh, Yi Ying Chin and Yi Wen Heng in Malaysia, and Sara Lemley in Australia, who have always been there for me emotionally be it locally or virtually.

Finally, I want to thank my big family (4.1 did it!), and my late grandmother Ah Ma, if only she was here to see where I am today. I am most grateful for my parents, Kay Beng and Siew Hui, and brother, Wei Khang for their endless support for me, without whom I would not have the means to strive to achieve *my* version of the American Dream.

1.0 Preparing Degenerately-Doped Semiconductor Nanoparticles for Next Generation Plasmonically-Driven Photocatalysts

(Portions of this work were previously published and reprinted with permission from Marbella, L. E., Gan, X. Y., Kaseman, D. C., Millstone, J. E., *Nano Letters* **2017**, *17*, 2414 – 2419. Copyright, 2017, American Chemical Society; Kaseman, D. C., Gamble Jarvi, A., Gan, X. Y., Saxena, S., Millstone, J. E., *Chemistry of Materials* **2018**, *30*, 7313 – 732. Copyright, 2018, American Chemical Society; Gan, X. Y., Crawford, S. E., Eikey, E. A., Sen, R., Killinger, J. R., Millstone, J. E., *The Journal of Physical Chemistry C* **2020**, *124*, 4747 – 4754. Copyright, 2020, American Chemical Society; and Gan, X. Y., Keller, E. L., Warkentin, C. L., Crawford, S. E., Frontiera, R. R., Millstone, J. E., *Nano Letters* **2019**, *19*, 2384 – 2388. Copyright, 2019, American Chemical Society.)

1.1 Introduction

From artificial photosynthesis to photovoltaics, designing materials that use light to drive chemical reactions has been a holy grail for materials science research. The initial step driving any of these processes is the absorption of incident light. A unique method of light absorption and subsequent transformation is a phenomenon termed, "localized surface plasmon resonance (LSPR)," which is a light-matter interaction that exists at the nanoscale and can enhance a wide variety of technologies including ultrasensitive detection and catalytic reactions.[1-2] LSPRs are typically observed in noble metal nanomaterials such as Au, Ag, and Cu, and many significant discoveries have been made towards understanding the plasmonically-driven processes of noble metals. Specifically, there has been a significant improvement in understanding the mechanisms behind plasmon-driven catalytic reactions, both from computational efforts in understanding the electronic structure of these materials, to experimental approaches for understanding the plasmon dynamics, probing reaction mechanisms, selectivity, and scope of plasmonically-driven chemistry.[2-7]

While most widely observed and studied in noble metal nanomaterials, a much broader selection of nanoscale materials may exhibit LSPRs. Recently, degenerately doped semiconductor nanoparticles (NPs) have been identified as a class of alternative plasmonic nanomaterials. These materials have the added benefit of being derived from earth abundant, low-cost elements. Additionally, degenerately doped semiconductor nanomaterials allow one to access LSPRs that span a uniquely broad spectral range, extending into the far infrared. Similar to all nanoscale phenomenon, the LSPR is tunable by changing particle size, shape, and even surface chemistry, but these relationships are largely unknown for these emerging earth-abundant materials.

In order to prepare these degenerately-doped semiconductor NPs to be comparable alternatives for plasmonically-driven catalysts, an important first step in determining the extent of their versatility is to understand basic aspects of their plasmonic features. To that end, we first look at the success of noble metal plasmonic systems in photocatalysis, pin-pointing important features and key figures of merit that have yet to be established for degenerately-doped semiconductors too, laying out a blueprint for building useful alternatives using more earth-abundant elements. Throughout this dissertation, we will focus on one class of degenerately-doped semiconductor NPs, copper chalcogenides (copper selenide, to be specific). We will first discuss the emergence of the LSPR in semiconductor NPs and establish methods to measure and control such optical properties (**Chapter 2.0**). Next, we outline several important features that will be useful for the community. Specifically, we discuss straightforward approaches to control molar extinction coefficient for copper selenide systems, which is an important quantitative readout on the magnitude of the LSPR properties (**Chapter 3.0**), and study the surface chemistry of copper selenide NPs, which clarifies the site of potential catalytic behavior, and provide finer modulations on the LSPR properties of copper selenide NPs once formed (**Chapter 4.0**). Next, in **Chapter 5.0**, we report the first ever plasmon-driven chemical conversion on the surface of degenerately-doped semiconductor NPs alone and introduce several early examples of plasmonically-driven chemical conversions using this new plasmonic material class. This dissertation concludes by discussing how we can leverage the plasmonic properties of degenerately-doped semiconductor NPs further by incorporating them as part of more synthetically complex heterostructures, which exhibit LSPR properties that can be used synergistically to improve their efficiencies as photocatalysts (**Chapter 6.0**).

Taken together, this dissertation provides an overview of the current status of alternative plasmonics as well as an outlook on how we can set up these materials for a bright future through enhanced understanding, design, and implementation of earth-abundant materials for light-driven chemical reactions.

1.2 Plasmonically-Driven Catalysis in Noble Metal Nanomaterials

LSPRs can be described as the collective oscillation of degenerate carriers (*e.g.*, electrons or holes) on a nanomaterial surface upon excitation by incident electromagnetic radiation. Since the earliest discoveries of plasmonic materials, including the famous Lycurgus cup in the 4th century,[8] this fundamental interaction between light and noble metal substrates has since been extensively studied and reported. By understanding the subsequent electronic events of the LSPR, these nanomaterials could be used to introduce new applications and improve existing technologies ranging from medicine to energy storage.[1-2, 9-10] For example, the electromagnetic field enhancement process (**Figure 1.1A**) that occurs immediately upon plasmonic excitation has been used to improve the signal and sensitivity of analytical tools such as surface-enhanced Raman spectroscopy (SERS) or surface-enhanced infrared absorption spectroscopy (SEIRAS),[1-2, 11-14] which have been useful in detecting low concentrations of analytes[1] or for rapid sensing in complex media.[15]

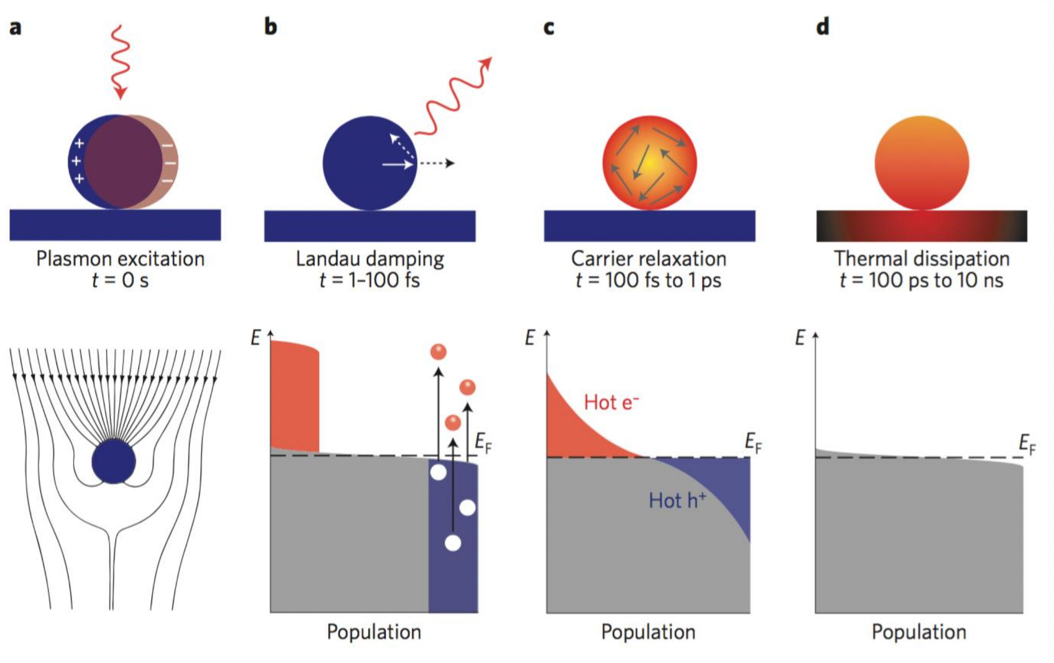

Figure 1.1. Schematic of plasmonic-driven processes and its corresponding energetics as several timestamps. Adapted with permission from Ref. 2, Copyright 2015 Nature Publishing Group.

Of course, the generation of hot carriers is the most relevant plasmonic event especially for plasmonically-driven photocatalytic applications.[2, 6, 16] Specifically, the photoexcited carriers undergo non-radiative decay termed "Landau damping" (**Figure 1.1B**), generating a population of electron-hole pairs that are much more energetic than the ground state electron density existing around the Fermi level.[2, 17] These femtosecond-long hot carriers relax through electron-electron scattering, forming a non-thermal Fermi-Dirac distribution, where these carrier distributions are hotter than the plasmonic NP substrate's lattice (**Figure 1.1C**). Importantly, the generated hot carriers can then be transferred to adjacent analyte molecules,[5, 18-20] charge acceptors,[17, 21] catalytically active metals[22-24] or semiconductors[3, 10, 25-27] that act as "antennas" for efficient charge transfer. Therefore, it is worth noting that the study of plasmonically-driven hot carrier transfer has a long history, and this field has also been extensively reviewed.[5-7, 17, 28] Importantly, the ultrafast process is disseminated into two mechanisms (**Figure 1.2A**): 1) direct charge transfer, where the plasmonically-generated hot carriers are directly injected to adjacent adsorbate with energetically-aligned HOMO and LUMO states, and 2) indirect charge transfer, where the hot carriers are first formed on the plasmonic substrate before they are effectively transferred into adjacent adsorbates as long as the hot carriers have sufficient kinetic energy.[5, 17, 29]

When the hot carriers are directly transferred to adsorbed molecules, reduction or oxidation reactions could occur based on either hot electron-, or hole-transfers, respectively.[6-7, 17] The canonical hot electron driven reaction used in many reports is the dimerization of nitrobenzenethiols (NBT) to dimethylazobenzene (DMAB).[7, 18, 30] These reactions are typically monitored using SERS as the analyte reactant and products have spectroscopically-distinct Raman features (**Figure 1.2B**), making the ability to determine the type of reaction as well as the reaction yields[31] and reaction timescale[32-33] straightforward. For example, Frontiera and coworkers determined that the gold substrates' SERS enhancement factor, which is a figure of merit that measures the magnitude of the electromagnetic field enhancement upon plasmonic excitation, does not play a role in influencing in the reaction yield. Instead, the reaction is limited by the proximity of nitrobenzenethiols to each other.[31] Conversely, hot hole-driven chemical reactions have also been demonstrated. Specifically, one of the first examples by Jin and coworkers reported is the photoinduced shape transformation from Ag nanospheres to prisms.[34] Upon further mechanistic studies, such shape transformation is caused by the photo-oxidation of the citrate capping ligands on the Ag NPs caused by hot holes generated from plasmonic excitation and subsequent reduction of Ag^+ ions in solution.[35-36]

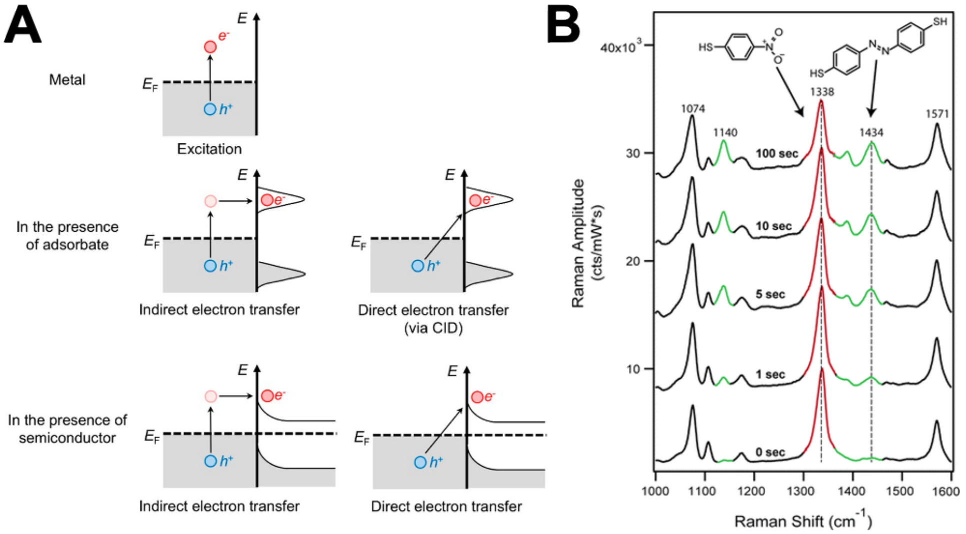

Figure 1.2. Mechanisms of plasmon-driven hot carrier transfer: direct or indirect charge transfer that could either be transferred to adsorbates or semiconductor system (A) and plasmon-driven nitrobenzenethiol dimerization reaction monitored using Surface Enhanced Raman Spectroscopy (B). (A) adapted with permission from Ref. 5, Copyright 2018 American Chemical Society. (B) adapted with permission from Ref. 31, Copyright 2016 American Chemical Society.

While examples of plasmon-mediated chemical reactions have been demonstrated, it is crucial to ask the next series of important questions: 1) which hot carrier is more efficient at charge transfer? 2) how does the identity of the plasmonic substrate play a role in determining which hot carriers are more energetic? and 3) how to improve the hot carrier transfer efficiency? To start answering these questions, several theoretical studies have focused on studying the hot carrier distribution and rate of hot carrier generation.

Specifically, Atwater and coworker's seminal work on using computational methods to study the generation of hot electrons and holes for four different plasmonic systems (gold, silver, aluminum, and copper demonstrates that the electronic band structure of each system plays a crucial role in determining the hot carrier energy distributions (**Figure 1.3A**).[37] Briefly, the based on allowed transitions, the authors were able to extract the relative probability of hot holes (negative energies relative of Fermi level, $E_F = 0$ eV) and hot electrons (positive energies relative to E_F) at various excitation energies. For example, aluminum's holes and electrons have similar and near-continuous energy distributions, while silver has hot electrons and holes that appear near its LSPR energy (~3.6 eV), and finally both copper and gold appear to have populations of hotter holes than electrons. Such interpretation in the energetic distribution of plasmonically-generated hot carriers is crucial because it can then be applied towards designing plasmonic devices more rationally and effectively. For example, the authors demonstrated that by understanding the hot carrier distribution of gold, they could then introduce gold with gallium arsenide (GaAs) semiconductor for charge separation application. Specifically, owing to the knowledge that gold's electrons are "colder" than its holes, coupling gold with a p-type GaAs instead of n-type GaAs experimentally (*i.e.*, in a fabricated device) is more beneficial as the hot holes can be easily transported out from the plasmonic substrate without needing additional thermal boost, making the design of this Schottky junction more efficient (**Figure 1.3B**).[37]

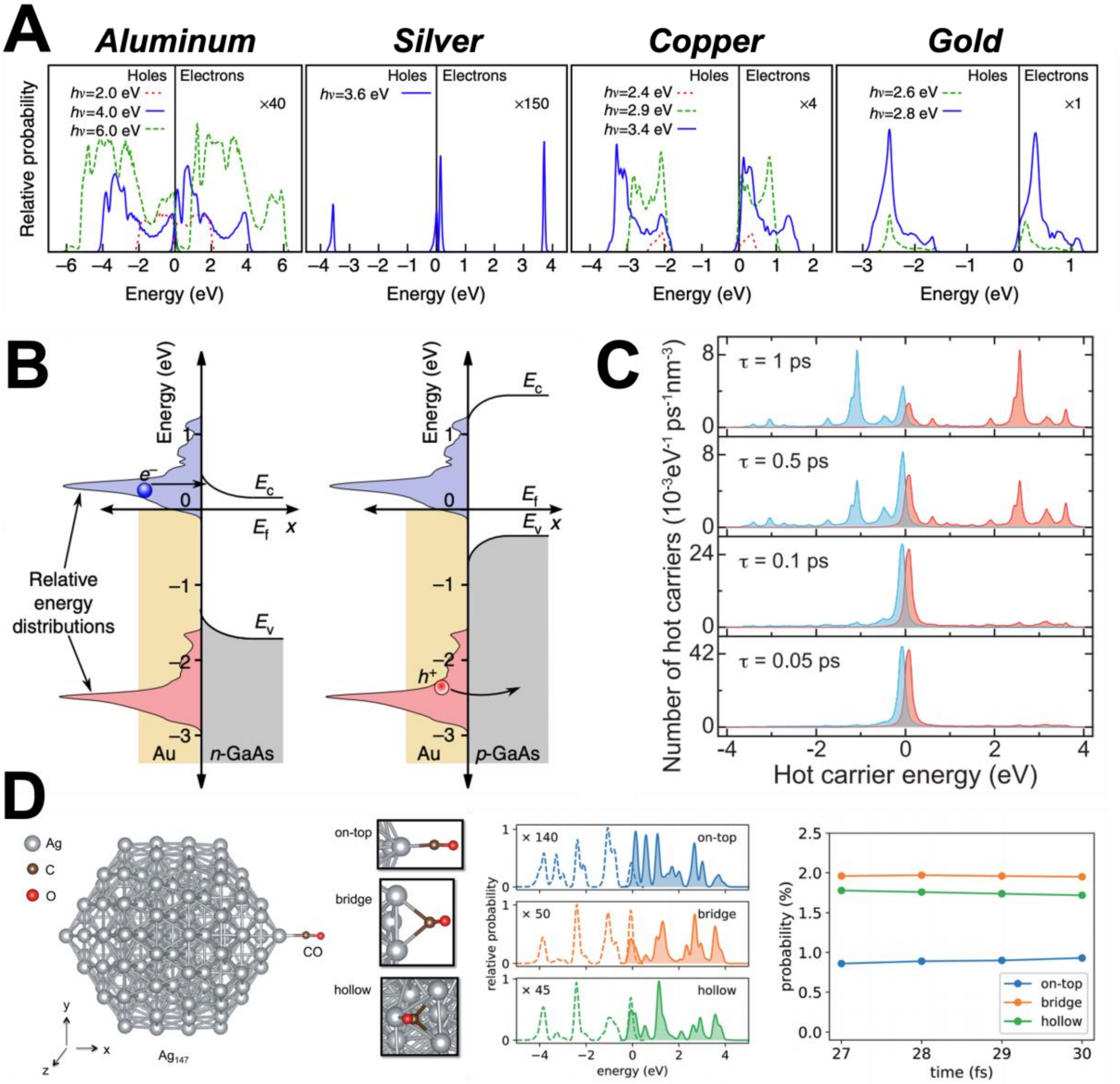

Figure 1.3. Hot carrier distribution of aluminum, silver, copper and gold (A). Hot electron and hole transfer from gold to n-type and p-type gallium arsenide Schottky barriers (B). Hot carrier generated in silver nanospheres across several picosecond timescales (C). Coordination of a CO molecule adsorbed onto a Ag_{147} nanocluster surface, along with the hot carrier transfer probability

as a function of various CO adsorption configuration (D). (A) and (B) adapted with permission from Ref. 37, Copyright 2014 Sundrararaman et al. (C) adapted with permission from Ref. 16, Copyright 2014 American Chemical Society. (D) adapted with permission from Ref. 38, Copyright 2019 Royal Society of Chemistry.

Additionally, Nordlander and coworkers also used computational methods to study hot carrier generation as a function of excitation wavelength and time.[16] The authors used a simple model to quantify the rate of hot carriers generated in a silver NP per unit time and volume, and found that the number of hot carriers produced closely follow the LSPR absorption feature of Ag NPs, where the LSPR max at ~3.6 eV produce the highest number of hot electrons. Additionally, by monitoring the hot carrier distribution over time, the authors also found that longer lifetimes produce more energetic carriers (**Figure 1.3C**). Importantly, these results provide important insights such as the excitation wavelength as well as reaction timescale for experimentalists to design efficient plasmonic substrates and experimental setups for optimal photocatalytic performance.

Another crucial piece of information extracted from computational studies that could improve the efficiencies of plasmon-driven chemical reactions focuses on the surface chemistry of the material. Specifically, the coordination environments of the adsorbate dictate the charge transfer efficiency. For example, Norris and coworker use real-time time-dependent density functional theory (RT-TDDFT) to study the hot carrier generation and transfer from the Ag_{147} cluster to a CO adsorbate molecule.[38] By studying three different coordinating configurations termed “on-top”, “bridge” and “hollow”, the authors found that the charge transfer probability is highest when the CO molecule adsorbs on the Ag_{147} surface in a bridging configuration (**Figure**

1.3D). Importantly, these results suggested that the direct charge transfer mechanism depends strongly on adsorption coordination, providing a step forward towards understanding ways to improve the charge transfer efficiency through the use of NP surface chemistry.

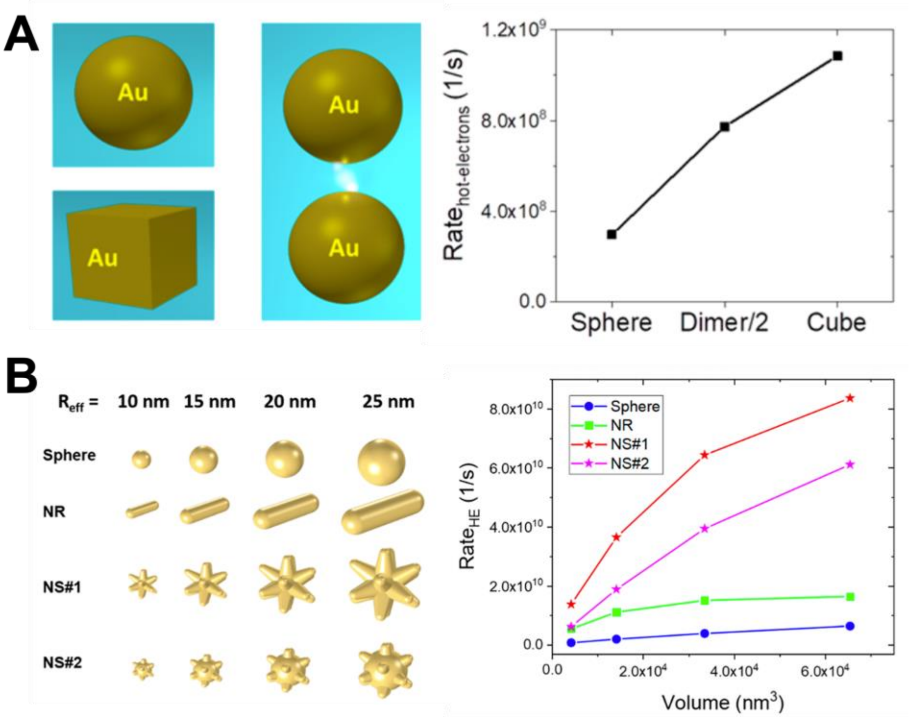

Figure 1.4. Rate of hot electrons generated in gold nanospheres, dimers formed between two nanospheres, and nanocubes (A). Rate of hot electrons generated in four different shapes of gold nanoparticles, spheres, rods, and nanostars with either large prongs or centers as a function of variable volume (B). (A) adapted with permission from Ref. 39, Copyright 2017 American Chemical Society. (B) adapted with permission from Ref. 40, Copyright 2020 American Chemical Society.

As alluded to previously, because the lifetimes of plasmon-generated hot carriers are very short, it is important to be able to transfer these charges efficiently, and there have been several strategies reported for noble metal plasmonic systems. For example, Govorov and coworkers have been using computational methods to study the rate of hot electrons generated from Au NPs of various sizes and shapes (**Figure 1.4**),[39-40] and found the hot electron generation rate trends with electromagnetic field enhancement. By designing plasmonic NPs with hot spots either by dimerizing two spheres**,** or creating higher surface energy sites through the use of anisotropic NPs such as nanocubes and nanostars, the rate of hot carrier generation can be effectively increased. Importantly, these results show that while particle size could be a useful parameter to improve hot carrier generation, creating hot spots through anisotropic particles is more effective.[40] Therefore, these observations are promoting the design and engineering of degenerately-doped semiconductor NPs with the goal of improving their field enhancement property in order to become good plasmonic photocatalysts (*vide supra*).

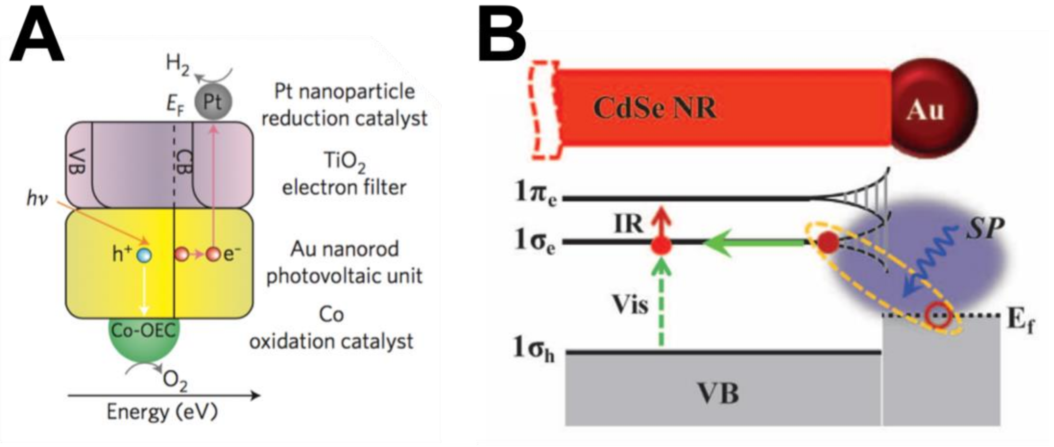

Figure 1.5. Schematic of a plasmonically-driven artificial photosynthetic heterostructure device depicting charge shuttling directions and a subsequent water splitting chemical reaction (A). Schematic of heterostructures of a CdSe nanorod with Au deposited at the end and its energetic diagram depicting plasmonically-driven charge separation and transfer (B). (A) adapted with

permission from Ref. 10, Copyright 2013 Nature Publishing Group. (B) adapted with permission from Ref. 27, Copyright 2015 The American Association for the Advancement of Science.

A different and perhaps more pragmatic strategy to promote efficient charge transfer is effectively by preventing charge recombination between the generated hot holes and electrons. One of the most efficient way of preventing charge recombination is through shuttling charges away from each other when plasmonic NPs are coupled with a semiconductor. Specifically, the presence of a metallic NP near a semiconductor realigns the Fermi level of the semiconductor and thus creates a Schottky barrier with the semiconductor valence and conduction bands.[10] Upon the generation of hot carriers due to plasmon excitation, the Schottky barrier allows a more efficient charge injection into the semiconductor while also offers a longer-lived separation between the hot electron-hole pairs. In this report, the authors developed an autonomous plasmonic solar water splitter using Au nanorods. Upon light absorption, electrons can be directed to the catalytically active Pt NPs through a Schottky barrier created by the TiO_2 semiconductor islands, while the hot holes can be simultaneously transferred to an oxidation catalyst on the other side of the nanorod (**Figure 1.5A**). By implementing plasmonic NPs in this system, increases in water splitting efficiencies and device lifetimes were observed compared to conventional semiconductor water splitters. Additionally, Lian and coworkers have also reported similar observations with heterostructures consisting of Au NPs and CdSe nanorods. Specifically, the authors also identified this phenomenon as a direct charge transfer mechanism, which is termed a "plasmonically induced charge transfer transition" (**Figure 1.5B**).[27] Interestingly, a recent report by Hattori et al. reveals that the plasmonically-generated hot carriers recombination rates of heterostructures consisting of Au and several types of metal oxides do not solely depend on the Schottky height (i.e. energetic alignments between Au E_F and metal oxide conduction and valence bands).[41] Instead, the authors noted that there is an interplay between the energetic levels and other metal oxide-specific parameters such as the electron bulk mobility that also helps prolonging the charge recombination rate. Importantly, these results showcase the ability to extract the short-lived plasmonically generated hot carriers efficient by preventing the hot carriers from recombining through several charge shuttling strategies. Further, these findings provide an important and practical synthetic goal, which is to incorporate plasmonic systems as a component in complex heterostructured nanomaterials.

Apart from the previously discussed charge transfer mechanisms, another debated mechanism for how some plasmonically-driven catalytic reactions operate is through thermal-dissipation. During the formation of energetic carriers due to plasmonic excitation, the most efficient way for the carriers to relax to the ground state is through thermal dissipation, generating localized heat (**Figure 1.1D**).[2] While one of the earliest applications for localized heating of plasmonic substrates is the design of photothermal cancer therapeutics,[9, 42-44] many reports have also postulate that some chemical transformations that occur on the plasmonic substrate surface are driven by an increase in temperature, pushing the reactions over their activation barriers thermodynamically.[20, 45] To that end, there are several reports that analyze the competition between the hot carrier transfer mechanism and thermal-driven chemical reactions.[45-47] For example, in an aluminum-iridium plasmonic heterostructures, Halas and coworkers reported that the reaction producing nitrogen and oxygen gases from nitrous oxide underwent a thermally-catalyzed mechanism rather than via the generation of hot carriers.[48] Specifically, the authors identified that the reaction's rate limiting step is the desorption of O_2 from Ir(111) surface, and that the reaction is independent of excitation intensity, further demonstrating that this step occurs through photothermal heating as its primary plasmon-mediated process. Importantly, while plasmonically powered thermal generation and catalysis is not within the scope of this chapter, these relevant reports and debate demonstrate that even though hot carrier charge transfer may be the preferred method, photothermally-driven chemical conversion could be used as a useful strategy for plasmonic systems to catalyze chemical reactions.

Taken together, using plasmonic noble metal nanomaterials as our guide owing to their vast examples and rich history, we begin to identify several parameters that are crucial to efficiently perform plasmonically-driven catalysis, being mindful that both hot carriers and thermal dissipation could both go over the reaction activation barriers. Additionally, energetic distributions of these generated hot carriers provide important insight in the types of plasmonic substrate to use, and deciding which reactions are feasible. Finally, a closer look at how plasmonically-driven reactions could be improved via hot spots or efficient prevention in hot carrier charge recombination by incorporating plasmonic substrates in heterostructures allows us to rationally design nanomaterials with optimal performance in mind. With these guideposts in mind, we can start branching out and identifying other classes of plasmonic materials that are more earth-abundant and cost-effective.

1.3 Preparing Degenerately-Doped Semiconductors for Plasmonic Photocatalysis

1.3.1 Emergence and Control of LSPRs in Degenerately-Doped Semiconductor Nanomaterials

Plasmonic properties of noble metal NPs have already been used in photocatalytic applications, but the commercialization of such materials is challenging because the LSPRs of noble metal NPs are often confined to the visible and near-IR energy ranges, in addition to high material cost. In order to enable and accelerate the translation of plasmonic materials, there is motivation to develop cheaper, earth abundant alternative materials with an expanded pallet of plasmonic properties ranging from ultraviolet (UV) to far-IR wavelengths. One of the alternative plasmonic systems is a class of materials known as degenerately-doped semiconductor NPs. It was first reported by Luther and coworkers, where they discovered that copper sulfide (CuS) semiconductor NPs exhibit an LSPR behavior through the oxidation of Cu^{1+} to Cu^{2+}.[49] The amount of Cu oxidation contributes to the number of holes present in the valence band of the system, and as just like conduction electrons in noble metals, these carriers are able to oscillate collectively. More importantly, this observation provides a crucial insight for the development of alternative plasmonic nanomaterials, where the LSPR output energy is directly related to the free carriers present in the plasmonic system, known as carrier density (**Figure 1.6A**). For example, the higher the carrier density is present, the higher the LSPR frequency is observed for these semiconductor NPs pushing the LSPR output wave from mid-IR to closer to the visible light region. Significantly, the report by Luther also additionally demonstrates that electrons are not the only carriers capable of oscillating collectively upon plasmonic excitation. As long as the dopants are localized or trapped in any state, these carriers could participate in the LSPR process in semiconductor NPs, hence the term “degenerate-doped”.

Importantly, regardless of the dopant identity and method of dopant introduction, the presence of a large number of dopants in semiconductor NPs allows these materials to start behaving like their metallic counterparts and exhibiting a plasmonic behavior. For example, through the introduction of aliovalent Al^{3+} dopants into ZnO NPs, Buonsanti and coworkers observed the emergence of an IR absorption upon increasing %Al incorporation, which they attribute to the LSPR.[50] Similarly, Schimpf et al. introduced electrons through a technique they termed “electronic doping”, where they use hole scavengers to trap and accumulate excited electrons in the conduction band of ZnO semiconductor NPs.[51] Through this process, the NPs become heavily n-type doped, and start to exhibit an LSPR behavior in the mid-IR region (**Figure 1.6B**). Similar to what was observed with CuS by Luther and coworkers, as a function of increasing in electrons in the ZnO, the LSPR feature blueshifts. An additional spectroscopic signature for the presence of extra carriers is the blueshift of the onset of absorption, also known as the Moss-Burstein effect.[52] Importantly, these experiments demonstrate that *any* semiconductor NP could exhibit an LSPR feature, as long as the carriers present could collectively oscillate. To that end, a wide class of degenerately-doped semiconductor NPs such as metal oxides,[53-55] metal pnictides,[55-56] and metal chalcogenides[54, 57-58] have recently been reported to exhibit LSPRs, creating an avenue towards the rational design and innovation of plasmonic technologies using earth-abundant elements through a wide variety of dopant introductions.

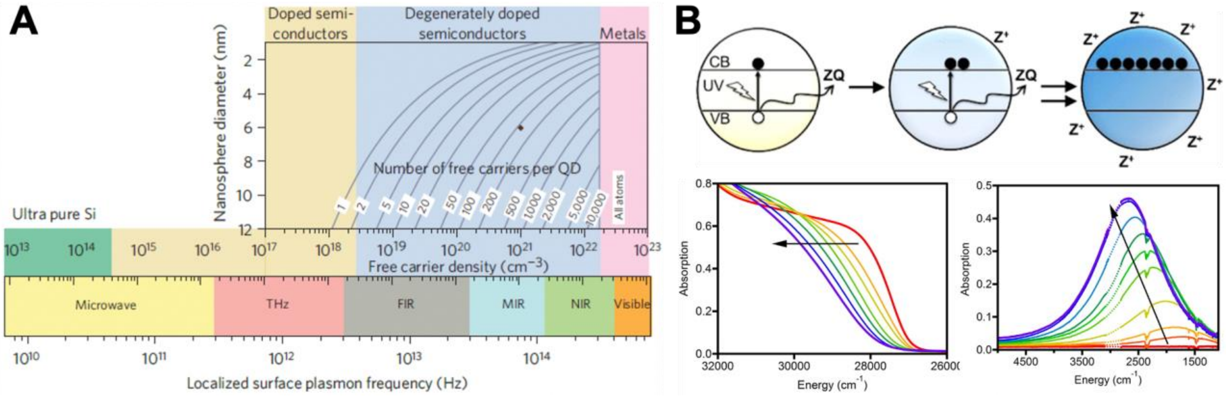

Figure 1.6. A comparison of the observed plasmonic output energy as a function of carrier densities compared between degenerately-doped semiconductors and metallic plasmonic systems (A). Schematic of electronic doping of semiconductors with electrons trapped in the conduction band due to the presence of hole scavengers (ZQ), and its subsequent optoelectronic property changes, the shift in the absorption features known as Moss-Burstein effect as well as the emergence of a LSPR feature, respectively (B, left, and right, respectively). (A) adapted with permission from Ref. 49, Copyright 2011 Springer Nature. (B) adapted with permission from Ref. 51, Copyright 2013 American Chemical Society.

Ultimately, the goal is to implement these alternative materials for plasmonically-driven catalysis, similar to what was observed with traditional noble metals. However, an important first step is to understand and subsequently compare the fundamental photophysical properties of LSPRs for degenerately-doped semiconductors and noble metals. Unlike free d-electrons in metallic systems, because the free carriers in semiconductor NPs do not exist inherently unless otherwise introduced, it is crucial to be able to quantify the number of such carriers present in degenerately-doped semiconductor NPs to enable comparison with their noble metal counterparts.

As described briefly, carriers can be introduced to semiconductor NPs through various methods: aliovalent-,[53, 55] electronic-,[52-53] self-,[55, 57] electrochemical and chemical-doping,[54, 58-59] and these methods of dopant introduction have been extensively reviewed. To observe and quantify this process, many have reported using the classical Drude model to quantify the carrier densities (N_e and N_h for electron and hole densities, respectively) present in the system.[49, 55, 58, 60] The carrier densities present in a system can be extracted from its corresponding extinction spectrum using the rearranged Drude Model equation described below:

Equation 1.1. Carrier Density Extracted From Drude Model

$$N_{e/h} = \frac{(\omega_{LSPR}^2 + \gamma^2)(\varepsilon_0 m_h^*)(\varepsilon_\infty + 2\varepsilon_m)}{e^2}$$

Specifically, the carrier density can be estimated using the measured LSPR peak maximum (ω_{LSPR}) and full width half maximum (γ), which can be experimentally extracted from the extinction spectrum, along with the use of solvent dielectric constant (ε_m), the material-specific parameters such as the high frequency dielectric function (ε_∞) and effective mass ($m^*_{e/h}$) of the free carrier, as well as physical constants such as the charge of carriers (e) and permittivity of free space (ε_0). For example, Luther et al.'s first demonstration of plasmonic CuS is estimated to have a N_h = 1.7 x 10^{21} cm^{-3}, compared to Au's N_e, which was reported to be 5.9 x 10^{22} cm^{-3}.[49]

The Drude model method of quantifying carrier density is straightforward, versatile and widely used to understand, control, and influence the LSPR feature of degenerately-doped semiconductor NPs. For example, by dispersing as-prepared CuS in solvents of various dielectric constants, Luther observed systematic shifts as described by the Drude model.[49] Additionally, Jain et al. used the LSPR feature of CuS nanorods as an optical readout to demonstrate the ability to use redox chemistry to manipulate the carrier densities present in CuS nanorods, effectively turning the optical response on and off.[61] However, it is worth noting that because the Drude model is a simplistic model, it is sometimes insufficient at quantifying the carrier densities in some degenerately-doped semiconductor NPs accurately. Moreover, there are several intrinsic and extrinsic system parameters that may influence both spectral features and the interpretation of those features via the Drude model such as the composition-dependent effective masses of electrons and holes in copper chalcogenides and metal oxides.[62-64] In addition to carrier density, sample properties such as particle aggregation and dispersity can influence the position and breadth of spectral features.[65] Next, the dielectric functions of both the particle and the surrounding medium (which may or may not be a convolution of solvent and pendant ligands), must both be known in order to apply this model.[60] Each of these parameters is sensitive to NP composition, and may introduce ambiguity in the extracted carrier density values.

Because of that, there have been development of several analytical techniques that complement the Drude model method of extracting carrier densities. One method that still uses optical absorption features as readouts is through chemical titration against oxidants such as decamethylferrocenium ($[FeCp^*_2]^+$) and nitrosonium ($NOBF_4$ or NO^+) and by quantifying the equivalents of oxidants used as a method for quantifying electrons in degenerately n-doped semiconductor NPs. For example, Schimpf and coworkers developed an electron counting method by titrating NP solutions with $[FeCp^*_2]^+$ to quantify amount of electronically doped ZnO,[51-52, 66] CdSe,[67] and In_2O_3 NPs,[52, 68] where $[FeCp^*_2]^+$ removes electrons that are present in the conduction bands of NPs, causing the LSPR feature in the IR region to deplete and redshift (**Figure 1.7A, left**).[68] Importantly, the authors reported that the N_e quantified using the chemical titration method is comparable to the carrier densities extracted using the Drude model method (**Figure 1.7A,**

middle and right). Further, they concluded that the number of electrons added through photodoping is independent of the existing aliovalent dopants present by comparing results from both originally undoped In_2O_3 NPs and Sn^{4+} doped In_2O_3 NPs, demonstrating the ability to further engineer degenerately-doped semiconductor plasmonic substrates.

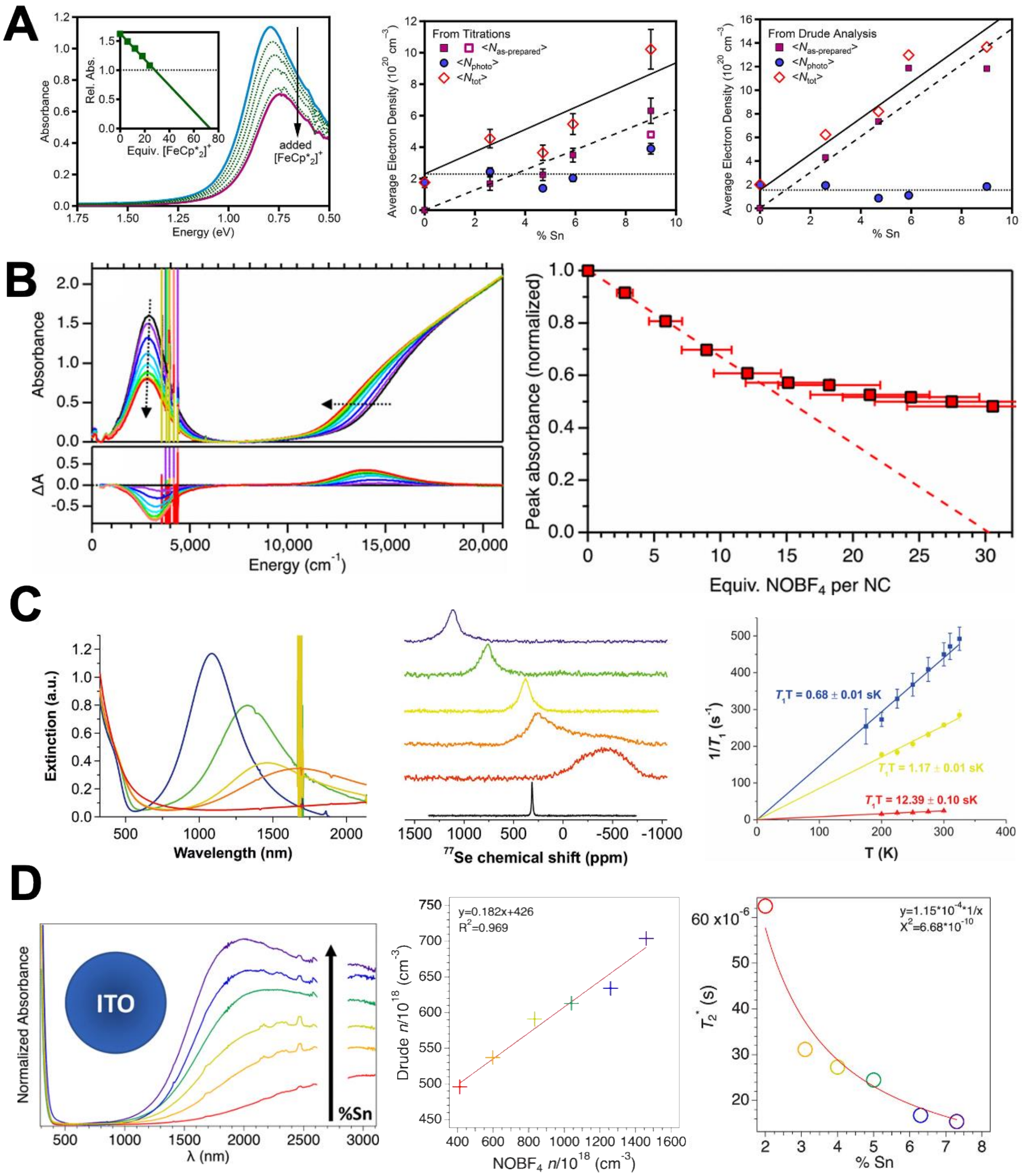

Figure 1.7. (A) Changes in the LSPR features of photodoped ITO NPs as a function of $[FeCp*_2]^+$ titration (left, inset shows intensity changes), and carrier densities measured using the titration method (middle) and Drude model method (right). (B) Changes in the LSPR and bandgap features of InN NPs as a function of $NOBF_4$ titration, DA indicating optical features subtracted from the

pre-titration spectrum (left), and changes in the LSPR intensity as a function of $NOBF_4$ equivalence titrated. (C) Changes in the LSPR features and ^{77}Se solid state NMR spectra of $Cu_{2-x}Se$ NPs as a function of oxidation in air (left and middle), and variable temperature T_1 values of three representative $Cu_{2-x}Se$ NPs of different oxidation stages (right). (D) Changes in the LSPR feature of ITO NPs as a function of increasing %Sn (left), differences in the carrier densities quantified via the Drude model method and the $NOBF_4$ titration method, where the slope of the linear regression indicates the % deviation between methods (middle), and changes in the T_2^* values of ITOs as a function of increasing %Sn measured using ^{119}Sn solid state NMR (right). (A) adapted with permission from Ref. 68, Copyright 2014 American Chemical Society. (B) adapted with permission from Ref. 69, Copyright 2017 American Chemical Society. (C) adapted with permission from Ref. 62, Copyright 2017 American Chemical Society. (D) adapted with permission from Ref. 64, Copyright 2020 American Chemical Society.

Similar to the chemical titration technique mentioned above, Liu et al. used a stronger oxidant, NO^+ as a titrant to count the number of electrons present in degenerately-doped in InN NPs.[69] Interestingly, this result reveals a potential downside of using the Drude model method of quantifying carrier densities. As a function of increasing in NO^+ addition, while the observed redshift in the bandgap energy of the InN NPs is consistent with the decrease in the carrier density due to the Moss-Burstein effect, the authors only observed a depletion of the LSPR intensity (i.e., the LSPR does not redshift as a function of decreasing in carrier density, (**Figure 1.7B, left**)). Instead of using the Drude model, by quantifying the equivalence of NO^+ titrated, the authors monitored the change in the LSPR intensity and extrapolated the linear regression to the x-intercept to extract the number of carriers present in the NPs at a given volume (**Figure 1.7B, right**).

Importantly, these experiments show the importance of using a secondary analytical method to accurately describe the carrier densities in NPs as a supplement to the current technique.

Apart from using a chemical titration method, solid state nuclear magnetic resonance (ssNMR) is also a powerful tool in support of the Drude model. Solid-state NMR can reveal general properties about electronic structure such as whether a material is metallic or semiconducting,[70-72] and can provide specific details including charge carrier density,[73-75] spatial electronic heterogeneity (e.g., distribution of p- and n-type regions),[74-77] and even the type of free carriers present (electrons vs holes).[78] An additional advantage of ssNMR is the ability to perform in situ measurements to monitor these features as a function of time, chemical environment, or external stimuli.[79-80] As it will be discussed in detail in **Chapter 2.0** for example, Marbella et al. specifically studied the emergence of a plasmonic response in copper selenide ($Cu_{2-x}Se$) NPs as a function increasing in Cu oxidation through air exposure.[62] Similar to what was observed with other reports both for copper chalcogenides and other degenerately-doped semiconductor NPs, they observed a spectroscopic feature in the near IR region that blueshifts as a function of oxidation, consistent with an increase in the carrier density (**Figure 1.7C, left**). However, one NP sample (red spectrum) did not display an LSPR feature, making the carrier density quantification using the Drude model technique challenging. Instead, the authors first obtained ^{77}Se ssNMR spectra for $Cu_{2-x}Se$ NP samples with different carrier densities monitored using the optical method (**Figure 1.7C, middle**). By extracting the spin-lattice relaxation rate (T_1), the authors quantified carrier densities present in $Cu_{2-x}Se$ NPs using the Korringa relationship.[71, 81] Importantly, by extracting T_1 values at variable temperature, the authors identified that even the fully reduced $Cu_{2-x}Se$ NPs sample (red spectrum) with the least amount of carriers present still exhibits similar electronic behavior to the other more oxidized samples (**Figure 1.7C, right**), which provided a complementary method to quantify carrier densities in samples that do not have optically discernible LSPR features using the traditional Drude model method.[62]

Recently, Conti and coworkers published a report that uniquely uses all three suggested methods for probing the carrier densities present in the degenerately-doped semiconductor NPs: the Drude model, chemical titration, as well as ssNMR for their systems.[64] Specifically, the authors studied the changes in the carrier densities in ITO NPs as a function of increasing in %Sn dopant concentration (**Figure 1.7D, left**) and quantified charrier densities using all three methods, providing additional insights on the advantages and disadvantages of using each analytical technique. For example, the authors reported that the Drude model method underestimates the carrier densities present in the NPs by 18% (**Figure 1.7D, middle**). Additionally, using the similar ssNMR technique reported by Marbella,[62] the authors also used ^{119}Sn ssNMR on ITO NPs and monitor the changes in the NMR features as a function of increasing in %Sn. They monitored changes in the spin dephasing relaxation times (T_2) as this parameter is more sensitive for ^{119}Sn isotopes instead of T_1 (**Figure 1.7D, right**). However, unlike the T_1 values exhibiting the Korringa behavior, there lacks a straightforward relationship between T_2 and carrier densities, therefore the authors were not able to directly compare the carrier densities measured using all three methods. Nonetheless, these results allow one to carefully select methods that would be most ideal depending on the types of degenerately-doped semiconductor NPs they choose to study.

1.3.2 Establishing Surface Chemistry of Degenerately-Doped Semiconductor Nanoparticles

Once it is established that the LSPR feature of degenerately-doped semiconductor NPs can be controlled with carrier densities, we next study several key features that are important for photocatalysis, accounting for both on the chemical and photophysical properties of the plasmonic

NPs. As discussed previously in **Section 1.2**, charge transfer mechanisms from plasmonic substrates to adsorbates (*i.e.*, analyte molecules, other metallic or semiconducting structures) are well-established photophysically for plasmon-mediated hot carrier transfer. However, in order for these carriers to be effectively transferred, these adsorbates would have to be chemisorbed on the NP surface or near NP surface for the hot carriers to be efficiently transferred. Additionally, the coordination configuration also plays a role in the efficiency of such hot carrier transfer.[38] Therefore, to understand how to effectively use degenerately-doped semiconductor NPs for plasmon-driven chemical conversion, it is important to first establish their surface chemistry and interfacial chemistry between the plasmonic substrates and the analytes.

Surface chemistry and its influence in many physical and chemical properties of noble metals have been extensively-studied.[82-83] For example, surface ligands (such as salts, short chain organic molecules, polymers and even biological systems) have been demonstrated to play a role in activating photoluminescence properties,[84] influencing surface oxidation process[85] and catalytic activity,[86] as well as directing growth of heterostructures.[87] While surface chemistry of semiconductor NPs have been established too and similar demonstrations for how surface ligands influence the optoelectronic properties have been made,[88-90] it is crucial to specifically study how the surface chemistry of degenerately-doped semiconductor NPs will aid or complicate the plasmon-driven photocatalytic reactions.

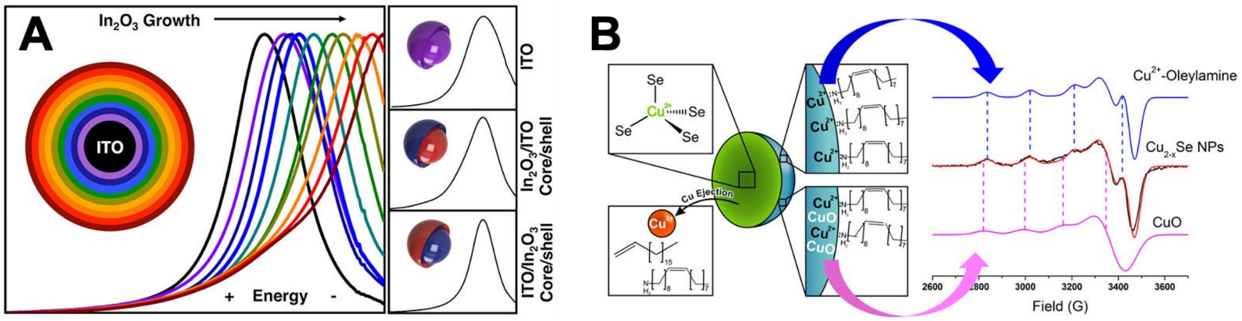

Figure 1.8. (A) Shell growth induced shifts in the LSPR features of ITO NPs and differences in the observed LSPR features for ITO NPs of similar %Sn content but varying in their radial distribution, where the dopants are randomly distributed (top), localized only on the shell (middle) and the core (bottom) of the NPs. (B) Schematic showing four potential fates of Cu^{2+} upon oxidation in $Cu_{2-x}Se$ NPs, and EPR results observed the presence of two: Cu^{2+} coordinated to the oleylamine surface ligand and forming an oxide species on the NP surface. (A) adapted with permission from Ref. 93, Copyright 2017 American Chemical Society. (B) adapted with permission from Ref. 99, Copyright 2018 American Chemical Society.

In a recent review, Gibbs and coworkers discussed the presence of surface depletion layers on aliovalently-doped metal oxide NPs,[91] and correlated how these depletion layers act as an insulating shell on the surface of the NPs that reduces the dipole-dipole interactions between metal oxide NPs, effectively reducing the performance of plasmonic metal oxide NPs for charge transport applications. The presence of insulating surface depletion layers, unsurprisingly, will also effectively reduce the hot carrier transfer efficiency in future plasmonic catalysis applications. Therefore, identifying methods to counteract that physical effect will be useful to design better performing plasmonic metal oxides. For example, by selectively controlling the radial distribution of dopants present within the NPs (*i.e.*, either having dopants be randomly distributed, or only concentrated in the core or shell) as demonstrated by Milliron and Hutchison separately,[92-93] the

LSPR properties of ITO NPs can be controlled to improve their LSPR quality factor, a figure of merit used to describe the ratio of LSPR energy to the peak full width half max (FWHM). For a plasmonic degenerately-doped semiconductor NPs to perform optimally, the materials should ideally have a high quality factor, which describes minimal electronic damping caused by the presence of aliovalent or impurity scattering within the lattice (*vide infra*).[92-94] Specifically, while the authors could systematically shift the LSPR of ITO NPs as a function of modulating In_2O_3 shell thickness, by fixing the amount of %Sn in a system but varying the radial distribution (either in random distribution through the NP, localized on the shell and the core), Crockett and coworkers could control the LSPR energy as well as the peak FWHM, indicating that the location of the aliovalent dopants could further activate the carriers participating in the collective oscillation upon incident light (**Figure 1.8A**).[93]

For plasmonic copper chalcogenide systems, as their plasmonic features arise from Cu^{1+} oxidation to Cu^{2+},[55, 57, 62] the radial distribution of dopants cannot be controlled systematically. However, the Cu ions are known to be mobile within the semiconductor lattice and there remains considerable ambiguity in the stoichiometry and chemical environments of Cu in copper chalcogenide NPs, and specifically the population and location of Cu^{+} and Cu^{2+} species.[95-98] For example, apart from identifying small CuO discrete NPs forming as function of time during the oxidation of the original Cu_2Se NPs, Manna and coworkers observed a thin coating of oxygen present at the NP surface.[95] Prieto et al. have also observed the presence of surface CuO on $Cu_{2-x}Se$ NPs and suggested that a diffusion gradient is established within the NP between Cu^{+} and Cu^{2+}, which drives Cu^{+} diffusion to the surface (i.e. vacancy formation) and results in x Cu deficiencies in the $Cu_{2-x}Se$ core.[98] Talapin, da Como, and coworkers also suggest that most copper does not leave the particle upon oxidation, and instead that Cu^{2+} species are distributed throughout the particle with some coordinated to pendant ligands and some ions sequestered in surface CuO layers.[96] Interestingly, recent work by Gamelin et al. has shown that the plasmonic features of $Cu_{2-x}S$ NPs can arise both with or without the presence of cation vacancies, and the presence of these vacancies is dictated by the particle oxidation pathway.[97] Finally, as it will be discussed in detail in **Chapter 3.0**, Kaseman et al. used electron paramagnetic resonance spectroscopy (EPR) to identify the presence of Cu^{2+} residing predominantly on $Cu_{2-x}Se$ NP surface, existing as two distinct identities: copper-ligand species as well as thin or even "patchy" copper oxide species (**Figure 1.8B**).[99] Importantly, these results not only start to address the ambiguity of the identities of Cu oxidation upon the emergence of the LSPR features in copper chalcogenide systems, they also provides a chemical picture of the surface chemistry of these materials as a function of Cu:X (X = S, Se, Te) composition changes, providing important insights into whether the surface of copper chalcogenide NP systems is amenable for plasmonically-driven catalytic reactions.

To test that idea, Gan et al. also discussed introducing some complexities in the surface chemistry of plasmonic $Cu_{2-x}Se$ NPs via mass action ligand exchange (see **Section 5.3.4**).[100] Specifically, they used ligand exchange methods to introduce a polymeric stabilizing ligand, polvinylpyrrolidone (PVP) to the NP surface, and probed how does the presence of a sterically bulk ligands influenced the reaction yield of a plasmonically driven dimerization reaction of NBT to DMAB on the NP surface. Interestingly, they did not observe any change in the reaction between using $Cu_{2-x}Se$ NPs before and after ligand exchange, and concluded that the presence of oleylamine, copper oxide, and even the additional PVP on the NP surface did not inhibit the dimerization process.[100-101] Importantly, this experiment also further supports the notion that the NBT dimerization reaction is limited by the proximity between two nitro molecules relative to one another, and demonstrates that this plasmon-mediated chemical reaction may be versatile in a more complex $Cu_{2-x}Se$ NP surface environment.

1.3.3 Improving Key Figures of Merit of Non-Noble Metal Plasmonic Substrates

Apart from establishing a chemical picture of the degenerately-doped NP surface, the photophysical properties of these alternative plasmonic systems also need to be understood. Specifically, in order to fully take advantage of the plasmonic properties of degenerately-doped semiconductor NPs, it is critical to identify figures of merit such as the plasmon dynamics. Referring back to how an LSPR perturbs the density of states around the Fermi level in noble metals (**Figure 1.1D**), we first want to compare whether or not the plasmon dynamics for degenerately-doped semiconductor NPs behave on the same timescale as their noble metal counterparts.[102] To that end, transient absorption (TA) spectroscopy has been a powerful technique for studying the photophysical aspects of degenerate-doped semiconductor NPs.

One of the first reports on the plasmon dynamics of $Cu_{2-x}Se$ NPs was reported in 2011 by Scotognella and coworkers using TA spectroscopy.[103] Specifically, by using a 1050 nm excitation wavelength at 150 fs pulses, the authors measure the bleach of the LSPR feature over a short period of time, which is a first indication of the perturbation on the free carrier distributions. Using the bleach in the LSPR intensity, the authors extracted carrier relaxation lifetimes and determined two distinct components: a fast component that can be attributed to the carrier-phonon relaxation time, and a slower component that can be attribute to the phonon-phonon relaxation time, both of which exist at comparable timescales as noble metal plasmonic NPs (**Figure 1.9A**). Importantly, the TA profiles indicate that the heat can be generated from the dephasing of the carriers upon collective oscillation, which is then transferred to the NP surrounding media, following the Two Temperature

Model that is often used to describe plasmon dynamics of hot carriers in noble metals.[102] Since then, Yang and Blemker have separately reported similar plasmon-mediated photothermal heating in $Cu_{2-x}Se$ and ITO NPs using similar ultrafast approaches.[104-105] Specifically, Yang et al. observed plasmonically-mediated heat transfer from $Cu_{2-x}Se$ to adsorbed Rhodamine B as a thermal reporter (**Figure 1.9B**),[104] while Blemker et al. reports similar timescale changes in the reflectivity of ITO NP thin films, demonstrating the ability of using degenerately-doped plasmonic semiconductor NPs for terahertz broadband photonic applications (**Figure 1.9C**).[105]

While the progress of understanding the photophysical properties of earth-abundant plasmonic materials are advancing, whether or not their performance can match or even surpass their noble metal counterparts remains to be established. An important step in determining the extent of their versatility is to establish and demonstrate the control over other important LSPR figures of merit. For example, plasmonic figures of merit such as the extinction coefficient of traditional noble metal NPs can be expressed in terms of the Mie-Gans theory, where their extinction intensities are comprised of both absorption and scattering components.[1, 23, 106] Further, for noble metals, it has been widely demonstrated that the plasmonic intensity can be easily manipulated through the scattering cross-section by modulating NP size and/or shape.[106-109] For example, Jain and El-Sayed’s simulations of plasmonic Au and Ag NPs show tunable extinction coefficients as a function of increasing NP size.[107] It was also demonstrated that the scattering intensities of the plasmonic substrates can be tuned via NP shape anisotropy and/or the formation of hot spots.[13, 23-24, 106-107, 110] To optimize and compare the performance of non-noble metal plasmonic NPs, it is important to understand and compare the plasmonic extinction tunabilities of semiconductor NPs to those of their noble metal counterparts.

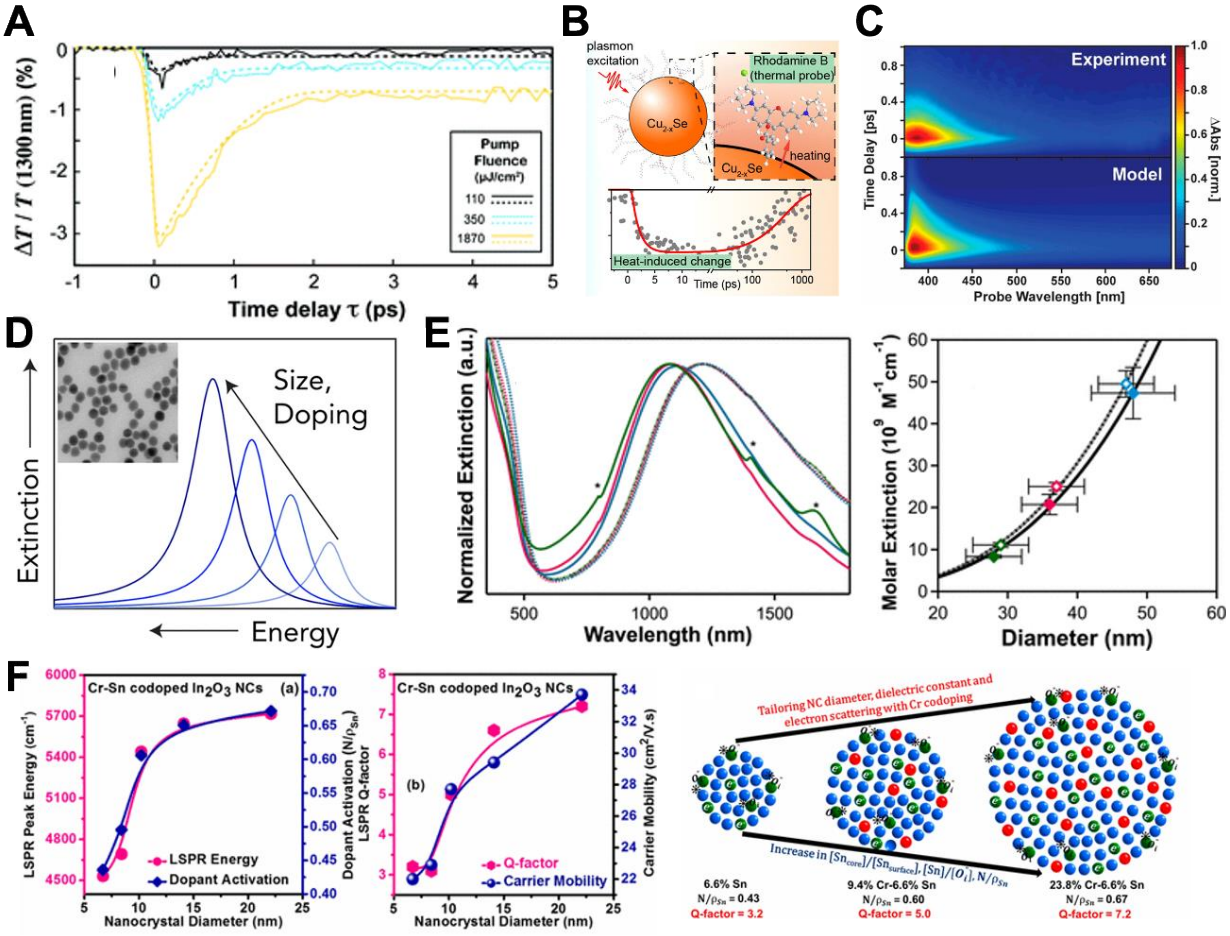

Figure 1.9. Ultrafast plasmon dynamics of degenerately-doped semiconductor NPs. (A) Transient absorption spectroscopy show depletion in the LSPR of $Cu_{2-x}Se$ NPs within picosecond timescale at different pump fluence. (B) Schematic showing plasmonically-driven heat transfer from $Cu_{2-x}Se$ to Rhodamine B. (C) Simulated and experimental reflectivity of ITO films within picosecond timescale. LSPR modulation: (D) Size dependent shifts in the LSPR energy and extinction intensity in ITO NPs. (E) LSPR energy of $Cu_{2-x}Se$ controlled by Cu:Se composition rather than NP diameter (left) and molar extinction coefficient controlled by NP diameter. Solid lines and diamonds represent $Cu_{1.4}Se$ NP samples, dotted lines and open diamonds represent $Cu_{1.8}Se$ NPs. (F) NP diameter induced shifts in LSPR peak energy and dopant activation as a function of %Cr incorporation in ITO NPs (left), NP diameter induced increase in LSPR Q factor and carrier

mobility as a function of % Cr incorporation in ITO NPs (middle), and schematic represents co-doping ITOs with Cr^{4+} increases NP diameter and LSPR performances while %Sn is kept constant (right). (A) adapted with permission from Ref. 103, Copyright 2011 American Chemical Society. (B) adapted with permission from Ref. 104, Copyright 2021 American Chemical Society. (C) adapted with permission from Ref. 105, Copyright 2020 American Chemical Society. (D) adapted with permission from Ref. 111, Copyright 2021 American Chemical Society. (E) adapted with permission from Ref. 101, Copyright 2020 American Chemical Society. (F) adapted with permission from Ref. 94, Copyright 2017 American Chemical Society.

Gibbs and coworkers have established the molar extinction coefficient of ITO NPs as a function of varying both the dopant incorporation as well as the NP volume.[111] Interestingly, the authors observed that by increasing the size of ITO NPs, not only do they observe an increase in the LSPR extinction coefficient, the LSPR energy also shifts to high energy (**Figure 1.9D**). They attribute such effects are likely due to the presence of the surface depletion layers discussed previously in **Section 1.3.2**, and the surface depletion effects are more prominent when the NP volume decreases. Importantly, this result provides an important insight: obtaining molar extinction coefficients of these materials can be challenging because of unavoidable convoluting factors such as carrier density anomalies, [111-112] surface depletion, [91, 111] and quantum confinement effects.[49, 66] Therefore, in order to study plasmonic extinction properties in this material class, it is important to select systems that have a suite of sizes available in which size-dependent changes in carrier density, surface depletions, and quantum confinement are minimized.

To that end, Gan et al. synthesized a range of $Cu_{2-x}Se$ NPs with increasing diameters and monitored changes in both the LSPR energy and intensities (see **Chapter 4.0** for details).[101]

Interestingly, unlike what was observed in ITO NPs, the energy of the LSPR output wave did not change as a function of increasing in NP diameter unless the Cu:Se compositions were deliberately altered (**Figure 1.9E, left**). Instead, when the LSPR intensities were established through extracting the molar extinction coefficients at various sizes, the authors observed that the size-dependent trends in molar extinction follow well the trends predicted by Mie theory traditionally used to describe noble metal NPs (**Figure 1.9E, right**). Additionally, while the size-dependent trend was also established for $Cu_{2-x}Se$ NPs of different carrier densities (*i.e.*, compositions), the authors still saw that the NP volume was the dominant factor in influencing the LSPR extinction coefficient, demonstrating the ability to modulate both LSPR intensities and energies through different experimental parameters.

Apart from establishing molar extinction coefficient, another important figure of merit that will determine the performance of alternative plasmonic systems is the LSPR quality factor (LSPR energy: FWHM ratio, *vide supra*). Briefly, the width of the LSPR is often used to determine the electronic damping within the semiconductor lattice, and this effect is mostly caused by the presence of aliovalent or impurity scattering in metal oxide NPs.[92-94, 113] While controlling the radial distribution of aliovalent dopants in metal oxides has been reported to improve the LSPR quality factor by “activating” the carriers that are participating in the collective oscillation, Tandon and coworkers introduced a secondary aliovalent dopant to improve the LSPR quality factor. Specifically, while keeping the %Sn constant, the authors introduce Cr^{4+} in ITO NPs, and the resulting lattice expansion from the infiltration of Cr dopants causes NP diameters to increase (**Figure 1.9F**). Further, the incorporation of Cr also causes the LSPR energy to blueshift while decreasing the peak FWHM. This is a remarkable observation because not only does it demonstrate that the LSPR feature can be further improved without altering the carrier densities present (%Sn), the incorporation of Cr also improves the ITO NPs' quality factor 3.2 to 7.2, demonstrating the importance of activating carriers that are participating in the LSPR photophysical process.[94]

Taken together, since the discovery of degenerate-doped semiconductor NPs as a viable non-noble metal plasmonic alternative was only made less than a decade ago, there has been enormous progress in the understanding of basic aspects of the LSPR features, as well as ways to improve the LSPR performance of degenerately-doped semiconductor NPs. Owing to thus growing body of knowledge, we can begin to test the plasmonic performance of these alternative materials in plasmon-mediated photocatalysis.

1.4 Examples of Plasmonic Photocatalysis using Degenerately-Doped Semiconductor Nanoparticles

Since the first report of degenerately-doped semiconductor NPs exhibiting plasmonic behavior in 2011,[49] these systems have been used for many exciting applications, and in particular for plasmon-driven catalysis. Recalling what was discussed previously in **Section 1.2**, the introduction of incident light causes the collective oscillations of carriers in plasmonic systems, generating athermal distribution of energetic holes and electrons that could either be transferred to nearby substrates including molecular adsorbates, catalytically active metal NPs, or Schottky barrier forming semiconductor systems. One of the first examples of plasmon-driven chemical reactions using degenerately-doped semiconductor NPs was reported in 2015, where Huang and coworkers used heterostructures containing plasmonic Cu_7S_4 and Pd NPs to catalyze Suzuki coupling reactions (**Figure 1.10A**).[114] Specifically, the authors studied the conversion rate between iodobenzene and various arylboronic acids in various conditions. They observed little to no conversion activity when monocomponents of either CuS or Pd NPs separately were used as catalysts, but observed a higher conversion rate when both components were combined in the form heterostructures under light illumination. This result first indicates the synergistic effects between both components, as the discrete mixtures of both components do not perform as well as the heterostructures. Additionally, the authors concluded that the Suzuki coupling reaction is catalyzed via plasmonically-mediated charge transfer instead of photothermal effect. Specifically, the hot holes generated by plasmonic Cu_7S_4 are transferred onto the Pd surface through a low energy Schottky barrier, facilitating the coupling reaction. Importantly, this first example demonstrates the feasibility of plasmonically-driven charge transfer using non-noble metal plasmonic alternatives.

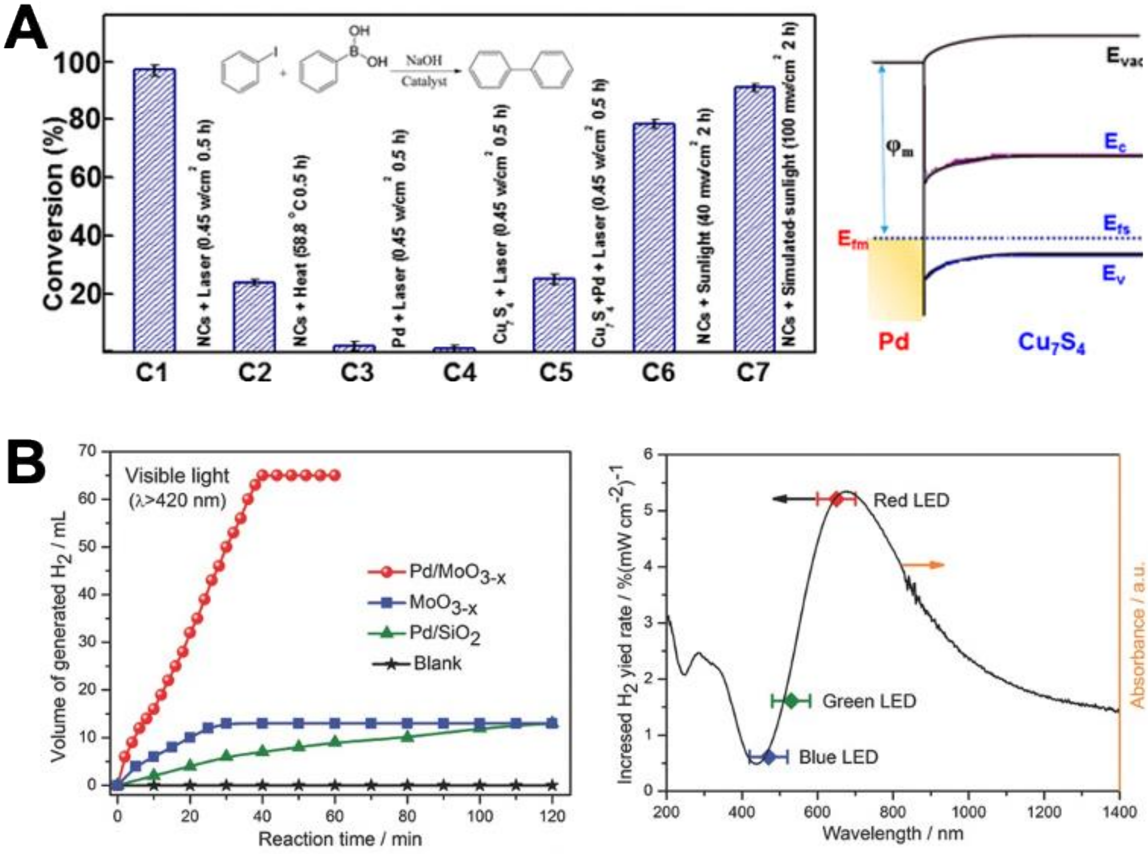

Figure 1.10. (A) Suzuki coupling reaction conversion rate using Cu_7S_4-Pd heterostructures under different reaction conditions including individual Cu_7S_4 and Pd components (left) and energy diagrams of Cu_7S_4-Pd heterostructures (right). (B) Light-driven H_2 generation reaction efficiencies between Pd-MoO_{3-x} heterostructures and MoO_{3-x} and Pd-SiO_2 control experiments (left), and excitation energy dependent H_2 generation reaction efficiencies following the LSPR of the Pd-MoO_{3-x} heterostructures (right). (A) adapted with permission from Ref. 114, Copyright 2015 American Chemical Society. (B) adapted with permission from Ref. 115, Copyright 2015 WILEY-VCH Verlag GmbH & Co. KGaA, Weinheim.

Subsequently, similar synergistic behavior between other plasmonic degenerately-doped semiconductors and catalytically active metals such as Pd and Pt have been reported.[115-116]

Specifically, Yamashita et al. reported a plasmonically-catalyzed H_2 generation reaction through the hydrolysis of NH_3BH_3 using degenerately-doped molybdenum oxide (MoO_{3-x}) and Pd heterostructures.[115] Similar to what was reported by Huang, the heterostructures perform better than the individual components under illumination (**Figure 1.10B, left**), where they observed the highest H_2 volume produced at the fastest rate when a red LED (λ_{max} = 650 nm) is used, which is close to the LSPR peak maximum of the MoO_{3-x} substrates (**Figure 1.10B, right**). Xue also reported similar Suzuki coupling reactions as Huang using Pd decorated degenerately-doped tungsten oxide (WO_{3-x}) nanowires and observed no reaction when only using Pd NPs alone.[116] Interestingly, they observed some reaction (though with much lower yields) in the dark, indicating that thermal effects could still play a role catalyzing the reaction. Nonetheless, the authors reported that the plasmonically-generated hot carriers that are transferred to Pd surfaces are the dominant factor in this catalytic reaction. While these examples do not demonstrate catalysis using the plasmonic components alone, they do importantly demonstrate that degenerately-doped semiconductor NPs can still power photocatalytic processes by coupling with other catalytically active metals.

Instead of coupling degenerately-doped semiconductor NPs with catalytically-active metals, another useful strategy to efficiently extract hot carriers from these alternative plasmonic substrates is by creating heterostructures with other semiconductor NPs. Similar to noble metal plasmonic systems,[3, 10, 25-27] the presence of a semiconductor NPs nearby can improve the charge transfer efficiency by preventing charge carrier recombination.[117-118] For example, by making CuS/CdS heterostructures, Teranishi and coworkers used time-resolved IR spectroscopy to study the lifetimes of plasmonically generated hot holes.[118] Specifically, by monitoring the carrier relaxation behaviors both in the picosecond range and microsecond range, the authors rationalized that the generated hot holes are transferred to CdS deposited on the CuS nanoplatelets and that these holes are then trapped in CdS trap states (**Figure 1.11A**). The authors discovered three different relaxation components instead of the two components which are traditionally observed in the LSPR decay behavior, where the third component is much longer (nanosecond range). The longer-lived carrier is consistent with the hypothesis that the presence of semiconductor NPs along with plasmonic systems prevent hot carrier recombination. As a proof of concept, the authors also studied the degradation of methylene blue as an example of a catalytic reaction, and reported that the heterostructures are more efficient as plasmonically-driven photocatalysts than just the plasmonic CuS alone. Importantly, these results are the first extensive studies on the charge transfer timescale and mechanism using degenerately-doped semiconductor NPs, which are important figures of merit to establish for improving the performance of plasmonically-driven catalytic reactions.

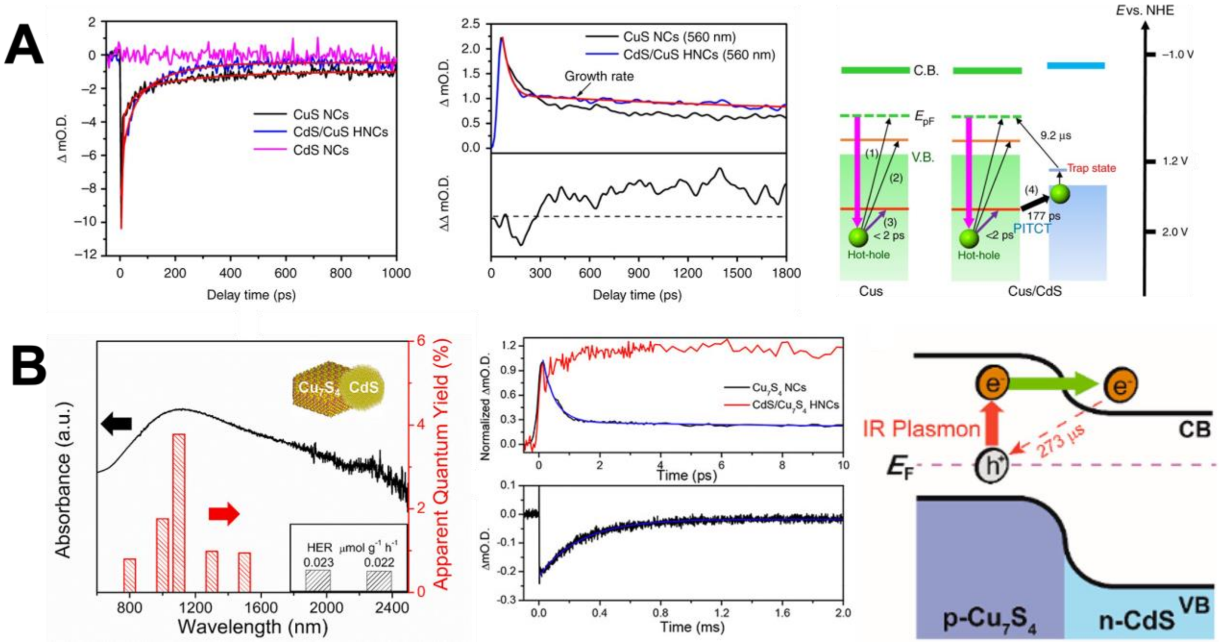

Figure 1.11. (A) Transient absorption spectroscopy shows relaxation profiles of CuS and CuS-CdS heterostructures, observing a fast and slow component in the picosecond timescale (left), transient absorption spectroscopy of CuS-CdS heterostructures show a ternary component that decays much slower well into the nanosecond timescale (middle), schematic showing plasmon-generation hot hole injection from CuS to a trap state within the CdS domain, which is attributed to the ternary relaxation component. (B) Hydrogen evolution efficiencies of Cu_7S_4-CdS heterostructures expressed as apparent quantum yield as a function of excitation wavelength, following the LSPR profile of the heterostructures (left), transient absorption spectroscopy shows relaxation profiles of Cu_7S_4-CdS heterostructures compared to Cu_7S_4 alone, indicating a much longer-lived component well into the millisecond timescale (middle), which the authors attribute to the hot carrier separation due to the formation of a p-n junction formed between Cu_7S_4-CdS domains (right). (A) adapted with permission from Ref. 118, Copyright 2018 Lian et al. (B) adapted with permission from Ref. 117, Copyright 2019 American Chemical Society.

Further, Teranishi also reported that the Schottky barrier generated between plasmonic Cu_7S_4 and CdS heterostructures significantly increased the H_2 generation product when excitation wavelength of 1100 nm was used in the experiment (**Figure 1.11B**).[117] Upon monitoring the carrier relaxation dynamics using ultrafast spectroscopy, the authors observed an ultralong-lived separation between plasmonically-generated hot electrons and holes in the millisecond range, which the authors attribute is due to the presence of a p-n heterojunction (**Figure 1.11B, right**). Remarkably, this is currently the highest record of apparent quantum yield (3.8%) reported for IR light-induced H_2 evolution, demonstrating that non-noble metal plasmonic substrates perform as comparably with other state-of-the-art plasmonic hydrogen evolution catalysts reported.[119]

Interestingly, Sun and coworkers recently reported using Au@CuS core@shell heterostructures and demonstrate multimodal photocatalytic reactions by exciting either the Au or CuS LSPR.[120] Using the Rhodamine B (RhB) degradation reaction in the presence of H_2O_2 as the model catalytic reaction, the authors studied the rate of reaction mediated by different excitation wavelength (l_{Ex} = 980 nm, 638 nm, and 445 nm) to probe various photochemical processes: CuS LSPR-mediated charge transfer, Au LSPR-mediated charge transfer, and CuS excitonic charge transfer, respectively (**Figure 1.12A**). The authors identified that the plasmonically driven hot electron is transferred to H_2O_2 to initiate $^{\bullet}OH$ generation, while the hot holes are consumed by O_2 evolution in water. Interestingly, the reactions rates show that both LSPRs are comparable to each other as well as the high-energy excitonic-mediated mechanism, indicating that either plasmonic excitation is able to catalyze the RhB degration reaction (**Figure 1.12B**). Importantly, not only does this report demonstrate the use of dual-plasmonic behaviors to drive chemical reactions, it also demonstrates that the CuS alternative plasmonic systems perform on a similar caliber as the well-understood traditional noble metal counterpart.

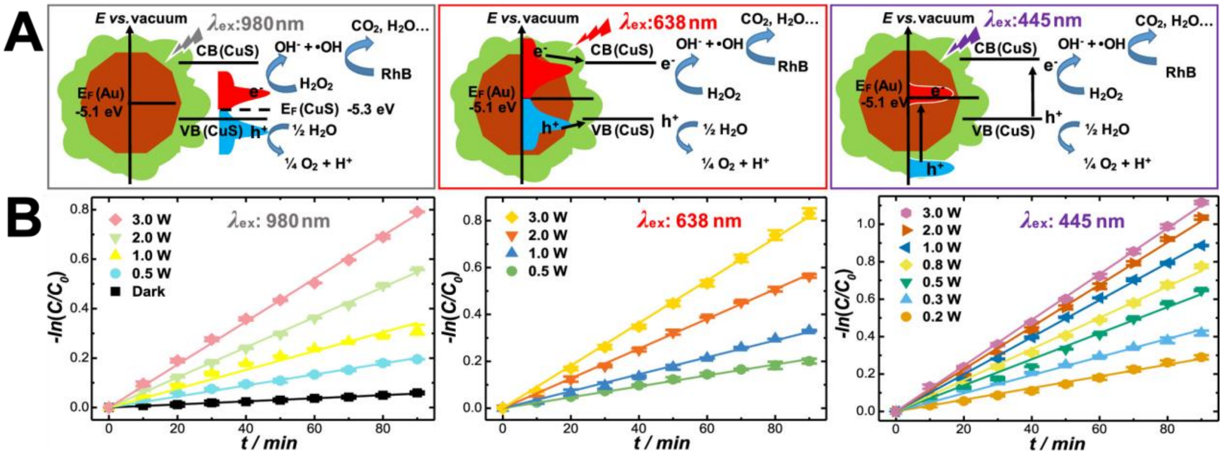

Figure 1.12. (A) Schematic depicting various light-driven mechanisms for the degradation of Rhodamine B using Au@CuS heterostructures either through the excitation of CuS LSPR (left), Au LSPR (middle), and CuS excitonic transition coupled with Au interband transition (right), and their corresponding power-dependent reaction rates (B). (A) adapted with permission from Ref. 120, Copyright 2020 American Chemical Society.

Ultimately, it is important to note that Sun's work did not demonstrate synergistic effects between Au and CuS, indicating that it is possible to use degenerately-doped semiconductor plasmonic substrates alone as comparable photocatalysts.[120] Similarly, as it will be discussed in **Chapter 5.0**, Gan et al. reported using monocomponent plasmonic $Cu_{2-x}Se$ NPs alone to drive the dimerization of NBTs (**Figure 1.13A**).[100] Using SERS and exciting the $Cu_{2-x}Se$ LSPR, the authors observed the formation of Raman features that were assigned to the DMAB products. By measuring the ratio of the intensities of product over the reactant peaks, the authors measured reaction yield, and reported that the dimerization reaction yield is comparable to what was reported using noble metal plasmonic substrates.[31] Importantly this result provide several insights: 1. although the dimerization reaction is plasmonically-driven, it is limited by the proximity between

NBT molecules on NP surface, and 2. even though the LSPR of copper chalcogenides such as $Cu_{2-x}Se$ NPs is initiated by the collective oscillation of degenerate holes, the plasmonically-generated hot electrons are more energetic than holes to drive this reduction reaction, indicating that similar to plasmonic noble metal nanomaterials, both hot holes and electrons are amenable to be transferred to catalyze different reactions, depending on their hot carrier energetic distributions.

Additionally, Zhou and coworkers recently used transient absorption spectroscopy to report the use of monocomponent plasmonic F and In co-doped cadium oxide (FICO) NPs to generate hot electrons which are then indirectly-transferred to the LUMO orbital of RhB molecules.[121] Specifically, the authors used variable pump energy to study the charge transfer quantum yield and experimentally identified the energy difference between the FICO NP's Fermi level and RhB's LUMO orbital (E_b) to be 0.68 eV (**Figure 1.13B**). Importantly, this example demonstrates that the plasmonically-driven hot carriers generated by degenerately-doped semiconductor NPs can be transferred to adsorbates using similar mechanisms identified in noble metal plasmonic systems.[5, 17, 29]

Taken together, while the design and development of degenerately-doped semiconductor NP are still at its infancy, the increase in the number of examples showcasing plasmonically-driven photocatalysts demonstrate a promising outlook in the burgeoning field of light-driven catalytic applications.

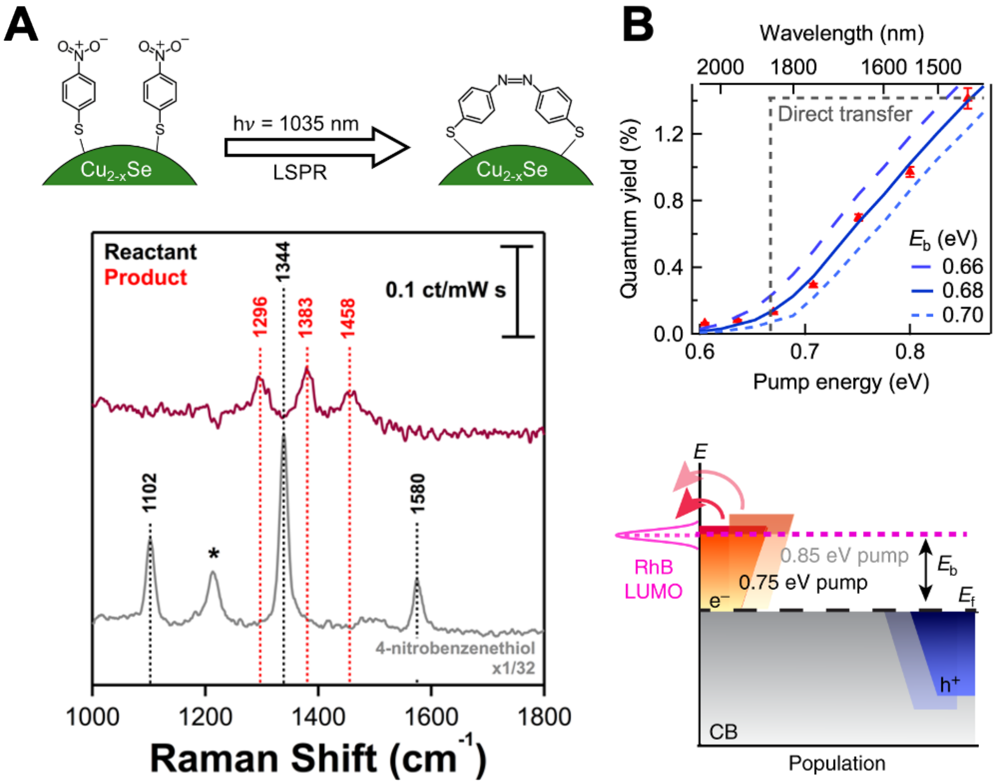

Figure 1.13. (A) Scheme depicting the dimerization reaction of NBT to DMAB on $Cu_{2-x}Se$ NP surface (top) observed using the difference surface-enhanced Raman spectrum (bottom). (B) Pump energy-dependent hot electron transfer quantum yield observed in F and In co-doped cadmium oxide NPs and scheme depicting indirect hot electron transfer from plasmonic NPs to Rhodamine B LUMO orbital. (A) adapted with permission from Ref. 100, Copyright 2019 American Chemical Society. (B) adapted with permission from Ref. 121, Copyright 2020 Zhou et al.

1.5 Conclusion and Outlook

This dissertation highlights the wealth of opportunities that plasmonically-driven chemistry can provide, and the implementation of plasmonic systems in real-world technologies can be accelerated through the use of cost-effective, earth-abundant alternative materials such as degenerately-doped semiconductor NPs. While the fundamental understanding and demonstrations of plasmonically-driven photocatalysis using degenerately-doped semiconductor NPs are still at their early stages, having the well-understood noble metal counterparts as guideposts will allow researchers to map out the next series of studies to be tackled. Importantly, by comparing plasmonically-driven photocatalysis in both systems, we outline several missing links and other pieces of information that require more attention within the community that could provide a leap forward for the translation of earth-abundant plasmonic systems as effective and comparable alternatives.

In particular, the hot carrier dynamics (i.e., timescales and energetic distributions of the electrons and holes) of degenerately-doped semiconductor NPs will be an important piece of information to fully understand the LSPR process in these systems, which, in turn, will enable them to be effectively used as photocatalysts. For example, from several seminal computational works discussed previously, the energetic distributions of photoexcited holes and electrons vary as a function of the identity of the plasmonic system, because these energetic distributions are derived from the electronic band structures of the material.[2, 4, 16, 37] While the density of states in noble metals are mostly focused between d and sp bands, an additional feature that would complicate the analysis of the hot carrier distribution would be the presence of conduction and valence bands, as well as a bandgap. Thus, an important next step is to be able to extract hot carrier energetic distribution while separating out bandgap transitions.

Additionally, information about the timescale of hot carrier relaxation in degenerately-doped semiconductor plasmonics will provide important insights in the feasibility of plasmon-driven hot carrier transfer. For example, Frontiera and coworkers used an ultrafast SERS method to study the timescale of the plasmon-mediated NBT dimerization reaction on Au NP aggregates, and discovered transient changes in the carrier densities on plasmonic substrates due to charge transfer.[33] While an exciting step forward was the first demonstration of the NBT dimerization reaction using plasmonic $Cu_{2-x}Se$ NPs,[100] the dynamics, decay and transfer of hot carriers are largely unknown and need to be studied, likely via similar ultrafast measurements and computational models.

Once the timescale and dynamics of hot carriers are established, one can systematically start designing complex heterostructures containing these plasmonic degenerately-doped semiconductor NPs to facilitate the hot carrier transfer process, much like the use of semiconductors to act as Schottky barriers for plasmonic noble metals that prevents the recombination of hot electrons and holes.[2, 10, 27, 41] It would be interesting to design heterostructures with several key components, for example, heterostructures containing only semiconductors with different purposes, one acting as the plasmonic substrate, while the other acting as a Schottky barrier to aid in efficient charge transfer. Additionally, as observed in several reports, many plasmonic semiconductor NPs participate in plasmonically-mediated catalysis through the assistance of catalytically active metals. With these structural differences in mind, it would be ideal to be able to establish design rules to create heterostructures with either another semiconductor component or a metallic component, starting with the plasmonic semiconductor NPs (**Chapter 6.0**). Once these synthetic strategies are established, we can begin to study the charge transfer properties in more detail and identify the importance of these heterostructure domains and their synergistic effects in the development of plasmonic photocatalysts using earth-abundant alternatives.

2.0 Correlating Carrier Density and Emergent Plasmonic Features in $Cu_{2-x}Se$ Nanoparticles

(Portions of this work were previously published and reprinted with permission from Marbella, L. E., Gan, X. Y., Kaseman, D. C., Millstone, J. E., *Nano Letters* **2017**, *17*, 2414 – 2419. Copyright, 2017, American Chemical Society.)

2.1 Introduction

As described in **Chapter 1.0**, plasmonic materials have been shown to enhance or enable a myriad of technologies including theranostics,[122] heterogeneous catalysis,[3] water purification,[123] and photovoltaic design.[124] The vast majority of these demonstrations use noble metal (e.g., Au and Ag) nanoparticles (NPs), but the cost of these materials has motivated the study of alternatives,[56, 125] such as Al-based NPs,[22, 126] degenerately doped metal chalcogenide and metal oxide NPs,[49, 52, 127-130] as well as carbon-based nanomaterials.[131] The synthesis and characterization of non-noble metal plasmonic NPs can be significantly more challenging than their noble metal analogues, in part due to additional complexity in synthetic outcomes such as oxide layer thickness in Al-based NPs,[126, 132] and spatial distribution of dopants in semiconductor NPs.[92] Therefore, successful non-noble metal plasmonic technologies depend not only on the development of new material syntheses but also on detailed structural characterization of the particle products in order to understand and control their properties once formed.

For example, in degenerately doped semiconductor NPs, the charge carrier density can be manipulated via dopant concentration, providing an additional handle (alongside particle morphology and surface chemistry) with which to tune localized surface plasmon resonance (LSPR) features such as the wavelength of maximum emission.[133] Further, changes in carrier properties such as carrier heat capacity and effective carrier temperature may influence scattering and absorption cross sections as well as subsequent electromagnetic field enhancements.[103] Similarly, differences in carrier density and type (i.e., holes vs electrons) in a given material may offer the ability to drive specific reactions (e.g., reduction vs oxidation)[2, 35-36] with unprecedented control. Yet, fundamentally, in order to correlate charge carrier properties with behavior in NP systems, one must be able to measure charge carrier figures of merit quantitatively and routinely. Then, charge carrier properties can be correlated with NP features including crystallinity, composition, size, shape, and surface chemistry to comprehensively describe and leverage NP structure–property relationships.

Unfortunately, traditional material characterization techniques are often insufficient to describe charge carrier figures of merit that influence emergent optoelectronic properties in degenerately doped semiconductor NPs. For instance, the relatively high population of stabilizing ligands on NP surfaces (with respect to the number of constituent atoms in the particle core) often prohibits the extraction of carrier properties such as Hall and Seebeck coefficients, which are readily measured for non-colloidal materials.[134] In place of these traditional descriptors, extinction spectroscopy has been widely used to determine carrier density, most commonly via the Drude model.[58, 60, 66, 135] However, there are drawbacks to using the NP extinction spectrum to determine carrier densities for degenerately doped semiconductor NPs, because a variety of intrinsic and extrinsic system parameters may influence both spectral features and the interpretation of those features via the Drude model.[60, 66] For example, in addition to carrier density, sample properties such as particle aggregation and dispersity can influence the position and breadth of spectral features. In addition, the dielectric functions of both the particle and the surrounding medium (which may or may not be a convolution of solvent and pendant ligands), must both be known in order to apply this model. Each of these parameters is sensitive to NP composition, and may introduce ambiguity in the extracted carrier density values.[60] Finally, the type of carriers and their distribution in the material cannot be assessed from extinction spectroscopy without computational simulations and/or additional experimental characterization.

One powerful technique to address these issues is solid-state NMR (ssNMR) spectroscopy. Solid-state NMR can reveal general properties about electronic structure such as whether a material is metallic or semiconducting,[70-72] as well as provide specific details including charge carrier density,[73-75] spatial electronic heterogeneity (e.g., distribution of p- and n-type regions),[74-77] and even the type of free carriers present (electrons vs holes).[78] An additional advantage of ssNMR is the ability to perform in situ measurements to monitor these features as a function of time, chemical environment, or external stimuli.[79-80]

In this chapter, we analyze the emergence of a near-infrared (NIR) LSPR band in a well-studied, degenerately doped semiconductor NP system, $Cu_{2-x}Se$.[49, 60, 95-96, 98, 133, 136] Specifically, we use a combination of ^{77}Se ssNMR and traditional materials characterization (e.g., powder X-ray diffraction (PXRD) and high-resolution transmission electron microscopy (HRTEM)) to correlate $Cu_{2-x}Se$ NP composition and chemical structure with the resulting optoelectronic features (specifically, carrier density and the emergence of the LSPR). In addition, we compare carrier densities derived from NMR and extinction spectroscopy and analyze the origin of discrepancies between the two approaches.

2.2 Experimental Section

2.2.1 General Methods and Materials

Copper(I) chloride ($CuCl$, 99.995%), copper(I) selenide ($Cu_{2-x}Se$, 99.95%), selenium powder (Se, ≥ 99.5%), octadecene (90%, technical grade), oleylamine (70%, technical grade), hexanes (≥ 99.9%), anhydrous toluene (99.8%), and dimethyl selenide (Me_2Se, 99%) were purchased from Sigma Aldrich (St. Louis, MO). Absolute ethanol (EtOH) was purchased from Thermo Fisher Scientific (Pittsburgh, PA). Anhydrous solvents were freeze-pump-thawed at least three times before use. All other chemicals were used as received. Prior to use, all glassware and Teflon-coated stir bars were washed with aqua regia (3:1 ratio of concentrated HCl to HNO_3) and rinsed with copious amounts of water prior to drying. ***Caution:*** *Aqua regia is highly toxic and corrosive, and should only be used with proper personal protective equipment and training. Aqua regia should be handled only inside a fume hood.*

2.2.2 Synthesis of $Cu_{2-x}Se$ Nanoparticles

$Cu_{2-x}Se$ NPs were prepared according to a modified literature procedure using standard air-free techniques.[136] Briefly, 80 mg (1 mmol) of Se powder was added to 1 mL of octadecene and 2 mL of oleylamine and heated to 195 °C overnight in a round bottom flask. In a separate flask, 200 mg (2 mmol) of CuCl was added to 5 mL of octadecene and 5 mL of oleylamine in a three-neck flask. While stirring, the mixture was heated to 120 °C under vacuum. After holding at 120 °C for 30 min, the mixture was heated to 285 °C under Ar. The Se-octadecene-oleylamine mixture was rapidly injected into the CuCl-octadecene-oleylamine mixture, which led to a temperature drop to

275 °C. The resulting $Cu_{2-x}Se$ (x ~ 0) NPs were allowed to grow for 10 min before removing the heating mantle and cooling to room temperature.

The $Cu_{2-x}Se$ (x ~ 0) NP product was purified via centrifugation. First, the as-synthesized NPs were cannula-transferred to air-free centrifuge tubes containing 10 mL of EtOH and centrifuged in an Eppendorf 5804R centrifuge with a swing bucket rotor (A-44-4) (Eppendorf, Inc.) at a force of 2850 rcf at 20 °C for 5 min. The resulting supernatant was removed and the pellet was resuspended in a small amount of hexane or toluene for additional centrifugation in another 5 mL of EtOH. This washing procedure was repeated once. Stoichiometric $Cu_{2-x}Se$ (x ~ 0) NPs were either transferred to the glovebox for air-free characterization preparation or resuspended in hexane or toluene and exposed to air to produce oxidized $Cu_{2-x}Se$ ($x > 0$) NPs that could be handled outside the glovebox. All purified NPs were then characterized by electron microscopy techniques, ultraviolet-visible-near infrared (UV-vis-NIR) extinction spectroscopy, powder X-ray diffraction (PXRD), and ^{77}Se ssNMR spectroscopy.

2.2.3 Extinction Spectroscopy

Purified $Cu_{2-x}Se$ NPs were suspended in toluene and characterized by UV-vis-NIR extinction spectroscopy using a Cary 5000 spectrophotometer (Agilent, Inc.) in air-free quartz cuvettes (Starna Cells, Inc.) with a 1 cm path length modified with a high vacuum straight valve and PTFE plug (Kimble Chase). All spectra were baseline corrected with respect to the spectrum of toluene.

2.2.4 Transmission Electron Microscopy

Samples were prepared for electron microscopy by drop casting an aliquot of purified NP solution (diluted 1:10 or 1:100 with toluene) onto Formvar-coated copper transmission electron microscopy (TEM) grids (Ted Pella, Inc.) for routine bright field imaging analysis or thin film (< 10 nm) molybdenum 400 mesh carbon grids (Pacific Grid Tech, Inc.) for high resolution characterization. Air-free $Cu_{2-x}Se$ (x ~ 0) NPs were drop cast inside the glovebox and stored in an air-tight container for transport to the microscope. TEM characterization was performed on an FEI Morgagni TEM with an accelerating voltage of 80 kV. The size distributions of the NPs were determined from TEM images of at least 200 NPs from various areas of the grid using ImageJ 1.47d (National Institutes of Health, USA). High resolution transmission electron microscopy (HRTEM) characterization was performed using a FEI Tecnai G2 F20 S-Twin TMP microscope operating at 200 kV (Mechanical Engineering and Materials Science Department, University of Pittsburgh).

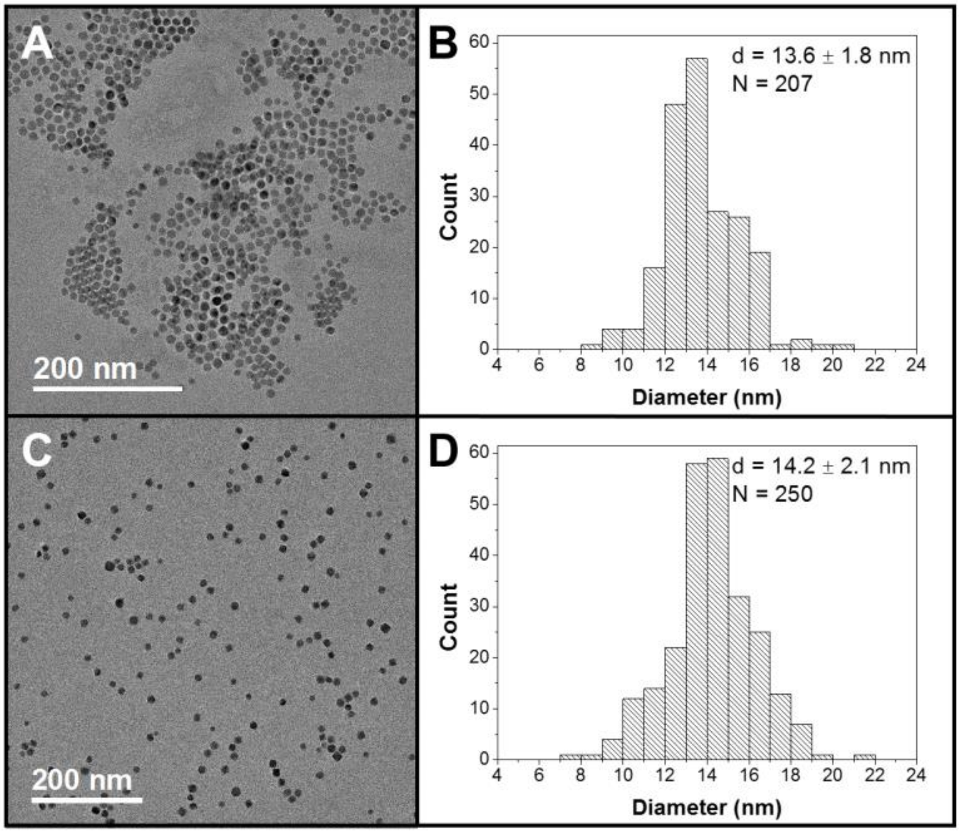

Figure 2.1. Transmission electron micrographs (A, C) and corresponding size histograms (B, D) for air-free (A, B) and air exposed (C, D) $Cu_{2-x}Se$ NPs.

2.2.5 Powder X-Ray Diffraction

For air-free preparations, $Cu_{2-x}Se$ NP powders were packed in 0.50 mm capillary tubes (Hampton Research) in the glovebox, plugged with grease, and flame sealed for PXRD characterization. PXRD patterns were collected on a Bruker X8 Prospector Ultra (Department of Chemistry, University of Pittsburgh) at 45 kV, 0.65 mA equipped with a IµS micro-focus Cu Kα X-ray source ($\lambda = 1.54178$ Å) with a scan speed of 0.5 s/step from 12.00-108.00° with a step size of 0.02°. Oxidized $Cu_{2-x}Se$ ($x > 0$) NPs were characterized by PXRD using a Bruker AXS D8

Discover XRD (NanoScale Fabrication and Characterization Facility, Petersen Institute of NanoScience and Engineering, Pittsburgh, PA) at 40 kV, 40 mA for Cu Kα (λ = 1.5406 Å) X-ray source with a scan speed of 0.5 s/step from 10.00-90.00° with a step size of 0.02°. Samples were prepared by drop casting an aliquot of purified NP solution (diluted 1:10 or 1:100 with toluene) on a glass microscope slide (Fisher Scientific).

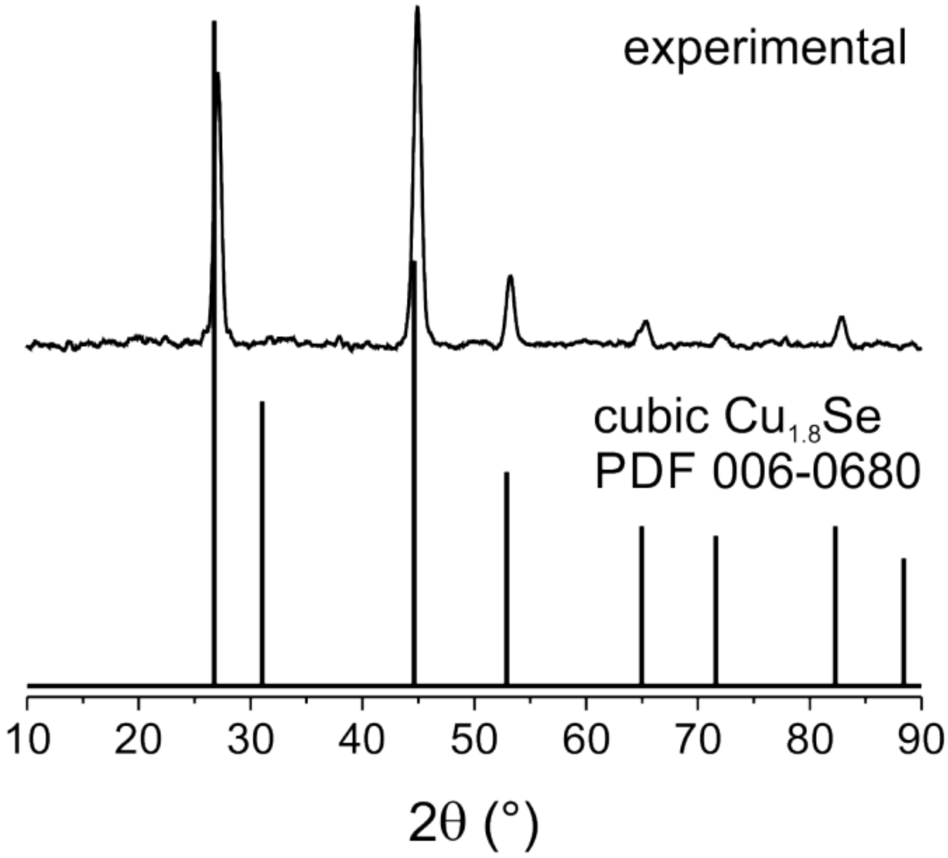

Figure 2.2. Experimental PXRD of $Cu_{2-x}Se$ NPs after oxidation (top) compared to PDF card 006-0680 for cubic $Cu_{1.8}Se$ (bottom).

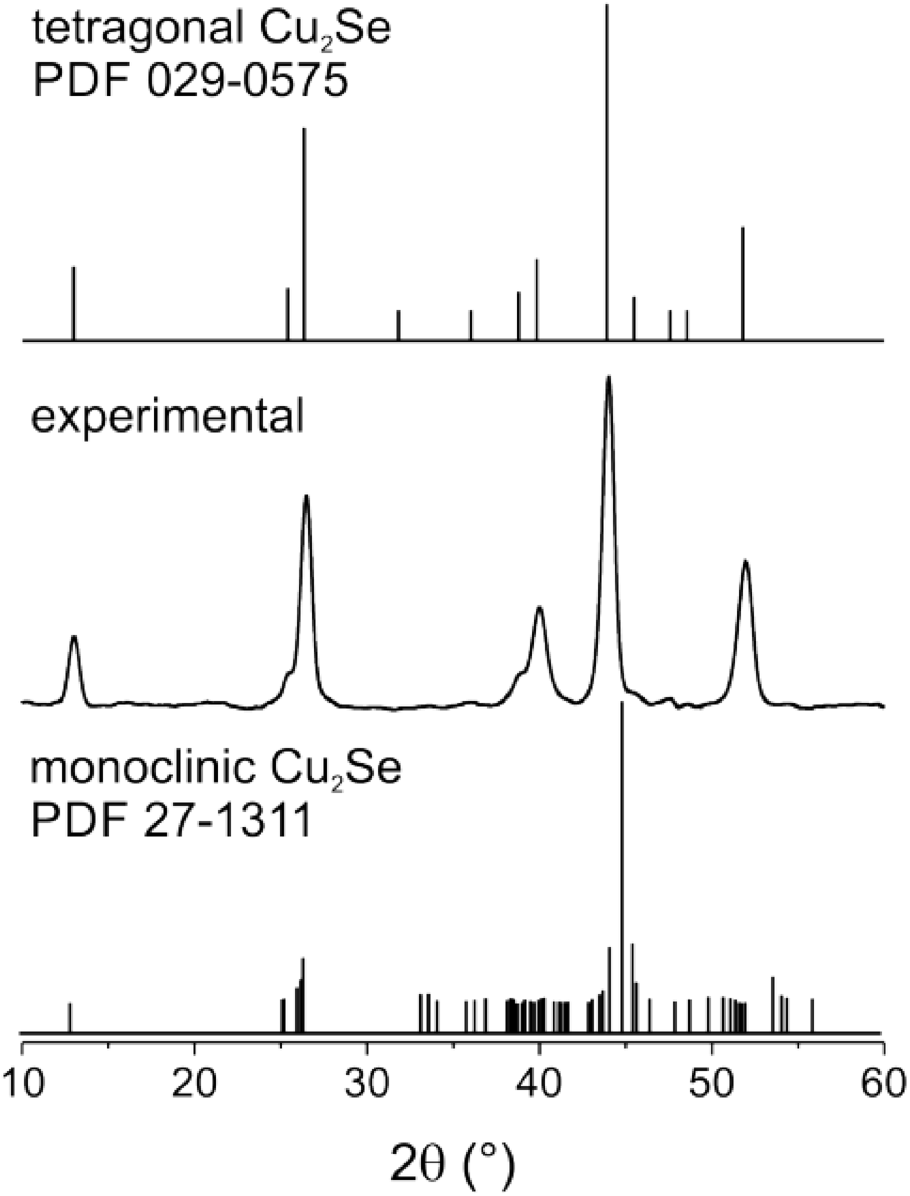

Figure 2.3. Experimental PXRD of $Cu_{2-x}Se$ (x ~ 0) NPs prepared in the glovebox (middle) compared to PDF cards 029-0575 (top) and 027-1311 (bottom) for tetragonal and monoclinic Cu_2Se, respectively.

Table 2.1. PXRD Derived Lattice Parameter, *a*, Corresponding Value of *x*, and Associated $Cu_{2-x}Se$ Electronic Properties.

Sample	*a* (Å)	Value of x^a	$m_h^{*\,b}$	$\varepsilon_\infty{}^b$	N_h PXRD (cm^{-3})
$Cu_{2-x}Se$ NPs	5.818	0.00	1.1	N/A	$<3.0 \times 10^{20}$
$Cu_{2-x}Se$ NPs	5.787	0.07	0.394	8	1.4×10^{21}
$Cu_{2-x}Se$ NPs	5.706	0.47	0.334	7	9.4×10^{21}
$Cu_{2-x}Se$ NPs	5.706	0.47	0.334	7	9.4×10^{21}
$Cu_{2-x}Se$ NPs	5.705	0.48	0.334	7	9.6×10^{21}
$Cu_{2-x}Se$ bulks	5.719	0.41	0.334	7	8.0×10^{21}

[a] $Cu_{2-x}Se$ sample compositions were evaluated using the data provided by Shafizade et al.[137] (**Figure 2.4**).

[b] These values were taken from Mansour et al.[63] based on the observed compositional changes. Although this reference does not describe m_h^* or ε_∞ for values of $x < 0.2$, work described by Gorbachev et al.[138]

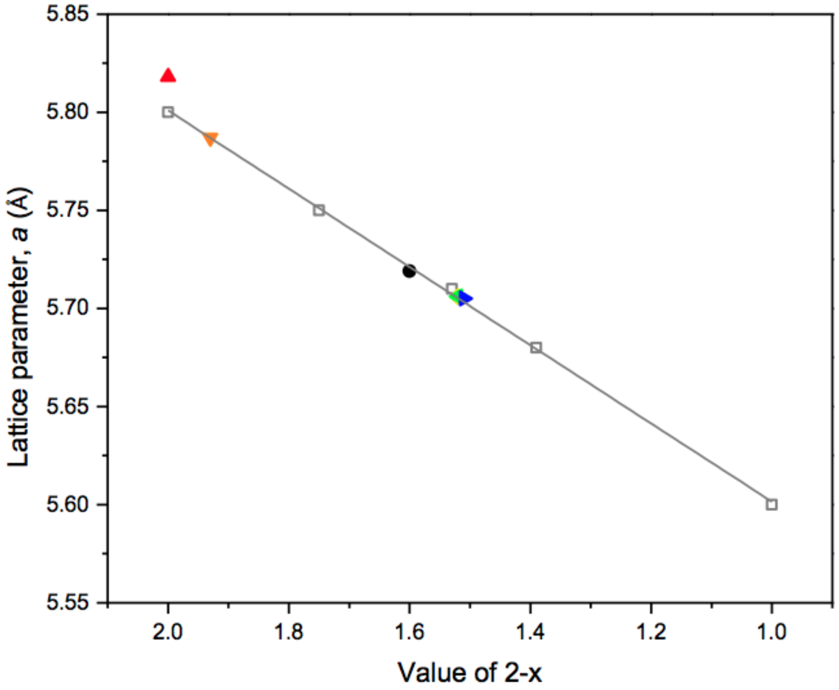

Figure 2.4. Lattice parameter, *a*, measured from the [220] PXRD peak (the 2θ peak at approximately 44-45°) for $Cu_{2-x}Se$ samples. The gray, open symbols correspond to composition dependent data compiled from Shafidaze et al.,[137] while the closed symbols represent the experimental data measured in our laboratory for bulk $Cu_{2-x}Se$ (black) and $Cu_{2-x}Se$ NPs (colored).

2.2.6 Inductively Coupled Plasma-Mass Spectroscopy

Inductively coupled plasma-mass spectrometry (ICP-MS) analysis was performed using an argon flow with a NexION spectrometer (PerkinElmer, Inc.). An ultrapure aqua regia solution was prepared with a 3:1 ratio of hydrochloric acid (Sigma-Aldrich, > 99.999% trace metal basis) to nitric acid (Sigma-Aldrich, > 99.999% trace metal basis) and diluted with water for a 5% (by volume) aqua regia matrix. Purified $Cu_{2-x}Se$ ($x > 0$) NP products were taken from the purified, concentrated pellet and digested overnight in ~100 µL of fresh, concentrated aqua regia solution. From the digested solution, 1 µL was further diluted to 2 mL using the 5% aqua regia matrix. To test for free Cu in solution upon particle oxidation (presumably in the 2+ oxidation state), the $Cu_{2-x}Se$ (x > 0) NP product was purified via centrifugation once more, as described above, to remove any unreacted Cu precursor in the as-synthesized reaction mixture. An aliquot of the resulting supernatant was taken and digested overnight in ~30 µL of fresh, concentrated aqua regia solution. From the digested solution, 10 µL was diluted to 2 mL using the 5% aqua regia matrix.

Unknown Cu concentrations were determined by comparison to a 5-point standard curve with a range of 1 - 30 ppb (1, 5, 10, 20, and 30 ppb prepared by volume) from a copper standard for ICP (Fluka, TraceCERT 1,001 ± 2 mg/L Au in HCl) diluted in the 5% aqua regia matrix. All standards were measured 5 times and averaged, while all unknown samples were measured in triplicate and averaged. A 5-minute flush time with 5% aqua regia matrix was used between all runs, and a blank was analyzed before each unknown sample to confirm removal of all residual metals from the instrument. (*N. B.* Se could not be detected using ICPMS due to argon interferences.)

Upon oxidation, Cu_2Se NPs undergo structural changes as detected by PXRD and ^{77}Se NMR. However, previous studies have hypothesized that Cu^{2+} may not leave the NP during oxidation in the form of molecular or hydrated complexes, but rather, may remain coordinated to the particle surface. To determine whether or not Cu^{2+} leaves the particle after oxidation, we used ICP-MS to determine Cu concentration in both the sample and the supernatant of oxidized $Cu_{2-x}Se$ (x > 0) NPs. ICP-MS analysis showed that the Cu concentration in the NP digest was 4.685 ± 0.020 mg/L (which accounts for Cu in the particle and possibly Cu^{2+} ions that remain bound to the surface post-oxidation). According to the carrier density calculated from NMR ($N_h = 1.8 \times 10^{22}$ cm^{-3}) and extinction spectroscopy ($N_h = 6.3 \times 10^{21}$ cm^{-3}), we expect to have approximately 2.6 mg/L and 1.5 mg/L, respectively, of Cu present in the supernatant if Cu^{2+} leaves the particle during oxidation (assuming that hole formation occurs from one Cu^{+} atom oxidizing to Cu^{2+} and subsequently leaving the original lattice position as a Cu vacancy). We find that the Cu concentration in the supernatant solution is far too low (0.0336 mg/L) to correlate with Cu^{2+} ions leaving the particle during oxidation. (*N. B.* Even for the lower range of carrier densities found with NMR and extinction spectroscopy (x ~ 0.1), the concentration of Cu is anticipated to be at least an order of magnitude larger than that found in the supernatant.) These results are consistent with observations reported by Kriegel et al, who hypothesized that Cu remains bound to the particle surface even after particle oxidation via air exposure. Work to determine the position of oxidized Cu centers in the NP lattice after air exposure is on-going in our laboratory.

2.2.7 Solid State NMR Spectroscopy

Dried $Cu_{2-x}Se$ NPs were packed in a glovebox into 4mm zirconia rotors with Kel-F inserts and air-tight Vespel caps for analysis with ssNMR. All ssNMR spectra were recorded on a Bruker Avance 500 MHz (11.7 T) spectrometer, equipped with a triple-resonance 4 mm CPMAS probehead operating at a ^{77}Se Larmor frequency of 95.38 MHz. ^{77}Se chemical shifts were externally referenced to Me_2Se at 0 ppm. Temperature was maintained with a BVT3000 variable temperature unit and nitrogen cooling was used for all low temperature measurements.

Static ^{77}Se NMR spectra of $Cu_{2-x}Se$ NPs were recorded using a standard $(\pi/2)_x$-τ_{echo}-$(\pi)_y$-acquire spin echo pulse sequence. In general, $\pi/2$ pulse lengths were ~2.5 μs and $\tau_{echo} = 30$ μs. Recycle delays were set to $5\times T_1$ and typically ranged from 50-200 ms, depending on the degree of oxidation of the sample. Static T_1 measurements were collected from temperatures ranging from

175-350 K using a previously described inversion-recovery sequence.[80] Here, a composite-π pulse was used for inversion with spin echo detection as follows: $(\pi/2)_x$-$(3\pi/2)_y$-$(\pi/2)_x$-τ-$(\pi/2)_x$-τ_{echo} -$(\pi)_y$-τ_{echo} -acquire.[139]

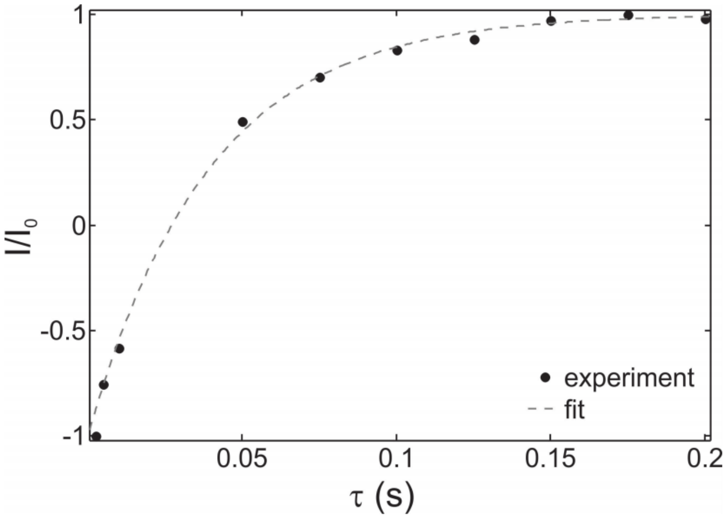

Figure 2.5. Representative inversion-recovery T_1 relaxation data and corresponding single exponential fit to extract the T_1 values listed in **Error! Reference source not found.** for air-free $Cu_{2-x}Se$ (x ~ 0) NPs at T = 300 K.

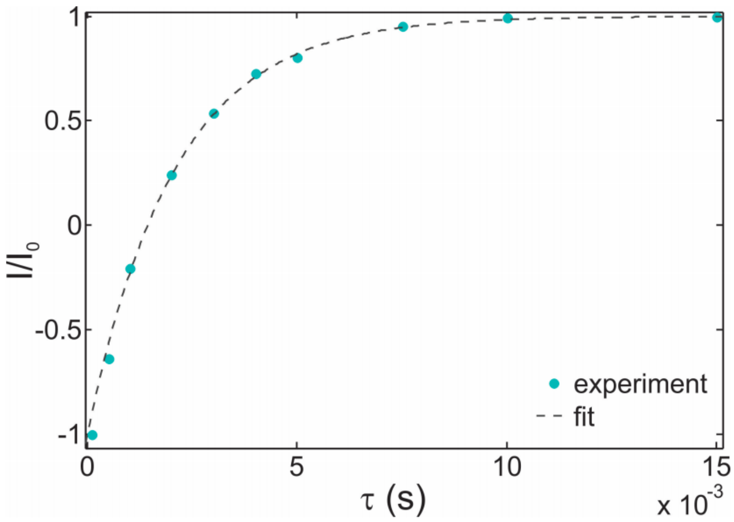

Figure 2.6. Representative inversion-recovery T_1 relaxation data and corresponding single exponential fit to extract the T_1 values listed in **Error! Reference source not found.** for oxidized $Cu_{2-x}Se$ ($x > 0$) NPs at $T = 300$ K.

2.3 Results and Discussion

2.3.1 Canonical Nanoparticle Structural Characterization

$Cu_{2-x}Se$ NPs were synthesized via a hot injection method using standard air-free techniques (see **Section 2.2.2** for experimental details).[136] Upon exposure to air, Cu is oxidized which results in the formation of holes in the valence band[140] and a degenerately doped, nonstoichiometric $Cu_{2-x}Se$ ($x > 0$) phase[63, 138, 141] in the NP. Transmission electron micrographs showed average particle diameters of 14.2 ± 2.1 nm and 13.6 ± 1.8 nm for oxidized and air-free samples (**Figure**

2.1 and Figure 2.7), respectively, indicating that air exposure did not result in significant changes in core size. If maintained in an inert atmosphere prior to analysis, selected area electron diffraction (SAED) patterns of the $Cu_{2-x}Se$ NPs (**Figure 2.7B**) exhibited a monoclinic crystal structure. Conversely, upon exposure to air, SAED patterns showed evidence of a lattice contraction (**Figure 2.7D**) in the $Cu_{2-x}Se$ NPs, consistent with the appearance of a cubic phase.

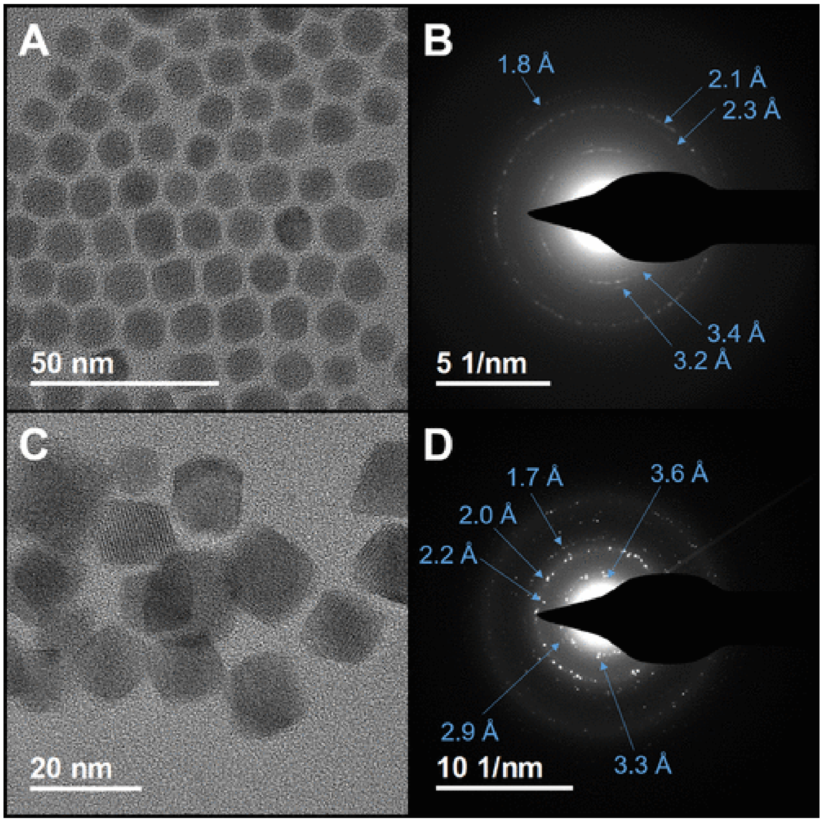

Figure 2.7. HRTEM micrographs (A, C), and corresponding SAED patterns (B, D,) for air-free (A, B) and air-exposed (C, D) $Cu_{2-x}Se$ NPs.

Comparing these results to PXRD spectra, we find good agreement. For fully reduced samples, characteristic 2θ peaks are observed at 12.0°, 26.2°, 40.0°, 43.8°, and 51.8° in the PXRD spectrum (**Figure 2.8E**), consistent with previous reports.[96, 98] Upon oxidation, the 2θ peaks at

12.0° and 40.0° begin to decrease in intensity (**Figure 2.8A−D**). Concurrently, the peaks at 43.8° and 51.8° shift to higher 2θ angles, consistent with the lattice contraction observed in the corresponding SAED. Taken together, these data indicate a transformation into a cubic phase as x is increased. For smaller values of x in $Cu_{2-x}Se$ NPs, the crystal structure has been primarily assigned as either tetragonal[96] or monoclinic,[98] although cubic[142] and hexagonal[143] structures have also been reported. The spectrum that we observe for $Cu_{2-x}Se$ NPs maintained in an air-free environment (**Figure 2.8E**) is closest to reports assigning a tetragonal or monoclinic unit cell.

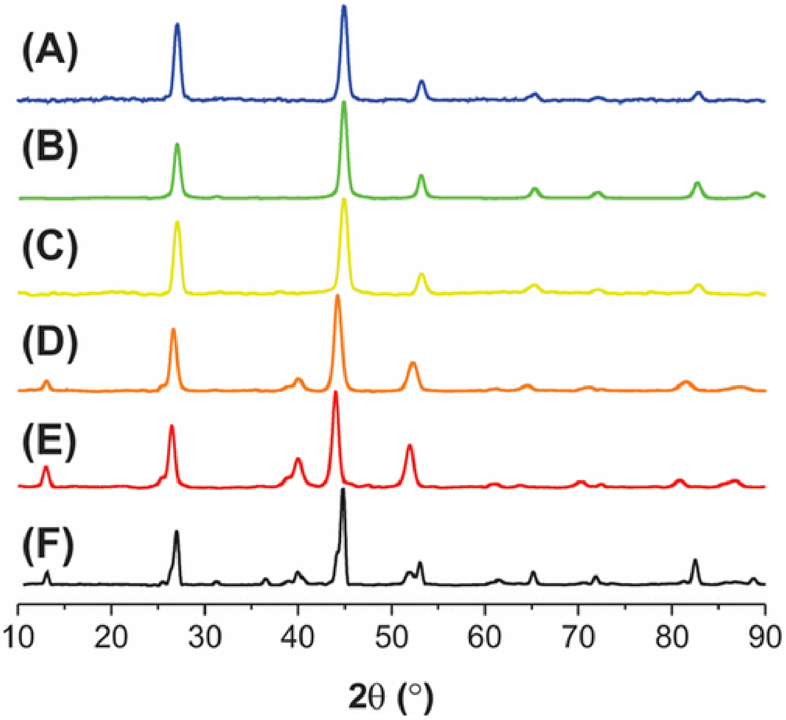

Figure 2.8. PXRD patterns of (A-E) $Cu_{2-x}Se$ NPs exhibiting decreasing degrees of oxidation from (A) to (E) and (F) bulk $Cu_{2-x}Se$.

2.3.2 Short Range Structural Characterization using NMR Linewidth

To gain additional insight into the crystal structure of the NPs, we also examine the corresponding static ^{77}Se NMR spectra (**Figure 2.9**). For samples with low values of x (x = 0.00−0.07), the static ^{77}Se line shape is broader and more asymmetric compared to the cubic $Cu_{2-x}Se$ NPs. This broad, asymmetric line shape is consistent with changes in both chemical shift anisotropy and chemical shift distributions that are anticipated when several distinct, lower symmetry Se sites are present in the crystal structure. Further, the distribution of low symmetry Se environments is consistent with reports of Se sites in monoclinic[144] $Cu_{2-x}Se$ crystal structures (**Figure 2.9E**) and bolsters assignment of this crystal phase for the reduced $Cu_{2-x}Se$ NP samples. Similarly, the PXRD assignment of a cubic structure for both the oxidized $Cu_{2-x}Se$ NPs (**Figure 2.8A− C**, x = 0.48 and 0.47) and the bulk sample (**Figure 2.8F**, x = 0.41) is also consistent with the static ^{77}Se NMR spectra, where the peak shape and line width is comparatively more symmetric and narrow (**Figure 2.9A−C and F**) than the reduced phases. More symmetric line shape features are expected in the cubic phase, since Se atoms in these compositions are in a symmetric coordination environment. The increase in line width for the $Cu_{2-x}Se$ NP samples compared to the bulk is typical for nanoscale systems and has been attributed to the larger surface-to-volume ratio and associated distribution of distinct surface and subsurface motifs (i.e., disorder).[145] (See **Section 2.3.5** for an additional discussion concerning details of the structural assignment of $Cu_{2-x}Se$ using a combination of PXRD and NMR approaches, including specific, possible Se coordination environments.)

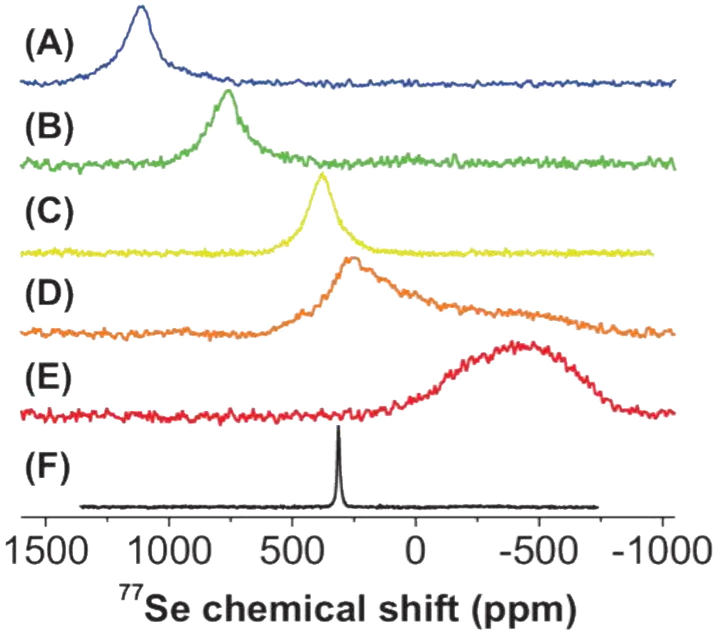

Figure 2.9. Static ^{77}Se NMR spectra of (A-E) $Cu_{2-x}Se$ NPs with decreasing degrees of oxidation from (A) to (E), and (F) bulk $Cu_{2-x}Se$.

2.3.3 Plasmonic Properties of $Cu_{2-x}Se$ Nanoparticles

With PXRD and ^{77}Se NMR structural characterization in hand, we next determine carrier density as a function of NP composition. In order to accurately evaluate carrier densities in $Cu_{2-x}Se$ systems using the Drude model (see **Section 2.3.8** for detailed analysis), composition assignment is necessary to choose the appropriate value for the high-frequency dielectric constant as well as the effective hole mass.[63, 138] Here, we use the changes in lattice parameter, *a*, as measured by PXRD to make those composition assignments.[137] Unfortunately, we note that we and others find that traditional methods of composition analysis such as inductively coupled plasma-mass spectrometry (ICP-MS) or energy dispersive X-ray spectroscopy (EDS) do not show consistent differences in particle stoichiometry that track with the observed lattice and electronic structure changes.[95-96] This discrepancy is likely due to the fact that, when a Cu^+ center in the particle becomes oxidized to Cu^{2+}, and creates a hole, it does not necessarily leave the particle. Instead, consistent with previous reports,[96] we find that despite differing degrees of oxidation (as determined by extinction spectroscopy and clear structural changes in both PXRD and ^{77}Se NMR) the amount of Cu detected in both the supernatant and digested particles is not consistent with Cu^{2+} leaving the particle (see **Section 2.2.6** for ICPMS data and discussion). For example, Kriegel et al. were able to tune particle composition post-air exposure with mild reducing agents without any additional Cu, suggesting that, upon oxidation, Cu^{2+} remains bound to the particle surface over several oxidation/reduction cycles or does not migrate from the original Cu^+ position. Taken together, these observations indicate that there is structural ambiguity in $Cu_{2-x}Se$ systems, and the position of oxidized Cu centers within the particle lattice after air exposure is not clear.

Figure 2.10 shows the corresponding UV−vis−NIR extinction spectra for the various compositions of $Cu_{2-x}Se$ NPs discussed above. Correlating the ^{77}Se NMR spectra with observed LSPR features, we find that the most oxidized NP sample (**Table 2.1**, $x = 0.48$) resonated at the highest ^{77}Se frequency (δ_{obs} (center of gravity) = 1136 ppm) and exhibited the most intense, blueshifted LSPR band at approximately $\lambda_{max} = 1085$ nm. Three samples showed intermediate degrees of oxidation (**Table 2.1**, $x = 0.47$, 0.47, and 0.07) with ^{77}Se $\delta_{obs} = 771$, 382, and 90 ppm and LSPRs at approximately $\lambda_{max} = 1328$, 1456, and 1668 nm, respectively. (*N. B.* although the PXRD calculated compositions for these intermediate oxidation states give the same value of x for two of the samples (**Figure 2.9C, D**) their ^{77}Se NMR and extinction spectra clearly show structural and/or electronic differences between the two samples emphasizing the need for additional analysis.) The near-stoichiometric (**Table 2.1**, x = 0.00) Cu_2Se NPs that were maintained in an air-free environment exhibited $\delta_{obs} = -365$ ppm and did not show a LSPR band in the optical window examined here, but did display a tail that may indicate an LSPR at lower energy ($\lambda_{max} > 2300$ nm). According to the Drude model (see **Section 2.3.7**), the successive redshift in the extinction spectra is consistent with a progressive decrease in carrier density. A Moss−Burstein effect is also observed where the optical bandgap of the $Cu_{2-x}Se$ (x ~0) NPs at approximately 550 nm blueshifts upon oxidation, indicating the presence of additional carriers in the valence band.[58, 96]

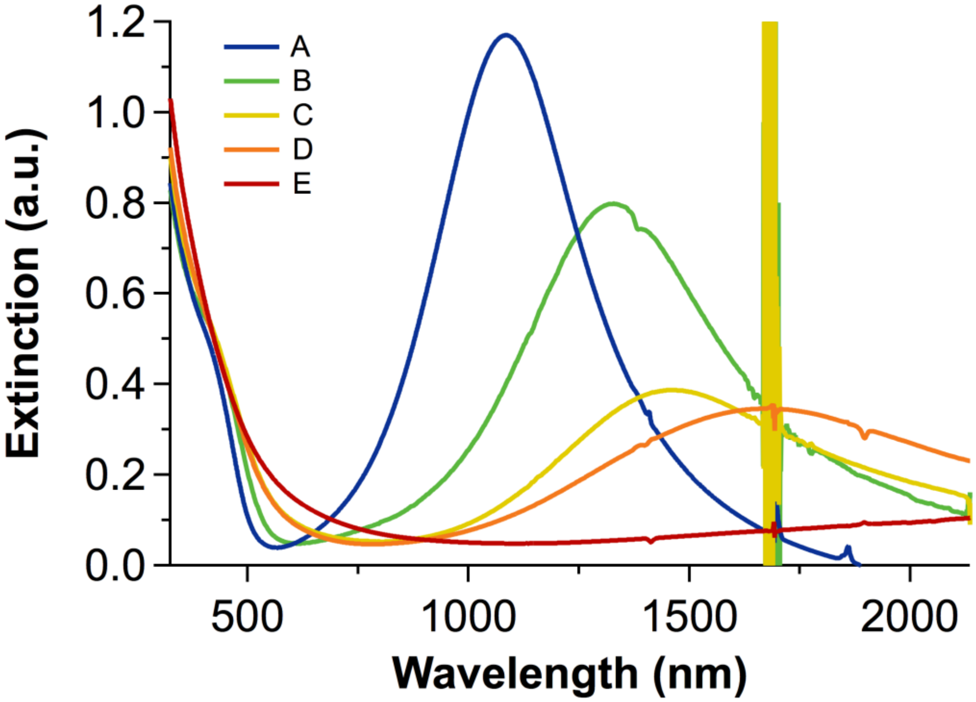

Figure 2.10. Extinction spectra of (A-E) $Cu_{2-x}Se$ NPs with decreasing degrees of oxidation from (A) to (E). Spikes in extinction spectra (~1650 – 1700 nm) are due to interfering solvent absorption).

2.3.4 Presence of Knight Shift

By comparing the emergent optical features, the observed ^{77}Se frequency clearly depends on the value of x (and thus, carrier density), with more oxidized structures resonating at higher frequencies (**Figure 2.9B−E**). The change in observed ^{77}Se shift can be the result of an increasing Knight shift (δ_{KS}) contribution to δ_{obs} as a result of additional free holes as x is increased, which is described by the following relationship:

Equation 2.1. Observed ^{77}Se NMR Chemical Shifts

$$\delta_{obs} = \delta_{CS} + \delta_{KS}$$

Here, the observed shift is comprised of contributions from the chemical shift (δ_{CS}) of the material as well as the Knight shift component, which is dependent upon spin and orbital contributions from free charge carriers. Knight shifts can lead to large frequency changes as a result of holes coupling to ^{77}Se nuclei by the isotropic exchange interaction[146] and, therefore, are exceptionally sensitive to changes in electronic structure. The assignment of a Knight shift from charge carriers in the particle is supported by decreasing spin−lattice relaxation (T_1) values[81] for higher frequency ^{77}Se resonances (see **Section 2.3.7** and **Table 2.1**). The successive change in the magnitude of the Knight shift indicates a progressive change in the charge carrier population and/or crystallographic structure within the NPs (i.e., the chemical shift component of **Equation 2.1**). The ^{77}Se Knight shift for the most oxidized $Cu_{2-x}Se$ NPs (x = 0.48) is the same sign (positive) as the sign reported for metallic RuSe NPs,[147] further supporting the assignment of a Knight shifted resonance. We note that the observed ^{77}Se shift is different for $Cu_{2-x}Se$ NPs vs RuSe NPs (1136 vs 1670 ppm), but it is difficult to assess the origin of this difference without a more thorough understanding of the factors contributing to both the chemical shift and Knight shift component of the RuSe system.[147] For instance, the magnitude of a Knight shift will be influenced by the degree of s orbital mixing (only electrons in orbitals with s character contribute to Knight shifts because these electrons have a nonzero probability of being located at the nucleus).[148] Qualitatively, a comparison of the oxidized $Cu_{2-x}Se$ NPs to other Se containing semiconductor systems also supports the assignment of a large Knight shift component in the observed ^{77}Se shift in $Cu_{2-x}Se$ NPs. For example, undoped or lightly doped metal chalcogenide systems (e.g., CdSe,[149] PbSe,[150] ZnSe[145]) typically exhibit peaks between −300 and −700 ppm.

2.3.5 Local $Cu_{2-x}Se$ Nanoparticle Structure

Once the composition-dependent changes in electronic behavior for $Cu_{2-x}Se$ NPs were established, the impact of chemical structure on NP properties was evaluated with a combination of SAED, PXRD, and ^{77}Se ssNMR. The nuances of assigning the crystal structures of copper(I) chalcogenides from diffraction-based techniques alone is well-known and has been discussed elsewhere.[128] Compounding this issue is conflict in the literature where reduced Cu_2Se NPs have been assigned to both monoclinic[98] and tetragonal[96] structures since both exhibit similar PXRD and SAED patterns. Further, many bulk Cu_2Se phases have not been characterized by single crystal analyses, prohibiting definitive assignment of atomic positions. In structures that have been solved, some peaks in the powder diffraction patterns cannot be assigned from the single crystal data,[144] suggesting the presence of additional structural variation and/or disorder in the material. Such crystallographic defects/disorder have the potential to play an important role in plasmonic behavior of $Cu_{2-x}Se$ NPs. The presence of Cu vacancies facilitates the emergence of LSPRs and thus requires changes to the local, short range structure that are potentially not observable by PXRD.

However, changes in local structure are reflected in the chemical shift anisotropy (CSA) of ssNMR spectra, making it possible to examine the influence of Cu vacancies and other defects on the emergence of the LSPR in $Cu_{2-x}Se$ NPs. We find that both the linewidth and the lineshape of the static ^{77}Se peaks varies with air exposure. For the most reduced samples ($Cu_{2-x}Se$ (x ~ 0) NPs) that were maintained in an air free environment (δ_{obs} = -365 ppm, **Figure 2.9E**), the asymmetric lineshape is incredibly broad with fwhm = 44.7 kHz, suggesting a low symmetry coordination environment for Se atoms in this structure, consistent with the CSA magnitude that would be anticipated from Se sites in the proposed monoclinic structure.[98] As additional Cu vacancies are introduced, the lineshape changes dramatically and is increasingly distorted – showing a broad base spanning 143.9 kHz, a shoulder that coincides with the ^{77}Se spectra of fully reduced $Cu_{2-x}Se$ at approximately -365 ppm, and a relatively sharp shoulder in the downfield regime, with a slight narrowing of the fwhm = 35.7 kHz (, **Figure 2.9D**). In the PXRD of this sample (**Figure 2.8D**), the peaks at 2θ = 12.0° and 40.0° slightly decrease in intensity and the peaks at 2θ = 26.2°, 43.8°, and 51.8° shift to higher values, seemingly progressing towards the fully oxidized crystal structure (vide supra). Unfortunately, with the resolution of PXRD for NPs of this size regime, it is difficult to discern if this is due to two populations of particles with different compositions (*i.e.,* values of x) or if the material is in an intermediate phase transition between fully reduced and fully oxidized.

Upon increasing oxidation of $Cu_{2-x}Se$ (x > 0) NPs (**Figure 2.9A-C**), δ_{obs} shifts to higher ppm values and exhibits a relatively isotropic static ^{77}Se lineshape that initially reaches a minimum fwhm at 11.8 kHz and then increases to 13.3 kHz as x increases, despite no obvious change in PXRD after the cubic phase is reached (**Figure 2.8A-C**). The isotropic static lineshape is consistent with octahedrally coordinated Se environments in the antifluorite structure of $Cu_{2-x}Se$. However, the physical source of line broadening observed with increasing oxidation is not clear. It may result from nuclear coupling to free carriers that have fast relaxation rates and/or from a distribution of shifts due to alterations in the ^{77}Se coordination environment (e.g. overlap of resonances corresponding to more Se atoms near crystallographic defects (Cu vacancies) and their anticipated motion or lattice distortions (specifically, small random displacements of Cu atoms in the chalcogenide sublattice) observed both theoretically[151] and experimentally[152] in copper(I) chalcogenides).

2.3.6 Using Korringa Behavior to Determine Types of Carrier

The presence of the Knight shift is consistent with free carriers in the particle. In order to definitively assign the presence of a Knight shift and investigate charge carrier density directly, we analyzed the relaxation behavior of the ^{77}Se nuclei as a function of temperature for three representative samples: the most oxidized ($x = 0.48$), an intermediate composition ($x = 0.47$), and the most reduced ($x = 0.00$) samples. For materials that are metallic, the inverse of spin−lattice relaxation rate (T_1^{-1}) exhibits a linear relationship with temperature (T), with an intercept through zero, whereas T_1^{-1} in semiconductors shows a linear relationship with $T_{1/2}$ below the Debye temperature.[150] The linear relationship between T_1^{-1} and T is known as Korringa behavior[71] and indicates that free carriers couple to constituent nuclei in the material, allowing T_1T to provide a direct probe of the local density of states at the Fermi level (E_F -LDOS),[153] and thus how the population of free carriers at the Fermi level changes as a function of composition in $Cu_{2-x}Se$ NPs. Surprisingly, we find that all $Cu_{2-x}Se$ NP samples studied show a linear relationship between ^{77}Se T_1^{-1} and T, meaning that all of the particles exhibit Korringa behavior (**Figure 2.11**).

The presence of Korringa behavior indicates that all particle samples measured have free carriers at the Fermi level. Yet, T_1T varies between different values of x for $Cu_{2-x}Se$ NPs, where increasing T_1T indicates decreasing Ef -LDOS. Based on this analysis, the most oxidized, cubic $Cu_{2-x}Se$ NPs with an observed ^{77}Se shift at 1136 ppm have the lowest Korringa product (i.e., the highest Ef -LDOS (Ry^{-1} $atom^{-1}$)) with $T_1T = 0.68 \pm 0.01$ sK, followed by the cubic sample at 382 ppm and $T_1T = 1.17 \pm 0.01$ sK, and the near-stoichiometric $Cu_{2-x}Se$ NPs at −365 ppm and $T_1T = 12.39 \pm 0.10$ sK. These data suggest that T_1T is a sensitive figure of merit for the emergence of the LSPR in nanomaterials given that this value changes by over an order of magnitude from the most reduced (x = 0.00) to the most oxidized (x = 0.48) $Cu_{2-x}Se$ NPs.

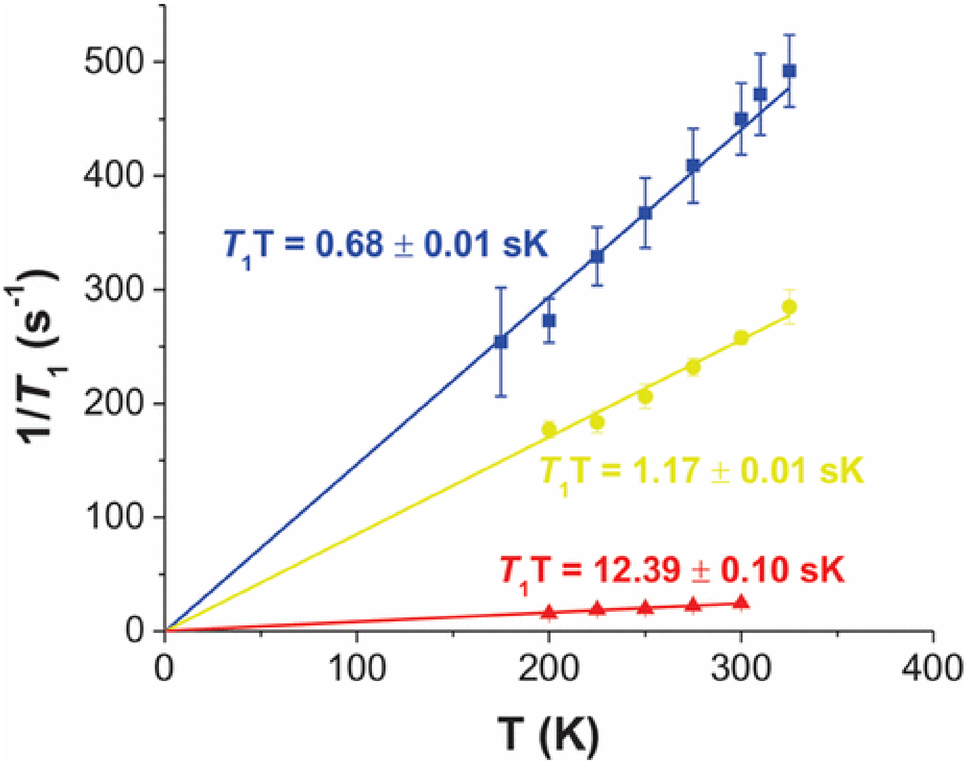

Figure 2.11. Temperature dependence of spin-lattice relaxation rate of $Cu_{2-x}Se$ NPs with blue to red representing decreasing amounts of oxidation, and corresponding to samples A, C, and E, respectively, from Figure 2.9.

2.3.7 Carrier Density Quantification Using NMR and Drude Model

In addition to using T_1T to identify charge carrier populations, material standards with a similar composition and known carrier properties can be used as reference materials to quantify the magnitude of these populations.[74, 81, 150] In order to quantify carrier densities from NMR data, the following relationship can be used:

Equation 2.2. NMR Derived Carrier Density Calculation

$$N_{h,s} = \left[\frac{(m_r^*)^2 N_{h,r}^{\frac{2}{3}}}{(m_s^*)^2}\left(\frac{T_{1,r}}{T_{1,s}}\right)\right]^{\frac{3}{2}}$$

where N_h is the carrier density, m^* is the effective mass of the free carriers, and T_1 is the spin−lattice relaxation where subscripts s and r refer to the unknown sample of interest and the reference material, respectively.[73] Here, we used bulk $Cu_{1.54}Se$ (the composition and N_h of our bulk standard was calculated from PXRD shifts, **Table 2.1**) as our reference compound, with the following parameters at room temperature: $m^* = 0.334\ m_0$,[63] $N_h = 8.0 \times 10^{21}\ cm^{-3}$,[63] and $T_1 = 4.0 \pm 0.1$ ms measured in-house. The effective mass for each $Cu_{2-x}Se$ NP system was adjusted based on the compositional changes observed in PXRD and are listed in **Table 2.1**.[63]

Table 2.2. Static ^{77}Se NMR Chemical Shifts and T_1 Values at T = 300 K, Calculated Carrier Densities and Composition of $Cu_{2-x}Se$ NPs.

Sample	Static ^{77}Se δ_{obs} (ppm)	T_1 (ms)	N_h NMR (cm^{-3})	*x* in $Cu_{2-x}Se$ (NMR)
$Cu_{2-x}Se$ NPs	1136 ± 58	2.3 ± 0.1	1.8×10^{22}	0.56
$Cu_{2-x}Se$ NPs	771 ± 57	2.8 ± 0.4	1.4×10^{22}	0.42
$Cu_{2-x}Se$ NPs	382 ± 52	3.9 ± 0.1	8.3×10^{21}	0.25
$Cu_{2-x}Se$ NPs	90 ± 156	6.6 ± 1.0	2.3×10^{21}	0.07
$Cu_{2-x}Se$ NPs	−365 ± 195	40.6 ± 2.9	6.9×10^{18}	0.00
$Cu_{2-x}Se$ bulks	313 ± 5	4.0 ± 0.1	N/A	N/A

Using room temperature T_1 measurements, we find that higher frequency ^{77}Se shifts and shorter T_1 values are coincident with higher carrier densities (**Table 2.2**). The carrier densities derived from NMR measurements (**Table 2.2**) are in good agreement with those obtained from estimating carrier density based on PXRD data (See **Section 2.2.5** and **Table 2.1**). However, differences are noted between carrier densities derived from the extinction spectra using the Drude model (**Table 2.3**) when compared to both PXRD and ssNMR derived values. We hypothesize that this discrepancy is due to the sensitivity of the Drude model to effective mass of the free carriers, the high frequency dielectric constant, the dielectric constant of the medium, and the contribution of the dielectric constant of the capping ligands (which is not taken into account in the standard Drude model). The Drude model used to estimate carrier densities here is as follows:

Equation 2.3. Drude Model

$$\omega_{sp} = \sqrt{\frac{\omega_P^2}{\varepsilon_\infty + 2\varepsilon_H} - \gamma^2}$$

where ω_{sp} is the frequency of the LSPR, γ is the fwhm of the LSPR peak, ε_∞ is the high frequency dielectric constant, ε_H is the dielectric constant of the solvent, and ω_P is the bulk plasma frequency, which is related to carrier density, N_h, as follows:

Equation 2.4. Bulk Plasma

$$\omega_P^2 = \frac{N_h e^2}{m^* \varepsilon_0}$$

where e is the elementary charge, m^* is the effective mass of the free hole carriers, and ε_0 is the permittivity of free space.[49, 60]

Table 2.3. Extinction Properties, Calculated Carrier Densities and Composition of $Cu_{2-x}Se$ NPs.

Sample	**λ_{max} (nm)**	**fwhm (nm)**	**N_h Drude (cm^{-3})**	***x* in $Cu_{2-x}Se$ (Drude)**
$Cu_{2-x}Se$ NPs	1136 ± 58	2.3 ± 0.1	1.8×10^{22}	0.56
$Cu_{2-x}Se$ NPs	771 ± 57	2.8 ± 0.4	1.4×10^{22}	0.42
$Cu_{2-x}Se$ NPs	382 ± 52	3.9 ± 0.1	8.3×10^{21}	0.25

$Cu_{2-x}Se$ NPs	90 ± 156	6.6 ± 1.0	2.3 x 10^{21}	0.07
$Cu_{2-x}Se$ NPs	−365 ± 195	40.6 ± 2.9	6.9 x 10^{18}	0.00
$Cu_{2-x}Se$ bulks	313 ± 5	4.0 ± 0.1	N/A	N/A

2.4 Conclusions

Overall, while local crystallographic defects, such as Cu vacancies, have long been correlated with the emergence of metallic behavior in $Cu_{2-x}Se$ NPs, the ^{77}Se ssNMR analysis presented here not only quantifies carrier densities but also facilitates correlation between these carrier populations and NP composition and crystallinity for the first time, even for those NP compositions that do not exhibit a spectroscopically discernible LSPR. We highlight the importance of using a widely accessible technique like NMR spectroscopy to provide a complement to extinction spectroscopy, especially in cases where use of the Drude model may be complicated by factors such as quantum confinement[66] or particle surface chemistry.[60] The carrier density evaluation with NMR only needs the effective mass and does not need to account for dielectric constants of either the NP or surrounding medium which reduces variability that arises from approximation of these values. Importantly, the fact that NMR can evaluate carrier densities, even in cases where no absorption band is observed with a standard UV−vis−NIR spectrometer, makes it a particularly attractive technique for analyzing samples with low dopant concentrations and/or particles at the boundary of emergent plasmonic behavior.

In conclusion, we describe the carrier densities and composition transformations as a function of oxidation for $Cu_{2-x}Se$ NPs and correlate these features with optoelectronic properties of the resulting NPs. $Cu_{2-x}Se$ NPs that showed little to no change in PXRD displayed a dramatic change in ^{77}Se NMR in terms of both observed shift and relaxation behavior, indicating changes in both the short-range crystal structure as well as charge carrier properties. Ultimately, charge carrier density determination via NMR is anticipated to be a valuable tool to probe physical phenomena of doped semiconductor NPs, especially their emergent properties in the low doping limit, where weak and/or broadened extinction features make charge carrier determination using the Drude model challenging. Overall, we anticipate that quantitative routes to access the impact of chemical and/or crystallographic changes in these and other semiconductor NPs should be pivotal in their development, understanding, and implementation in next generation plasmonics.

3.0 Surface Chemistry of Copper Selenide Nanoparticles and Their Influence in the Plasmonic Features

(Portions of this work were previously published and reprinted with permission from Kaseman, D. C., Gamble Jarvi, A., Gan, X. Y., Saxena, S., Millstone, J. E., *Chemistry of Materials* **2018**, *30*, 7313 – 732. Copyright, 2018, American Chemical Society.)

3.1 Introduction

Copper chalcogenide ($Cu_{2-x}S$, $Cu_{2-x}Se$, and $Cu_{2-x}Te$) nanoparticles (NPs) display localized surface plasmon resonances (LSPRs) in the mid- to near-infrared region, making them attractive for applications such as photothermal therapy, sensing, and spectroscopy. The appearance of an LSPR in these materials depends on the oxidation of Cu^+ sites, which generates hole charge carriers. For example, several studies have shown that these LSPR features can then be tuned by controlling the extent of Cu oxidation and several spectroscopic methods have been used to quantify the carrier densities present in these NPs, which effectively measures the degree of Cu oxidation.

However, even qualitative understanding the Cu oxidation in copper chalcogenide NPs remains a challenge. In particular, there remains considerable ambiguity in the stoichiometry and chemical environments of Cu in copper chalcogenide NPs, which ultimately influence both the internal structures of these NPs as well as their surface chemistry. Importantly, a fundamental understanding of the surface chemistry of these materials is crucial to obtain, tailor, and apply their optoelectronic properties. For example, surface-enhanced sensing and plasmonically-driven chemical conversion reactions are known to occur on NP surfaces, and the presence of surface-terminating ligands, oxidation species, and the surrounding media are reported to able to influence the plasmonic features of NPs, and ultimately their optoelectronic performance. Therefore, the ability to detect and illustrate a detailed chemical picture of the surface chemistry is crucial in both the copper chalcogenides and indeed, all classes of semiconductor NPs. This information not only allows one to control and interpret their optoelectronic features, but also to rationally modify final particle architectures, and ultimately to dictate their technological performances.

In order to effectively study the surface chemistry of copper chalcogenide NPs, we first have to study the population and location of $Cu^{1+/2+}$ species in these materials once formed. Here, we investigate the evolution of Cu^{2+} environments during $Cu_{2-x}Se$ NP oxidation via air exposure using electron paramagnetic resonance (EPR) spectroscopy, which is an effective tool uniquely suited to study the oxidation of Cu in these materials because only Cu^{2+} is detectable using this technique. Our results provide insight into the time scales of Cu^{2+} oxidation in air, and identify Cu^{2+} chemical environments. We next study the impact of Cu oxidation on the structure and observed plasmonic properties of the resulting $Cu_{2-x}Se$ NPs, elucidating and demonstrating how we could further tune the plasmonic properties using NP surface chemistry. Finally, we extend the use of both EPR and extinction spectroscopies as a diagnostic tool to study the coordination of NP surface with ligands as well as solvents, which ultimately provides a detailed chemical picture of how these NPs can be used in plasmonically-driven chemical reactions.

3.2 Experimental Section

3.2.1 Materials and Methods

Copper(I) chloride (CuCl, > 99.995%), copper(II) chloride ($CuCl_2$, > 99.99%), selenium powder (Se, > 99.5%), octadecene (ODE, 90% technical grade), oleylamine (OLA, 70% technical grade), chloroform (> 99%), chloroform-d (99.8%), copper(II) acetylacetonate (Cu-acac, > 99.99%), bulk copper(I) selenide (Cu_2Se, > 99.95%) and copper(II) oxide (CuO, > 99.99%) were purchased from Sigma Aldrich (St. Louis, MO). Absolute ethanol (EtOH) was purchased from Thermo Fisher Scientific (Pittsburgh, PA). All chemicals were used as received with no additional purification unless otherwise noted. Prior to use, all glassware and Teflon stir bars were washed in aqua regia and rinsed with copious amounts of water prior to oven drying. Caution: aqua regia is highly toxic and corrosive, and should only be used with proper personal protective equipment and training. Aqua regia should be handled only inside a fume hood.

3.2.2 Synthesis of $Cu_{2-x}Se$ NPs

$Cu_{2-x}Se$ NPs were synthesized using a previously described hot injection method.[62, 136] The synthetic procedure was completed using standard air-free techniques and is described in detail below. The selenium-octadecene-oleylamine mixture was created by dissolving 80 mg Se in 1 mL of ODE and 2 mL of OLA. The solution was heated in a round bottom flask for 12 hrs under argon gas at 195 ^{o}C. In a 3-neck round bottom flask, 200 mg CuCl was added with 5 mL OLA and 5 mL of ODE. The Cu-ODE-OLA mixture was heated to 140 ^{o}C under vacuum for 30 min then heated to 285 ^{o}C under Ar. Then, the Se mixture was injected into the Cu mixture. The precursors reacted for 10 min at ~285 ^{o}C to form $Cu_{2-x}Se$ NPs. The NPs were cooled to room temperature by removing the heating mantle.

NPs were purified by centrifugation to remove unreacted precursors, reaction byproducts, and excess ligands. For purification, 6.5 mL aliquots of as-synthesized particle mixture were separated and transferred to centrifuge tubes 10 mL of EtOH was then added to each tube, and centrifuged in an Eppendorf 5804R centrifuge at 2850 rcf for 10 min. The supernatant was discarded and the precipitate was re-suspended with chloroform and sonicated. To this suspension, 10 mL of EtOH was added and the centrifugation procedure was repeated. The purified particles were characterized using TEM, extinction spectroscopy, EPR, powder X-ray diffraction, X-ray photoelectron spectroscopy and nuclear magnetic resonance (NMR) spectroscopy.

3.2.3 Mass Action Ligand Exchange Protocol

Following purification, the NPs were diluted with chloroform to 8.00 mL. To the NP solution, 4.00 mL of chloroform and 8.0 mM of new ligand solution were added. The new ligands were DDT or PEGSH (1 kDa, 2 kDa and 5 kDA). The particles were then placed on a stir plate for ~16 h. After mixing, the $Cu_{2-x}Se$ (x ~ 0) NP product was again purified via centrifugation in EtOH for 5 min. The resulting supernatant was removed and the pellet was resuspended in a small amount of hexane or toluene for additional centrifugation in another 5 mL of EtOH. This washing procedure was repeated once more.

3.2.4 Synthesis of Cu@CuO NPs

Cu@CuO NPs were synthesized using a modified procedure outlined by Yang et al.[154] In this synthesis, 105 mg Cu-acac was added to 10 mL of OLA in a 25 mL 3-neck round bottom flask on a magnetic stir plate. The solution was placed under Ar and degassed three times for 5 min each. The mixture was slowly heated to 230 ^{o}C and kept at 230 ^{o}C for 6 hrs before cooling to room temperature. The particles were washed three times using a chloroform-ethanol (1:10) mixture and centrifugation at 2850 rcf for 10 min.

3.2.5 Electron Paramagnetic Resonance Spectroscopy (EPR)

Continuous wave (CW) EPR measurements were performed on a Bruker Elexsys E580 CW/FT X-band spectrometer using a Bruker ER4118X-MD5 resonator at 80 K. All CW experiments were run with a center field of 3100 G and a sweep width of 2000 G, modulation amplitude of 4 G, and a modulation frequency of 100 kHz for 1024 data points using a conversion time of 20.48 ms. All EPR simulations were performed using EasySpin software.[155]

Three-pulse electron-spin echo envelope modulation (ESEEM) experiments were performed on a Bruker ElexSys 580 X-band FT/CW spectrometer equipped with a Bruker ER4118X-MD5 resonator. The temperature for all experiments was controlled using an Oxford ITC503 temperature controller with an Oxford ER 4118CF gas flow cryostat. Experiments were performed at X-band frequencies at 80 K. A $\pi/2 - \tau - \pi/2 - T - \pi/2$ – echo pulse sequence was used. The $\pi/2$ pulse length was 16 ns, the initial time delay, τ, was 144 ns and the second time, T, was initially set to 288 ns and incremented by 16 ns. A four-step phase cycling was used to eliminate unwanted echoes.[156-157] ESEEM data was phase corrected, baseline subtracted and Fourier transformed using Bruker WinEPR software.

3.2.6 EPR of $Cu_{2-x}Se$ NP Oxidation Study

The oxidation process of the NPs was performed by transferring the washed NPs, suspended in 150 μL of chloroform to a 4 mm quartz EPR tube. The aging study was performed by blowing house air into an EPR tube via a needle at a pressure that created turbulence on the surface of the solution. Before each EPR measurement, the particles were diluted to 150 μL with chloroform to account for any solvent evaporation and sonicated for 10 min before flash freezing in liquid N_2.

3.2.7 Extinction Spectroscopy

Extinction spectroscopy measurements were performed on a Cary 5000 spectrophotometer (Agilent, Inc.) using 1 cm path length quartz cuvettes. Purified $Cu_{2-x}Se$ particles were suspended in 1 mL chloroform and placed in the cuvettes. The spectra were recorded from 2000 nm to 350 nm at a rate of 1000 nm/min, with a source and detector changeover occurring at 850 nm. Spectra were baseline corrected with respect to 1 mL of neat chloroform.

3.2.8 Transmission Electron Microscopy (TEM)

Samples were prepared for TEM by drop casting 6 μL of the particles (optical density (O. D.) = 1) on a carbon-coated Cu 200 mesh grid (Ted Pella, Inc.). TEM characterization was performed using a Hitachi 9500 TEM with an accelerating voltage of 300 keV. The size distribution of the particles was determined using >200 NPs from various positions on the grids and using ImageJ software (Nation Institute of Health, USA).

3.2.9 X-Ray Photoelectron Spectroscopy (XPS)

XPS spectra were obtained using an ESCALAB 250XI XPS with a monochromated, micro-focused Al Kα X-ray source (spot size = 600 μm). Survey and high-resolution spectra were collected with a pass energy of 150 and 50 eV and a step size of 1.0 eV and 0.1 eV, respectively. Spectra were charge referenced to adventitious carbon (284.8 eV). NPs were drop-cast onto p-doped (boron) silicon wafers (University Wafer, Boston, MA) that had been cleaned for ultra-high vacuum analysis.

3.2.10 Powder X-Ray Diffraction (PXRD)

$Cu_{2-x}Se$ NPs were characterized by PXRD using a Bruker AXS D8 Discover XRD (NanoScale Fabrication and Characterization Facility, Petersen Institute of NanoScience and Engineering, Pittsburgh, PA) at 40 kV and 40 mA for Cu Kα (λ = 1.5406 Å) X-ray source with a scan speed of 0.8 s/step from 10.00° to 90.00° with a step size of 0.02°. Samples were prepared by drop-casting an aliquot of purified NP solution dispersed in chloroform on a glass microscope slide (Fisher Scientific). The as-prepared $Cu_{2-x}Se$ sample on the glass slide was left to oxidize in air over the course of several weeks and re-characterized. Bulk Cu_2Se and $Cu_{2-x}Se$ powders were packed in a 0.50 mm capillary tubes (Hampton Research) and flame sealed for PXRD characterization. The PXRD pattern of these samples was collected using a Bruker X9 Prospector Ultra (Department of Chemistry, University of Pittsburgh) at 45 kV and 0.65 mA equipped with a IμS micro-focus Cu Kα (λ = 1.54178 Å) X-ray source with a scan speed of 0.5 s/step from 12.00° to 108.00° with a step size of 0.02°.

3.2.11 ^{1}H NMR Spectroscopy

All ^{1}H NMR measurements were performed on a Bruker 400 Ultrashield magnet with an AVANCE III 400 Console or a Bruker 600 Ultrashield magnet with an AVANCE III 600 Console (Bruker Biospin, Billerica, MA) at 298 K. For all experiments, a minimum recycle delay of 15 s was used, which was sufficiently greater than T_1. NMR samples were prepared as described above by dissolving OLA, ODE, EtOH in deuterated $CHCl_3$, and by concentrating the $Cu_{2-x}Se$ NPs in deuterated $CHCl_3$.

3.2.12 ^{77}Se Solid State NMR Spectroscopy

Dried $Cu_{2-x}Se$ NPs were packed in a glovebox into 4 mm zirconia rotors with Kel-F inserts and air-tight Vespel caps for analysis with solid state nuclear magnetic resonance (ssNMR). All ssNMR spectra were recorded on a Bruker Avance 500 MHz (11.7 T) spectrometer, equipped with a triple-resonance 4 mm CPMAS probehead operating at a ^{77}Se Larmor frequency of 95.38 MHz. ^{77}Se chemical shifts were externally referenced to $(NH_4)_2SeO_4$ at 1040.2 ppm. Temperature was maintained with a BVT3000 variable temperature unit. Nitrogen cooling was used for all low temperature measurements and a steady stream of compressed air was used for all room temperature measurements.

3.2.13 Hahn Echo Experiments

Static ^{77}Se NMR spectra of $Cu_{2-x}Se$ NPs were recorded using a standard $(\pi/2)_x$-t_{echo}-$(\pi)_y$-acquire spin echo pulse sequence. In general, π/2 pulse lengths were ~2.5 μs and t_{echo} = 30 μs. Recycle delays were set to 5 x T_1 and typically ranged from 50 - 200 ms, depending on the degree of oxidation of the sample.

3.2.14 Inversion Recovery Experiments: Measuring T_1

Static T_1 measurements were collected from temperatures ranging from 175 - 350 K using an inversion-recovery experiment. All T_1 simulations were fit to a mono-exponential recovery curve of the form:

Equation 3.1. Inversion Recovery Equation for Extracting T_1

$$m_z(t) = m_0\left(1 - 2exp^{\left(-\frac{t}{T1}\right)}\right)$$

where *t* was varied from 100 μs to 200 ms, depending on the degree of oxidation of the sample.

3.3 Results and Discussion

3.3.1 Assigning Cu^{2+} Chemical Environment using EPR

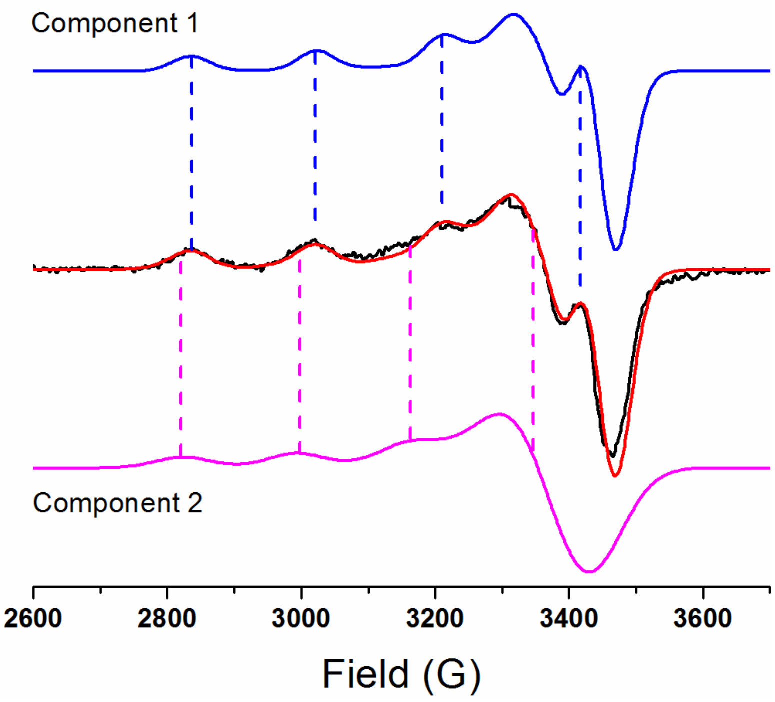

Figure 3.1. Representative simulation (red) of CW EPR spectrum obtained for $Cu_{2-x}Se$ NPs after 43 hrs of oxidation (black). The multicomponent simulation (red) is a summation of component 1 (blue) and component 2 (pink). The $A_{\parallel}$ splittings of each component are denoted by the blue and pink dashed lines.

A representative CW EPR spectrum of the partially oxidized $Cu_{2-x}Se$ NPs and the corresponding spectral simulation are shown in **Figure 3.1.** The spectrum was best fit using two components, and these are shown in blue and pink. Each component is characterized by two second rank tensors, the **g** tensor (**g**) and the hyperfine (**hf**) tensor. The **g** tensor is indicative of electronic environments of the unpaired electron, while the **hf** tensor is related to electron–nuclear interactions (represented as A). These tensors are diagonalized in their principal axis systems resulting in three principal components: g_{xx}, g_{yy}, and g_{zz} and A_{xx}, A_{yy}, and A_{zz}. The measured spectra were consistent with axially symmetric **g** and **hf** tensors, in which $g_{xx} = g_{yy} \equiv g_{\perp}$, $g_{zz} \equiv g_{\parallel}$, $A_{xx} = A_{yy} \equiv A_{\perp}$, and $A_{zz} \equiv A_{\parallel}$.[158-159] The splittings due to $A_{\parallel}$ are more pronounced as shown by dashed lines (**Figure 3.1**). The presence of a second component indicates more than one electronic environment.

Table 3.1. Best Fit Parameters for EPR Simulations of $Cu_{2-x}Se$ NPs from Figure 3.1.

	Component 1	**Component 2**
$g_{\perp}$	2.0468	2.0577
$g_{\parallel}$	2.2182	2.2475
$A_{\perp}$ (G)	22	18
$A_{\parallel}$ (G)	204	184
$LB_{\perp}$ (G)	62	127
$LB_{\parallel}$ (G)	70	107

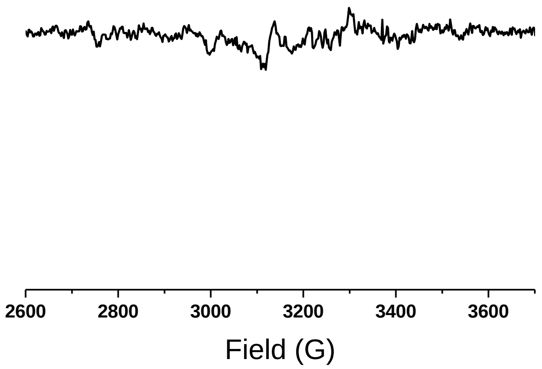

Figure 3.2. EPR spectrum collected immediately after washing the NPs, displaying no detectable EPR signatures.

The evolution of the EPR spectra as a function of oxidation was monitored from 0 to 230 h (**Figure 3.3**). The best fit **g** and **hf** parameters are reported in **Table 3.1** along with the line broadening (LB) used for the simulations for each component. The proportion of the second component increases with oxidation time. (Note: The EPR spectrum at “0 h” of air exposure is the EPR spectrum obtained immediately after particle purification, which involves ~20 min of air exposure. This air exposure is enough to result in the emergence of an LSPR. However, at this time point, while there may be free charge carriers, no EPR signal is observed, indicating that the concentration of Cu^{2+} is below the detection limit of the EPR instrument (**Figure 3.2**).)

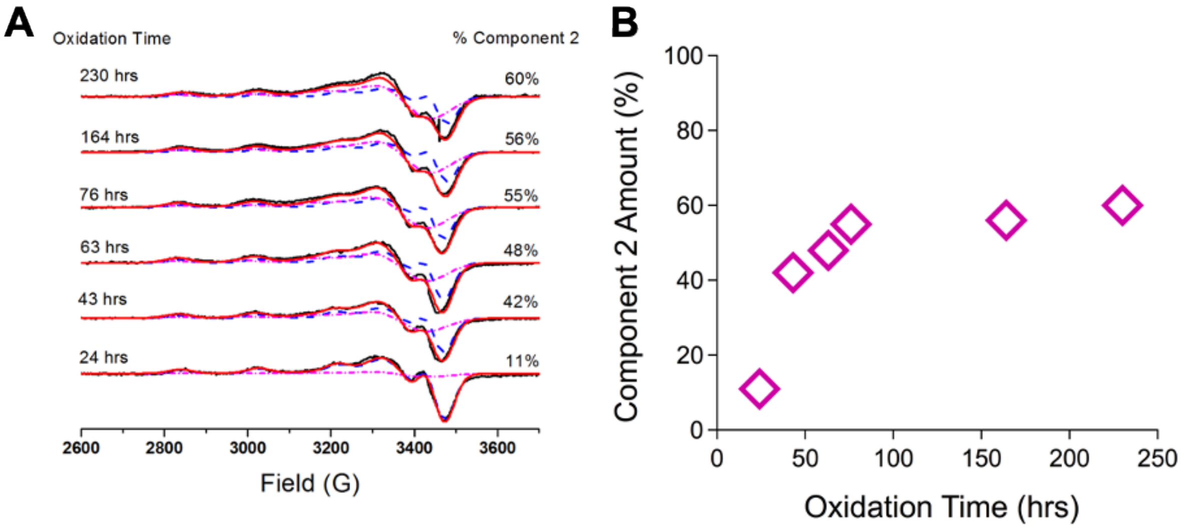

Figure 3.3. (A) Experimental CW EPR spectra (solid black) and corresponding 2 component simulations (solid red) of $Cu_{2-x}Se$ NPs as a function of oxidation. The simulated spectra of component 1 and component 2 are shown by a blue dashed line and a pink dot-dash line, respectively. Total amount of time of oxidation is denoted to the left of each spectrum. The percentage of component 2 in each simulation (relative to component 1) is listed to the right of each spectrum. (B) Time evolution of the second electronic environment, which reaches a steady state after ~76 hrs and comprises ~60% of the total Cu^{2+} environments.

As the ambient exposure time of the NPs increases, there is a change in the relative fractions of the two components present in the EPR spectra (**Figure 3.3A**). The changing component fractions suggest an evolution in the population of Cu^{2+} electronic environments in the NP. The relative fraction of component 2 as a function of exposure time is plotted in **Figure 3.3B**. After ~76 h of air exposure, the NPs reach a steady state between the two environments, with ~60% of the Cu^{2+} in the second electronic environment. This time scale and the corresponding environment fractions are consistent across multiple synthetic batches of NPs (**Figure 3.4**).

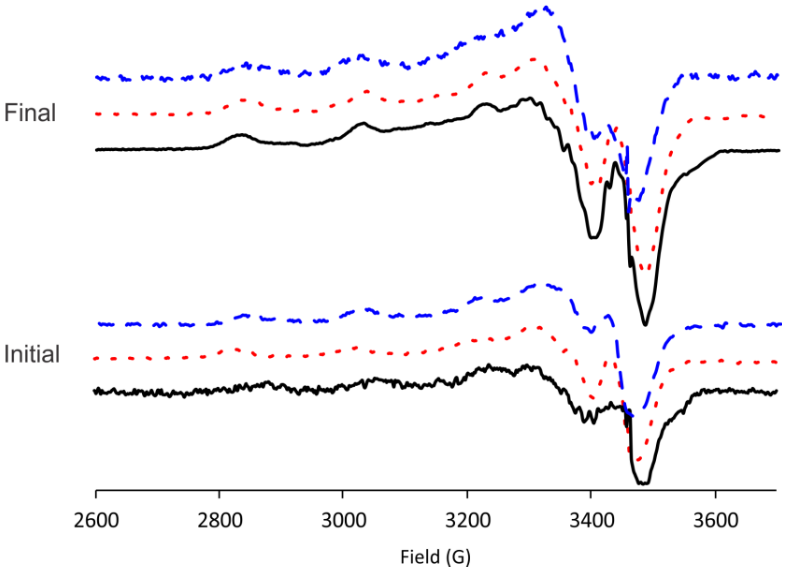

Figure 3.4. Multiple synthetic batches showcase similar lineshapes before and after oxidation indicating reproducibility of the EPR spectra.

While two Cu^{2+} environments are observed in our initial EPR assessment, these Cu^{2+} environments could correspond to four possible families of Cu^{2+} positions: (1) Cu^{2+} coordinating to the OLA capping ligand on the particle surface, (2) Cu^{2+} coordinating to surface or core Se atoms, (3) Cu^{2+} coordinating to O in a copper oxide, or (4) Cu^{2+} being ejected from the NP to form "free" Cu^{2+} coordinated to various ligands (or solvent) in solution (**Figure 3.4**). To assign the two observed Cu^{2+} environments, we compare our experimental results to the spectra of known systems.

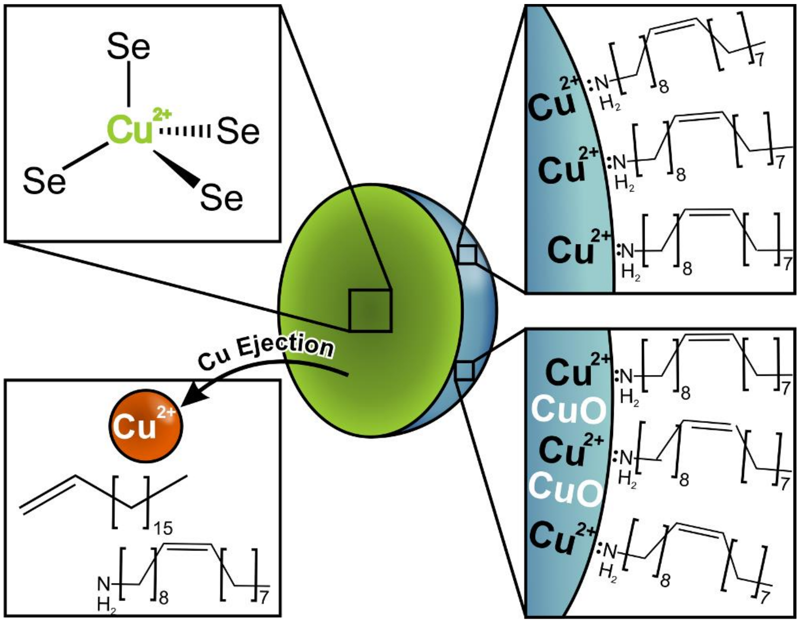

Figure 3.5. Illustration of the potential Cu^{2+} environments contained in $Cu_{2-x}Se$ NP samples. Starting from the top left and moving clockwise, there is Cu^{2+} coordinated to Se in tetrahedral positions in the antifluorite $Cu_{2-x}Se$ lattice, Cu^{2+} at the surface of the nanoparticle coordinating the OLA capping ligand, Cu^{2+} in a surface oxide layer, or Cu^{2+} ejected from the NP and coordinating to excess OLA capping ligand and/or solvent. (N.B. selenium environments are omitted for clarity.)

First, we consider the case of the "free" Cu^{2+} coordinating to ligands available in solution. To study this possibility, we measured the CW EPR spectra of a standard Cu^{2+} control (here, $CuCl_2$ in water), CuCl (i.e., the Cu^{+} precursor used in synthesis) mixed with oleylamine (Cu + OLA) in chloroform, and CuCl mixed with octadecene (Cu + ODE) in chloroform, all subjected to the same heat treatment and washing procedures as outlined in the $Cu_{2-x}Se$ NP synthesis (vide supra, **Figure 3.6**). We also investigated the CW EPR spectrum of an additional Cu^{2+} control where $CuCl_2$ salt was mixed with oleylamine suspended in chloroform *without* heat treatment (i.e., not mimicking synthesis conditions, referred to here as Cu + OLA + no heat.)

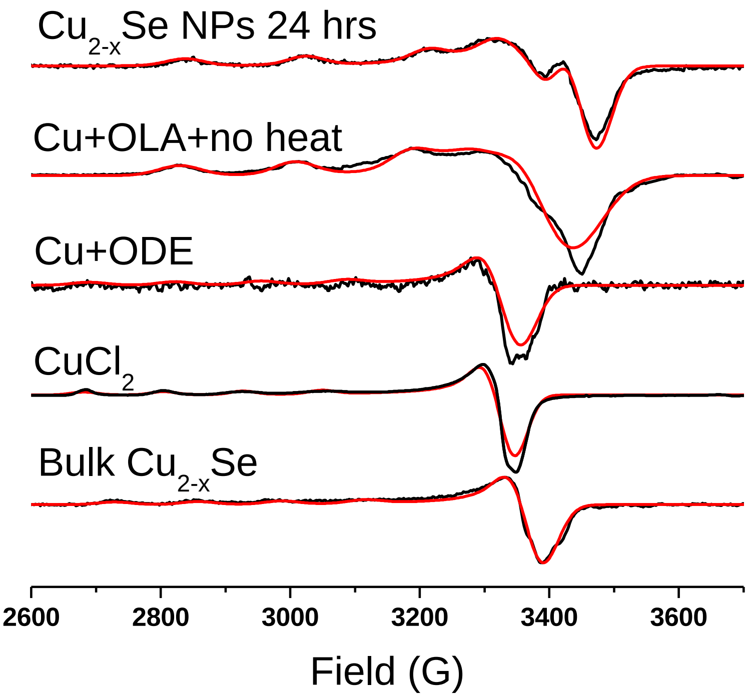

Figure 3.6. CW EPR spectra (black) and simulations (red) of additional Cu mixture controls compared to Cu$_{2-x}$Se NPs oxidized for 24 hrs. Cu+OLA+no heat represents the spectra from CuCl$_2$ mixed with OLA in chloroform. Cu+ODE are spectra from a heat treated mixture of CuCl, ODE, and chloroform. CuCl$_2$ are spectra from the mixture of CuCl$_2$ salt in water. Bulk Cu$_{2-x}$Se is a powdered sample obtained commercially.

Table 3.2. Best Fit Parameters for EPR Simulations for Spectra Shown in Figure 3.6, Figure 3.7, and Figure 3.12.

Compound	**$g_{\perp}$**	**$g_{\parallel}$**	**$A_{\perp}$ (G)**	**$A_{\parallel}$ (G)**	**LB⊥ (G)**	**LB∥ (G)**
CuCl$_2$	2.0770	2.4117	5	136	45	70
Cu+OLA	2.0443	2.2198	25	205	63	71
Cu+OLA+no heat	2.0478	2.2560	20	178	135	75
Cu+ODE	2.0777	2.3930	5	155	65	72

Cu_{2-x}Se Bulk	2.0654	2.3780	1	150	60	70
Cu@CuO NPs Component 1	2.0428	2.2083	22	211	62	70
Cu@CuO NPs Component 2	2.0577	2.2475	18	184	162	89
Cu_{2-x}Se NPs Component 1	2.0468	2.2182	22	204	62	70
Cu_{2-x}Se NPs Component 2	2.0577	2.2475	18	184	127	107

Their corresponding EPR simulation parameters for each of these spectra in **Figure 3.6** are given in **Table 3.2**. The heat-treated $CuCl_2$ as well as the Cu + ODE mixtures exhibit different **g** and **hf** parameters from those measured for either of the two components of the NPs. Specifically, the $g_{\perp}$ values are larger (~0.04) while the $A_{\parallel}$ values are smaller (~30–50 G) than those derived for the two components of the NPs. Likewise, the Cu + OLA + no heat mixture has unique **g** and **hf** tensors that are different from either NP component (**Figure 3.6** and **Table 3.2**).

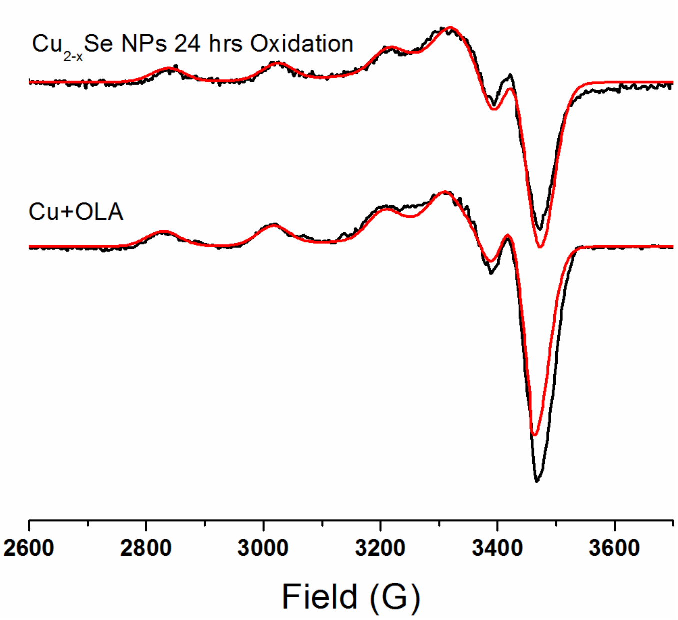

Figure 3.7. Experimental CW EPR spectra (black) and simulations (red) of $Cu_{2-x}Se$ NPs oxidized for 24 hrs (top) compared to Cu-OLA coordination complex (bottom) formed via heating. The results indicate component 1 is a surface Cu-OLA environment.

Interestingly, the **hf** and **g** tensors of the Cu + OLA mixture (the mixture that underwent treatment consistent with synthesis conditions including heat) are similar to those derived for component 1 of the NPs, but the spectrum does not contain evidence of component 2 (**Figure 3.7**). SEM of this mixture (**Figure 3.8**) shows no discernible particles formed upon heating and instead indicates the formation of a Cu–OLA coordination polymer aggregate. Because component 1 from the NPs does not resemble any of the other above controls, including Cu + OLA + no heat, we may deduce that the similarities between component 1 of the NPs and the Cu + OLA mixture indicate that the first Cu^{2+} environment is associated with OLA bound on the particle surface (i.e., we do not expect OLA–Cu^{2+} interactions occurring on the interior of the particle). In turn, it could also be argued that there is a fraction of Cu–OLA polymer aggregate present in the NP sample. However, no EPR signal was detected from the initial NP sample (**Figure 3.1**), and therefore no detectable coordination polymer is present in the NP sample after washing. Taken together, these results support the assignment of one Cu^{2+} environment to surface bound Cu–OLA complexes. These results are in agreement with previous ICP-MS results, which indicate that Cu is not ejected from the NP and is not coordinating to solvent ligands during the oxidation process.[62]

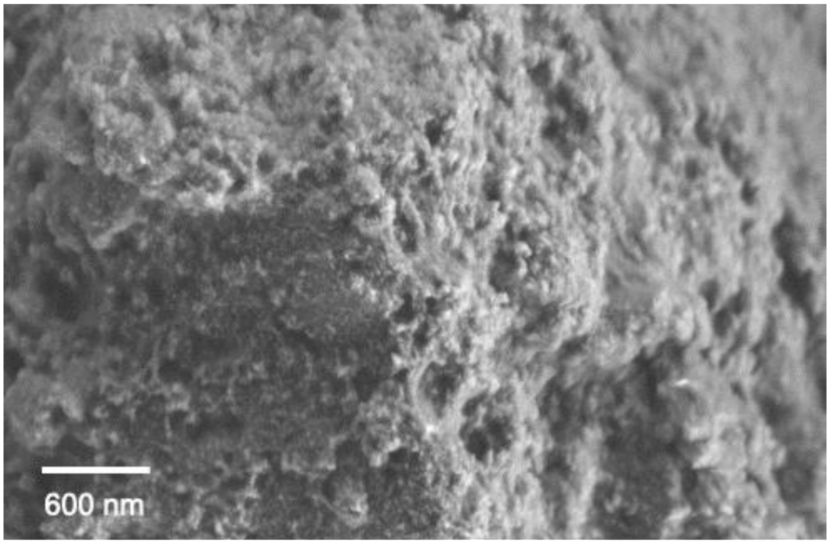

Figure 3.8. SEM micrograph of the Cu+OLA coordination polymer.

Having initially assigned one electronic environment to Cu–OLA surface sites, we next study whether there is formation of a distinct surface oxide layer. Surface oxide formation is suspected in previous studies of $Cu_{2-x}Se$ NP systems[95-96, 98] and has also been observed in pure Cu NPs (forming Cu@CuO, core@shell morphologies).[160-164] To investigate whether the second Cu^{2+} environment is due to the formation of a copper oxide layer, we measured the CW EPR spectrum of Cu@CuO NPs for comparison. Here, Cu NPs were synthesized with OLA as a capping ligand, using a previously reported procedure.[154, 165] XPS, TEM, and extinction spectra characterization of the resulting particles are shown in **Figure 3.9**, **Figure 3.10**, and **Figure 3.11**, respectively.

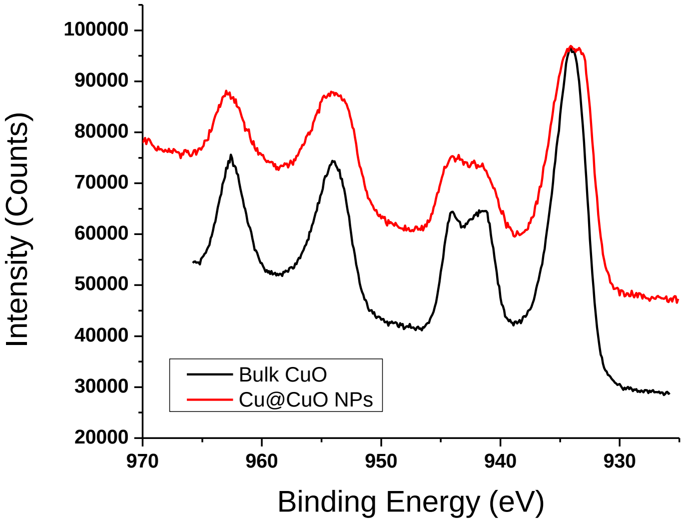

Figure 3.9. Cu 2p XPS peaks for bulk CuO and Cu@CuO NPs. Note that the strong satellite peaks near ~940-945 and ~962 eV indicate the formation of Cu^{2+}. Likewise, the peak at 934.1 eV is typically characteristic of the Cu^{2+}, and is present in both samples. The Cu@CuO NPs display additional broadening near 933 eV, which is characteristic of lower Cu oxidation states, consistent with the low valent Cu metal core of the NPs, which is absent in the bulk CuO.

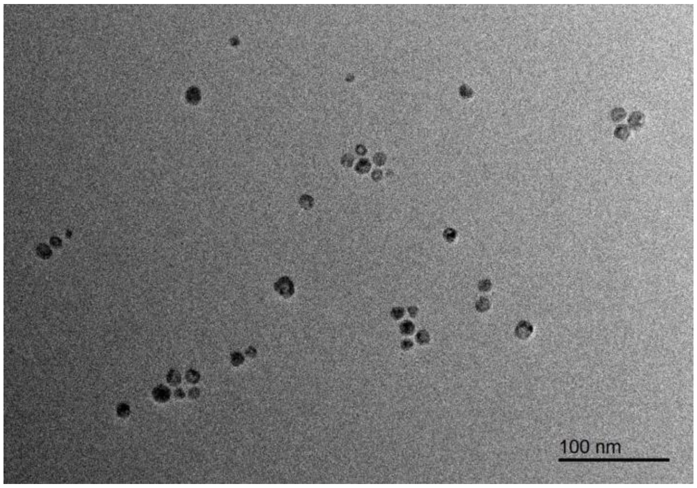

Figure 3.10. TEM of Cu@CuO NPs.

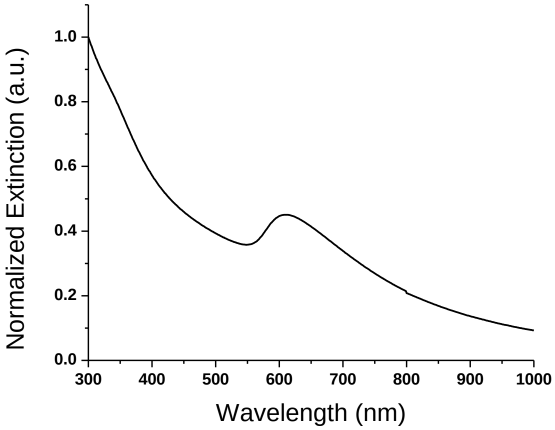

Figure 3.11. Extinction spectrum of Cu@CuO NPs.

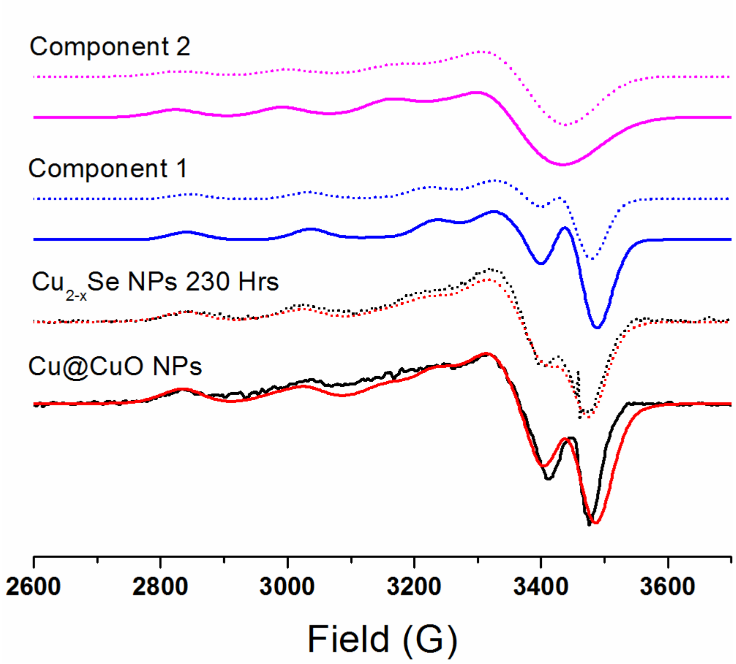

Figure 3.12. CW EPR spectra (black) and corresponding simulations (red) for Cu@CuO NPs (solid lines) and Cu$_{2-x}$Se NPs oxidized for 230 hrs (dotted lines). The spectra have been referenced to the same frequency to highlight to similarities between the g and hf values obtained for

component 1(blue) and component 2 (pink) of the 2 NP systems. These results indicate that component 2 of the $Cu_{2-x}Se$ NPs is likely a CuO environment.

In the Cu@CuO NP system, only paramagnetic Cu^{2+} in the oxide layer results in an EPR signal. Simulation of the CW EPR spectrum of Cu@CuO NPs also requires a two-component fit. Comparison of the components for fully oxidized $Cu_{2-x}Se$ NPs and Cu@CuO NPs is shown in **Figure 3.12**. The $g_{\parallel}$ and $A_{\parallel}$ values obtained for Cu@CuO NPs components 1 and 2 agree well with components 1 and 2 of $Cu_{2-x}Se$ NPs, respectively (**Table 3.2**), which indicates similar electronic environments between the NP systems. The OLA capping ligand is consistent for both NP systems providing a similar surface Cu–OLA environment for the Cu@CuO and $Cu_{2-x}Se$ NPs, which is already assigned to component 1. Therefore, we assign component 2 of the EPR spectrum from Cu@CuO NPs to CuO. By analogy, these results indicate the formation of CuO on $Cu_{2-x}Se$ NPs as well. Importantly, in both the Cu@CuO NPs and $Cu_{2-x}Se$ NPs, the CuO component shows increased broadening, a decrease in the $A_{\parallel}$ splittings, and an increase in $g_{\parallel}$ compared to the Cu–OLA component. These trends are consistent with decreasing nitrogen and increasing oxygen coordination.[166]

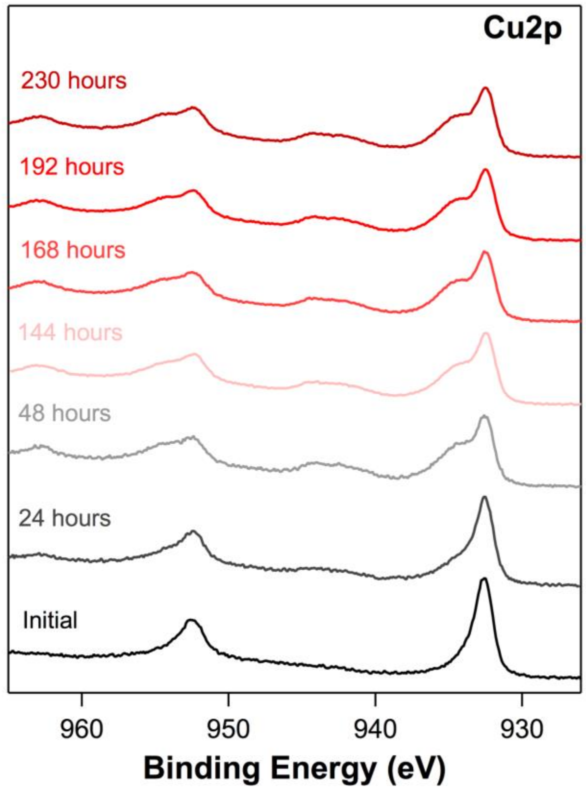

Figure 3.13. Cu 2p XPS peaks for $Cu_{2-x}Se$ NPs. Note that the strong satellite peaks near ~940-945 and ~962 eV indicate the formation of Cu^{2+}, which increases in intensity as the NPs oxidize.

The presence of CuO in the $Cu_{2-x}Se$ NPs was also evaluated using XPS measurements (**Figure 3.13**). We observe the emergence of Cu 2p satellite peaks near ∼940–945 and ∼962 eV, which increase in intensity with increasing oxidation time, similar to results obtained by Prieto et al.[98] The appearance of these peaks is consistent with the XPS spectra of Cu@CuO NPs (**Figure 3.9**) and further corroborates the formation of CuO species on the surface of $Cu_{2-x}Se$ NPs. Unfortunately, the CW EPR spectrum of the Cu@CuO NPs cannot be directly compared to bulk CuO because bulk CuO is antiferromagnetic and will not yield an EPR signal unless annealed at high temperatures.[167] In both the Cu@CuO and $Cu_{2-x}Se$ NPs, the domain size of the CuO must be small enough that antiferromagnetic behavior is not observable. Indeed, a previous study of the magnetic behavior of CuO NPs clearly demonstrates antiferromagnetic behavior at room temperature in particles with diameters of 6.6 nm, which inadvertently gives an upper limit on the size of the CuO domains we are observing in the $Cu_{2-x}Se$ NPs.

It is important to note that the second electronic environment observed from the $Cu_{2-x}Se$ NPs may also be a Cu–Se interaction. To evaluate whether the second environment was associated with Cu–Se interactions, we obtained a bulk, powdered sample of Cu_2Se and stored the material in air. After storage, the formation of $Cu_{2-x}Se$ in the sample was discernible in PXRD spectra (**Figure 3.14**). The PXRD indicates the presence of both cubic $Cu_{2-x}Se$ and monoclinic Cu_2Se phases. The EPR spectra and corresponding simulation parameters of bulk Cu_2Se powders are given in **Figure 3.6** and **Table 3.2**. Here, the **g** ($g_{\parallel}$ = 2.3780 $g_{\perp}$ = 2.0654) and **A** ($A_{\parallel}$ = 150 G, $A_{\perp}$ = 1 G) values are in agreement with $Cu(OH)_2$ formation and are not representative of either component observed from the $Cu_{2-x}Se$ NPs.[168]

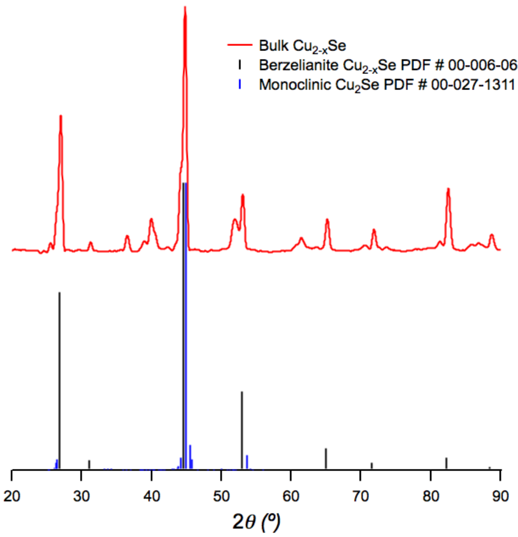

Figure 3.14. PXRD of bulk $Cu_{2-x}Se$ after oxidation (red) showing an mixture of multiple copper selenide phases.

3.3.2 Impact of Oxidation on the Structure of LSPR and Cu$_{2-x}$Se NPs

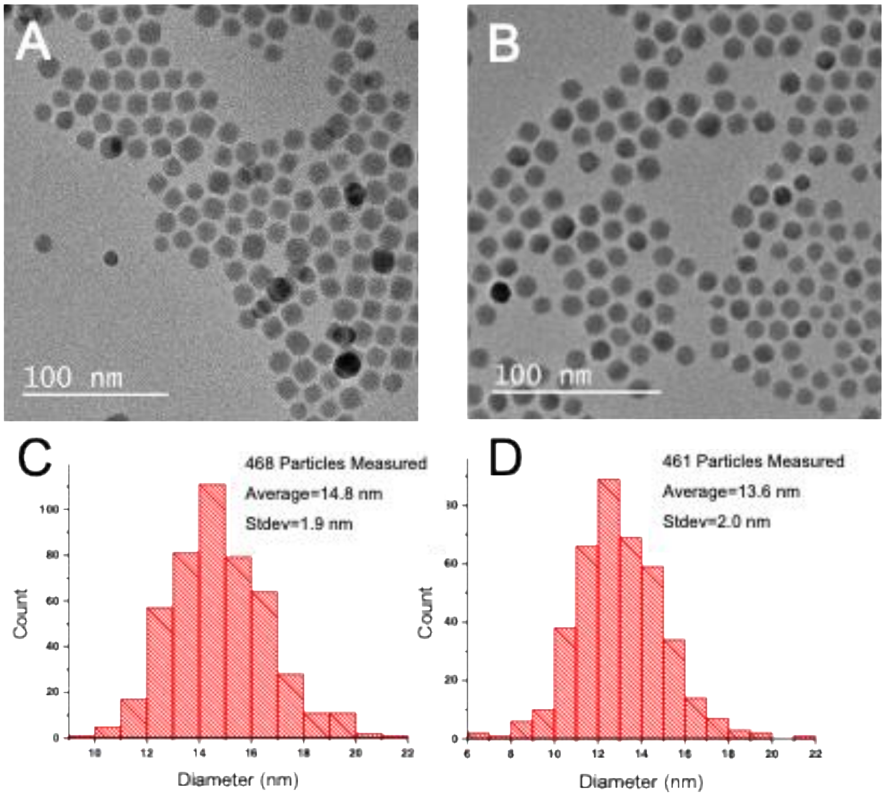

Figure 3.15. Transmission electron micrographs (A,B) and corresponding histograms of particle diameter (C,D) for Cu$_{2-x}$Se NPs oxidized for 0 hrs (A,C) and 230 hrs (B,D). Analysis of NPs via TEM before and after the oxidation study shows no detectable changes in the size or morphology of the NPs, and indicates that the NPs are robust with respect to the freeze-thaw procedure employed.

Our EPR analysis provides critical insight into the fate of the Cu^{2+} species which has implications for its crystal structure and stoichiometry. Nominally, fully reduced Cu_2Se NPs exhibit a monoclinic or orthorhombic structure. The oxidation of Cu_2Se NPs results in the formation of cubic antifluorite $Cu_{2-x}Se$.[57, 62, 95, 98] However, there remains debate about the fate of the Cu^{2+} in $Cu_{2-x}Se$ NPs. In bulk Cu_2Se, this structural transformation is accompanied by the formation of vacancies on the Cu sublattice. At the nanoscale, two scenarios have been previously reported: (1) Cu^{2+} leaves the NP to either form "free" Cu^{2+} species and/or small, discrete (2–5 nm) CuO NPs and/or (2) oxidized Cu^{2+} migrates to the surface of the NP.[95, 98, 169]

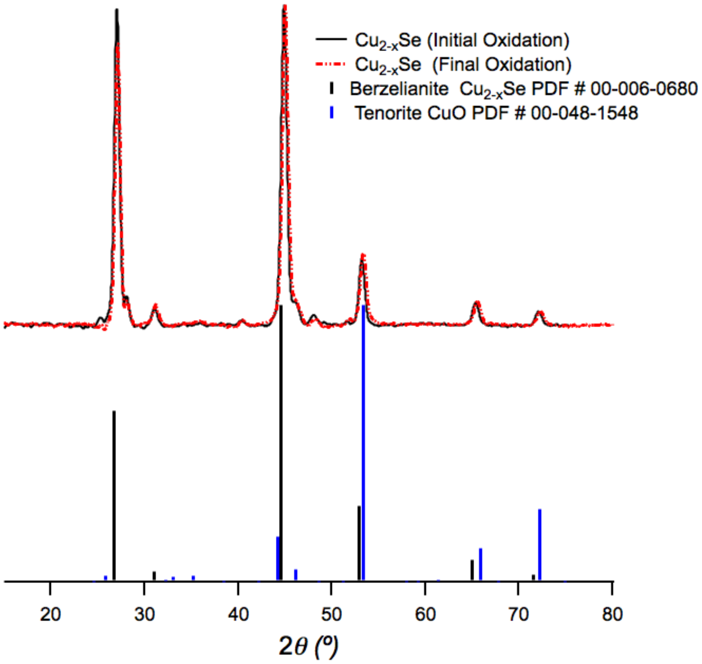

Figure 3.16. PXRD of $Cu_{2-x}Se$ NPs before (black solid line) and after oxidation (red dotted line).

The released Cu^{2+} ions would give a distinct EPR resonance, akin to that of $CuCl_2$ or Cu + OLA + no heat, which we do not observe in our experiments. On the other hand, the formation of

CuO NPs would give rise to similar EPR signatures to what we have observed, assuming the NPs stayed below the domain size of antiferromagnetic CuO (<6−7 nm). To assess the possibility that our samples may contain discrete CuO NPs, we analyzed samples via TEM techniques. Analysis of the resulting micrographs (**Figure 3.15**) showed no evidence of 2–5 nm particle formation, and we also did not observe CuO phases in the XRD patterns of any of the tested particles (**Figure 3.16**), although the absence of PXRD features is not definitive to exclude the presence of CuO NPs. In our experiments, case 1 (Cu leaving to form CuO or free Cu) is not supported. Instead, our results indicate that Cu^{2+} either exists as part of a CuO surface layer or may occupy the initial Cu positions within the particle lattice.[96, 98] Taken together, our results suggest the Cu^{2+} environments are localized at the surface of the NP (case 2).

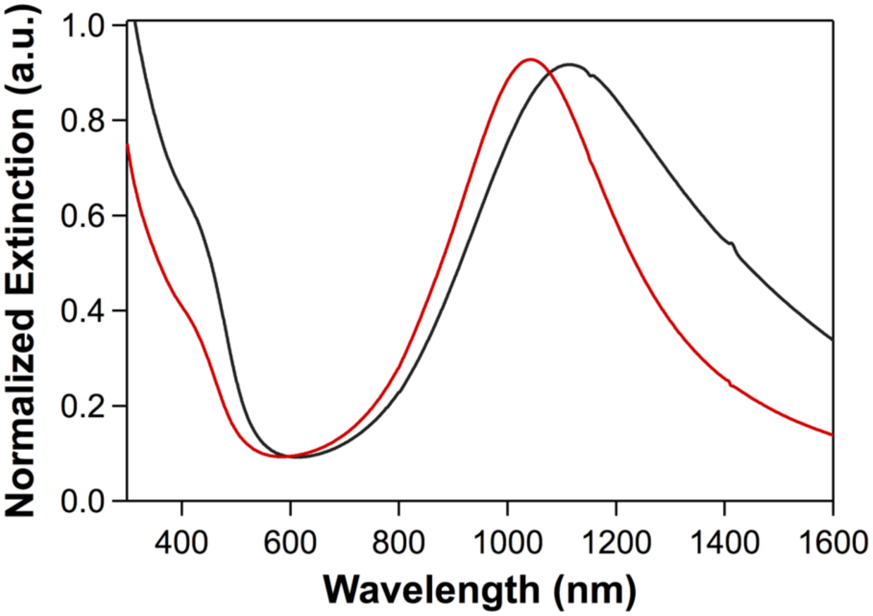

Figure 3.17. End point extinction spectra of $Cu_{2-x}Se$ NPs taken immediately after washing (black) and after 230 hrs of oxidation (red). After oxidation, the λ_{max} shifts 70 nm, the peak width narrows, and the intensity increases relative to the bandgap transition near 500 nm.

In addition to monitoring the CW EPR spectra of $Cu_{2-x}Se$ NPs as a function of air exposure over time, corresponding extinction spectra were also obtained (**Figure 3.17**). The time of air exposure plays an important role in the observed optoelectronic properties of the NPs. As has been previously reported by several groups, including our own, the frequency of the LSPR is dependent on the degree of NP oxidation.[62, 95-96, 169] Our LSPR studies start with NPs that have been oxidized during the washing procedure (**Figure 3.17**, black), and compared with NP sample after 230 hours of oxidation in air (**Figure 3.17**, red). Note that the washing procedure requires the use of ethanol, a known hole scavenger, and therefore the presence of ethanol could influence the LSPR properties of $Cu_{2-x}Se$.[52] However, all particles are dried after the ethanol purification procedure, which removes remaining solvent (**Figure 3.18**).

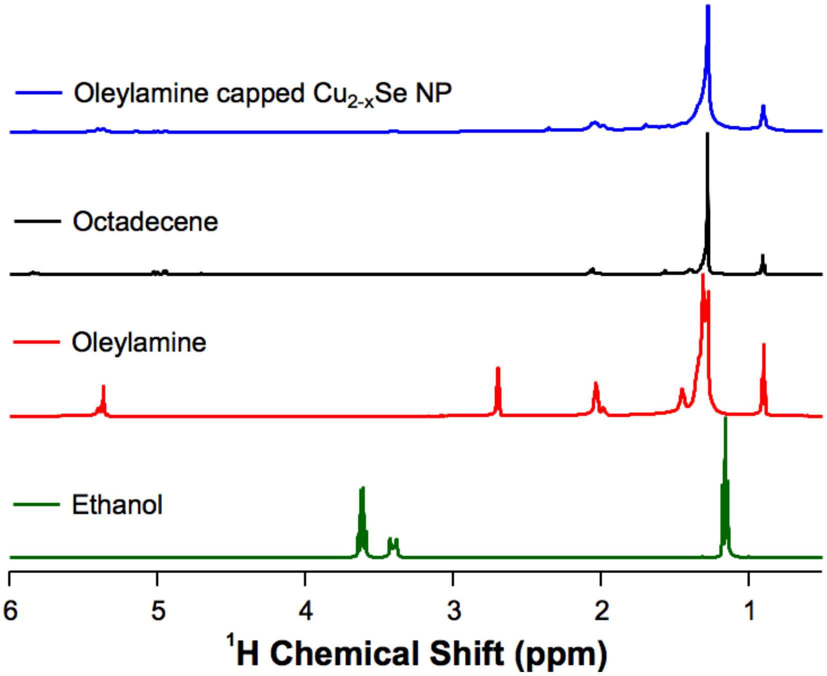

Figure 3.18. ^{1}H NMR spectrum of purified OLA capped $Cu_{2-x}Se$ NPs dispersed in d-$CHCl_3$ (blue) compared to ODE (black), OLA (oleylamine) and EtOH (green) in d-$CHCl_3$.

After the final CW EPR measurement, the extinction spectrum was recorded again. In this spectrum, the LSPR λ_{max} has blue-shifted ~70 nm and is coupled with a decrease in the peak width. In addition, the relative intensity of the LSPR increases over the time course of the EPR measurements (230 h), as benchmarked to the band gap transition intensity at ~500 nm. We solved for the charge carrier density of the tested particles using both these extinction spectra and NMR-based approaches. We used the extinction spectra and the Drude model, which is given as:

Equation 3.2. Drude Model Equation

$$\omega_{sp} = \sqrt{\frac{N_h e^2}{(m^* \varepsilon_0)(\varepsilon_\infty + 2\varepsilon_m)} - \gamma^2}$$

where ω_{sp} is the frequency of the LSPR, N_h is the charge carrier density, e is the elementary charge, m^* is the effective mass of the charge carrier, ε_0 is the permittivity of free space, ε_∞ is the high frequency dielectric constant of $Cu_{2-x}Se$, ε_m is the dielectric constant of the solvent, and γ is the full width at half-maximum (fwhm) of the LSPR.[49, 60] The charge carrier densities obtained for the end-point spectra using this method are 6.45×10^{21} and 7.96×10^{21} cm^{-3}, respectively. However, as noted elsewhere, shifts in λ_{max} may represent a change not only in N_h but also in dielectric environment, particle structure, and/or aggregation state, among other variables.[53, 60, 93]

3.3.3 Controlling LSPR Properties using Surface-Terminating Ligands

With the structural characterization presented in this work, there are several research questions that remain elusive. For example, while it is observed that the formation of a CuO surface species causes a blueshift in the LSPR, how would changes in other surface species impact the observed LSPR of $Cu_{2-x}Se$ NPs? Using the Drude model equation as a frame of reference, we can pinpoint several tunable parameters that can be controlled synthetically (and post-synthetically), such as the carrier densities and dielectric constant of the surrounding medium. As demonstrated previously in **Chapters 1.0** and **2.0**, the carrier densities of copper chalcogenide NPs are typically controlled via Cu oxidation, and that the surrounding medium can be tuned via the solvents the NPs are dispersed in.[49, 62] However, recently, while its contributions are generally ignored, the surface terminating ligands could be used to control the observed LSPR.[60]

The use of capping ligands to tune electronic properties is appealing due to the nearly endless variety of available capping ligands, which can range from monatomic ions to sterically bulky polymers or proteins.[82] Typically, ligands consist of multiple components that can be systematically studied: a head group that could bind to the NP surface as well as a substituent group (often a carbon chain) that facilitates the stabilization of NPs in solvents (**Figure 3.19**). Here, we propose that various components of the surface passivating ligands can influence the plasmonic properties of the $Cu_{2-x}Se$ NPs, both by changing carrier densities in the NPs as well as altering the dielectric constant of the surrounding medium.

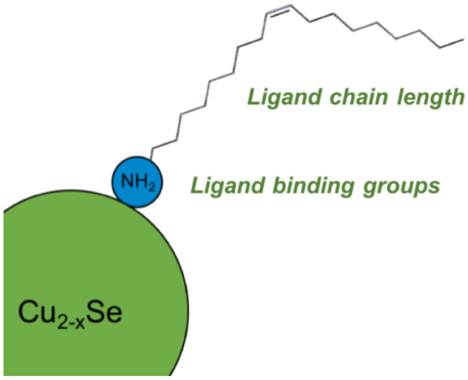

Figure 3.19. Schematic representation of two distinct components of surface ligands on $Cu_{2-x}Se$ NPs.

Specifically, using the as-synthesized OLA-capped $Cu_{2-x}Se$ NPs, we can perform mass action ligand exchange to post-synthetically modify the NP surface with different passivating ligands. The resulting ligand-induced changes in their optoelectronic properties and their carrier densities are then monitored using the combination of both the Drude model and the Korringa model. To facilitate interpretation between the interplay of ligand structure and resultant electronic behavior, these studies will focus on two aspects of the ligand structure: the role of the ligand binding moiety (*i.e.*, a thiol versus amine) and the ligand chain length.

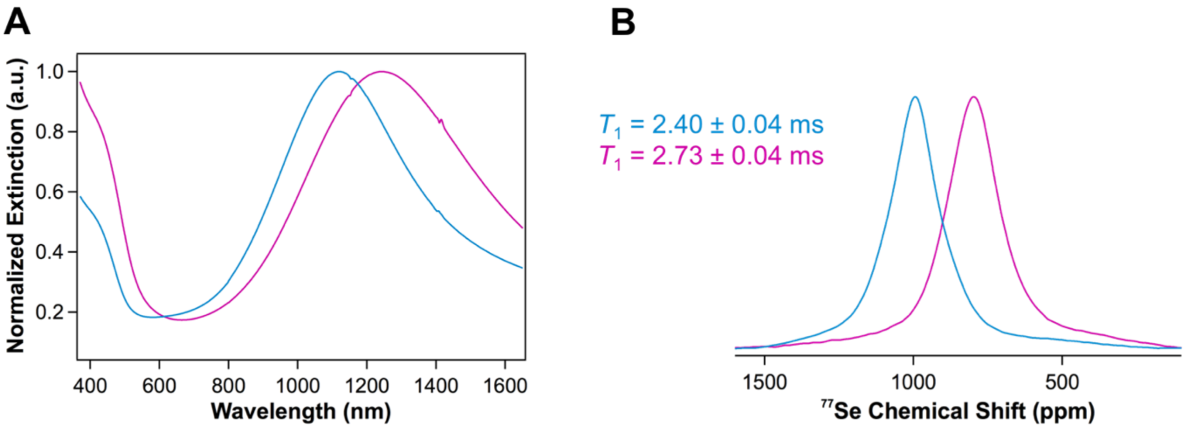

Figure 3.20. Extinction spectra (A) and observed chemical shifts and their corresponding relaxation rates (B) of OLA-capped (teal) and DDT-capped (pink) $Cu_{2-x}Se$ NPs, respectively.

By changing the ligand binding group from an amine (OLA) to a thiol (DDT) while keeping ligand chain length constant, we observed a dramatic change in the extinction spectrum (**Figure 3.20A**). The LSPR peak redshifts from around 1100 nm to 1250 nm and decreases in intensity, with a corresponding increase in intensity at the optical bandgap transition approximately at 580 nm. These observations suggest that there is a decrease in the carrier densities of $Cu_{2-x}Se$ NPs. The result is also consistent with the Moss-Burstein effect observed in the redshift of the optical bandgap transition from approximately 550 nm to 580 nm. Using the Drude model, we can quantify the decrease in the carrier densities from 6.9 ± 0.2 x 10^{21} cm^{-3} to 5.4 ± 0.7 x 10^{21} cm^{-3} upon ligand exchange to thiolated ligands. Consistently, similar to what was observed with $Cu_{2-x}Se$ NPs of various carrier densities discussed in **Chapter 2.0**,[62] the ^{77}Se NMR spectra of $Cu_{2-x}Se$ NPs show a shift to a lower ppm and an increase in its corresponding T_1 value upon ligand exchanging from the OLA- to DDT-capped NPs. Similar to the Drude model-extracted carrier densities, the NMR method also supports the decrease in the carrier density from 1.8 ± 0.3 x 10^{22} cm^{-3} to 1.4 ± 0.2 x 10^{21} cm^{-3}.

Table 3.3. Carrier Densities of Amine and Thiol-Terminated $Cu_{2-x}Se$ NPs Extracted Using Both Drude and NMR Methods. Error Indicates Standard Error Collected for At Least 3 Experimental Replicates.

Ligand Binding Group	Drude Extracted Carrier Density (cm^{-3})	NMR Extracted Carrier Density (cm^{-3})
Amine	$6.9 \pm 0.2 \times 10^{21}$	$1.8 \pm 0.3 \times 10^{22}$
Thiol	$5.4 \pm 0.7 \times 10^{21}$	$1.4 \pm 0.2 \times 10^{22}$

Based on the results summarized in **Table 3.3**, we hypothesized that thiolated ligands decrease the number of holes in the $Cu_{2-x}Se$ NPs due to the electron-donating nature of thiol headgroups compared to amines. The observed change in the carrier densities due to the presence of an electron-donating ligand has been previously observed in plasmonic $Cu_{2-x}Se$, where it was demonstrated that only 7% of the NP surface needs to be modified to produce a 200 nm shift in the LSPR.[170] Interestingly, using quantification methods established in **Chapter 2.0**, though differences are noted between the carrier densities of $Cu_{2-x}Se$ NPs extracted using the Drude model and the NMR model, both carrier density extraction methods show a consistent 20% decrease in the carrier density by changing the ligand binding group. To confirm that the change in the carrier densities observed are not due to any structural transformation of the NPs upon ligand exchange, TEM images and PXRD patterns of the NPs are evaluated before and after ligand exchange. TEM images and their corresponding size distributions show a minimal change in the NP size and shape (**Figure 3.21A- D**), while the PXRD patterns show that the DDT-capped NPs retained the cubic crystal structure, similar to the OLA-capped NPs (**Figure 3.21E**). However, there is a minor 2θ shifts observed around 45°, which could indicate that some of the anions in the $Cu_{2-x}Se$ lattice are replaced with a smaller S^{2-} anion, most probably located on the NP surface upon ligand exchange.

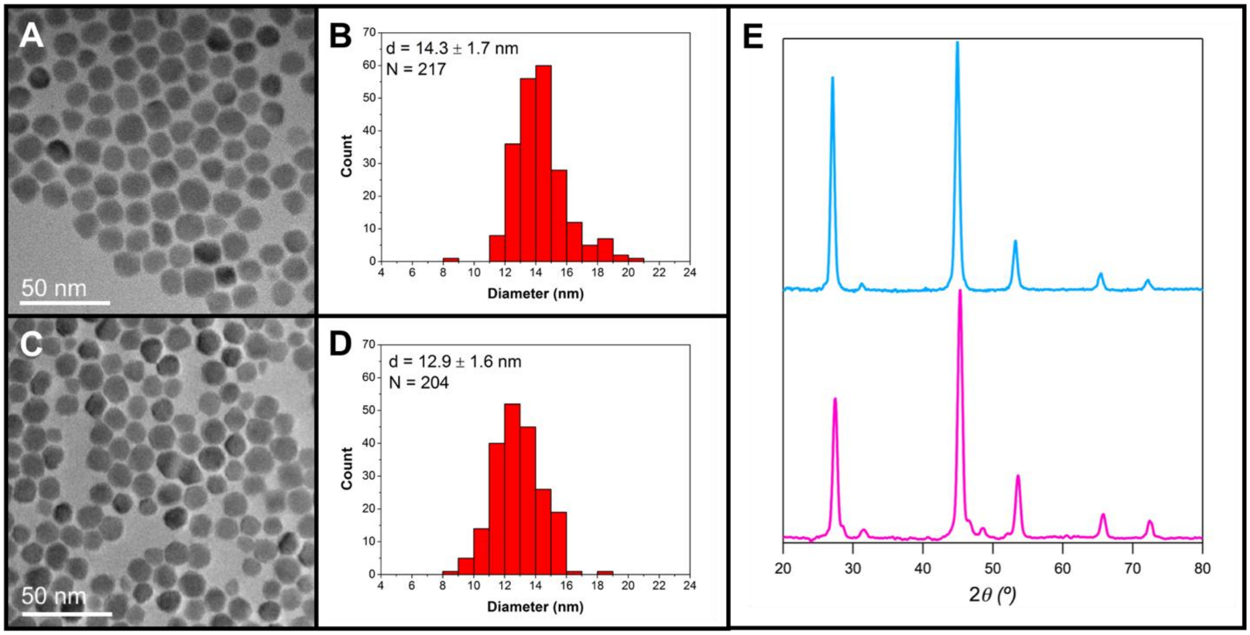

Figure 3.21. Transmission electron micrographs (A, C), their corresponding size histograms (B, D), and PXRD patterns (E) for OLA- (A, B, E teal) and DDT-capped (C, D, E pink) $Cu_{2-x}Se$ NPs.

Conversely, we can evaluate the influence of the ligand substituent group by keeping the ligand binding group constant while altering the ligand chain length. The effects of such ligand exchanges can also be monitored in the observed changes in optoelectronic properties of $Cu_{2-x}Se$ NPs and carrier densities. Here, we compare the influence of ligand chain length on $Cu_{2-x}Se$ NP electronic properties experimentally by introducing PEGSH of different average molecular weights on the NP surface via a similar ligand exchange protocol (**Figure 3.22**). Similarly, with the ability to measure the changes in the carrier densities concurrently with both the LSPR features and the ^{77}Se T_1 values using NMR, we can correlate ligand-induced LSPR shifts to either changes in the carrier density or the dielectric constant of the NP surrounding medium. For example, the influence of ligand shells have also been evaluated computationally on $Cu_{2-x}Se$ systems, where the authors also observed a ligand-induced shift in the LSPR when a NP core@ligand shell model is incorporated in the Mie theory scattering calculations.[60]

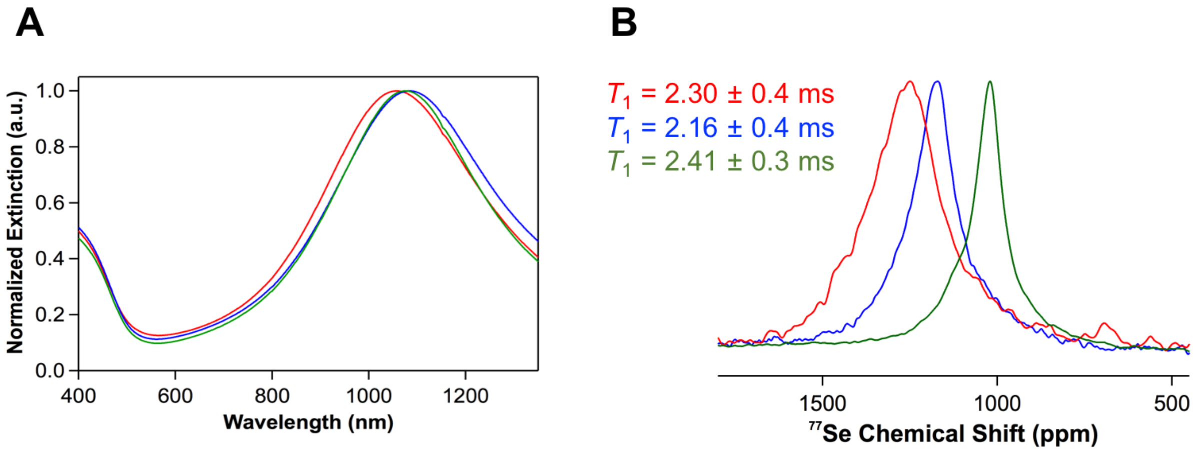

Figure 3.22. Extinction spectra (A) and observed chemical shifts and their corresponding relaxation rates (B) of 1 kDa (blue), 2 kDa (green), and 5 kDa (red) PEGSH-capped $Cu_{2-x}Se$ NPs, respectively.

Interestingly, both extinction spectra and extracted ^{77}Se T_1 values (**Figure 3.22**) showed minimal change between $Cu_{2-x}Se$ NPs that are passivated by PEGSH of any average molecular weight (of the three tested), indicating that there is a minimal change in the carrier densities extracted via either method. The carrier densities are evaluated using ANOVA and are considered to be statistically the same. We can again confirm that the process of ligand exchange does not alter the NP core sizes by analyzing the size distribution of $Cu_{2-x}Se$ NPs obtained in HRTEM (**Figure 3.23**). Similarly, as summarized in **Table 3.4**, the Drude model extracted carrier densities also show no statistical differences between each PEGSH molecular weights. The lack of a trend in the LSPR shift as a function of increasing in molecular weight is likely due to PEGSH ligands tend to be flexible on the NP surface, rather than forming organized, fully extended structures. Additionally, the long ethylene glycol (EG) units are also known to wrap around the NP surface in random order, so the oxygen in each EG monomer could also bind directly on the NP surface, thus influencing the electronic structure of $Cu_{2-x}Se$ NPs. Finally, the PEGSH ligands are most-likely hydrated with solvent molecules embedded between each ligand chain. Therefore, instead of having a NP@ligand core@shell morphology, it is more likely that it could be a NP@ligands-solvent configuration. Unfortunately, as alluded previously, the presence of an oxide species on NP surface adds additional complexity in analyzing the PEGSH influence in the LSPR dielectric environment. Nonetheless, the lack of statistical differences observed via NMR suggest that this is not a solvent effect as all samples are dried completely prior to NMR characterization.

Table 3.4. Carrier Densities of Thiol-Terminated $Cu_{2-x}Se$ NPs with Different Chain Length Extracted Using Both Drude and NMR Methods. Error Indicates Standard Error Collected for At Least 3 Experimental Replicates.

Ligand Chain Length	Drude Extracted Carrier Density (cm^{-3})	NMR Extracted Carrier Density (cm^{-3})
1 kDa PEGSH	$7.3 \pm 0.1 \times 10^{21}$	$1.8 \pm 0.4 \times 10^{22}$
2 kDa PEGSH	$6.9 \pm 0.8 \times 10^{21}$	$1.9 \pm 0.4 \times 10^{22}$
5 kDa PEGSH	$7.3 \pm 0.4 \times 10^{21}$	$2.0 \pm 0.6 \times 10^{22}$

Thus far, our preliminary results have shown that the presence of pendant ligands significantly influence the NP plasmonic properties. With robust analytical methods to identify the influences of ligand structure and dielectric environment on the electronic structure of the NPs, we have shown that the ligand binding groups have the ability to donate or withdraw electrons into the NPs, whereas the changes to the ligand chain lengths do not alter the carrier densities present in the NP system. Further, both the Drude model and NMR method of quantifying carrier densities yield results that are consistent with each other. Importantly, these observations allow us to use the changes in the observed LSPR as a diagnostic feature to probe changes in the surface structure, which will be useful in downstream applications such as plasmon-enabled chemical sensing and conversions. For example, as it will be discussed further in detail in **Chapter 5.0**, LSPR shifts are used to determine the concentrations of analytes used to establish the electromagnetic field enhancement factor for $Cu_{2-x}Se$ NPs.[100]

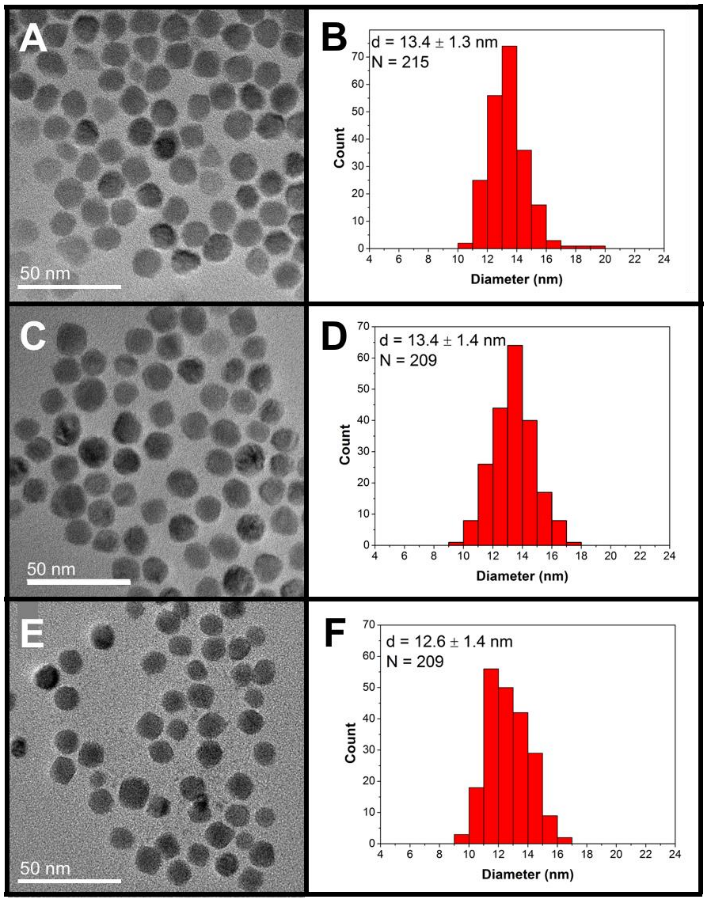

Figure 3.23. Transmission electron micrographs (A, C, E) and their corresponding size histograms (B, D, F for 1 kDa PEGSH-capped (A, B) and 2 kDa PEGSH-capped (C, D), and 5 kDa PEGSH-capped (E, F) $Cu_{2-x}Se$ NPs.

3.4 Conclusion

We report the evolution of Cu^{2+} environments in $Cu_{2-x}Se$ NPs during air-mediated oxidation. The EPR results indicate the presence of two distinct Cu environments, one associated with surface bound Cu atoms coordinating to the molecular ligand OLA, and the other attributed to the formation of surface-bound CuO. With the structural characterization presented in this work, we also studied its surface-induced changes in the plasmonic features of $Cu_{2-x}Se$ NPs. Importantly, by understanding how the formation of CuO species change the extracted carrier densities, we can further modulate the NP surface chemistry to tune its LSPR properties. Specifically, we demonstrate the ability the use LSPR extinction spectra as a diagnostic tool for adsorption of ligands and/or analytes of various electron-donating behavior for downstream sensing and catalytic applications.

4.0 Optoelectronic Impacts of Particle Size in Water-Dispersible Plasmonic Copper Selenide Nanoparticles

(Portions of this work were previously published and reprinted with permission from Gan, X. Y., Crawford, S. E., Eikey, E. A., Sen, R., Killinger, J. R., Millstone, J. E., *The Journal of Physical Chemistry C* **2020**, *124*, 4747 – 4754. Copyright, 2020, American Chemical Society.)

4.1 Introduction

Degenerately doped semiconductor nanoparticles (NPs) such as metal oxides,[53-54] chalcogenides,[49, 55, 57] and pnictides[56, 171] have recently emerged as promising complements to their noble metal NP counterparts. This semiconductor class is attractive because these materials are often not only earth-abundant, but also have wide and well-established tunability in their localized surface plasmon resonance (LSPR) frequency, ranging from the visible region to the mid-infrared. The most well-studied method to tune LSPR frequency in semiconductor NPs is by controlling their carrier densities via aliovalent-,[50] electronic-,[51] chemical-,[61] or self-doping,[49] and these works have been comprehensively reviewed.[52, 54-55, 57, 172]

However, while tunability of the LSPR *energy* is well-understood as demonstrated previously in **Chapter 2.0**,[62] control over the *intensity* (e.g., molar extinction coefficient) of such LSPR excitations remains elusive for semiconductor NPs. One challenge in determining parameters such as the molar extinction coefficient for semiconductor NPs is that it can be difficult to deconvolute the impact of structural effects, such as particle size, from the impact of other particle parameters such as NP carrier density,[111-112] surface depletions,[91, 111] and sometimes even quantum confinement effects.[49, 66] Therefore, in order to study extinction properties in this material class, it is important to select systems that have a suite of sizes available in which size-dependent changes in carrier density, surface depletions, and quantum confinement are minimized.

Plasmonic figures of merit such as the extinction coefficient of traditional noble metal NPs can be expressed in terms of the Mie-Gans theory, where their extinction intensities are composed of both absorption and scattering components.[1, 23, 106] Further, for noble metals, it has been widely demonstrated that the plasmonic intensity can be easily manipulated through the scattering cross-section by modulating NP size and/or shape.[106-109] For example, Jain and El-Sayed's simulations of plasmonic Au and Ag NPs show tunable extinction coefficients as a function of increasing NP size.[107] It was also demonstrated that the scattering intensities of the plasmonic substrates can be tuned via NP shape anisotropy and/or the formation of hot spots.[13, 23-24, 106-107, 110] To optimize and compare the performance of non-noble metal plasmonic NPs in applications such as surface-enhanced sensing,[2, 100, 173] hot carrier-driven catalysis,[6, 100, 118] and photothermal applications,[42, 174] it is important to understand and compare the plasmonic extinction tunabilities of semiconductor NPs to those of their noble metal counterparts.

In this chapter, we report a straightforward synthesis that can control particle diameter within a size range that avoids these convolutions, and then use these materials to establish their molar extinction coefficients. Specifically, we synthesize size-controlled NPs with two distinct $Cu_{2-x}Se$ stoichiometries (i.e., carrier densities), each with 3 comparable diameters between 25 and 50 nm, and demonstrate that the extinction coefficient trends with size as predicted by Mie theory at both stoichiometries. Overall, we show that NP size does not influence the NP LSPR frequencies or carrier densities, but instead has a unique, significant impact on extinction intensities.

Importantly, this observation mirrors the reported extinction coefficient tunabilities of traditional noble metal plasmonic NPs.[107]

4.2 Experimental Section

4.2.1 General Methods and Materials

Copper(II) sulfate pentahydrate ($CuSO_4{\cdot}5H_2O$, >98%), selenium dioxide (SeO_2, >99.9%), polyvinylpyrrolidone (PVP, average molecular weight 3.5 kDa), and L-ascorbic acid (>99%) were purchased from Sigma-Aldrich (St. Louis, MO). Deuterium oxide (D_2O, 99.9%) was purchased from Cambridge Isotope Laboratories, Inc. (Tewskbury, MA). All chemicals were used as received with no additional purification unless otherwise noted. NANOpure (>18.2 MΩ cm, Thermo Fisher Scientific, Waltham, MA) water was used in the preparation of all solutions. Prior to use, all glassware and Teflon stir bars were washed in aqua regia and rinsed with copious amounts of water prior to oven-drying. ***Caution:*** *Aqua regia is highly toxic and corrosive and should only be used with proper personal protective equipment and training. Aqua regia should be handled inside a fume hood only*.

4.2.2 Synthesis of Size-Tunable 3.5 kDa PVP-Capped $Cu_{2-x}Se$ (x = ~0.6) NPs

Unless otherwise noted, when NPs are referenced as $Cu_{2-x}Se$ NPs, they have an average Cu/Se ratio of 1.4:1 as determined by inductively coupled plasma-optical emission spectrometry (ICP-OES). $Cu_{2-x}Se$ NPs were synthesized using a modified ambient condition, room temperature, seed mediated procedure.[175-176] First, 3.5 kDa PVP (concentrations ranging from 5 to 35 mM) was dissolved in 10 mL of water prepared in a scintillation vial equipped with a Teflon-coated stir bar. A 500 μL portion of 0.25 M SeO_2 aqueous solution was added to the PVP solution followed by a rapid injection of 200 μL of 1.15 M aqueous ascorbic acid solution to promote the nucleation of selenium seeds, as indicated by a color change of the solution from clear to bright orange. After being stirred at 450 rpm for 10 min, 500 μL of 0.50 M $CuSO_4$ aqueous solution was added to the orange Se seed solution, followed by another quick injection of 300 μL of 1.15 M aqueous ascorbic acid solution. After 10 s, the solution turned dark brown. The solution was allowed to stir for approximately 15 h during which the solution turned dark green.

The $Cu_{2-x}Se$ NP product was purified via centrifugation. First, the as-synthesized NPs were transferred to a 50 mL Falcon tube and diluted with water. The NP solutions were centrifuged in an Eppendorf 5804 centrifuge with a fixed angle rotor (FA−45−6−30, Eppendorf, Inc., Hauppauge, NY) at a force of 16639 rcf at 25 °C for 10 min. The resulting supernatant was carefully removed, and the soft NP pellet was resuspended in approximately 50 mL of H_2O for additional centrifugation. This washing procedure was repeated 2 more times. All purified NPs were suspended in H_2O and characterized by high-resolution transmission electron microscopy (HRTEM), ultraviolet−visible−near-infrared (UV−vis−NIR) extinction spectroscopy, powder X-ray diffraction (PXRD), and inductively coupled plasma-optical emission spectrometry (ICP-OES) analysis.

4.2.3 Synthesis of Size-Tunable 3.5 kDa PVP-Capped $Cu_{2-x}Se$ (x = ~0.2) NPs

$Cu_{2-x}Se$ NPs (in this case, x = ~0.2 instead of ~0.6, as determined by ICP-OES) were synthesized using the protocol described above with several modifications.[175-176] First, 3.5 kDa

PVP (concentrations ranging from 5 to 15 mM) was used. Then, a premixed yellow solution containing 500 μL of 0.50 M $CuSO_4$ aqueous solution and 3.09 mL of 1.15 M aqueous ascorbic acid solution was added quickly to the orange Se seed solution. The dark brown solution was allowed to stir for approximately 15 h during which the solution turned yellow-brown. The $Cu_{2-x}Se$ NP product was purified using the same purification method, with a modified spinning speed of 166 rcf for 20 min. All purified NPs were suspended in D_2O and characterized using the same techniques mentioned above.

4.2.4 High-Resolution Transmission Electron Microscopy (HRTEM)

$Cu_{2-x}Se$ NPs and Se seeds were prepared for TEM by drop-casting an aliquot of purified solution (diluted 1:100 with water) onto carbon film-coated copper TEM grids (Ted Pella, Inc., Redding, CA) for routine bright field imaging analysis. TEM characterization for all $Cu_{2-x}Se$ NPs was performed on a Hitachi H9500 Environmental TEM with an accelerating voltage of 300 kV (Nanoscale Fabrication and Characterization Facility, Petersen Institute of Nanoscience and Engineering, Pittsburgh, PA). TEM characterization for Se seeds was performed on a JEOL JEM-2100F TEM with an accelerating voltage of 200 kV (Nanoscale Fabrication and Characterization Facility, Petersen Institute of Nanoscience and Engineering, Pittsburgh, PA). The size distributions of the NPs were determined from TEM images of at least 200 NPs from various areas of the grid per experimental replicate using ImageJ 1.47d (National Institutes of Health, USA).

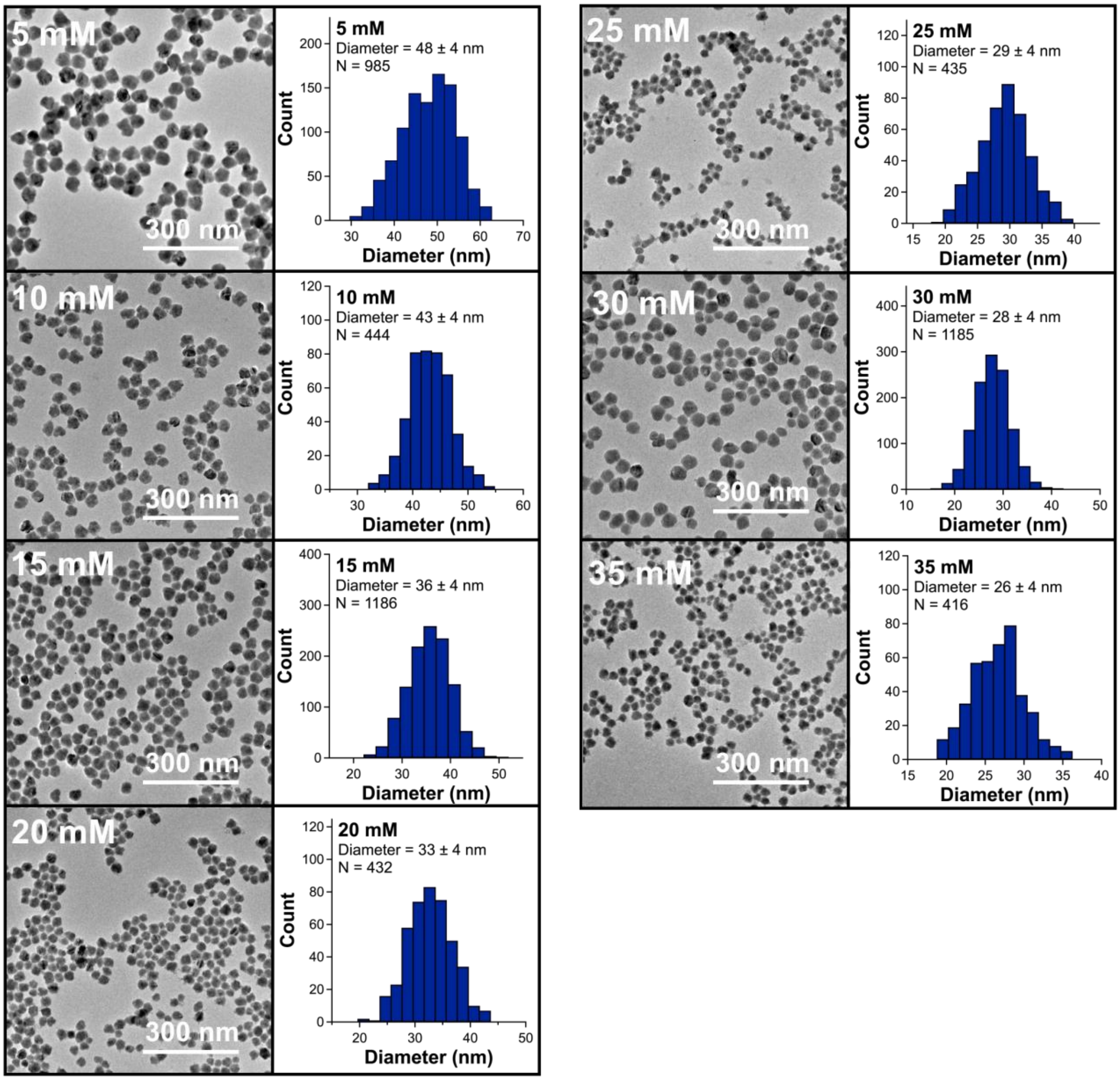

Figure 4.1. Representative TEM images and their corresponding TEM-derived histograms of $Cu_{2-x}Se$ (x = ~0.6) NPs synthesized using various PVP concentrations.

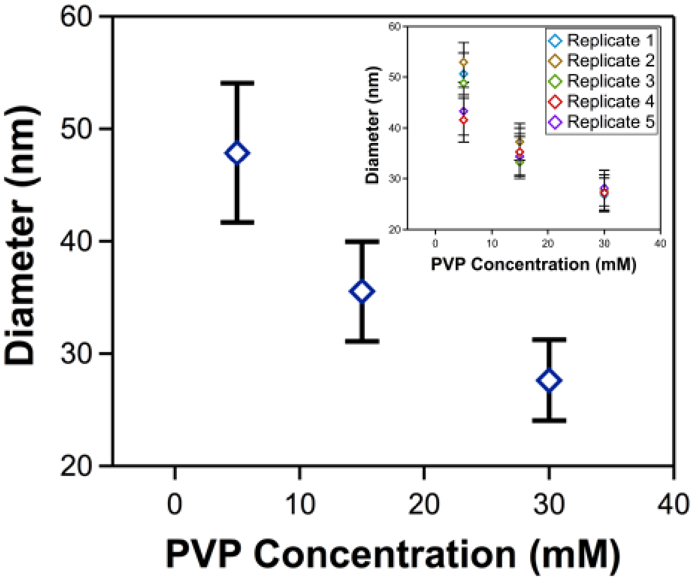

Figure 4.2. Representative TEM-derived size distributions for 5 independent experimental replicates of $Cu_{2-x}Se$ (x = ~0.6) NPs synthesized with 5 mM, 15 mM, and 30 mM 3.5 kDa PVP concentrations. Inset shows size distributions for 5 independent trials.

4.2.5 Powder X-Ray Diffraction (PXRD)

Purified $Cu_{2-x}Se$ NPs were lyophilized using a LabConco Freezone 6 Lyophilizer (Department of Chemistry, University of Pittsburgh) to obtain a dry powder. The NP powders were packed in 0.50 mm capillary tubes (Hampton Research, Aliso Viejo, CA) and flame-sealed for PXRD characterization. PXRD patterns were collected on a Bruker X8 Prospector Ultra (Department of Chemistry, University of Pittsburgh) at 45 kV, 0.65 mA equipped with a IμS microfocus Cu Kα X-ray source (λ = 1.54178 Å) with a scan speed of 0.5 s/step from 12.00 to 108.00° with a step size of 0.02°. All spectra were baseline corrected with respect to the spectrum of the amorphous glass background.

4.2.6 Ultraviolet−Visible−Near-Infrared (UV−vis−NIR) Extinction Spectroscopy

The extinction spectra of $Cu_{2-x}Se$ NPs were collected using a Cary 5000 UV−vis−NIR spectrophotometer (Agilent, Inc., Santa Clara, CA). Purified NPs were suspended in 1 mL of H_2O (or D_2O) and placed in 1 cm quartz cuvettes (Hellma, Inc., Plainview, NY). The spectra were recorded from 1800 to 300 nm at a scanning rate of 1010 nm/min and from 1800 to 800 nm at a rate of 600 nm/min for extinction coefficient measurements (vide infra) with a detector changeover occurring at 800 nm. Spectra were baseline corrected with respect to 1 mL of H_2O for $Cu_{2-x}Se$ (x = ~0.6) NPs and D_2O for $Cu_{2-x}Se$ (x = ~0.2) NPs.

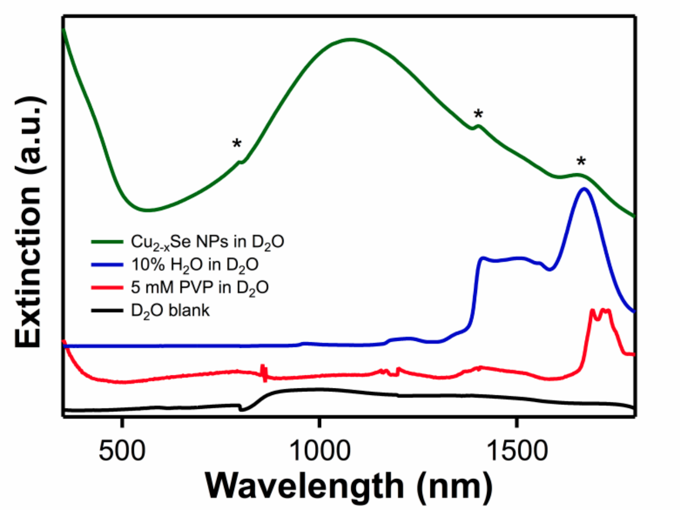

Figure 4.3. Extinction spectrum of $Cu_{2-x}Se$ (x = ~0.6) NPs in D_2O with spectra of D_2O blank, aqueous solution of 5 mM PVP and 10% H_2O in D_2O as comparison.

4.2.7 Inductively Coupled Plasma-Optical Emission Spectrometry (ICP-OES)

ICP-OES analysis was performed using an argon flow with a PerkinElmer, Inc. Optima spectrometer (Department of Chemistry, University of Pittsburgh). An ultrapure aqua regia solution was prepared with a 3:1 ratio of hydrochloric acid (Sigma-Aldrich, > 99.999% trace metal basis) and nitric acid (Sigma-Aldrich, > 99.999% trace metal basis) and diluted with water for a 5% v/v aqua regia matrix. Unknown Se and Cu concentrations were determined by comparison to a 7-point standard curve with a range of 0.10− 10 ppm of Cu and Se (0.10, 0.50, 1.0, 2.5, 5.0, 7.5, and 10 ppm of each metal) prepared by volume using a Se standard for ICP (Fluka, TraceCERT 1000 ± 2 mg/L Se in HNO3) and Cu standard for ICP (Fluka, TraceCERT 1000 ± 2 mg/L Cu in HNO_3), both diluted in a 5% aqua regia matrix. All standards and unknown samples were measured 6 times and averaged. A 7-minute flush time with 5% aqua regia matrix was used between all runs, and a blank was analyzed before each unknown sample to confirm removal of all residual metals from the instrument.

4.2.8 Calculating $Cu_{2-x}Se$ NP LSPR Extinction Coefficients

The LSPR molar extinction coefficients (ε_{Ext}) of $Cu_{2-x}Se$ NPs in M^{-1} cm^{-1} were calculated using the Beer-Lambert Law, described in the equation below:

Equation 4.1. Beer-Lambert Law

$$Ext_{LSPR} = \varepsilon_{Ext} c L$$

where $\mathrm{Ext}_{\mathrm{LSPR}}$ is the extinction intensity in optical density (O.D.) at the LSPR peak max for each individual sample, c is the NP concentration in M, and *L* is the cuvette path length (*L* = 1 cm). The extinction intensities were first determined using the UV-vis-NIR spectrum of the purified $Cu_{2-x}Se$ (x = ~0.6) and $Cu_{2-x}Se$ (x = ~0.2) NPs dispersed in H_2O and D_2O, respectively. The extinction spectra of five to seven serial dilutions of the concentrated NP stock with three NP size ranges were recorded, and five independent trials were collected for each of the 3 NP sizes. Each spectrum was recorded from 1350 nm to 800 nm for $Cu_{2-x}Se$ (x = ~0.6) NPs and from 1600 nm to 900 nm for $Cu_{2-x}Se$ (x = ~0.2) NPs (**Figure 4.4**). 900 µL of serial dilution aliquots were collected and digested using 5% ultrapure aqua regia and then further diluted in 10-mL volumetric flasks with 5% ultrapure aqua regia for ICP-OES to obtain the concentrations of Se in ppm.

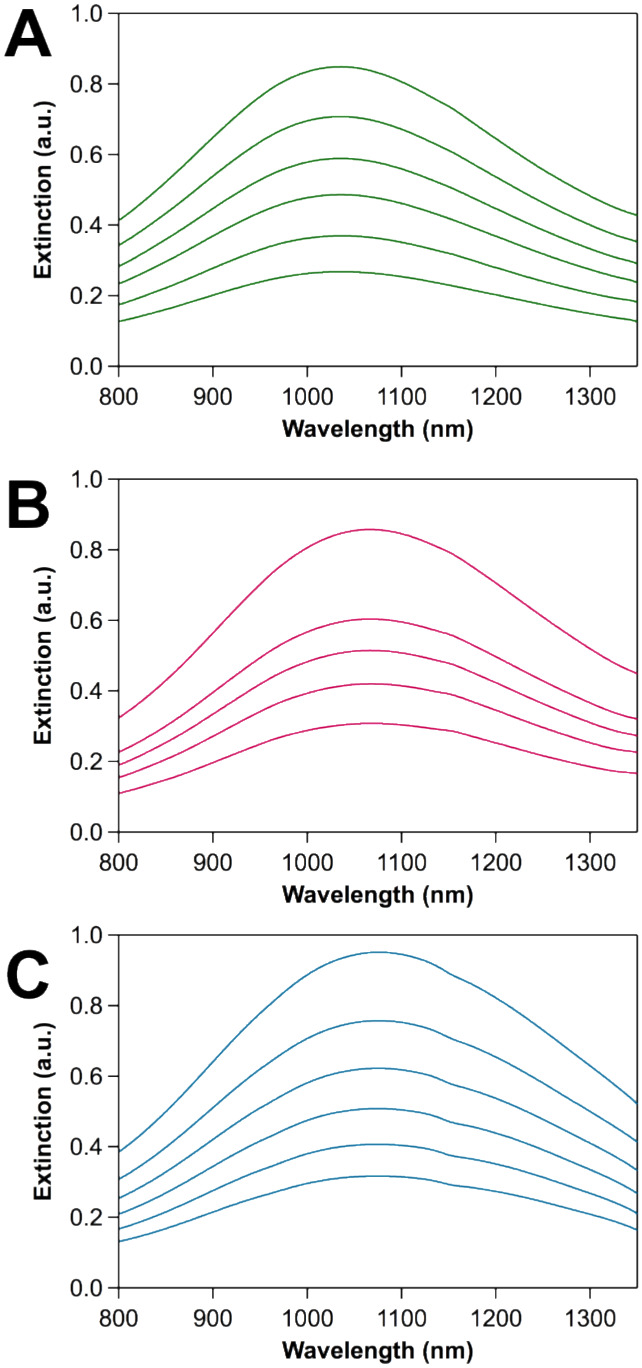

Figure 4.4. Representative serial dilution aliquot extinction spectra of $Cu_{2-x}Se$ (x = ~0.6) NPs dispersed in H_2O for (A) small, (B) medium, and (C) large size ranges.

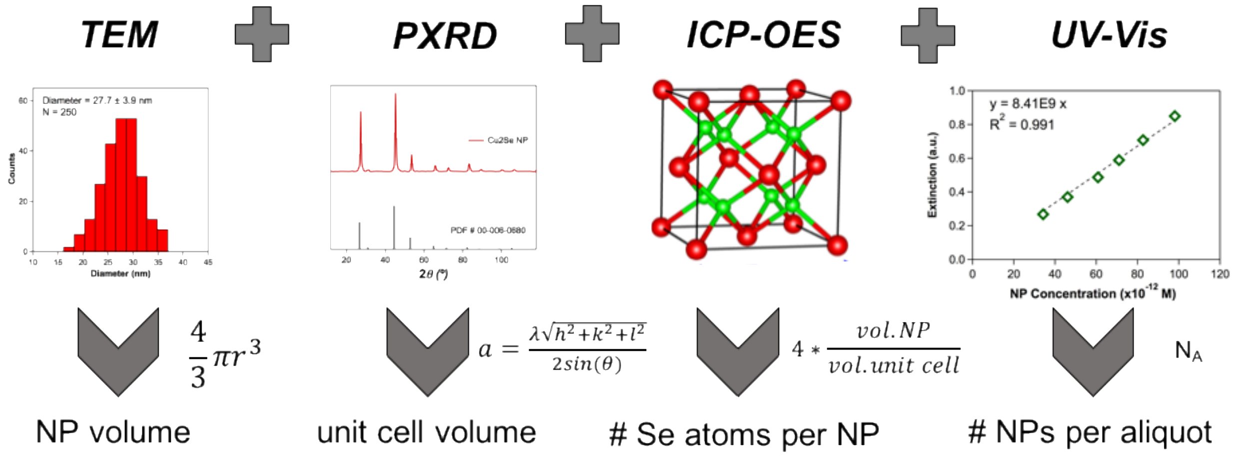

Figure 4.5. Schematic of the molar extinction coefficient calculations using a combination of various analytical tools.

The NP concentrations can be measured using a combination of HRTEM, PXRD, UV-Vis-NIR extinction spectroscopy, and ICP-OES, simplified in **Figure 4.5**. Specifically, using the average diameters of $Cu_{2-x}Se$ estimated using HRTEM (**Figure 4.8A-C**), we calculated the volume of the NP by assuming that they are perfect spheres. The volumes of the unit cell were then established using their corresponding PXRD patterns (**Figure 4.8D** and **Figure 4.13**). Briefly, the lattice parameter (a) of the antifluorite structure was determined using the PXRD peak at approximately 27°, which corresponds to the cubic (111), and this peak position is constant for all NP size ranges. Using the Bragg equation described below:

Equation 4.2. Bragg Equation

$$a = \frac{\lambda\sqrt{h^2 + k^2 + l^2}}{2sin(\theta)}$$

where λ is the X-ray source ($\lambda = 0.154178$ nm), h=k=l=1 for (111), the lattice parameter (a) was calculated to be 0.57 nm, resulting in corresponding unit cell volume of 0.19 nm^3. The total number of unit cells per particle was estimated by dividing the volume of the NP sphere for each size ranges by the volume of the antifluorite lattice of Cu_2Se (in this case, 0.19 nm^3 for all size populations). By multiplying the number of unit cells per particle by 4, the number of Se atoms present in the unit cell, the total number of Se atoms per particle was then estimated. This number is used to normalize the Se concentration in ppm, determined by ICP-OES, to quantify the number of NPs in each serial dilution aliquots, and the NP molar concentrations can be expressed by diving the values by Avogadro's number. These values were used as the x-axis to plot extinction intensity at $LSPR_{max}$ in O.D. against NP concentration in M (**Figure 4.6**), where the slope of the linear regression can be extracted as the LSPR extinction coefficients of the $Cu_{2-x}Se$ NPs. The LSPR extinction coefficients were measured on at least 5 synthetic replicates for each representative size ranges.

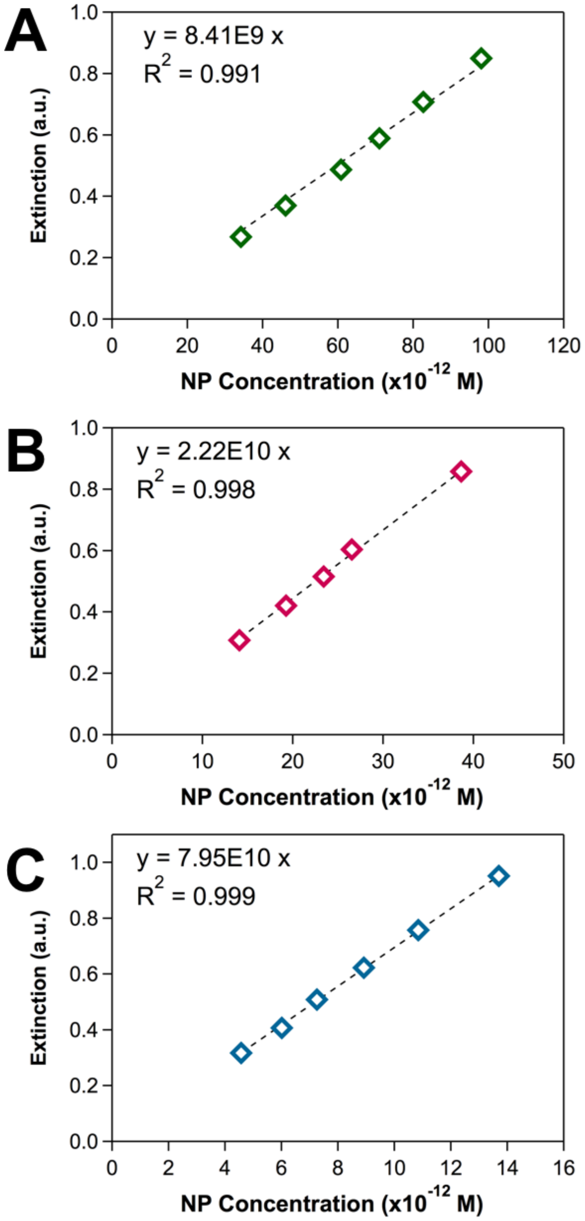

Figure 4.6. Example of linear regressions of $Cu_{2-x}Se$ LSPR extinction intensities vs. NP concentrations for (A) small, (B) medium, and (C) large NP size ranges for $Cu_{2-x}Se$ (x = ~0.6) NPs including their corresponding linear regression equations and R^2 values.

4.3 Results and Discussion

4.3.1 $Cu_{2-x}Se$ Nanoparticle Size Tunability Via Ligand Concentration

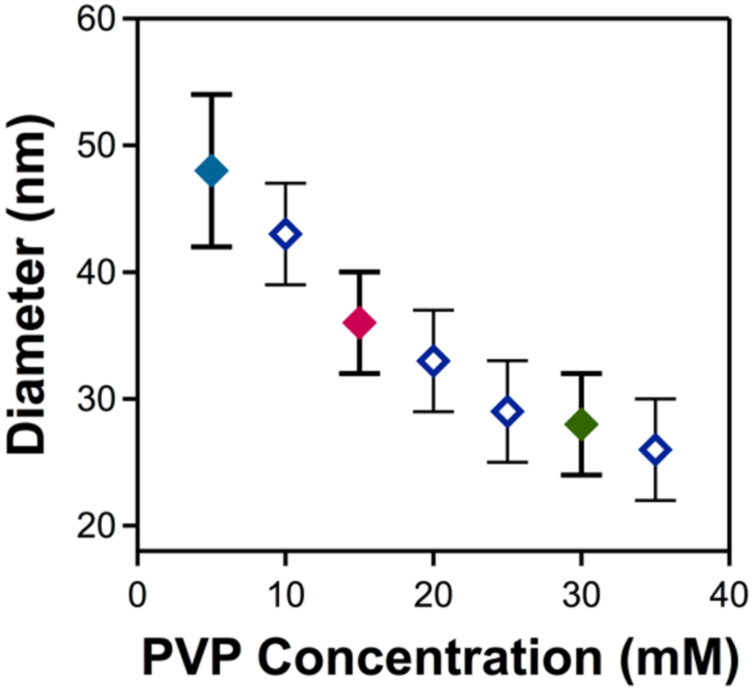

Figure 4.7. TEM-derived size distributions of $Cu_{2-x}Se$ NPs as a function of increasing PVP concentration. Solid diamonds represent the sizes studied in this chapter, which are statistically different (see *Statistical Analyses of Cu2-xSe NP Diameters* in Appendix A.1). Blue, maroon, and green solid diamonds represent large, medium, and small NPs, respectively. Error bars represent the standard deviations from at least 3 independent trials. Open diamonds represent other particle sizes accessible by varying PVP concentration. All $Cu_{2-x}Se$ NPs have an x value ~0.6, as determined by ICP-OES unless otherwise specified.

We first prepared water-dispersible, plasmonic $Cu_{2-x}Se$ NPs using a modified seed-mediated protocol (all $Cu_{2-x}Se$ NPs have a stoichiometric *x* value ~0.6, as determined by ICP-OES unless otherwise specified).[175-176] Briefly, in a scintillation vial containing the selenium precursor (selenium dioxide, SeO_2) and surfactant solution (3.5 kDa polyvinylpyrrolidone, PVP), we quickly introduced reducing agent (ascorbic acid) to form Se seeds. After the Se seeds were allowed to nucleate and grow for 10 min, the copper precursor (copper sulfate, $CuSO_4$) was added, followed by another addition of ascorbic acid to yield $Cu_{2-x}Se$ NPs. By altering the concentration of surfactant used in the synthesis from 5 to 35 mM, we tuned the average diameter of pseudospherical $Cu_{2-x}Se$ NPs from approximately 25 to 50 nm with an average standard deviation of < 15% (**Figure 4.1** and **Figure 4.7**). Similar to what was observed in the classic plasmonic Au NP syntheses developed by Turkevich and Frens, the NP diameters measured by TEM decrease when the ligand to metal precursor concentration ratio increases.[177-178] We note that while the TEM size distributions are similar for NPs synthesized in PVP concentrations between 30 mM and 35 mM, size and shape heterogeneity becomes more prominent at higher PVP concentrations (**Figure 4.1**). Specifically, particle anisotropy arises and a bimodal NP size distribution is observed.

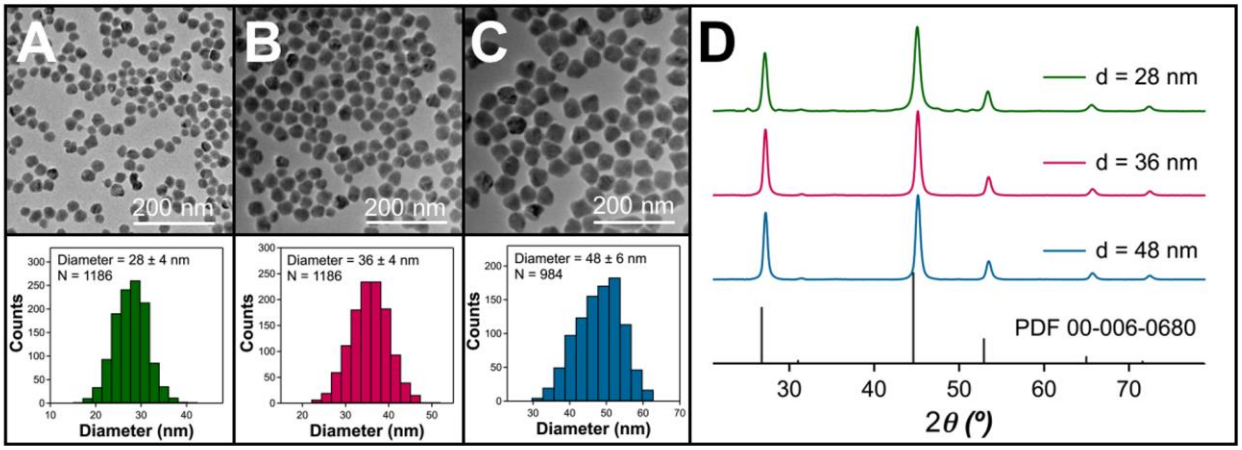

Figure 4.8. (A−C) Representative TEM images and their corresponding size distributions of small (green), medium (maroon), and large (blue) PVP-capped $Cu_{2-x}Se$ NPs. (D) Corresponding, representative powder diffraction patterns of PVP-capped $Cu_{2-x}Se$ NPs as a function of NP size referenced to PDF 00-006-0680 pattern.

To ensure we were studying the optoelectronic properties of well-defined, statistically distinct $Cu_{2-x}Se$ NP populations, we used particles synthesized with 30, 15, and 5 mM 3.5 kDa PVP solutions which produce statistically distinct average particle diameters of 28, 36, and 48 nm and are denoted here as “small,” “medium,” and “large,” respectively, for the sake of simplicity (**Figure 4.2** and **Figure 4.8A−C**). For each of these PVP concentrations, we performed at least 5 independent synthetic trials and successfully achieved reasonable (< 15% standard deviation) size distributions that are statistically different from one another (**Figure 4.2**, **Figure 4.8A−C**, and see *Statistical Analyses of Cu2-xSe NP Diameters in* **Appendix A.1**). It is important to note that there are other methods for controlling copper chalcogenide NP diameter; however, these strategies focus on sizes between 3−15 nm, which were not suitable for the current studies due to quantum confinement and surface depletion concerns described in **Section 4.1**.[49, 111-112, 179]

4.3.2 Size Control Achieved During Seed Formation

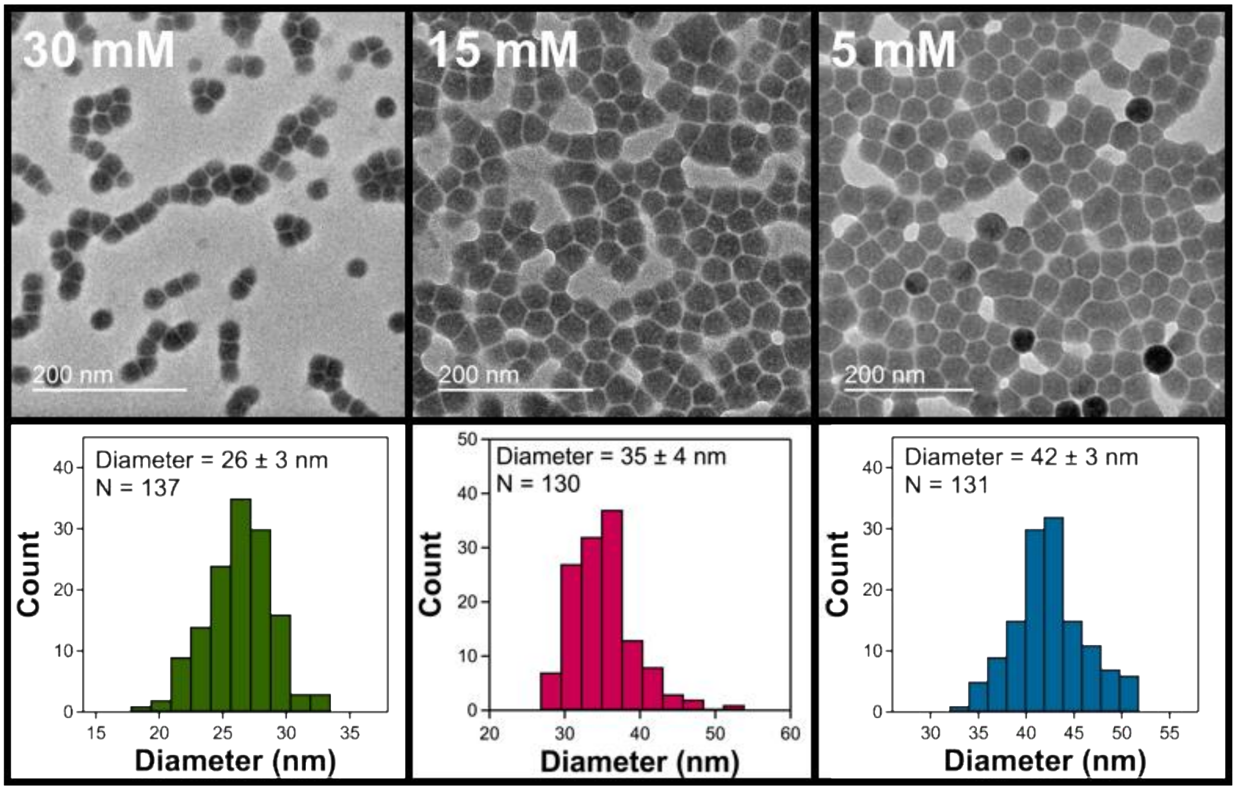

Figure 4.9. Representative TEM images and their corresponding TEM-derived histograms of Se seeds synthesized with 5 mM, 15 mM, and 30 mM 3.5 kDa PVP concentrations.

Since this synthetic method is a seed-mediated process, we hypothesized that the overall size control is achieved by first altering the size of the Se seeds during the synthesis. To test our hypothesis, we stopped the reaction upon Se seed formation following the first addition of ascorbic acid. Similar to the complete synthesis, a range of PVP concentrations (5, 15, and 30 mM) were used, and after the mixtures were allowed to stir for 10 min, the reactions were halted and the bright orange Se seeds were collected. TEM analysis of the resulting NPs revealed that the diameter of Se seeds decreased as a function of increasing PVP concentration and that the diameters of the seeds are similar to the final $Cu_{2-x}Se$ NPs (**Figure 4.9**). These observations are consistent with our hypothesis that NP size control can be achieved by controlling the size of the Se seeds, similar to what was reported previously but using a different approach to manipulate Se seed size.[174]

4.3.3 Carrier Density and Number of Carriers Quantifications for $Cu_{2-x}Se$ NPs

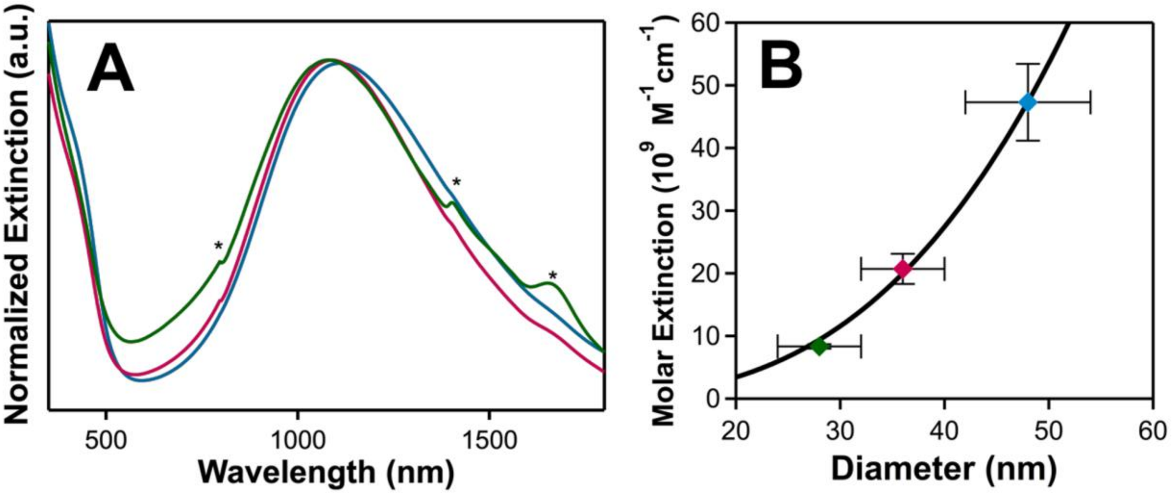

Figure 4.10. (A) Representative extinction spectra of small (green), medium (maroon), and large (blue) PVP-capped $Cu_{2-x}Se$ (x = ~0.6) NPs. Asterisks denote spectrometer and solvent artifacts (see Figure 4.3 for solvent and free ligand spectra). (B) Average LSPR molar extinction coefficients of $Cu_{2-x}Se$ NPs as a function of NP diameter. Error bars on the x-axis correspond to the standard deviations of the TEM size distributions, and error bars on the y-axis correspond to the standard errors of the molar extinction coefficients measured across 5 independent trials. The trend line fits to a $y = ax^3 + y_0$ function, where $a = 4.29 \pm 0.08 \times 10^5$ and $y_0 = 0$.

We next study the optoelectronic properties of $Cu_{2-x}Se$ (x = ~0.6) NPs as a function of the 3 distinct size distributions described previously, using UV−vis−NIR extinction spectroscopy (Figure 3A). Interestingly, the LSPR features of the $Cu_{2-x}Se$ NPs show minimal change as a function of NP size, suggesting no change in the NP carrier densities. In order to analyze the extinction features quantitatively, the carrier densities for each $Cu_{2-x}Se$ NP size population can be determined through the interpretation of its extinction spectrum. Specifically, we use the Drude model to estimate carrier densities (N_h) by combining **Equation 2.3** and **Equation 2.4** described in **Chapter 2.0**,[49, 55] where $\varepsilon_\infty = 10$ and $m^* = 0.334\ m_0$ are used for consistency,[60, 62-63, 103] and $\varepsilon_\infty = 80.1$ for water. After rearranging the equations above, N_h can be expressed and extracted as follows:

Equation 4.3. Carrier Density Equation

$$N_h = \frac{(\omega_{LSPR}^2 + \gamma^2)(\varepsilon_0 m_h^*)(\varepsilon_\infty + 2\varepsilon_m)}{e^2}$$

It is also important to note that the surface ligand could influence both the carrier density and the dielectric constant of the surrounding medium in the Drude model.[55, 60, 170] However, similar to many reports for plasmonic semiconductor NPs,[49, 62] since we use the same surface ligand type and molecular weight for each particle, we assume the coating is approximately uniform across all NP samples, and therefore we ignore the ligand contributions (of course, because the concentration of PVP used does vary for each NP size, the density of the surface coating may vary, and this ligand density is a contribution we do not account for in our analysis). Averages of the measurable parameters (both ω_{LSPR} and γ) for each $Cu_{2-x}Se$ NP size population as well as their corresponding carrier densities for 5 independent trials and standard error are summarized in **Table 4.1**. We note that we have previously reported the use of NMR to determine particle carrier densities;[62] however, in a subsequent report,[99] we observed complementary sensitivity regimes for the Drude model and NMR-based approaches, where the Drude model is more sensitive at high N_h regimes ($>10^{21}$ cm^{-3}) and NMR is more sensitive at lower N_h regimes ($<10^{19}$ cm^{-3}). Therefore, the Drude model was more appropriate for the NPs considered in the current report ($N_h \approx 10^{22}$ cm^{-3}).

Table 4.1. Summarized NP Diameters, Cu/Se Ratios, Extinction Features and Calculated Carrier Densities, Number of Carriers Per NP, and Measured Extinction Coefficients of $Cu_{2-x}Se$ (x = ~0.6 and x = ~0.2) NPs.

NP Size Range	NP Diameter* (nm)	Cu:Se by ICP-OES*	LSPR Max* (nm)	LSPR FWHM* (nm)	Carrier Density* (x10^{22} cm^{-3})	Carriers per NP* (x10^{6})	Molar Extinction Coeff.* (x10^{9} M^{-1} cm^{-1})
Small	28 ± 4	1.35 ± 0.03	1093 ± 6	471 ± 8	6.10 ± 0.10	0.70 ± 0.04	8.2 ± 0.3
	29 ± 4	1.85 ± 0.02	1205 ± 7	730 ± 20	4.67 ± 0.04	0.66 ± 0.05	10 ± 1
Medium	36 ± 4	1.40 ± 0.06	1071 ± 4	465 ± 7	6.30 ± 0.10	1.53 ± 0.03	21 ± 1
	37 ± 4	1.85 ± 0.02	1200 ± 10	740 ± 40	4.70 ± 0.10	1.40 ± 0.30	25.4 ± 0.1
Large	48 ± 6	1.44 ± 0.03	1076 ± 8	480 ± 20	6.10 ± 0.02	3.53 ± 0.03	54 ± 5
	47 ± 4	1.90 ± 0.06	1233 ± 7	740 ± 40	4.50 ± 0.20	2.90 ± 0.50	50 ± 3

[a] All values are averages from 5 independent experimental trials.

Interestingly, unlike what was previously reported for smaller copper chalcogenide systems,[112, 179] the carrier densities calculated here using the Drude model are statistically the same even for NPs with a 25 nm size difference, as determined by analysis of variance (ANOVA) with 95% confidence (see *Statistical Analyses of Cu2-xSe Carrier Densities* in **Appendix A.2**). Of course, the number of carriers per NP (n_h) does increase as a function of particle diameter, since carriers per NP scales with NP volume (**Table 4.1**). Specifically, n_h can be extracted by multiplying N_h by the NP volume:

Equation 4.4. Number of Carriers Equation

$$n_h = N_h \frac{4}{3} \pi r^3$$

where r is the average nanoparticle radius derived by TEM.

It has previously been reported that the presence of carriers in copper chalcogenide nanomaterials is due to the presence of Cu deficiencies within the NP lattice.[96-97, 99] Thus, we would expect to observe minimal change in the Cu deficiencies for each NP size population, as there is no change in their carrier densities. To investigate the presence of Cu deficiencies for each $Cu_{2-x}Se$ NP population, we used ICP-OES to determine the ensemble Cu/Se ratios (**Table 4.1**). Additionally, we examined their corresponding PXRD patterns and found good agreement with our ICP-OES results (**Figure 4.8D**). There are no shifts in 2θ and no significant changes in the Cu/Se ratios overall between each NP size sample, indicating that there are not significant differences in Cu deficiencies or lattice structures in each of the $Cu_{2-x}Se$ ($x = \sim 0.6$) NP sizes studied. These observations are consistent with the lack of statistical difference in the Drude model-derived carrier densities for each $Cu_{2-x}Se$ NP size population.

4.3.4 Size Dependent LSPR Molar Extinction Coefficient

In order to establish the magnitude of the plasmonic intensities of $Cu_{2-x}Se$ NPs, we determined their molar extinction coefficients using a combination of TEM, PXRD, ICP-OES, and extinction spectroscopy (**Figure 4.5**). First, LSPR extinction spectra were measured by analyzing aliquots of $Cu_{2-x}Se$ NPs dispersed in H_2O at various concentrations and prepared using serial dilutions (**Figure 4.4**). After extinction measurements, these aliquots were then digested using ultrapure aqua regia and their corresponding Se concentrations were analyzed using ICP-OES to estimate the number of NPs present in each aliquot. Using the Beer−Lambert law expressed in **Equation 4.1**, we plotted linear regressions of Ext_{LSPR} against c for each $Cu_{2-x}Se$ size population. By forcing the y-intercepts to be zero, we extract the slopes of the linear regressions (**Figure 4.6**), which correspond to the molar extinction coefficients ($\varepsilon_{Ex,}$ summarized in **Table 4.1**; see **Section 4.2.8** for detailed calculations and explanations, and

Statistical Analyses of Cu2-xSe Molar Extinction Coefficients in **Appendix A.3**).

4.3.5 Curve-Fitting of $Cu_{2-x}Se$ NP LSPR Extinction Coefficients vs. Size

The size-dependent LSPR molar extinction coefficients of $Cu_{2-x}Se$ NPs calculated previously can be fit to a power function with the power term constrained to 3 with 95% confidence, using the following equation:

Equation 4.5. Curve Fitting Power Function

$$y = ax^3 + y_0$$

where the y-axis represents the measured LSPR molar extinction coefficients, the x-axis is the NP diameter, a is the fitted slope of the function, and y_0 is the y-intercept.

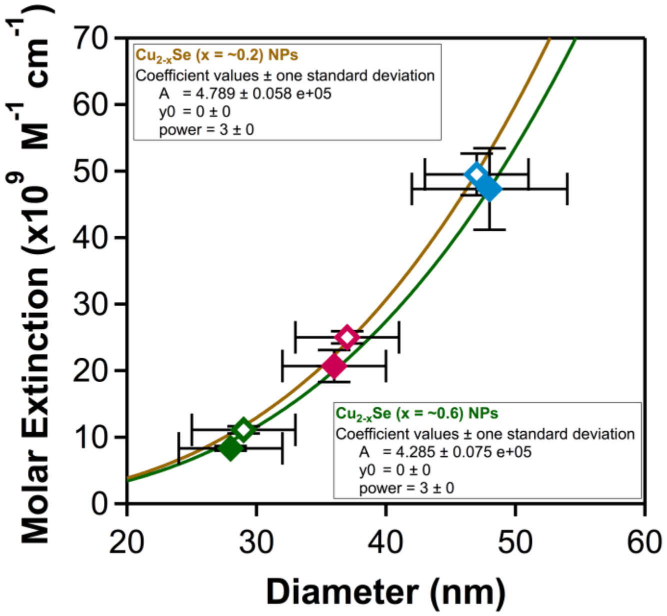

Figure 4.11. Fitted LSPR extinction coefficients of both $Cu_{2-x}Se$ (x = ~0.2) and (x = ~0.6) NPs as a function of NP diameters, with the corresponding parameters included in the inset.

4.3.6 $Cu_{2-x}Se$ Molar Extinction Coefficients Follow Mie Theory Description

By plotting the molar extinction coefficients of $Cu_{2-x}Se$ NPs as a function of increasing NP diameter (**Figure 4.10B**), we demonstrate that the $Cu_{2-x}Se$ NP size can be used to tune the plasmon intensity. Because their NP carrier densities are statistically the same, we attribute the changes in molar extinction coefficients to changes in the plasmon scattering cross-sections. This is a remarkable observation because it is consistent with the size-dependent extinction coefficients reported for their well-studied noble metal counterparts. Specifically, seminal reports by Jain and

El-Sayed observed similar plasmonic extinction coefficient trends with Au and Ag NPs with increasing NP diameters.[107] Additionally, the size-dependent molar extinction coefficients can be fitted to a cubic function (**Figure 4.11** and **Section 4.3.5**), which is consistent with the Mie theory approximations for spherical plasmonic systems summarized in the equation below:

Equation 4.6. Mie Theory Equation

$$Ext_{LSPR}(\omega) = 4\pi R^3 k(\varepsilon_m)^{\frac{1}{2}} Im\left\{\frac{\varepsilon_p(\omega) - \varepsilon_m}{\varepsilon_p(\omega) + 2\varepsilon_m}\right\}$$

where R is the NP radius, k is the wavevector of the incident light, ε_m is the dielectric constant of the surrounding medium, and ε_p is the dielectric function of the plasmonic NPs.[55, 60, 95, 103]

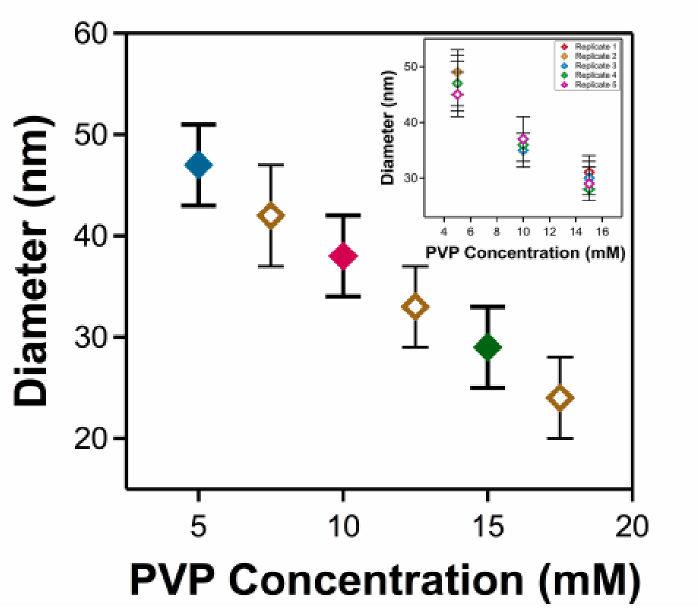

Figure 4.12. Representative TEM-derived size distributions for $Cu_{2-x}Se$ (x = ~0.2) NPs synthesized with 3.5 kDa PVP concentrations range from 5 mM to 17.5 mM, in increments of 2.5

mM. Inset shows size distributions for small, medium, and large NPs across 5 independent replicates.

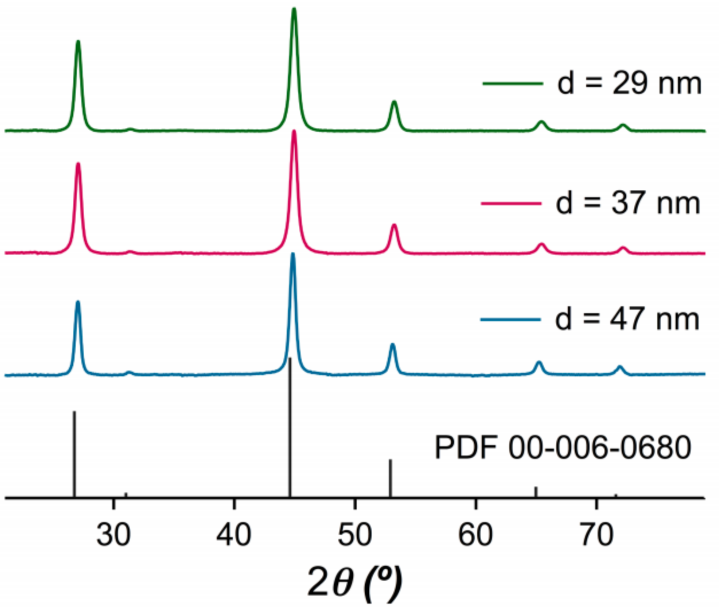

Figure 4.13. Representative powder X-ray diffraction patterns for small (green), medium (maroon), and large (blue) $Cu_{2-x}Se$ (x = ~0.2) NPs referenced to PDF 00-006-0680.

To challenge our findings that the $Cu_{2-x}Se$ NP diameter is the predominant factor for tuning the LSPR molar extinction coefficients, we synthesized $Cu_{2-x}Se$ NPs of similar sizes but with lower carrier densities. These NP products could be achieved by premixing the $CuSO_4$ solution with a higher concentration of ascorbic acid before adding them into the Se seed solutions (see **Section 4.2.3** for synthetic details, **Figure 4.12** and **Figure 4.13** for NP TEM and PXRD characterizations, respectively). These NPs have Cu/Se ratios of 1.8:1 instead of 1.4:1 as determined by ICP-OES and are denoted here as $Cu_{2-x}Se$ (x = ~0.2). As expected, their corresponding LSPR spectra (**Figure 4.14A**, dotted lines) are red-shifted and broadened relative to their $Cu_{2-x}Se$ (x = ~0.6) counterparts. Further, these spectral features are accompanied by the redshift of an additional absorption feature near 500 nm, which can be attributed to the optical bandgap of the $Cu_{2-x}Se$ NPs, consistent with the Moss−Burstein effect observed when there is a decrease in carriers.[62, 96] It has been extensively reported that the plasmonic features of copper chalcogenide systems are highly tunable based on the Cu/Se ratio, which could be attributed to both the Cu deficiency and/or Cu oxidation states.[54-55, 62, 96-97, 99, 172]

Specifically, the decrease in the presence of Cu deficiencies and/or Cu^{2+} species present within the NP will result in the decrease of carrier densities present. As expected, the Drude model-derived carrier densities for $Cu_{2-x}Se$ (x = ~0.2) are statistically different and lower than the $Cu_{2-x}Se$ (x = ~0.6) NPs (**Table 4.1**). However, similar to what was observed in the $Cu_{2-x}Se$ (x = ~0.6) NP case, there is no significant change in the LSPR frequency as a function of increasing NP diameter at this new stoichiometry.

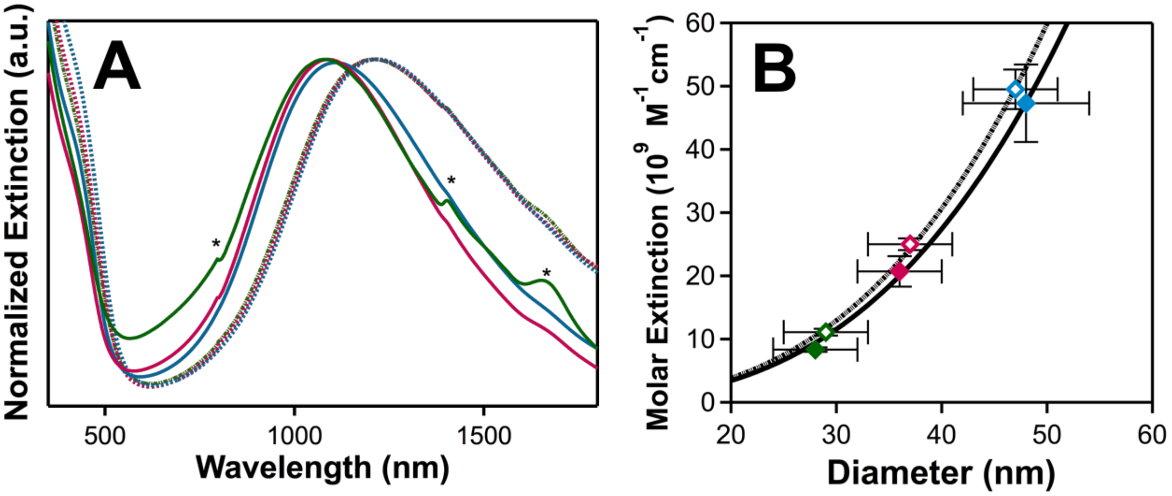

Figure 4.14. (A) Representative extinction spectra of small (green), medium (maroon), and large (blue) PVP-capped $Cu_{2-x}Se$ (x = ~0.2) NPs (dotted lines). Asterisks denote spectrometer and solvent artifacts. (B) Average LSPR molar extinction coefficients of $Cu_{2-x}Se$ (x = ~0.2) NPs as a function of NP diameter (open diamonds). Results for the $Cu_{2-x}Se$ (x = ~0.6) NP systems from

Figure 4.10 are included again here for comparison and clarity. Error bars on the x-axis correspond to the standard deviations of the TEM size distributions and error bars on the y-axis correspond to the standard errors of the molar extinction coefficients measured across 5 independent trials. The gray trend line fits to a $y = ax^3 + y_0$ function, where $a = 4.79 \pm 0.06 \times 10^5$ and $y_0 = 0$.

Similar to what was observed with the $Cu_{2-x}Se$ (x = ~0.6) NP samples, $Cu_{2-x}Se$ (x = ~0.2) LSPR molar extinction coefficients scaled with NP diameter (**Figure 4.14B**, open diamonds). When fitting molar extinction coefficients of $Cu_{2-x}Se$ NPs to a cubic function, it becomes apparent that the LSPR molar extinction coefficients scale with the volume of the NPs. These results further support the hypothesis that the molar extinction of $Cu_{2-x}Se$ LSPRs is influenced predominantly by the NP diameter, and this observation not only mirrors the noble metal counterparts but also behaves in close agreement with Mie theory predictions for spherical NPs (**Equation 4.6**). It is interesting and important to note that the slopes of the fitted power functions between $Cu_{2-x}Se$ (x = ~0.6) and (x = ~0.2) NPs are statistically different (**Figure 4.10B** and **Figure 4.14B**). We attribute this difference to the dielectric functions of $Cu_{2-x}Se$ (x = ~0.6) and (x = ~0.2) NPs. It has been established previously that the carrier densities present within $Cu_{2-x}Se$ NPs can influence the NP dielectric constants.[55, 103] Specifically, we observe the slope of the cubic function to be inversely proportional to N_h, as has been derived elsewhere[111] and which we derive in detail (see *Derivation of Extinction Coefficient Dependence on NP Carrier Density* in **Appendix B**).

4.4 Conclusions

In conclusion, we have demonstrated that the LSPR intensity of water-dispersible $Cu_{2-x}Se$ NPs can be altered by NP size via straightforward synthetic strategies. We see minimal changes in the LSPR maximum frequencies and calculated carrier densities as a function of NP size. However, when molar extinction coefficients for each of the $Cu_{2-x}Se$ NP populations were measured, we observed that they systematically increased as a function of size, proportional to R^3, as described by the traditional Mie theory spherical approximation. Importantly, these observations provide a way to deconvolute NP size effects from various factors including carrier densities, suggesting that the size control in this case primarily influences the scattering cross-sections of the $Cu_{2-x}Se$ NPs. Taken together, these results advance the design, optimization, and implementation of earth-abundant, water-dispersible copper chalcogenide systems as a promising alternative in plasmonically-driven applications.

5.0 Plasmon-Enhanced Chemical Conversion Using Copper Selenide Nanoparticles

(Portions of this work were previously published and reprinted with permission from Gan, X. Y., Keller, E. L., Warkentin, C. L., Crawford, S. E., Frontiera, R. R., Millstone, J. E., *Nano Letters* **2019**, *19*, 2384 – 2388. Copyright, 2019, American Chemical Society.)

5.1 Introduction

Localized surface plasmon resonances (LSPRs) have been broadly studied and are a property of nanomaterials that can be used to enhance or enable a wide variety of technologies including cancer treatment,[9, 43] light-driven catalysis,[5, 180] and ultrasensitive detection.[1, 181-182] Upon excitation of surface plasmons with an incident electromagnetic wave, the delocalized conduction electrons near the Fermi level of the material oscillate collectively, leading to the enhancement of the electromagnetic field at the nanoparticle surface and the subsequent generation of "hot" carriers (i.e., holes and electrons).[2]

Though short-lived, these hot carriers can be efficiently transferred to adsorbates on nanomaterial surfaces.[2, 5] The mechanisms of hot carrier generation and transfer have been well studied on noble metal plasmonic substrates (i.e., Au, Ag, and Cu). Specifically, computational efforts have been used to understand the energy distribution,[37] dynamics,[4] number,[16] and transport[26] of the hot carriers generated in noble metal nanomaterials of various sizes and shapes. Additionally, experimental approaches coupled with analytical techniques including surface-enhanced Raman spectroscopy (SERS)[18] and electrochemistry[183] have been used to understand the hot carrier transfer mechanism[29, 33, 183] and efficiency.[5-6, 31]

While traditionally studied in noble metal nanomaterials, a broader selection of nanoscale materials supports LSPRs.[49] Apart from being more earth-abundant and cost-effective, non-noble metal nanomaterials, such as aluminum[126, 184] and degenerately doped semiconductor nanoparticles (including metal oxides,[53, 55] metal nitrides,[171] and metal chalcogenides[54, 57]), enable plasmonic properties that span a wider range of the electromagnetic spectrum from the ultraviolet to the infrared region. Similar to their noble metal counterparts, the observed LSPRs of degenerately doped semiconductor nanoparticles (NPs) can be tuned via particle size,[49] shape,[185] and surface chemistry,[170] as well as by the additional "handle" of free carrier density and distribution.[62, 92-93] However, it is currently unclear whether the plasmonic features of these alternative plasmonic materials will perform in a comparable, inferior, or superior manner to their noble metal counterparts.

While single-component noble metal plasmonic substrates have shown promise in driving various photocatalytic reactions, chemical conversions using plasmonically active degenerately doped semiconductor NPs alone (i.e., not in a hybrid architecture with a metal NP[114, 186]) have not yet been reported. In this chapter, we demonstrate that plasmonic excitation of colloidal, p-doped copper selenide ($Cu_{2-x}Se$) NPs can be used to promote chemical conversions. By measuring the enhanced amplitudes of the Raman modes using SERS, we monitor the plasmon-mediated reduction of 4-nitrobenzenethiol (NBT) to 4,4′-dimercaptoazobenzene (DMAB). These results represent the first evidence of plasmon-driven photoredox chemistry on single-component degenerately doped semiconductor NPs.

5.2 Experimental Section

5.2.1 General Methods and Materials

Copper(I) chloride (CuCl, > 99.995%), selenium powder (Se, > 99.5%), octadecene (ODE, 90% technical grade), oleylamine (OAm, 70% technical grade), chloroform (> 99%), polyvinylpyrrolidone (PVP, average molecular weight 10,000), benzenethiol (BT, ≥ 98%), 4-nitrobenzenethiol (NBT, 80% technical grade) were purchased from Sigma Aldrich (St. Louis, MO). Absolute ethanol (EtOH) was purchased from Thermo Fisher Scientific (Pittsburgh, PA). All chemicals were used as received with no additional purification unless otherwise noted. Prior to use, all glassware and Teflon stir bars were washed in aqua regia and rinsed with copious amounts of water prior to oven drying. ***Caution:*** *Aqua regia is highly toxic and corrosive, and should only be used with proper personal protective equipment and training. Aqua regia should be handled inside a fume hood only.*

5.2.2 Synthesis of OAm-Capped $Cu_{2-x}Se$ NPs

$Cu_{2-x}Se$ NPs were synthesized using a previously described hot injection method.[62, 136] The synthetic procedure was completed using standard air-free techniques and is described in detail below. The selenium-octadecene-oleylamine mixture was created by dissolving 80 mg Se in 1 mL of ODE and 2 mL of OAm. The solution was heated in a round bottom flask for 12 hrs under argon gas at 195 °C. In a 3-neck round bottom flask, 200 mg CuCl was added with 5 mL OAm and 5 mL of ODE. The Cu-ODE-OAm mixture was heated to 140 °C under vacuum for 30 min then heated to 285 °C under Ar. Then, the Se mixture was injected into the Cu mixture. The precursors reacted for 10 min at ~285 °C to form $Cu_{2-x}Se$ NPs. The NPs were cooled to room temperature by removing the heating mantle.

The $Cu_{2-x}Se$ NP product was purified via centrifugation. First, the as-synthesized NPs were transferred to glass centrifuge tubes containing 10 mL of EtOH and centrifuged in an Eppendorf 5804R centrifuge with a swing bucket rotor (A-44-4) (Eppendorf, Inc.) at a force of 2850 rcf at 20 °C for 5 min. The resulting supernatant was removed and the pellet was resuspended in a small amount of $CHCl_3$ for additional centrifugation in another 10 mL of EtOH. This washing procedure was repeated once. All purified NPs were then characterized by high resolution transmission electron microscopy (HRTEM), ultraviolet-visible-near-infrared (UV-vis-NIR) extinction spectroscopy, powder X-ray diffraction (PXRD), and Raman spectroscopy.

5.2.3 Ligand Exchange of $Cu_{2-x}Se$ NPs with 10 kDa PVP

Purified OAm-capped $Cu_{2-x}Se$ NPs were dispersed in 4mL $CHCl_3$. 6 mL of 8 mM of 10 kDa PVP solution in $CHCl_3$ was added into the dispersed NP solution and the mixture solution was left stirring overnight at room temperature. After incubation, the $Cu_{2-x}Se$ NP product was purified via centrifugation. First, the as-synthesized NPs were distributed to Eppendorf tubes in aliquots of 0.5 mL. 1 mL hexanes were added into the Eppendorf tubes and centrifuged in an Eppendorf 5424 centrifuge with a fixed angle rotor (F-45-30-11) (Eppendorf, Inc.) at a force of 15,000 rpm at 20 °C for 10 min. The resulting supernatant was removed and the pellet was resuspended in a small amount of $CHCl_3$ for additional centrifugation in another 1 mL of hexanes. This washing procedure was repeated once. All purified NPs were then characterized by HRTEM, UV-vis-NIR extinction spectroscopy, and Raman spectroscopy.

5.2.4 High Resolution Transmission Electron Microscopy

$Cu_{2-x}Se$ NPs were prepared for electron microscopy by drop casting an aliquot of purified NP solution (diluted 1:10 or 1:100 with $CHCl_3$) onto carbon film-coated copper transmission electron microscopy (TEM) grids (Ted Pella, Inc.) for routine bright field imaging analysis. TEM characterization was performed on a Hitachi H9500 Environmental TEM with an accelerating voltage of 300 kV (NanoScale Fabrication and Characterization Facility, Petersen Institute of NanoScience and Engineering, Pittsburgh, PA). The size distributions of the NPs were determined from TEM images of at least 200 NPs from various areas of the grid using ImageJ 1.47d (National Institutes of Health, USA).

5.2.5 Powder X-Ray Diffraction

Purified $Cu_{2-x}Se$ NPs were characterized by PXRD using a Bruker AXS D8 Discover XRD (NanoScale Fabrication and Characterization Facility, Petersen Institute of NanoScience and Engineering, Pittsburgh, PA) at 40 kV, 40 mA for Cu Kα ($\lambda = 1.5406$ Å) X-ray source with a scan speed of 0.7 s/step from 10.00 - 90.00° with a step size of 0.02°. Samples were prepared by drop casting an aliquot of purified NP solution (diluted 1:10 or 1:100 with toluene) on a glass microscope slide (Fisher Scientific). All spectra were baseline corrected with respect to the spectrum of the amorphous glass background.

The lattice parameter (a) of the antifluorite structure was determined using the PXRD peak at 27° in **Figure 5.1**, which corresponds to the cubic (111). Using Bragg equation (**Equation 4.2** described previously) where λ is the X-ray source, $h=k=l=1$, the lattice parameter was calculated to be 0.57 nm, and this value was used to estimate the volume of the unit cell for the quantification of NP concentration.

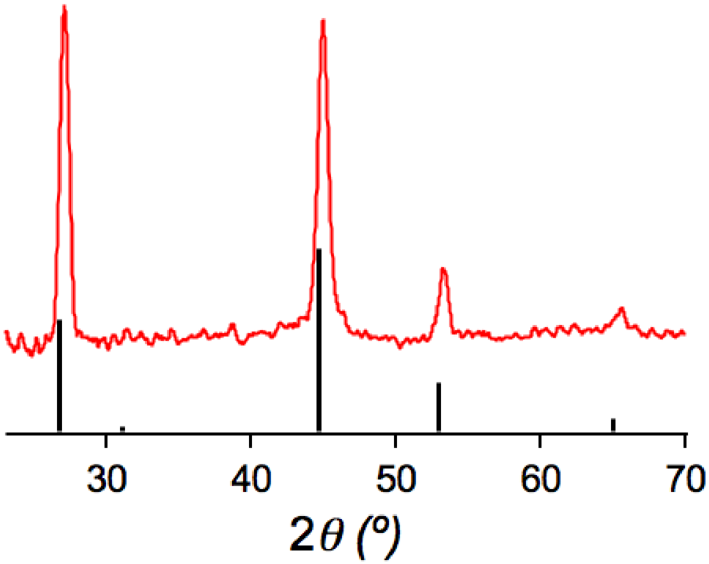

Figure 5.1. Representative PXRD pattern of $Cu_{2-x}Se$ NPs referenced to PDF # 00-006-0680.

5.2.6 Inductively Coupled Plasma-Optical Emission Spectrometry Analysis

ICP-OES analysis was performed using an argon flow with an Optima spectrometer (Perkin Elmer, Inc.). An aqua regia solution was prepared with a 3:1 ratio of hydrochloric acid (Sigma Aldrich, > 99.999% trace metal basis): nitric acid (Sigma Aldrich, > 99.999% trace metal basis) and diluted with water for a 5% v/v aqua regia matrix. Unknown Se and Cu concentrations were determined by comparison to a 7-point standard curve with a range of 0.10 - 10 ppm Cu and Se (0.10, 0.50, 1.0, 2.5, 5.0, 7.5, and 10 ppm of each metal prepared by volume) using a selenium standard for ICP (Fluka, TraceCERT 1000 ± 2 mg/L Se in HNO_3) and Cu standard for ICP (Fluka, TraceCERT 1000 ± 2 mg/L Cu in HNO_3), diluted in a 5% aqua regia matrix. All standards and unknown samples were measured 6 times and averaged. A 7-minute flush time with 5% aqua regia matrix was used between all runs, and a blank was analyzed before each unknown sample to confirm removal of all residual metals from the instrument.

5.2.7 Addition of Raman Analytes to $Cu_{2-x}Se$ NPs

To prepare the BT solutions of various concentrations listed in **Figure 5.6A**, 250 μL of OAm-capped $Cu_{2-x}Se$ NPs dispersed in $CHCl_3$ with an estimated optical density of ~1.5 at $LSPR_{max}$ was added into a 1.5 mL Eppendorf tube, followed by a 200 mM BT solution of volumes ranging from 154 to 769 μL in $CHCl_3$ into the Eppendorf tubes to reach a final solution volume of 1.5 mL to ensure that the NP concentrations and the final volume of each sample aliquot were constant. The solution was thoroughly mixed by incubation on the thermomixer (Eppendorf R Thermomixer) for at least one hour. In order to maintain NP dispersity in solution, it is important to note that all mixtures containing $Cu_{2-x}Se$ NPs and Raman analytes were not purified after the addition of analytes. The mixture solutions were then characterized by UV-vis-NIR extinction spectroscopy and Raman spectroscopy.

To prepare the NBT solutions for the plasmonically driven dimerization reactions represented in **Figure 5.8** and **Figure 5.10**, 250 μL $Cu_{2-x}Se$ NPs (either OAm- or PVP-capped) dispersed in $CHCl_3$ with an estimated optical density of ~1.5 at $LSPR_{max}$ was added into a 1.5 mL Eppendorf tube, followed by a 300 mM NBT solution of volumes ranging from 154 to 769 μL in $CHCl_3$ into the Eppendorf tubes to reach a final solution volume of 1.5 mL to ensure that the NP concentrations and the final volume of each sample aliquot were constant. The solution was thoroughly mixed by incubation on the thermomixer (Eppendorf R Thermomixer) for at least one hour. In order to maintain NP dispersity in solution, it is important to note that all mixtures containing $Cu_{2-x}Se$ NPs and Raman analytes were not purified after the addition of analytes. The mixture solutions were then characterized by UV-vis-NIR extinction spectroscopy and Raman spectroscopy.

5.2.8 Raman Spectroscopy Analysis

The SERS instrument is a modified version of a previously published set-up.[33] Briefly, 6W of <250 fs pulses, centered at 1035 nm, from a fiber amplifier (Clark MXR, Impulse), are sent through a spectral filter to generate picosecond pulses. In the spectral filter, the beam is directed through a transmission grating and focused onto a slit. The beam is then focused onto the sample. The spectral resolution is 17.8 cm^{-1} as measured by the 786 cm^{-1} peak in toluene and the pulse duration is 2.8 ps, as measured by the optical Kerr effect in toluene. After the sample, the spontaneous Raman signal is sent through a 1064 nm Razor Edge Raman filter and focused into a spectrograph (Princeton Instruments, Acton SP2300) containing a 300 gr/mm grating blazed at 1 µm. The Raman signal is collected with a 1024 pixel, liquid N_2 cooled InGaAs array (Princeton Instruments, Pylon-IR 1.7). The spectra were collected as 3 frames with 20 s acquisitions. The frames were averaged together and the spectra were scaled with respect to acquisition time and laser power. For all SERS EF measurements, the flux was 560 W/cm^2, which corresponds to 40 MW/cm^2 peak power. For all plasmonically driven dimerization reactions, the flux was 350 W/cm^2, which corresponds to 5.4 MW/cm^2 peak power.

5.2.9 Estimating SERS Enhancement Factor for $Cu_{2-x}Se$

The SERS enhancement factor (EF) for $Cu_{2-x}Se$ NPs was determined by the following equation:

Equation 5.1. SERS Enhancement Factor

$$EF = \frac{N_{NRS}}{I_{NRS}} \cdot \frac{I_{SERS}}{N_{SERS}}$$

where I_{SERS} and I_{NRS} are the Raman intensities of a specific mode for the SERS and normal Raman spectroscopy (NRS) measurements, respectively, while N_{SERS} and N_{NRS} correspond to number of BT molecules adsorbed on the plasmonic substrate and in solution, respectively, for the probed volume. Details on how we obtain each component that makes up the SERS EF estimation are explained below in the following subsections.

5.2.9.1 Measuring I_{NRS} and Quantifying N_{NRS}

In **Figure 5.6A** in **Section 5.3.2**, the grey dotted spectrum represents a normal Raman spectrum of a 200 mM BT solution in $CHCl_3$. We can fit each Raman peak to a Gaussian to extrapolate the peak amplitude which is equivalent to I_{NRS} for each mode. From the known concentration of the solution, we can calculate N_{NRS} after measuring the focal volume of the laser. The spot radius of the laser beam at the focus was determined by measuring the power before and after a 50 μm diameter pinhole at the sample position and placing the values in the following equation:

Equation 5.2. Laser Spot Size

$$spot\ radius = 2\sqrt{\frac{-2\left(\frac{d}{2}\right)^2}{ln\left(1-\frac{p_a}{p_b}\right)}}$$

where d is the diameter of the pinhole, p_b is the power before the pinhole, and p_a is the power after the pinhole. For these experiments, the focal volume was 1.80 x 10^{-5} mL. By multiplying the focal volume by the concentration of the BT solution and converting moles to molecules using Avogadro's number, N_{NRS} is 2.18 x 10^{15} molecules. Obtaining these values give us the ability to express N_{NRS}/I_{NRS} as 8.04 x 10^{15}.

5.2.9.2 Quantifying N_{SERS}

N_{SERS} was calculated by first determining the concentration of NPs in the focal volume (1.80 x 10^{-5} mL).

5.2.9.2.1 Calculating $Cu_{2-x}Se$ NP Concentrations

$Cu_{2-x}Se$ NP concentrations were determined using the UV-vis-NIR spectrum of the NPs before BT addition in $CHCl_3$. Spectra were taken using a Cary 5000 UV-vis-NIR (Agilent, Inc.). UV-vis-NIR measurements were collected of NP suspensions diluted in $CHCl_3$ using 1.0 cm quartz cuvettes (Hellma, Inc.). Three trials of six serial dilutions of the concentrated NP stock were prepared. These particles were air dried, digested in 5% aqua regia and then further diluted for analysis. The extinction spectra were measured from 800-1500 nm, the concentrations of NPs were measured by ICP-OES (**Section 5.2.6**), and the average diameters of the NPs were determined using HRTEM micrographs. The total number of unit cells per particle was estimated by dividing the volume of the NP sphere by the volume of the cubic antifluorite lattice of Cu_2Se. The volume of the antifluorite unit cell was determined by PXRD (**Section 5.2.5, Figure 5.1**). The total number of Se atoms was then estimated per particle by multiplying the number of unit cells per particle by 4, which is the number of Se atoms present in an antifluorite unit cell. The slope of the linear regression can be used to estimate NP concentration in a specific optical density measured.

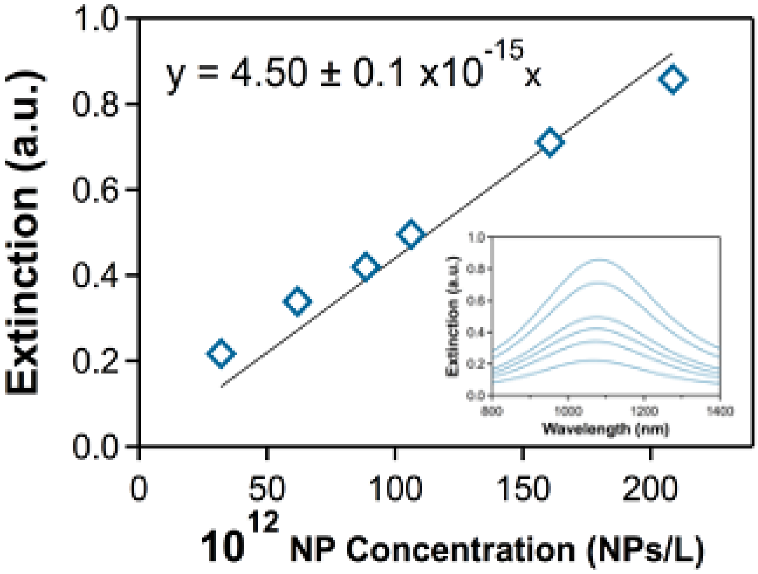

Figure 5.2. Molar extinction spectrum of the OAm-capped $Cu_{2-x}Se$ NPs dispersed in $CHCl_3$. The insets correspond to their extinction profiles.

Before the Raman excitation, we monitor the $Cu_{2-x}Se$ NP optical density (O.D.) at the LSPR maximum using extinction measurement. At approximately 0.302 O.D., which corresponds to 6.72 x 10^{13} particles/L based on the molar extinction coefficient (**Figure 5.2**). By multiplying the focal volume by the particle concentration, the number of particles in the focal volume is 1.2 x 10^6. Next, we can estimate the surface area of a particle from the average particle diameter measured by TEM (**Figure 5.5B**, 16.4 ± 1.5 nm). Assuming the particles are spheres, the surface area of a single particle is 7.9 x 10^{-4} μm^2.

5.2.9.2.2 Estimating the Theoretical Surface Coverage of BT

In addition to particle concentration, the other key component of determining N_{SERS} is estimating the packing density of the analyte on the NP surface. Theoretical BT footprint was determined using a model system generated by the Avogadro molecular editor (v1.2.0),[187] which was mainly used to aid in the measurement of atomic distances. Specifically, the geometry of BT was intentionally placed bound to a copper atom at a tilt angle of 30° consistent with reports by Osawa and coworkers for BT bound to a Au(111) surface.[188] The BT-Cu interaction was geometrically optimized by relaxation with the universal force field (UFF) to an average force of 10^{-4} kJ mol^{-1} $atom^{-1}$ before bond lengths were measured and bond angle was intentionally changed.

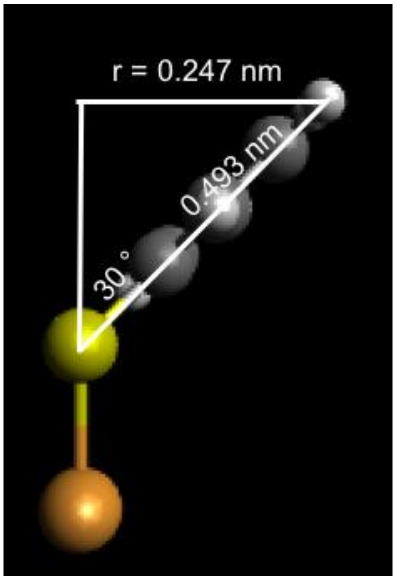

Figure 5.3. Lateral view of a representative BT bound to a copper atom and the measured S-para H distance at a tilt angle of 30°.

The distance between sulfur and hydrogen in the para position of the benzene ring was measured to be 0.247 nm (**Figure 5.3**), where the measurement is from one atom center to the other. Therefore, the van der Waals sphere must also be considered, where the Van der Waals radius for hydrogen was estimated to be 1.09 Å.[189] By summing the two values we obtain an overall molecular radius estimate of 0.356 nm and its corresponding footprint of 0.4 nm^2/ligand.

From this footprint, a calculated maximum of 2,122 ligands could be added to the surface of a $Cu_{2-x}Se$ NP. This density assumes that the analyte completely displaces the capping ligand on the surface of the NPs at a 1:1 equivalence.

From these packing density values and NP concentrations measured in **Section 5.2.9.2.1**, we conservatively estimate N_{SERS} to be 2.37 x 10^9 molecules. We note that this likely significantly overestimates the amount of BT on the nanoparticle surface, as the BT coverage reported on other metal chalcogenide systems are lower (0.73 nm^2/ligand on CdSe NPs.)[190] If the concentration of BT on the nanoparticle surface is lower than we have estimated (as it likely is), our enhancement factor will be higher than we have calculated. For example, if the ligand concentration is half of what we estimate, the SERS EF will be double what we have calculated based on that estimate.

5.2.9.2.3 Experimental BT Concentrations Necessary for Full Coverage

As noted previously, all BT-$Cu_{2-x}Se$ NP mixtures were *not* purified after the addition of analytes in order to maintain NP dispersity in solution. To ensure the concentrations of BT used were sufficient to achieve full coverage on the surface of the NPs, the LSPR peak positions of $Cu_{2-x}Se$ NPs before and after the addition of BT were analyzed using UV-vis-NIR spectroscopy. As a function of increasing BT concentration, the LSPR of $Cu_{2-x}Se$ NPs redshifted and plateaued (**Figure 5.4**). This observation resulted from the interaction between the thiol binding moiety present in both the Raman analytes and the NP surface, where the more electron donating thiolated head groups reduce the carrier densities in $Cu_{2-x}Se$ NPs. Overall, these experiments indicate that an excess of 100x is sufficient to saturate the $Cu_{2-x}Se$ NP surfaces with BT. This 100x excess of BT, then becomes our benchmark for BT concentrations used in Raman measurements.

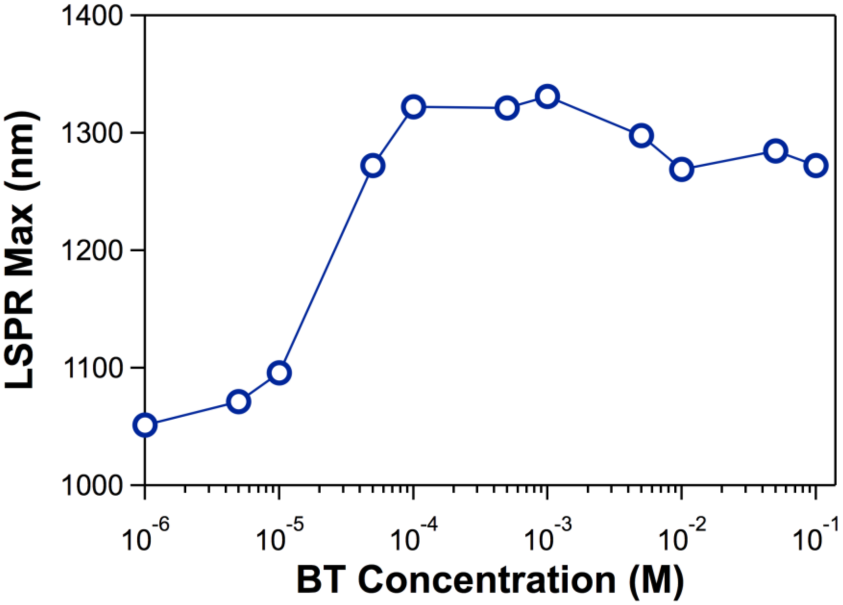

Figure 5.4. Shifts of LSPR maximum for OAm-capped $Cu_{2-x}Se$ NPs as a function of increasing BT concentration in $CHCl_3$ ranging from 1 μM to 0.1 M.

5.2.9.3 Extrapolating I_{SERS}

The total intensity (I_{Total}) at each BT concentration is measured by fitting each peak (**Figure 5.6A**) to a Gaussian to extrapolate the peak amplitude, which includes intensities coming from both bound (I_{SERS}) and excess (I_{Excess}) BT molecules (**Table 5.1**). After finding the I_{Total} for each BT concentration, we can calculate the I_{Total}/N_{SERS} ratio. As noted previously, in these experiments, at least 100x excess of BT was used and this excess must be considered by subtracting our estimated N_{SERS} from N_{Total} at the focal volume, where N_{SERS} is constant for all concentrations.

Table 5.1. Relative SERS Intensities of 1002 cm^{-1} mode of BT of Various Concentrations for the Quantification of an Enhancement Factor for Cu$_{2-x}$Se NPs.

[BT] (mM)	I_{Total} (I_{SERS} + I_{Excess})	I_{Total}/N_{SERS}	N_{Excess} ($N_{Total} - N_{SERS}$)
20.5	0.0279 ± 0.0041	1.17 ± 0.31 x 10^{-11}	2.23 x 10^{14}
41.1	0.0451 ± 0.0073	1.90 ± 0.17 x 10^{-11}	4.47 x 10^{14}
61.6	0.070 ± 0.0049	2.95 ± 0.21 x 10^{-11}	6.71 x 10^{14}
82.0	0.0921 ± 0.0056	3.88 ± 0.23 x 10^{-11}	8.93 x 10^{14}
102.5	0.110 ± 0.0063	4.63 ± 0.27 x 10^{-11}	1.12 x 10^{15}

5.2.9.4 Calculating SERS EF

In **Figure 5.6B**, we plot the I_{Total}/N_{SERS} ratio against the N_{Excess} at each concentration. If we fit these data to a linear regression, the y-intercept (an average of 2.41 ± 1.04 x 10^{-12}) represents the case where $N_{excess} = 0$, in other words, the intensity due only to the SERS active molecules. With this value in hand, we can bring together all the components acquired in the previous sections and obtain a SERS EF. By multiplying the y-intercept value by N_{NRS}/I_{NRS}, we obtain an enhancement factor of ~10^4.

5.3 Results and Discussion

5.3.1 $Cu_{2-x}Se$ NP Synthesis and Characterization

In a typical experiment, we prepared $Cu_{2-x}Se$ NPs via a hot injection method according to a modified literature procedure using standard air-free techniques (see **Section 5.2.2** for experimental details).[62, 136] Briefly, this synthesis produces colloidally stable $Cu_{2-x}Se$ NPs with oleylamine (OAm) as the surface passivating ligands. Similar to what has previously been reported, transmission electron micrographs show that purified OAm-capped $Cu_{2-x}Se$ NPs are pseudospherical with an average diameter of 16.4 ± 1.5 nm (**Figure 5.5A, B**) and an antifluorite crystal structure (**Figure 5.1**, PDF #00-006-0680).[62] When the NPs are exposed to oxygen under ambient conditions, they undergo a self-doping process where some Cu^+ ions are oxidized to Cu^{2+}, which results in the formation of valence band holes.[49] The presence of degenerate holes produces an LSPR at approximately 1100 nm with an additional absorption feature arising at approximately 500 nm, which we assign to the direct bandgap of $Cu_{2-x}Se$ NPs (**Figure 5.5C**). The concentration of degenerate holes formed in the NPs (i.e., carrier density, N_h) can be extracted from the extinction spectrum and quantified using the Drude model ($N_h = 6.3 \times 10^{21}$ cm^{-3}).[49, 55, 62]

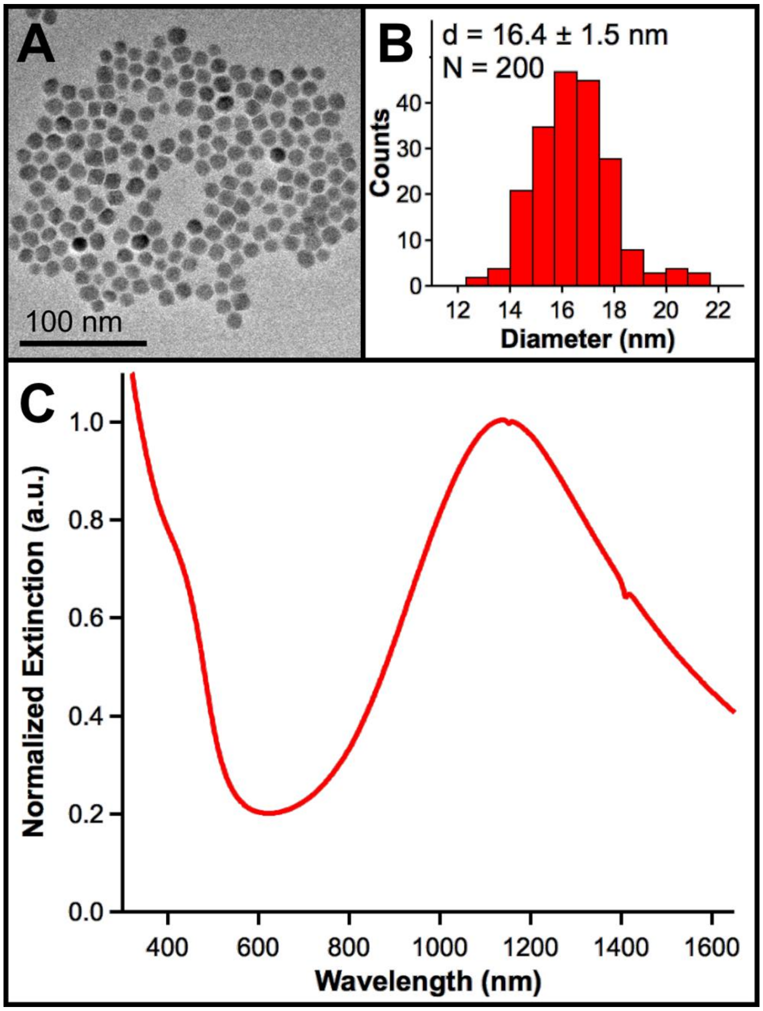

Figure 5.5. (A) High-resolution transmission electron micrograph showing monodispersed, pseudospherical OAm-capped $Cu_{2-x}Se$ NPs (B) with its size distribution represented in the histogram and (C) extinction spectrum of the NPs dispersed in $CHCl_3$.

5.3.2 Establishing $Cu_{2-x}Se$ SERS Enhancement Factor

A first step in comparing the plasmonic features of $Cu_{2-x}Se$ NPs to traditional noble metal NPs is establishing the magnitude of their plasmon-driven electromagnetic field enhancement. One common technique by which this enhancement may be measured is SERS, which is used in a variety of sensing applications.[181] The enhanced signal observed using SERS arises from the coupling of a material's LSPR with incoming resonant light and scattered Raman photons.[181]

In order to study the SERS properties of the OAm-terminated $Cu_{2-x}Se$ NPs, we introduced benzenethiol (BT) as a reporter molecule for the SERS measurement. Represented in the gray spectrum in **Figure 5.6A** as a reference, BT has two Raman active ring-breathing modes at approximately 1002 and 1024 cm^{-1}. When various concentrations of BT in $CHCl_3$ (ranging from 0–100 mM) were introduced to different aliquots containing the same amount of colloidally dispersed OAm-capped $Cu_{2-x}Se$ NPs, the resulting SER spectra show that there is a linear increase in the intensity of Raman peaks associated with the BT molecule, as a function of BT concentration.

To extract an enhancement factor (EF) for the $Cu_{2-x}Se$ NPs, we used **Equation 5.1**, described previously in detail, in **Section 0**,[31, 110] where, specifically, I_{SERS} and I_{NRS} are the Raman intensities of BT at 1002 cm^{-1} for the SERS and normal Raman measurement, respectively, while N_{SERS} and N_{NRS} correspond to number of BT molecules adsorbed on the plasmonic substrate and in solution, respectively, for the probed volume. First, the unenhanced intensity of BT Raman signal (I_{NRS}) was measured by preparing a 200 mM BT solution in $CHCl_3$, where N_{NRS} was approximately 2.18×10^{15} molecules. To account for the absorption effects in $Cu_{2-x}Se$ NP containing solutions, I_{NRS} was scaled by a normalization factor of 0.35, obtained by measuring the transmission of the excitation beam.

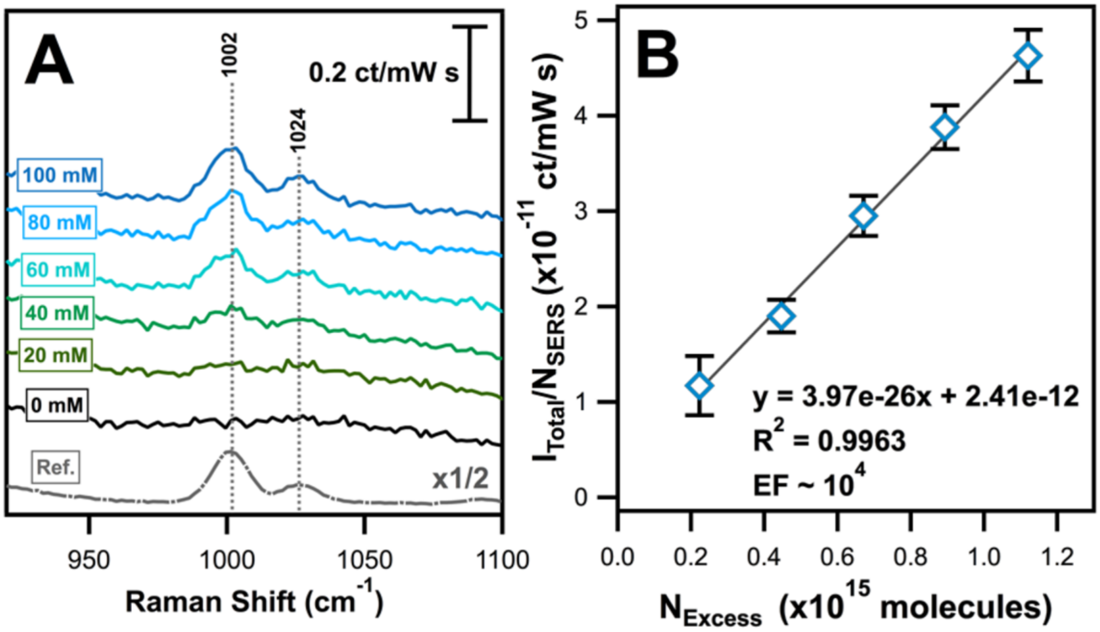

Figure 5.6. (A) SER spectra of BT adsorbed onto colloidal $Cu_{2-x}Se$ NPs as a function of increasing BT concentration (black to dark blue), where the gray spectrum shows BT in $CHCl_3$ without the presence of $Cu_{2-x}Se$ NPs as reference; dotted vertical lines indicate ring-breathing modes of BT. (B) Linear fit of the I_{Total}/N_{SERS} versus number of excess BT molecules (N_{Excess}) in solution from which the enhancement factor is extrapolated to 10^4 for $Cu_{2-x}Se$ NPs. The error bars in each data point represent the standard error for three trials. Full details of all measurements and calculations are described in Section 5.2.9.

We note that we were not able to extract I_{SERS} in a straightforward manner as all BT-$Cu_{2-x}Se$ NP-mixtures contained both particle-bound and free, excess BT in order to maintain NP dispersity in solution. Instead, all BT-$Cu_{2-x}Se$ NP-mixtures were prepared in conditions where there were excess BT molecules present, where we define “excess” as the BT concentration greater than that needed to fully functionalize the NP surface area in solution (see **Sections 5.2.9.2.2** and **5.2.9.2.3** for detailed explanation and calculations). Briefly, BT was estimated to have a theoretical maximum footprint of 0.4 nm^2/molecule, which is within the range of BT coverage reported on Au surfaces and CdSe nanocrystals.[187-188, 190] To assess whether the full coverage has been achieved, we used extinction spectroscopy and monitored the BT excess after which we could no longer observe a ligand-driven LSPR redshift (**Figure 5.4**). These experiments suggest that all BT-$Cu_{2-x}Se$ NP mixtures used in the SERS evaluation experiments were prepared in conditions where BT would have completely saturated the NP surface and produced a roughly constant N_{SERS} since the NP concentration is also constant in each aliquot.

In order to extract the SERS EF of $Cu_{2-x}Se$ NPs in the presence of excess BT molecules, the ratios between I_{Total} (accounting for intensities coming from both particle-bound and excess BT molecules) and N_{SERS} were plotted against the number of excess BT molecules in the probed volume (N_{Excess}), where N_{Excess} in each aliquot was obtained by subtracting the estimated N_{SERS} from the total BT molecules present (N_{Total}), and a linear regression was used to fit the data points (**Figure 5.6B**). Using the *y*-intercept of the fitted linear regression where $N_{Excess} = 0$, we can extrapolate an idealized I_{SERS}/N_{SERS} ratio. By using this ratio in **Equation 5.1** and reporting only to the order of magnitude (due to significant estimates necessary concerning the theoretical surface coverage of BT), we calculated a lower bound of $Cu_{2-x}Se$ NP SERS EF to be ~10^4 (see **Section 5.2.9** for additional details of this calculation, including quantifying NP concentrations and estimates of surface coverage). This EF is comparable to traditional high-performing noble metal SERS substrates, which have EFs between 10^3 and 10^7 depending on particle size, shape, and aggregation state.[110]

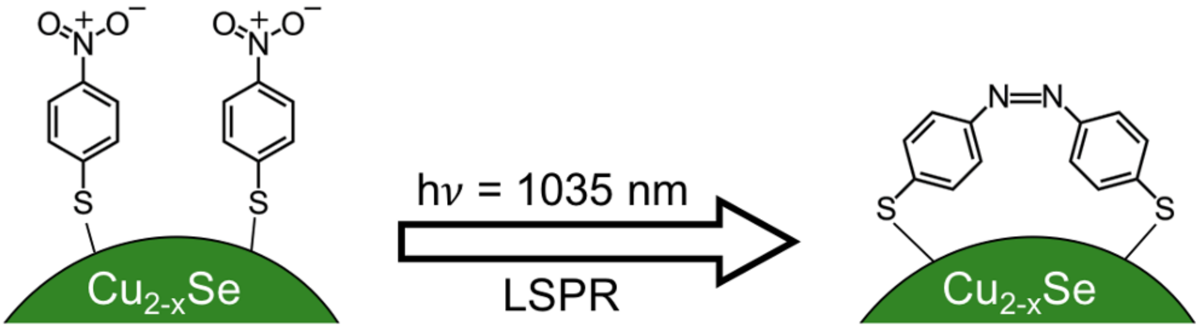

Figure 5.7. Schematic showing a simplified depiction of plasmonically-driven chemical conversion from 4-NBT to DMAB.

5.3.3 Plasmon-Enhanced Chemical Conversion from NBT to DMAB

Having established a conservative estimate of the SERS EF for $Cu_{2-x}Se$ NPs, we then examined whether this LSPR can mediate the dimerization of 4-nitrobenzenethiol (NBT) to 4,4′-dimercaptoazobenzene (DMAB) (**Figure 5.7**). NBT dimerization is a plasmon-mediated chemical reaction that is well-characterized on noble metal plasmonic substrates and is known to be mediated by the generation of plasmon-derived hot electrons to initiate the multi-electron reduction reaction.[31, 191] The light gray spectrum in **Figure 5.8** represents the normal Raman spectrum of NBT. The highlighted NBT modes (black dashed lines) at 1102, 1344, and 1580 cm^{-1} correspond to the ring breathing, NO_2 symmetric stretch and C–C stretch, respectively.[14] Within 5 min of irradiation at 1035 nm, a solution containing NBT adsorbed to the $Cu_{2-x}Se$ NP surface exhibited DMAB product peaks in the SER difference spectra (**Figure 5.8** and **Figure 5.10A**). The product peaks labeled in red at 1296, 1383, and 1458 cm^{-1} are assigned to DMAB based on comparison with normal Raman measurements and SERS measurements on Au and Cu substrates.[192-193] Modes at 1296, 1383, and 1458 cm^{-1} are attributed to ν(CC), ν(NN) + ν(CC), and ν(NN) + δ(CH), respectively, where ν indicates a stretching mode, and δ indicates an in-plane bending mode. Interestingly, the product peaks are shifted by ~10-20 cm^{-1} compared to those observed on noble metal plasmonic substrates, indicating a difference in the chemical environment and binding motifs on the $Cu_{2-x}Se$ NP surface.[99]

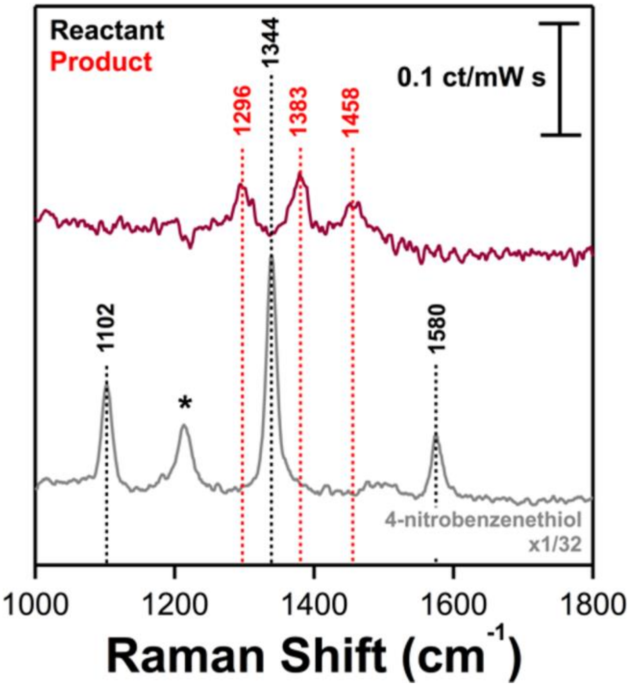

Figure 5.8. SER difference spectrum of OAm-capped $Cu_{2-x}Se$ NPs (maroon), shows the plasmon-driven dimerization of the reactant 4-nitrobenzenethiol (black dashed lines) to the product, 4,4′-dimercaptoazobenzene (red dashed lines). Light gray spectrum shows the normal Raman spectrum for NBT.

This plasmon-driven chemical conversion is particularly remarkable because the dimerization of NBT undergoes a reduction-based mechanism (i.e., requiring hot electrons from noble metal NPs),[18] while the LSPRs of $Cu_{2-x}Se$ NPs are generated by the coherent oscillation of delocalized holes in the valence band. Though copper chalcogenides primarily produce hot holes,[114, 118] the electrons of the initial hot electron-hole pairs appear to be energetic enough to drive these reactions, where the hot holes could be scavenged by various species, including oxygen dissolved in the solvent. However, in order to definitively understand the mechanism of this plasmon-driven reaction, dynamics of the decay and transfer of hot electrons and holes in degenerately doped semiconductor NPs need to be studied, likely via subsequent ultrafast measurements and/or computational models.[6-7]

Additionally, we performed a control experiment by irradiating a concentrated NBT solution in the absence of $Cu_{2-x}Se$ NPs at the same power and duration as the samples containing $Cu_{2-x}Se$ NPs. As can be seen in the difference spectrum in **Figure 5.9**, no DMAB peaks are present after 5 minutes of irradiation showing the necessity of the plasmonic $Cu_{2-x}Se$ NPs for the dimerization of NBT.

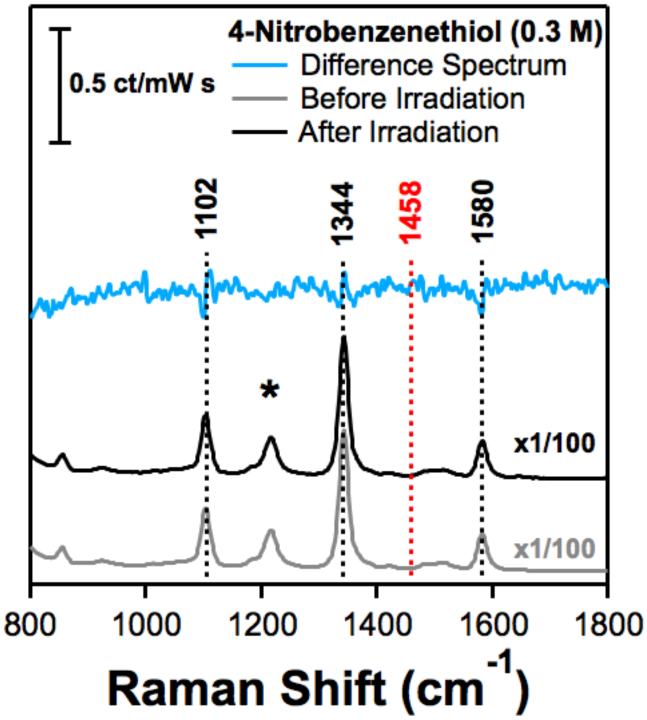

Figure 5.9. Time resolved SER spectra of NBT in the absence of $Cu_{2-x}Se$ NPs, where DMAB has not formed after 5 minutes of irradiation. Black dashed lines denote NBT and the red dashed line marks the growth of a DMAB peak in the spectrum obtained after 5 minutes of irradiation.

5.3.4 NBT Dimerization Reaction Yield and Efficiency using Time-Resolved SER Spectra

The representative difference spectra for OAm- (**Figure 5.10A**) and PVP- (**Figure 5.10B**) capped $Cu_{2-x}Se$ NP samples were obtained by subtracting the spectrum obtained upon initial exposure to the laser (0 min) from the spectrum obtained after 5 minutes of irradiation. The grey spectra in both **Figure 5.10** panels represent the normal Raman spectrum of NBT. The NBT peaks are marked by black dashed lines and the DMAB product peak is denoted with a red dashed line. Solvent ($CHCl_3$) peaks are denoted by asterisks.

From these spectra, we can estimate a percent yield for this reaction on $Cu_{2-x}Se$ NPs. First, we fit the 1344 and 1580 cm^{-1} reactant peaks before and after irradiation to a Gaussian function to extrapolate the peak amplitude. We account for any changes in signal by comparing the amplitude changes between the nitro stretch (1344 cm^{-1}) and the C-C stretch (1580 cm^{-1}) from before and after irradiation. Then we can fit the N=N stretch (1458 cm^{-1}), which corresponds to the product peak to obtain its peak amplitude. By placing the peak amplitudes into the equation below:[31]

Equation 5.3. Reaction Yield for NBT Dimerization

$$Percent\ Yield = \frac{Final\ Product\ Amplitude}{Final\ Reactant\ Amplitude}$$

we can obtain a percent yield for this reaction for OAm-capped and PVP-capped $Cu_{2-x}Se$ NPs to be 25 ± 3% and 24 ± 4%, respectively.

We estimated a percent yield for this reaction by comparing the final peak amplitude ratio of the 1344 cm^{-1} reactant peak and the 1458 cm^{-1} product peak (**Figure 5.10A**).[6] The percent yield for this reaction on $Cu_{2-x}Se$ NPs is 25 ± 3%, which is comparable to the yield measured for the reaction on Au NPs.[31] This estimate implies that the reaction goes to completion while being limited by the proximity of two nitro groups relative to one another. It is important to note that SERS signal magnitudes depend dramatically on the distance of the analyte from the surface, and thus this estimated yield is representative of only a subset of molecular species closest to the NP surface.

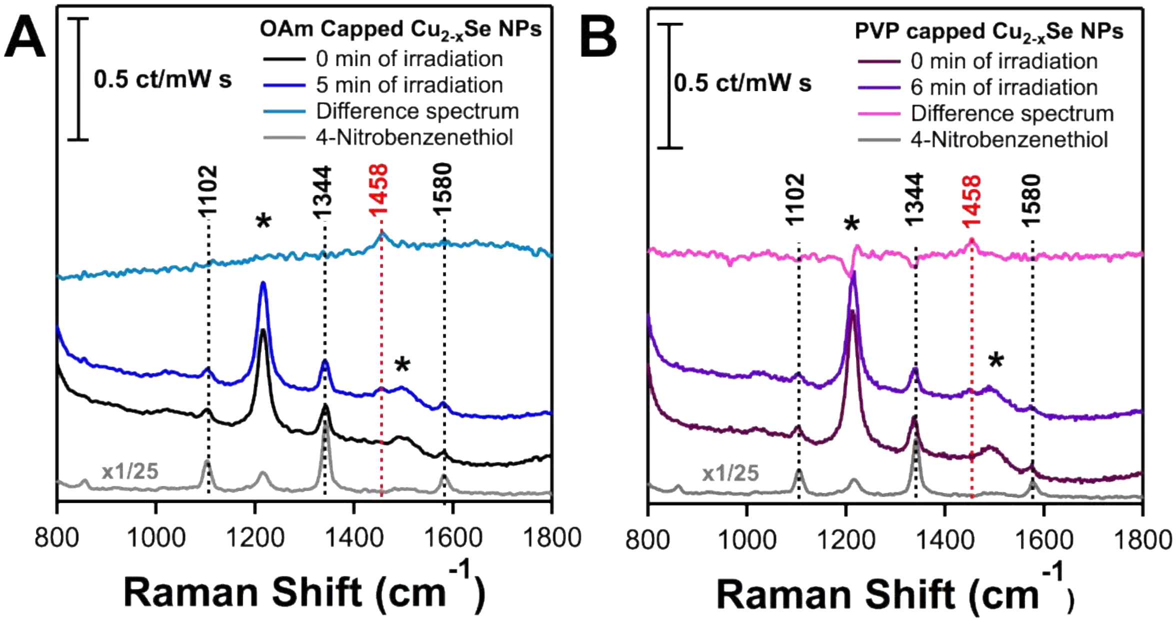

Figure 5.10. Time resolved SER spectra of NBT in the presence of (A) OAm-capped and (B) PVP-capped $Cu_{2-x}Se$ NPs.

In order to examine the role of sterics in the reaction efficiency, we performed similar

SERS EF and plasmon-driven chemical conversion experiments using a different ligand shell on the Cu2-xSe NPs. In this work, we hypothesized that the presence of a polymeric ligand (e.g.,polyvinylpyrrolidone (PVP)) on the NP surface could significantly influence the adsorption of NBT and/or the NBT dimerization process, thereby decreasing the overall yield of the reaction. To probe that effect, we first synthesized the OAm-capped NPs and then performed a mass-action ligand exchange to functionalize the NP surface with 10 kDa PVP (see **Section 5.2.3** for mass action ligand exchange details). The SER difference spectrum of NBT dimerization in the presence of PVP-capped $Cu_{2-x}Se$ NPs shows the presence of DMAB product (**Figure 5.10B**). The percent yield of the reaction as observed by SERS is approximately 24 ± 4%, suggesting that there is no statistically significant change in the percent yields between OAm- and PVP-capped NPs. These results show that NBT adsorption to the NP surface and/or its subsequent plasmon-mediated reduction are not significantly inhibited by sterics due to the presence of an initially bulky surface ligand. Importantly, these observations also demonstrate that this plasmon-mediated chemical reaction may be versatile in a more complex $Cu_{2-x}Se$ NP surface environment.

5.4 Conclusions

In summary, we demonstrate the first plasmonically-driven chemical conversion using degenerately doped semiconductor NPs with efficiencies comparable to LSPR-mediated reactions observed using noble metal NP analogues. Taken together, these results are a key step toward the translation of non-noble metal, specifically semiconductor, alternatives in plasmon-based technologies and in particular in key areas of photoredox chemistry such as solar light conversions.

6.0 Connecting Cation Exchange and Metal Deposition Outcomes via Hume-Rothery-Like Design Rules Using Copper Selenide Nanoparticles

(Portions of this work are being prepared for submission as Gan, X. Y., Sen, R., Millstone, J. E., **2021**, *In Review*.)

6.1 Introduction

Hume-Rothery rules are a fundamental guide for predicting the generation of either mixed metal (i.e. alloys) or segregated phases in bulk multimetallic materials.[194-195] Specifically, Hume-Rothery described that the miscibility of two metals is limited by their lattice distortion via atomic radii differences, valency and electronegativity.[194] Since then, these rules have been extended to predict a large subset of alloys, and have become a powerful way to both guide and discover new materials.[196-198] Not only have these guidelines been used as a starting place to successfully predict bulk multimetallic material morphology, they are also a starting place to predict nanoscale multimetallic architectures.[199-200]

Of course, metallic materials are not the only inorganic material class to incorporate multiple metals and to be impacted by the distribution of those elements within the final architecture. However, Hume-Rothery-like guidelines are not yet established for other inorganic material classes such as metal chalcogenides either in the bulk or at the nanoscale. Yet, manipulation and/or diversification of metal components within metal chalcogenides is common, and for nanoscale metal chalcogenides, there have been numerous reports on methodologies to introduce multimetallic components via either in-situ or post-synthetic strategies.[201-204]

The most explored methods to generate mixed metal chalcogenide systems are through post-synthetic modifications, as they offer better and simultaneous control over morphology, size, and spatial distribution of atoms in these composite nanoparticles (NPs) when compared to *in situ* methods.[202] One common post-synthetic modification strategy is cation exchange (CE) of the original metal chalcogenide. During CE, there is an efflux of the original metal cation and an influx of secondary metal cations that infiltrate the host lattice to form a new metal chalcogenide structure,[201, 205-206] and there are several experimental factors known to influence the extent of the CE process.[204-206] Specifically, in the seminal review by Manna and coworkers, factors such as incoming cationic radius, cation solubility, and lattice enthalpy (which they term thermodynamic factors), as well as parameters such as lattice volume and symmetry change (which are termed kinetic factors), can all influence the morphological and compositional outcomes of the CE process.[205] For example, Schaak and coworkers have generated a library of heterogenous metal sulfides using CE by modulating parameters such as lattice strain, atomic radii, and reaction time.[207]

Yet, the addition of a secondary metal cation to pre-formed metal chalcogenide nanomaterials can also lead to nucleation and growth of one or more metallic species on the surface of the metal chalcogenide starting material.[27, 208-209] The resulting multicomponent structures are a separate and equally important class of multimetallic chalcogenide structures alongside CE-derived NPs. These multicomponent structures contain at least one discrete metal-semiconductor interface, and are the result of metal deposition (MD) processes.[204, 209] These multicomponent metal-metal chalcogenide structures have been the subject of extensive synthetic research as well.[27, 208-210] For example, in a recent review, Liu and coworkers distilled key mechanistic principles known to guide the formation of these structures, including the pivotal role of lattice mismatch in forming multicomponent structures of either core@shell or Janus-type architectures.[204]

The products of both CE and MD processes are of significant interest for fundamental optoelectronic studies[209, 211] as well as downstream energy conversion[10, 25] and energy transfer applications.[27, 118] However, it remains to be understood why the introduction of one metal results in the formation of a CE product, and the introduction of another metal results in the formation of a MD product for the same metal chalcogenide NP substrate. It would be ideal to establish a set of principles directly analogous to the Hume-Rothery rules in metallic systems, where we can predict the generation of either a "mixed" metal chalcogenide phase or "segregated" metal-semiconductor heterostructures. Importantly, to be directly analogous, these new guidelines would use fundamental parameters of the system (such as lattice symmetry and volume change), rather than other, more environmentally sensitive parameters (such as reagent solubility and reduction potentials) to rationally obtain these multimetallic structures.

Here in this chapter, we report a Hume-Rothery-like design rule that allow us to predict the structural outcome of secondary metal cation addition to isotropic copper selenide ($Cu_{2-x}Se$) semiconductor NPs. Specifically, we demonstrate that the generation of a new metal selenide or ternary metal selenide phase is largely driven by the predicted change in the $Cu_{2-x}Se$ lattice symmetry. We find that the formation of a semiconductor-semiconductor interface occurs when the symmetry between phases retains mutually orthogonal lattice vectors (*i.e.* cubic, tetragonal, and orthorhombic crystal systems) otherwise MD products are observed. Taken together, these results yield two impactful outcomes: 1) they reveal important variables for rationally synthesizing broadly-sought composite materials: both multiphase mixed metal chalcogenides, as well as hybrid multicomponent structures containing one or more metal-semiconductor interfaces. 2) The mechanistic principles established here rely on properties of the resulting crystallite lattices, which are relatively invariant synthetic guideposts compared to factors such as precursor reactivity, and point toward the discovery of more such parameters that could provide a robust starting place for NP design and synthesis, in general.

6.2 Experimental Section

6.2.1 General Methods and Materials

Copper(II) sulfate pentahydrate ($CuSO_4 \cdot 5H_2O$, > 98%), selenium dioxide (SeO_2, > 99.9%), gold(III) chloride trihydrate ($HAuCl_4 \cdot 3H_2O$, ≥ 99.9%), silver nitrate ($AgNO_3$, > 99.0%), mercury(II) nitrate monohydrate ($Hg(NO_3)_2 \cdot H_2O$, ≥ 99.99%), potassium tetrachloroplatinate(II) (K_2PtCl_4, 98%), potassium tetrachloropalladate(II) (K_2PdCl_4, 99.99%), polyvinylpyrrolidone (PVP, average molecular weight 3.5 kDa), L-ascorbic acid (> 99%), and sodium borohydride ($NaBH_4$, ≥ 98.0%) were purchased from Sigma Aldrich (St. Louis, MO). Deuterium oxide (D_2O, 99.9%) was purchased from Cambridge Isotope Laboratories, Inc. (Tewskbury, MA). All chemicals were used as received with no additional purification unless otherwise noted. NANOpure (> 18.2 MΩ cm, Thermo Fisher Scientific, Waltham, MA) water was used in the preparation of all solutions. Prior to use, all glassware and Teflon stir bars were washed in aqua regia and rinsed with copious amounts of water prior to oven drying. *Caution*: aqua regia is highly toxic and corrosive and should only be used with proper personal protective equipment and training. Aqua regia should be handled inside a fume hood only.

6.2.2 Synthesis of Water Dispersible PVP-Capped $Cu_{2-x}Se$ NPs

$Cu_{2-x}Se$ NPs were synthesized using a modified ambient condition, room temperature, seed mediated procedure.[101, 175] First, 10 mL of 5 mM 3.5 kDa PVP was dissolved in water prepared in a scintillation vial equipped with a teflon-coated stir bar. 500 μL of 0.25 M SeO_2 aqueous solution was added to the PVP solution followed by a rapid injection of 200 μL of 1.15 M aqueous ascorbic acid solution to promote the nucleation of selenium seeds, as indicated by color change of the solution from clear to bright orange. After stirring at 450 rpm for 10 minutes, 500 μL of 0.50 M $CuSO_4$ aqueous solution was added to the orange Se seed solution, followed by another quick injection of 300 μL of 1.15 M aqueous ascorbic acid solution. After 10 seconds, the solution turned dark brown. The solution was allowed to stir for approximately 15 hours during which the solution turned dark green. The $Cu_{2-x}Se$ NP product was purified via centrifugation. First, the as-synthesized NPs were transferred to a 50 mL Falcon tube and diluted with water. The NP solutions were centrifuged in an Eppendorf 5804 centrifuge with a fixed angle rotor (FA-45-6-30) (Eppendorf, Inc., Hauppauge, NY) at a force of 16,639 rcf at 25 °C for 10 min. The resulting supernatant was carefully removed and the soft NP pellet was resuspended in approximately 50 mL of H_2O for additional centrifugation. This washing procedure was repeated 2 more times.

6.2.3 Post Synthetic Addition of M^{x+} on $Cu_{2-x}Se$ NPs ($M^{x+} = Ag^+, Au^{3+}, Hg^{2+}, Pd^{2+}, Pt^{2+}$)

The secondary metal addition on purified $Cu_{2-x}Se$ NPs was performed using modified ambient condition, room temperature procedure similar to the cation exchange and metal deposition protocols published by our group previously.[212-213] First, purified $Cu_{2-x}Se$ NPs was dissolved in H_2O to make a concentrated stock (70 optical density (O. D.) at the LSPR peak maximum (approximately 1100 nm) determined by UV-vis-NIR spectroscopy). 2mL of such NP solution was prepared in a scintillation vial equipped with a teflon-coated stir bar. 5.60 mL of 1.6 M aqueous ascorbic acid solution was added to the NP solution followed by an injection of, 5.60 mL of 2.0 mM aqueous solution of secondary metal salt (e.g. $HAuCl_4$ for Au, etc., see Materials listed) where the solution turned dark brown. As determined by ICP-OES and extinction spectroscopy reported previously,[212] the molar ratio of secondary metal to Cu present within the NP lattice is 2:1. The solution was allowed to stir for approximately 15 hours where the solution turned dark brown-green.

The composite NP product was purified via centrifugation. First, the as-synthesized NPs were transferred to a 50 mL Falcon tube and diluted with water. The NP solutions were centrifuged in an Eppendorf 5804 centrifuge with a fixed angle rotor (FA-45-6-30) (Eppendorf, Inc., Hauppauge, NY) at a force of 16,639 rcf at 25 °C for 10 min. The resulting supernatant was carefully removed and the soft NP pellet was resuspended in approximately 50 mL of H_2O for additional centrifugation. All purified NPs were then characterized by HRTEM, UV-vis-NIR extinction spectroscopy, PXRD, and XPS.

6.2.4 Post Synthetic Addition of Ag on $Cu_{2-x}Se$ NPs at Various Ascorbic Acid Concentrations

The Ag addition on purified $Cu_{2-x}Se$ NPs was performed using the protocol outlined previously. While keeping the concentration and volume of $AgNO_3$ solution constant, 5.60 mL of 0 M (plain H_2O), 4.0 mM, 40 mM, 0.4 M, and 1.6 M of aqueous ascorbic acid solution to simulate a 0, 2x, 20x, 200x, and 800x excess of reducing agent to cation solution, respectively. The solutions were allowed to stir for approximately 15 hours where the solution turned dark brown-green before purification.

6.2.5 Post Synthetic Addition of Ag on $Cu_{2-x}Se$ NPs Using Sodium Borohydride as a Reducing Agent

The Ag addition on purified $Cu_{2-x}Se$ NPs was performed using the protocol outlined previously. While keeping the concentration and volume of $AgNO_3$ solution constant, 5.60 mL of 0.4 M, and 1.6 M of aqueous $NaBH_4$ solution to simulate a 200x, and 800x excess of reducing agent to cation solution, respectively. The solutions were allowed to stir for approximately 15 hours where the solution turned dark brown-green before purification.

6.2.6 High Angle Annular Dark Field (HAADF) Imaging and Scanning Transmission Electron Microscopy Energy Dispersive X-ray Spectroscopy (STEM-EDS)

All samples were prepared for TEM by drop casting an aliquot of purified solution (diluted 1:100 with water) onto carbon film-coated 200 mesh nickel TEM grids (Ted Pella, Inc., Redding, CA) for STEM-EDS analysis. The collection of EDS elemental maps and linescans for was performed on a Thermo Fisher Titan Themis Cs-corrected microscope with an accelerating voltage of 200 kV (NanoScale Fabrication and Characterization Facility, Petersen Institute of NanoScience and Engineering, Pittsburgh, PA). Images were analyzed using Velox 2.13 was used for drift correction during acquisition and processing data. EDS elemental maps were post-filtered using Velox software using Gaussian blue.

6.2.7 Bright Field Transmission Electron Microscopy (BF-TEM)

Bright field imaging analysis for all samples was performed on a Hitachi H9500 Environmental TEM with an accelerating voltage of 300 kV (NanoScale Fabrication and Characterization Facility, Petersen Institute of NanoScience and Engineering, Pittsburgh, PA). The size distributions of the NPs were determined from TEM images of at least 200 NPs from various areas of the grid per experimental replicate using ImageJ 1.47d (National Institutes of Health, USA).

6.2.8 Powder X-Ray Diffraction (PXRD)

Purified samples of $Cu_{2-x}Se$ NPs, Au-, Ag-, Pt-, and Hg-containing composite NPs were lyophilized using a LabConco Freezone 6 Lyophilizer (Department of Chemistry, University of Pittsburgh) to obtain dry powders. The NP powders were packed in 0.50 mm capillary tubes (Hampton Research, Aliso Viejo, CA) and flame sealed for PXRD characterization. PXRD patterns were collected on a Bruker X8 Prospector Ultra (Department of Chemistry, University of Pittsburgh) at 45 kV, 0.65 mA equipped with a IµS micro-focus Cu Kα X-ray source ($\lambda = 1.54178$ Å) with a scan speed of 0.5 s/step from 12.00-108.00° with a step size of 0.02°. Pd-containing composite NPs were dropcasted on a glass microscope slide (Fisher Scientific) and characterized using a Bruker AXS D8 Discover XRD (NanoScale Fabrication and Characterization Facility, Petersen Institute of NanoScale and Engineering, Pittsburgh PA) at 40 kV, 40 mA for Cu Kα X-ray source (λ = 1.5406 Å) with a scan speed of 3 s/step from 20 to 80° with a step size of 0.02°. All spectra were baseline corrected with respect to the spectrum of the amorphous glass background.

6.2.9 X-Ray Photoelectron Spectroscopy (XPS)

Samples were prepared by drop casting an aliquot of purified NPs onto p-doped (boron) silicon wafers (University Wafer, Boston, MA) that had been cleaned for ultrahigh vacuum analysis. XPS spectra were obtained using an ESCALAB 250XI XPS with a monochromated, microfocused Al Kα X-ray source (Materials Characterization Laboratory, Department of Chemistry, University of Pittsburgh, PA) at a spot size of 500 μm. All samples were sputtered using Ar^+ ion at a beam energy of 4000 eV for 45 seconds prior to spectral collection to remove surface impurities. Survey and high-resolution spectra were collected with a pass energy of 150 and 50 eV and a step size of 1.0 and 0.1 eV, respectively. All spectra were charge referenced to adventitious carbon (284.8 eV) and fitted using Thermo Scientific Advantage software.

6.2.10 Ultraviolet-Visible-Near Infrared (UV-vis-NIR) Extinction Spectroscopy

The extinction spectra of $Cu_{2-x}Se$ NPs and Au-containing heterostructure NPs were collected using a Cary 5000 UV-vis-NIR spectrophotometer (Agilent, Inc., Santa Clara, CA). Purified NPs were suspended in 1 mL of D_2O and placed in 1 cm quartz cuvettes (Hellma, Inc., Plainview, NY). The spectra were recorded from 1800 nm to 300 nm at a scanning rate of 1010 nm/min, with a source and detector changeover occurring at 800 nm. Spectra were baseline corrected with respect to 1 mL of D_2O.

6.2.11 Calculating % Lattice Mismatch

The % lattice mismatch (*f*, reported in **Table 6.3**) can be calculated using the equation below:

Equation 6.1. Lattice Mismatch between $Cu_{2-x}Se$ and Depositing Metal Lattice

$$f = \frac{a_{host} - a_{guest}}{a_{host}}$$

where, a_{host} and a_{guest} are the lattice constants of $Cu_{2-x}Se$ and the secondary metal being added, respectively. **Table 6.1** below summarizes the lattice constant of $Cu_{2-x}Se$ extracted experimentally from PXRD data and each metal extracted from the CRC Handbook of Chemistry and Physics.[214] The lattice constant of Pd was extracted from their reference PXRD patterns obtained from the International Centre for Diffraction Data (ICDD).

Table 6.1. Lattice Constants of $Cu_{2-x}Se$ and Secondary Metals Used for Evaluating Lattice Mismatch.

Materials	Lattice Symmetry	Lattice Constants (Å)
$Cu_{2-x}Se$	Cubic	5.70
Au	fcc	4.078

Pt	fcc	3.923
Pd	fcc	3.890
Ag	fcc	4.086
Hg	Rhombohedral	3.00

6.2.12 Calculating % Volume Change

Similarly, the volume change (ΔV) can be calculated using the equation below:

Equation 6.2. Lattice Volume Change from $Cu_{2-x}Se$ to a New Metal Selenide Phase

$$\Delta V = \frac{V_{MSe} - V_{host}}{v_{host}}$$

where, V_{host} and V_{MSe} are the lattice volumes of the $Cu_{2-x}Se$ and the secondary metal selenides, respectively. The volumes of the secondary metal selenides are obtained from the PDF cards that matched experimental PXRD results or the metal selenides which were expected to be formed if the cation exchange process had taken place. **Table 6.2** below summarizes the lattice symmetry and lattice volumes of the metal selenides, and their corresponding % volume changes are summarized in **Table 6.3.**

Table 6.2. Lattice Symmetry and Volume of Secondary Metal Selenides and Their Corresponding PXRD References.

Metal Selenides	Lattice Symmetry	Lattice Volume (Å^3)	PDF Cards

$Cu_{2-x}Se$	Cubic	185.19	00-006-0680
AuSe	Hexagonal	79.23	01-071-4055
$PtSe_2$	Hexagonal	61.15	00-018-0970
$PdSe_2$	Orthorhombic	257.77	00-011-0453
Ag_2Se **CuAgSe**	Orthorhombic	237.58 105.42	00-024-1041 00-025-1180
HgSe	Cubic	225.31	00-008-0469
CuHgSe	Monoclinic	206.13	00-054-0988

6.3 Results and Discussions

In a typical experiment, we first synthesize water-dispersible $Cu_{2-x}Se$ NPs using a seed-mediated protocol (**Figure 6.1A**).[101] We chose $Cu_{2-x}Se$ NPs as our starting material for both its intrinsic structural features and its downstream optoelectronic properties. First, the $Cu_{2-x}Se$ system has an antifluorite crystal structure (**Figure 6.1B**, referenced to PDF # 00-006-0680),[96, 98] *i.e.* $Cu_{2-x}Se$ has an isotropic crystal structure which limits preferential secondary metal cation infiltration based on crystallographic directions.[215] Second, Cu atoms in the lattice are known to be mobile,[57, 95, 99] creating vacancy sites within the lattice that allow incoming cations to diffuse,[205, 216-217] while the Se lattice of metal chalcogenides is known to be relatively robust even under CE conditions.[215, 218-219] Finally, copper chalcogenides such as $Cu_{2-x}Se$ exhibit localized surface plasmon resonances (LSPRs),[57, 62, 98] which makes them an attractive class of earth-abundant plasmonic materials that can be implemented in applications such as light-driven sensing and catalysis.[55, 100, 114, 118, 173-174]

With these properties of $Cu_{2-x}Se$ NPs in mind, we then post-synthetically introduced five secondary metal cations and evaluated changes in $Cu_{2-x}Se$ NP composition and morphology.

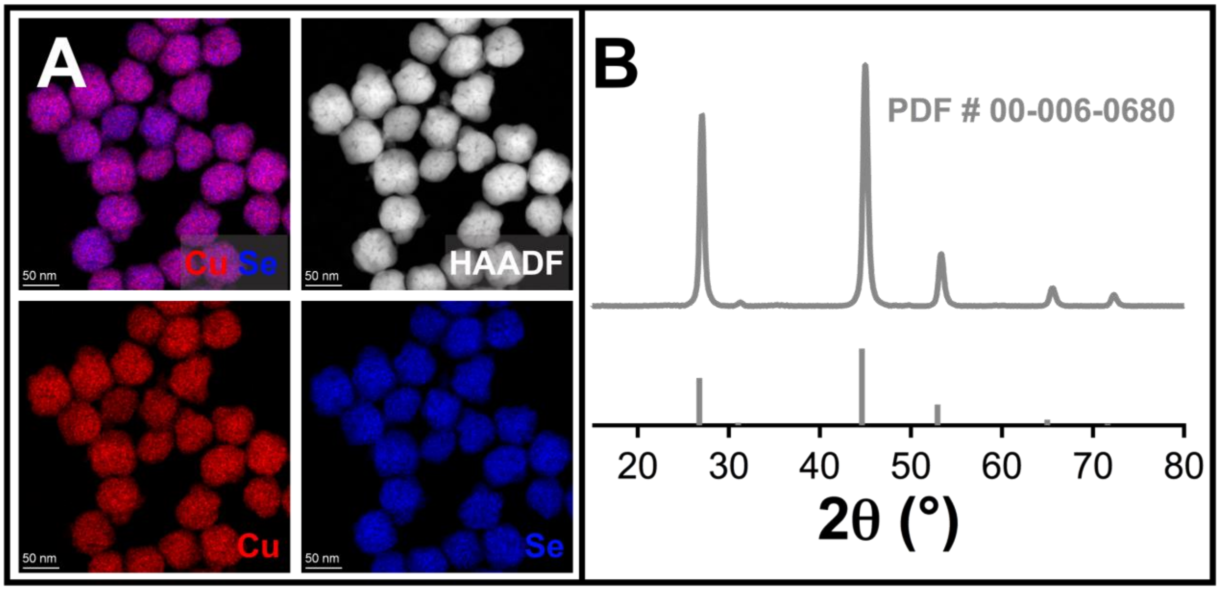

Figure 6.1. Representative STEM-EDS maps and HAADF images of $Cu_{2-x}Se$ NPs where Cu Kα signal is represented in red and Se Lβ signal is represented in blue (A) and PXRD of $Cu_{2-x}Se$ NPs referenced to PDF # 00-006-0680.

6.3.1 Secondary Metal Selection for Post-Synthetic Addition

In evaluating the driving forces behind obtaining a particular composite NP outcome (i.e., either CE or MD), we considered several possible variables when selecting the secondary metals to be used in our experiments, including lattice formation energy, lattice volume and symmetry change, ionic radii and solubility, metal cation reduction potential, and lattice mismatch between metal and $Cu_{2-x}Se$ (**Table 6.3**). For example, for reduction potentials, we selected metal cations that can all be reduced by a single mild reducing agent (here, ascorbic acid), because if a metal cation is too difficult to reduce (e.g., Sn, In, and Ir), the strength of the reducing agent used may introduce competing homogeneous nucleation processes alongside CE and MD possibilities in the presence of the $Cu_{2-x}Se$ NPs or not reduce at all in the presence of ascorbic acid.

Table 6.3. Summarized Metal Selenide and Metal Formation Guidelines from/on $Cu_{2-x}Se$ and Product Observed Experimentally

Cation Exchange (CE)	M-Se Lattice Symmetry	% Volume Change[a]	Metal Deposition (MD)	Reduction Potential (V SHE)[214]	Lattice Symmetry	% Lattice Mismatch[a]	Product Observed
$Cu_{2-x}Se$	Cubic	-	**$Cu_{2-x}Se$**	-	Cubic	-	**-**
HgSe	Cubic	+22	**Hg**	0.851	Rhombohedral	47	**CE**
$PdSe_2$	Orthorhombic	+39	**Pd**	0.591	fcc	32	**CE**
Ag_2Se **CuAgSe**	Orthorhombic	+28 -43	**Ag**	0.7996	fcc	28	**CE**
AuSe	Hexagonal	-57	**Au**	1.498	fcc	27	**MD**
$PtSe_2$	Hexagonal	-67	**Pt**	0.755	fcc	31	**MD**

[a]All values are calculated from their lattice constants provided either in the CRC Handbook of Chemistry and Physics[214] or their PXRD references and compared with Cu_2Se's lattice constant (5.7Å). See **Sections 0** and **6.2.12** for additional details.

For a MD process, it is also known that heterogeneous growth of a secondary metal on a solid substrate only occurs within a certain lattice mismatch range between the two components.[204, 209] Therefore, our selected metals also needed to exhibit lattice mismatches below 50% with $Cu_{2-x}Se$, such that an MD process would be feasible from this perspective. Here, the selected metals range from 27% (for Au metal) to 47% (for Hg metal) (**Table 6.3,** See **Section 0** for details on lattice mismatch calculations).

We then consider the range of ionic radii for the selected metal cations, which ideally would range from similar to the host $Cu^{1+/2+}$ to much larger ions (60 – 110 pm) while limiting to metal cations with a coordination number (CN) of 4,[214] to avoid further CE complications that could arise as reported elsewhere.[220] While the ionic radii and CN are considered when selecting the test metal cations, we note that there is some inherent heterogeneities in the valency of the metal cations as well as coordination geometry selected (e. g. Au, Pd and Pt salts are in a square planar geometry while others should adopt a tetrahedral geometry).

Next, we refer to lattice formation energies (ΔH_{latt}) of various metal selenides as well as their solubility constants (K_{sp}) to evaluate whether CE processes are favorable with $Cu_{2-x}Se$ as the starting material. As outlined by Manna, the general rule of thumb for determining whether or not the new metal selenide lattice will form is if its ΔH_{latt} is larger than that of Cu_2Se and its K_{sp} is less than that of the host lattice (*i. e.* the new metal selenide has a more stable lattice).[205]

Finally, we also sought a range of lattice volume changes and symmetry changes upon secondary metal selenide formation, exploring lattice volume changes ranging from 20 to 70% (see **Section 6.2.12**) and symmetry transitions from cubic $Cu_{2-x}Se$ to both crystal structure families with mutually orthogonal lattice vectors (cubic, tetragonal, and orthorhombic) and hexagonal symmetries (we note that the selenide compounds of the five metals chosen do have many other possible polymorphs theoretically accessible based on their reported bulk PXRD patterns.[221])

Taken together, after considering these (sometimes conflicting) variables, we identified a suite of five metal cations that gives us an acceptable range of metal cation valency, metal selenide lattice volume and symmetry changes, as well as feasible MD parameters such as cation reduction potential and metal-metal selenide lattice mismatches, that we could test: Au^{3+}, Ag^{+}, Hg^{2+}, Pd^{2+}, and Pt^{2+}.

With these strategically chosen metal cations in hand, we post-synthetically added ascorbic acid to the synthesized and purified $Cu_{2-x}Se$ NPs followed by each of the five metal cation aqueous solutions, at standard room temperature and pressure. (It is important to note that the addition of ascorbic acid is crucial to facilitate the reduction of metal cations, however the presence of ascorbic acid did not impact the pathway for CE outcome, which is evidence that the presence of a reducing agent is not the driving force for whether a metal undergoes CE or MD (*vide infra*).) Following the introduction of secondary metal cations, we used a variety of techniques to characterize the resulting particles including scanning transmission electron microscopy-energy X-ray dispersive spectroscopy (STEM-EDS) to evaluate the spatial distributions of Cu, Se, and secondary metals, powder X-ray diffraction (PXRD) to probe bulk crystallographic features, X-ray photoelectron spectroscopy (XPS) to determine the oxidation states of each element, and UV-vis-NIR extinction spectroscopy to monitor resulting optoelectronic properties.

6.3.2 Cation Exchange Outcomes for Hg, Pd, and Ag Addition to Cu$_{2-x}$Se

For Hg, Pd, and Ag metal addition we observe cation exchange products (Figure 6.2). Cation exchange of Hg2+ with Cu2-xSe was expected based on the crystallographic properties of HgSe, which exhibits a cubic lattice. The resulting lattice transformation from Cu would retain the cubic lattice and only impart a 22% volume expansion due to the infiltration of Hg2+ ions. As

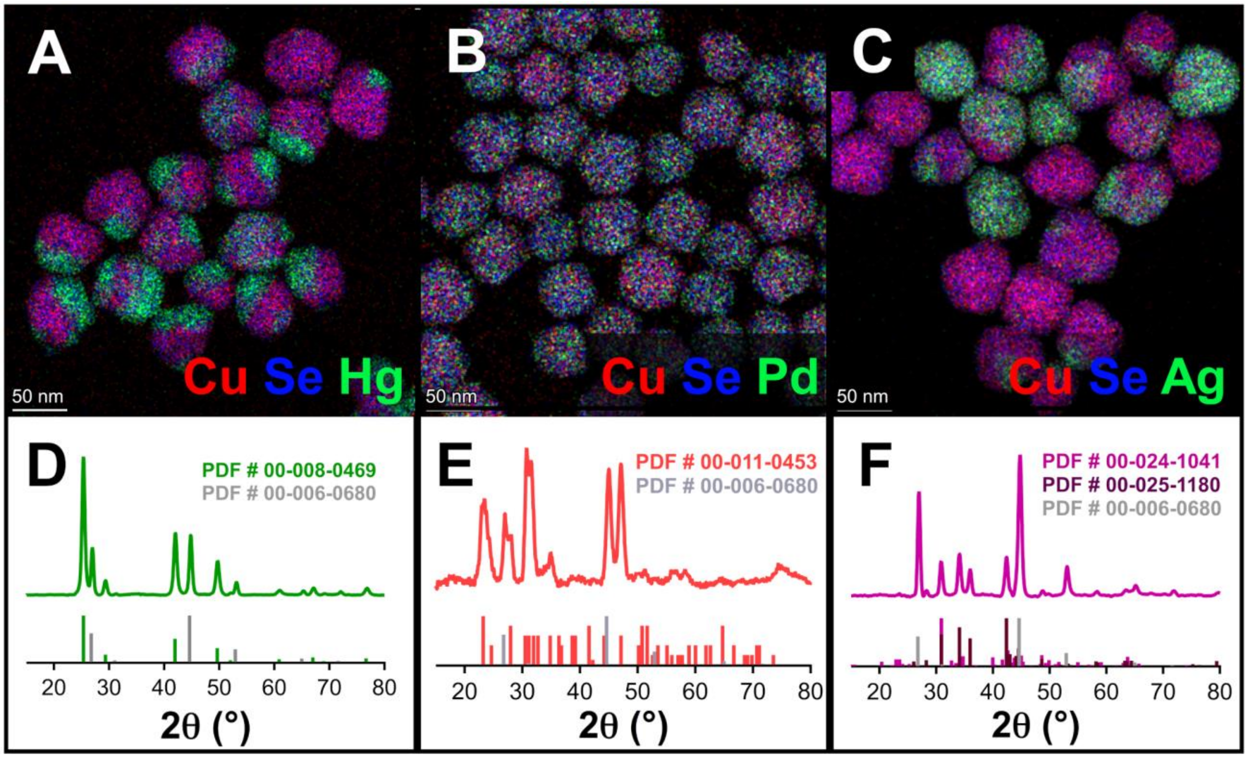

Figure 6.2. Representative STEM-EDS maps and PXRD mercury- (A, D), palladium- (B, E), and silver-containing CE composite NPs (C, F). Cu Kα and Se Lβ signals are represented in red and blue while all secondary metals (Hg Lα, Pd Lα, and Ag Lα) signals are in green. HAADF and individual elemental maps can be found in the Supporting Information. N.B. Any difference in contrast between maps should not be taken as quantitative. Included PXRD references are $Cu_{2-x}Se$ (PDF # 00-006-0680, grey), HgSe (PDF # 00-008-0469, green), $PdSe_2$ (PDF # 00-011-0453, red), Ag_2Se (PDF #00-024-1041, pink), and CuAgSe (PDF #00-025-1180, purple) are represented in vertical lines. See **Figure 6.21** and **Figure 6.23** for size distributions and NP population analyses.

indicated by STEM-EDS maps (**Figure 6.2A** and **Figure 6.3**), there are HgSe domains observed within the NP structure along with $Cu_{2-x}Se$. PXRD patterns (**Figure 6.2D**) confirmed the presence of both the original $Cu_{2-x}Se$ patterns (gray vertical lines) as well as HgSe (green vertical lines). In addition to the XRD reflections, XPS analysis is consistent with the presence of Hg^{2+} species at 99.8 ± 0.2 eV ($Hg4f_{7/2}$), which is within the reported range for HgSe (**Figure 6.4**).[222-224]

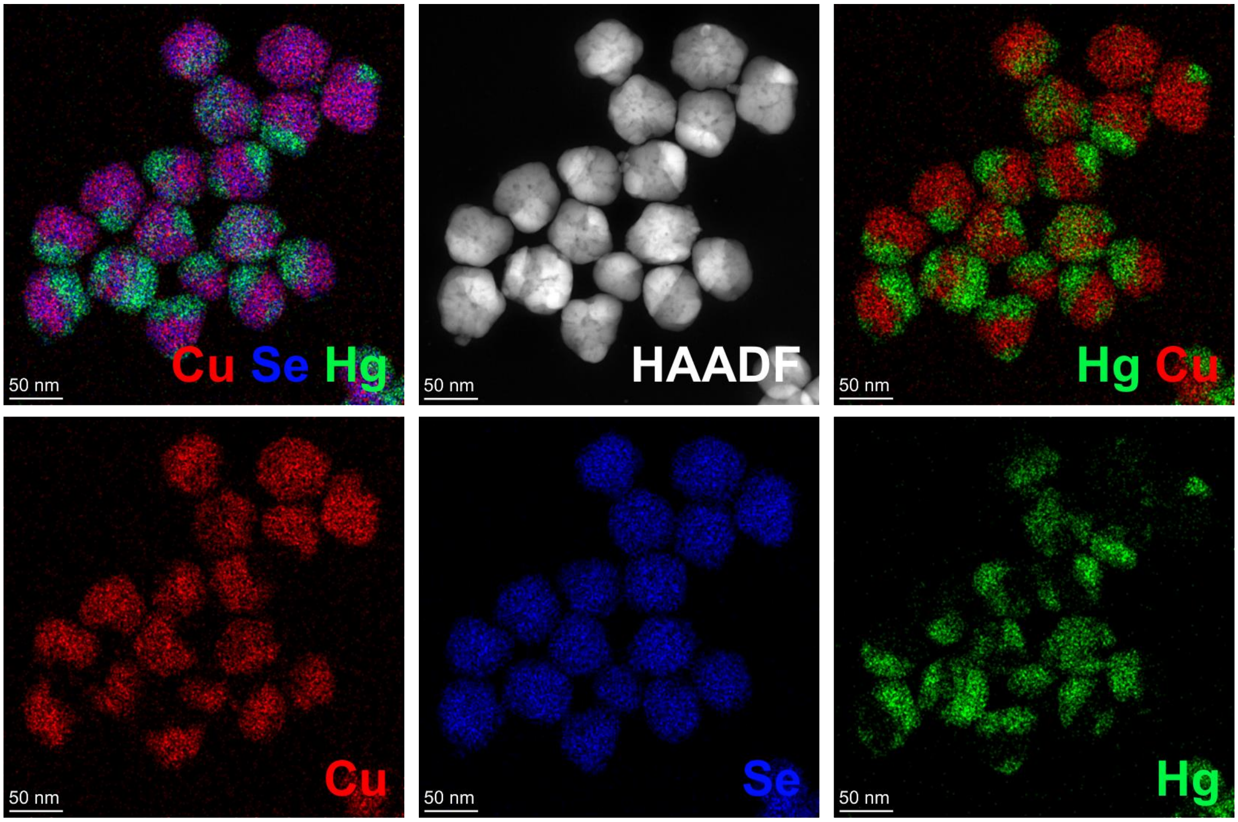

Figure 6.3. Representative STEM-EDS maps and HAADF images of $Cu_{2-x}Se$ NPs after post-synthetic addition of Hg, where Cu Kα, Se Lβ, and Hg Lα signals are represented in red, blue, and green, respectively.

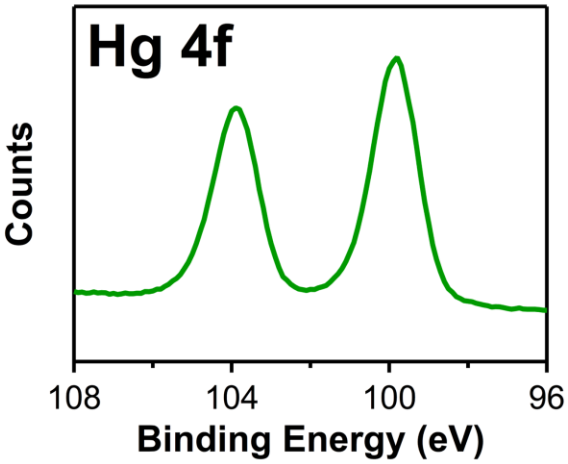

Figure 6.4. Hg 4f XPS spectrum of Hg-containing composite NPs, averaged across 4 experimental replicates.

Interestingly, although the existence of a ternary Cu_2HgSe_2 phase requires only an 11% lattice volume change, it is accompanied by a transition to a low-symmetry monoclinic structure, and we do not observe any evidence of this phase forming in the resulting particles (**Figure 6.5**). This lack of a CuHgSe ternary structure observed by STEM-EDS and PXRD indicates that lattice symmetry plays a key role in restricting CE outcomes, even in cases where lattice volume changes are small, and potentially deconvolutes the sometimes-concurrent influences of lattice symmetry and volume changes.

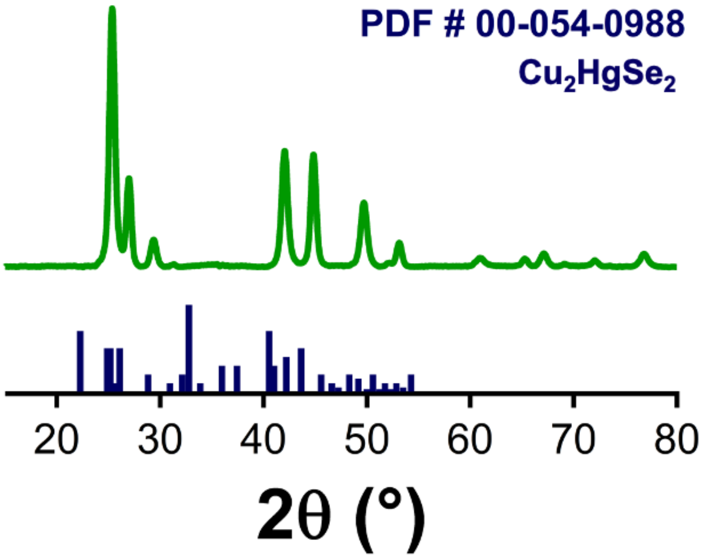

Figure 6.5. PXRD pattern of Hg-containing composite NPs showing lack of consistent match to monoclininc Cu_2HgSe_2 reference (PDF # 00-054-0988).

For Pd^{2+}, the formation of a $PdSe_2$ lattice would result in a 39% volume expansion, and a shift to an orthorhombic symmetry, where the lattice retains mutually orthogonal lattice vectors. STEM-EDS maps of Pd-containing samples (**Figure 6.2B** and **Figure 6.6**) indicate that Pd is incorporated homogenously throughout the particle, suggesting a CE process has occurred. (*N. B.* We were not able to make a definitive structural assignment of the Pd^{2+}-$Cu_{2-x}Se$ NP products. The PXRD of the resulting structures match an orthorhombic $PdSe_2$ reference (**Figure 6.2E**, red vertical lines), but also contain unidentified peaks that do not match either a pure metal, CuPd alloy, or other reported palladium selenide phase(s), **Figure 6.8**). Further, XPS confirms the presence of Pd^{2+} (Pd $3d_{5/2}$ = 336.3 ± 0.1 eV) and indicates a lack of metallic Pd^0 (**Figure 6.7**, see SI for additional analysis).[225] Importantly, to the best of our knowledge, this is the first demonstration of a crystalline Pd-containing ternary metal selenide nanomaterial successfully synthesized at room temperature and in aqueous conditions.

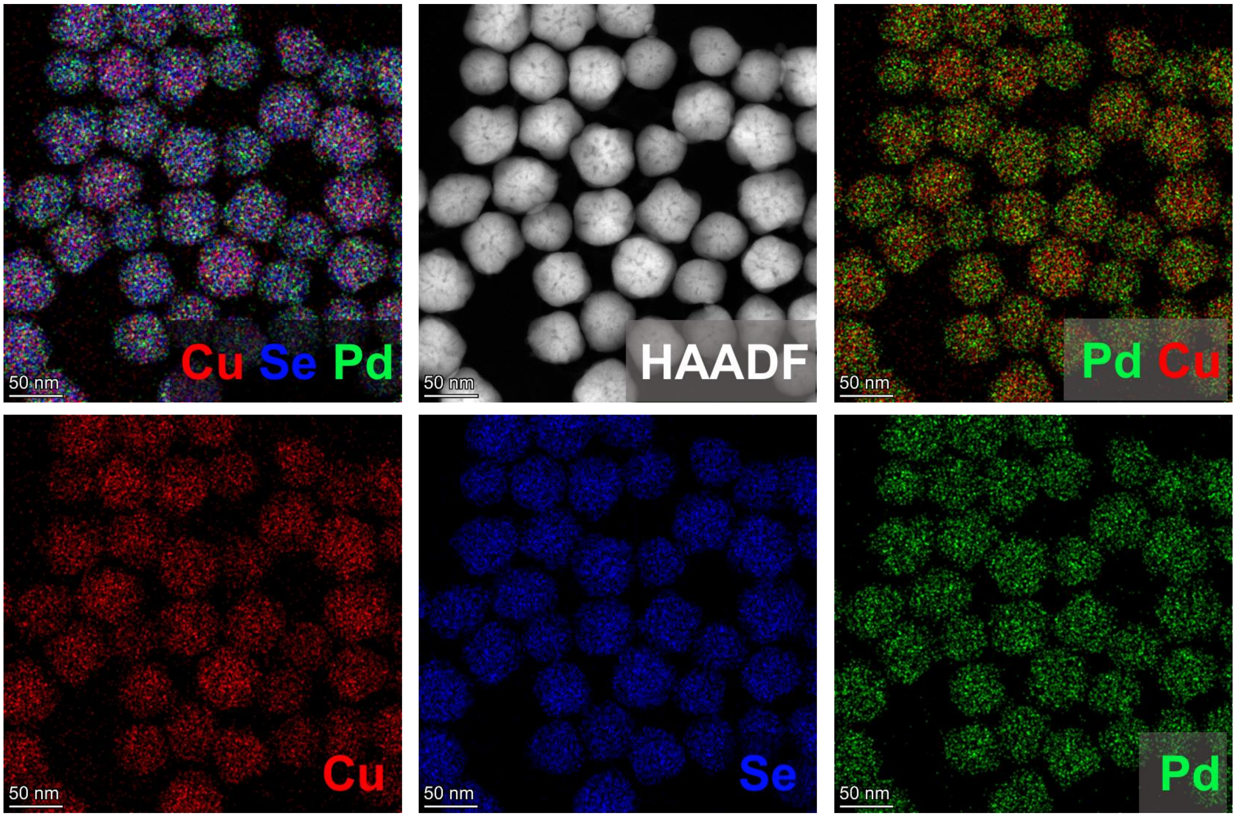

Figure 6.6. Representative STEM-EDS maps and HAADF images of $Cu_{2-x}Se$ NPs after post-synthetic addition of Pd, where Cu Kα, Se Lβ, and Pd Lα signals are represented in red, blue, and green, respectively.

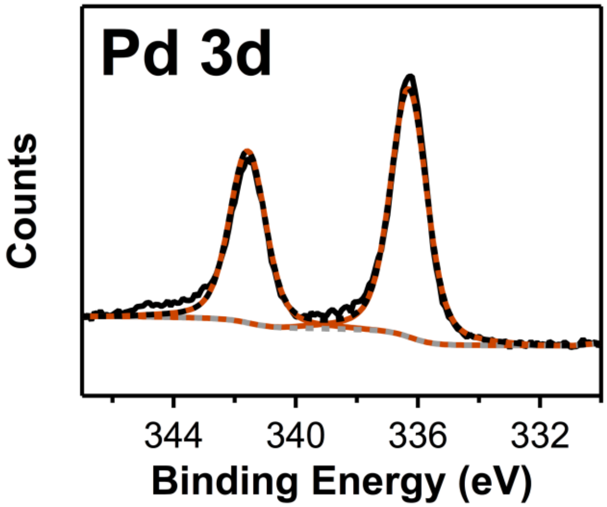

Figure 6.7. Deconvolutions of Pd 3d XPS spectrum of Pd-containing composite NPs, where solid and dotted black lines represent the raw and fitted spectrum, respectively. Fits include Pd^{2+} in orange, and the background is represented in light grey dotted lines.

Further analyzing the PXRD patterns of the Pd-containing $Cu_{2-x}Se$ cation exchange composite product, it is important to note that presence of peaks other than those that attribute to $Cu_{2-x}Se$ starting materials indicate that the products are not amorphous, unlike the report of an amorphous $CuPd_xS$ shell when Pd^{2+} were added to CuS nanodisks.[226] Further, our results do not seem to match other bulk CuPdSe ternary semiconductors as well (**Figure 6.8A**), indicating there may be a new and unreported metastable phase of $PdSe_2$ or CuPdSe ternary structure. While more structural analyses are needed to accurately assign the products, we believe that either a new $PdSe_2$ or CuPdSe phase, or a combination of the both are present in our particles. These XRD peaks do not match metallic Pd or CuPd either (**Figure 6.8B**), unlike a separate report where the formation of Pd MD product is observed.[227]

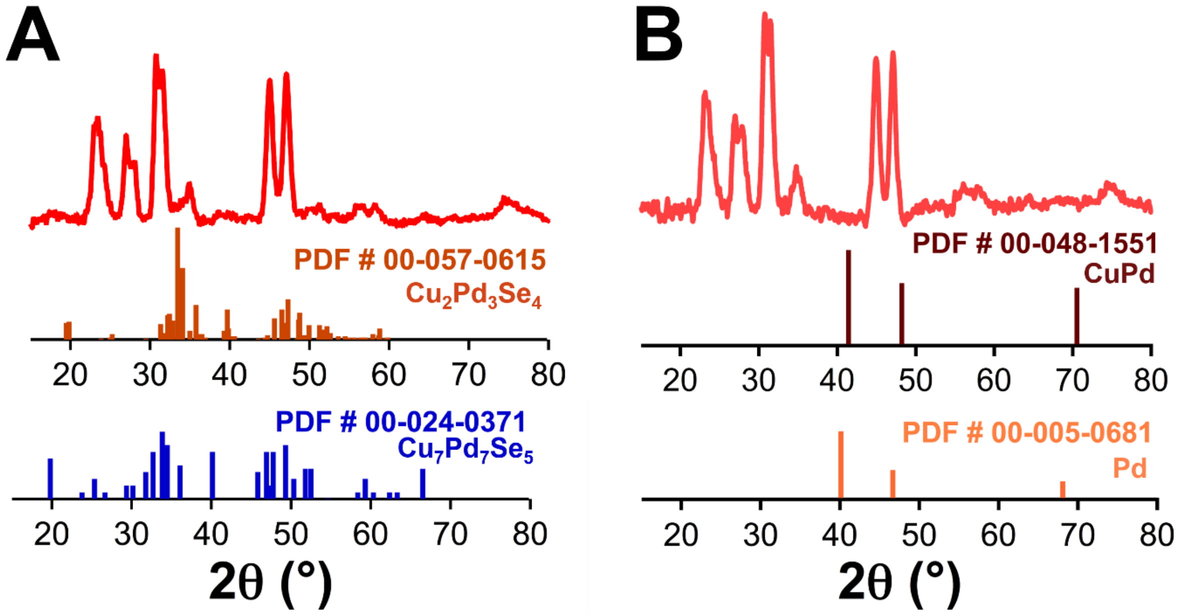

Figure 6.8. Representative PXRD of Pd-containing composite NPs showing lack of consistent matches to references $Cu_2Pd_3Se_4$ (PDF # 00-057-0615) and $Cu_7Pd_7Se_5$ (PDF # 00-024-0371) (A), and CuPd (PDF # 00-048-1551) and Pd fcc (PDF # 00-005-0681) (B).

Perhaps the most interesting observations come from comparing Hg^{2+} and Pd^{2+} to the addition of Ag^{+} ions, because Ag CE products would not be predicted based on parameters outlined by Manna and Jain.[205-206] First, the Ag^{+} ionic radius is larger than either Cu^{+} or Cu^{2+}, (as well as being the largest of the five cations we tested here), which according to previous summaries, would indicate that Ag^{+} would not be easily incorporated into the Se lattice. Additionally, while the lattice formation energy (ΔH_{latt}) of CuAgSe is unknown, the ΔH_{latt} of Ag_2Se is smaller than that of Cu_2Se, and further points toward either an MD product or no composite NP formation at all (*vide supra*).[205]

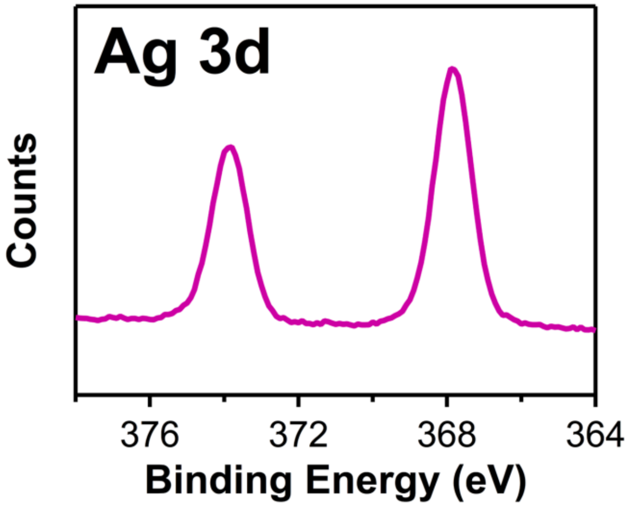

Figure 6.9. Ag 3d XPS spectrum of Ag-containing composite NPs averaged across 3 replicates.

From the MD product perspective, we would expect that Ag could easily be reduced and deposited on $Cu_{2-x}Se$ NPs due to a high reduction potential and low lattice mismatch between Ag fcc and $Cu_{2-x}Se$ (**Table 6.3**). However, post-synthetic addition of Ag^+ resulted in a CE reaction, where PXRD indicated the formation of both CuAgSe and Ag_2Se (**Figure 6.2F**). XPS findings confirm the identity of Ag in these samples to be in a 1+ oxidation state with an average $Ag3d_{5/2}$ binding energy of 367.9 ± 0.2 eV and the absence of any loss features (**Figure 6.9**).[228-229] Studying the elemental distribution of Ag using STEM-EDS, we find that Ag is not distributed homogenously throughout the particles (**Figure 6.2C** and **Figure 6.10,** *i.e.* each particle does not exhibit the same extent of CE with Ag^+), indicating that the CE process occurs cooperatively (*i.e.*, incoming ions prefer to infiltrate the same host NP).[205, 212, 230] Cooperativity in CE processes suggest that the guest cations diffuse quickly via the presence of vacancies in the host $Cu_{2-x}Se$ lattice. Although the parameters of Ag favor a MD product, the observation of a CE reaction suggests that lattice volume changes up to 43% are acceptable when lattice symmetries retain mutually orthogonal lattice vectors and outcompete the alternatively available MD process.

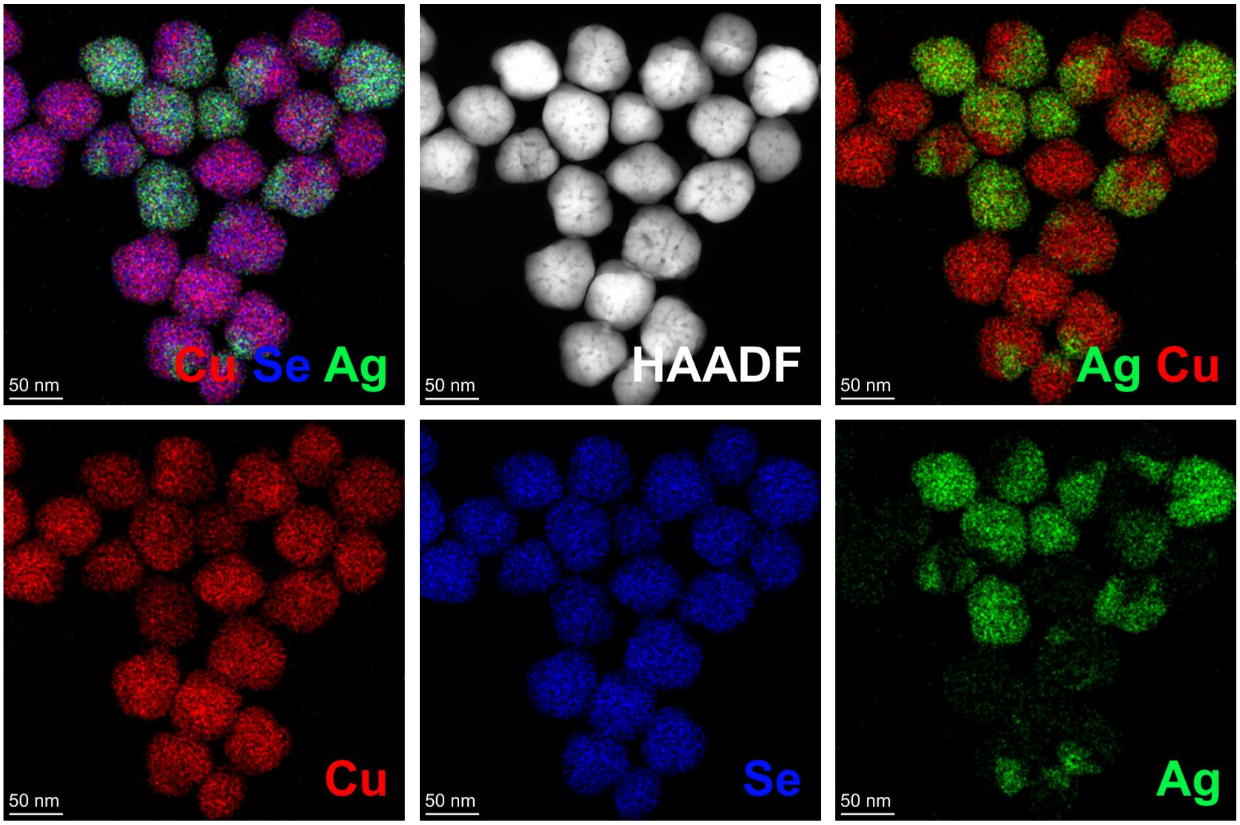

Figure 6.10. Representative STEM-EDS maps and HAADF images of $Cu_{2-x}Se$ NPs after post-synthetic addition of Ag, where Cu Kα, Se Lβ, and Ag Lα signals are represented in red, blue, and green, respectively.

When we examine the possible lattice volume changes associated with such a CE reaction, we expected only the presence of Ag_2Se since the formation of a Ag_2Se phase requires a lower volume change from Cu_2Se (28%) than to a ternary CuAgSe (43%). Yet, the presence of a CuAgSe phase indicates that it is possible to achieve this magnitude of lattice volume change as long as the lattice remains within the family of mutually orthogonal lattice vectors (both Ag_2Se and CuAgSe are orthorhombic), consistent with our previous report demonstrating that CuAgSe phase tends to be observed first during a partial CE process at low %Ag incorporation.[212]

6.3.2.1 Ag CE Products Form Regardless of Reduction Agent Strength

However, one may wonder if the preference for CE products over MD products in the Ag system are also a function of reducing agent concentration in the reaction mixture and/or the strength of the reducing agent used. To examine the influence of reducing agent concentration, we conduct Ag^+ addition with varying amounts of ascorbic acid, by changing the concentrations of ascorbic acid relative to a constant concentration $AgNO_3$, ranging from no ascorbic acid to 800 times excess with respect to $[Ag^+]$ (indicated here as “0x” to “800x”). Interestingly, at all concentrations tested not only is there no deposition of Ag metal, there is no observable change in morphologies observed for cooperative CE products (Figure 6.11A-E for STEM and Figure 6.11F for XRD).

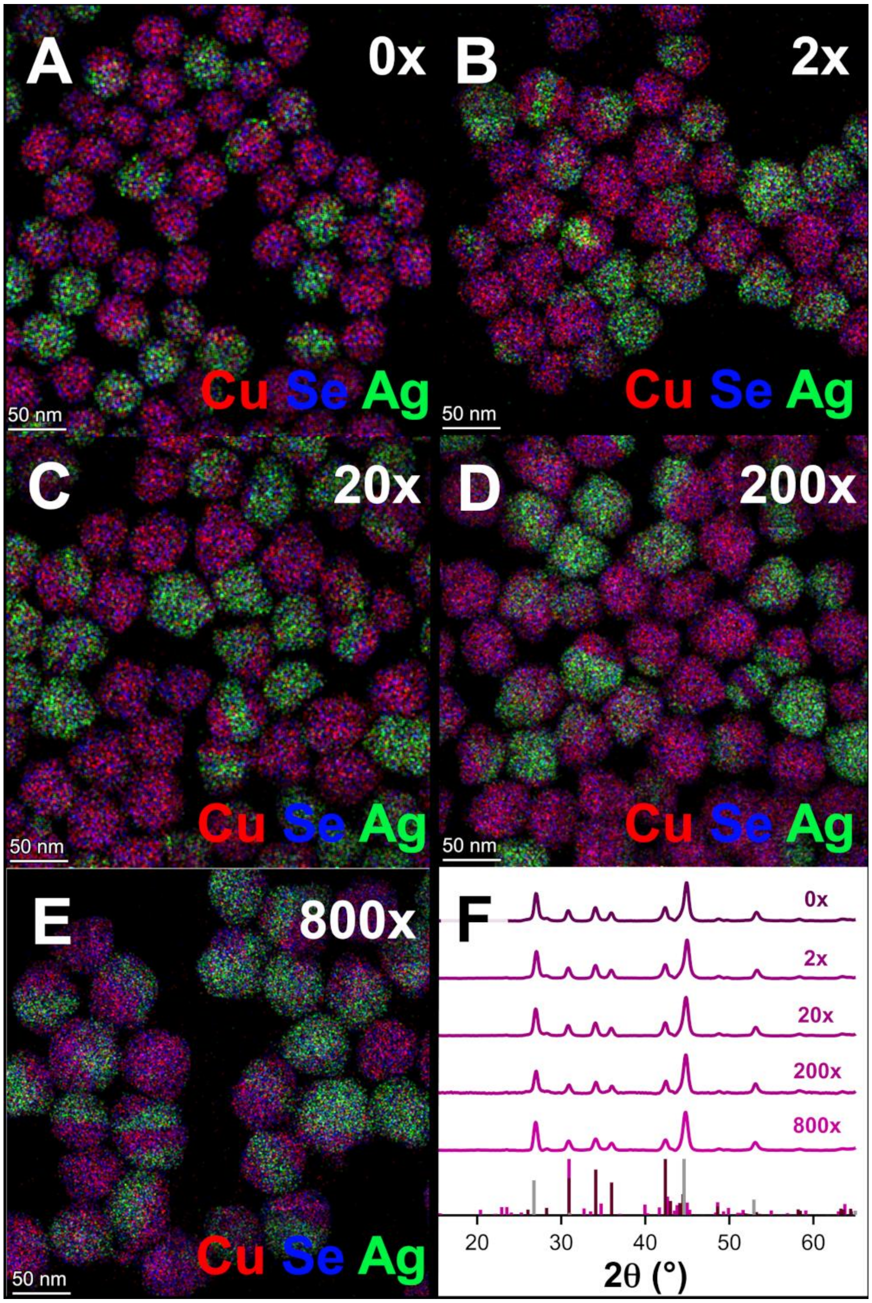

Figure 6.11. Representative STEM-EDS maps for cation exchanged Ag on $Cu_{2-x}Se$ NPs in the absence of ascorbic acid (A), and increasing amounts of ascorbic acid to Ag^+ ratio from 2:1 to 800:1 (B-E), and their corresponding PXRD patterns (F). Cu Kα, Se Lβ, and all secondary metal Lα signals are represented in red, blue, and green respectively. HAADF and individual elemental maps can be found in the Supporting Information. *N.B.* Any difference in contrast between maps

should not be taken as quantitative. Included PXRD references are $Cu_{2-x}Se$ (PDF # 00-006-0680, gray), Ag_2Se (PDF #00-024-1041, pink), and CuAgSe (PDF #00-025-1180, purple). See Figure 6.12 and Figure 6.13 for size distribution and NP population analyses.

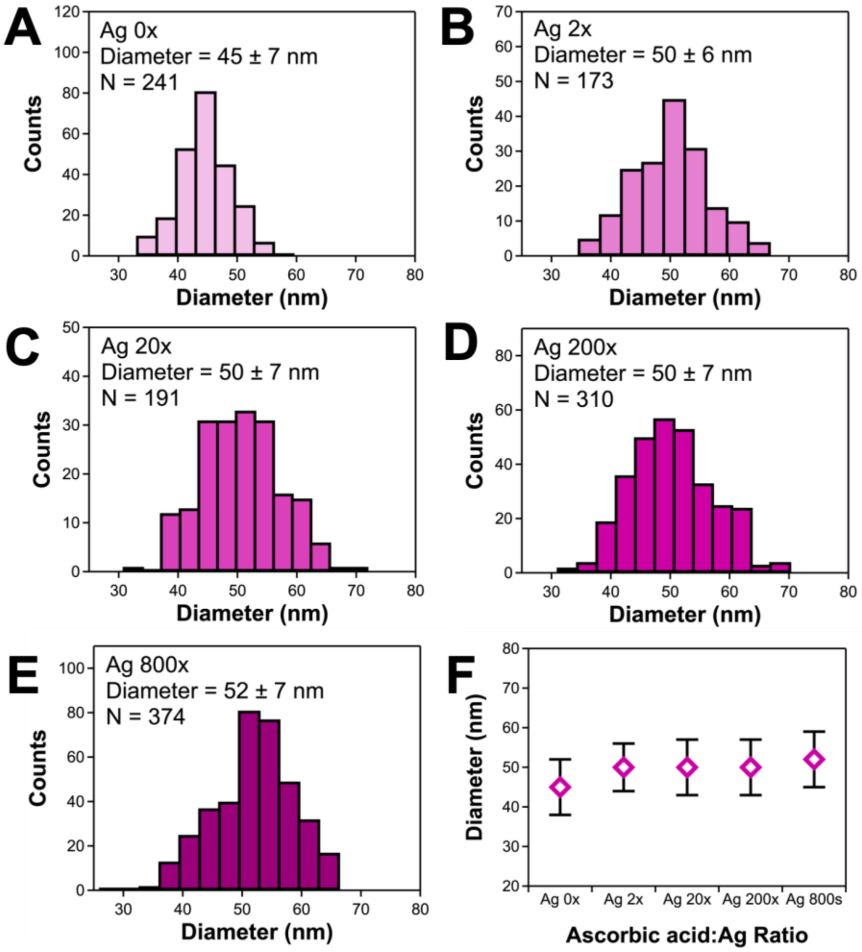

Figure 6.12. TEM-derived size distributions of $Cu_{2-x}Se$-containing domains in products after addition Ag salt at varying amounts of ascorbic acid:Ag concentration added, 0x, 2x, 20x, 200x, and 800x, respectively (A-E), and their size distribution comparisons (F), measured over 150 particles across at least 3 experimental replicates.

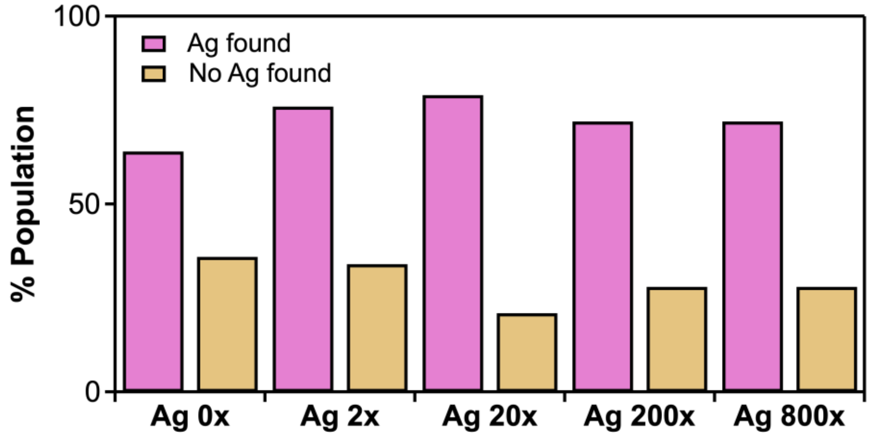

Figure 6.13. Populations of NPs containing the Ag added (blue) and without, indicating only "unperturbed" $Cu_{2-x}Se$ (yellow) at varying amounts of ascorbic acid:Ag concentration added, 0x, 2x, 20x, 200x, and 800x, respectively, measured over 150 particles across at least 3 experimental replicates.

Further, one could argue that a stronger reducing agent could be used in this reaction, such as sodium borohydride ($NaBH_4$),[231] and that this stronger reducing agent would then push the Ag^+ post-synthetic addition outcome from CE to MD products. To test this, we used 200x $NaBH_4$ in place of ascorbic acid during Ag^+ addition, but did not observe any Ag metal deposition (or CE incorporation) on the $Cu_{2-x}Se$ NPs. PXRD patterns of the purified products show only $Cu_{2-x}Se$ features, indicating that discrete Ag NPs were likely formed and removed during purification (**Figure 6.14**). When 800x $NaBH_4$ were used instead, the entire colloidal suspension degraded and fell out of solution immediately, likely due to polydispersed nucleation of agglomerated Ag NPs (since additional stabilizing ligands were not used in the reaction). These results suggest that the formation of CE products (vs. MD products) using Ag^+ are not a function of the strength and amount of reducing agent used, under the conditions studied here. Finally, an additional factor that could influence final morphology is the ratio of Ag^+ concentration to Cu concentration within the particle. However, based on a separate mechanistic study we reported previously, increases in $[Ag^+]$ added did not result in the formation of metallic Ag species. Instead, when Ag^+ concentrations were high, primarily Ag_2Se products are formed, indicating full CE conversion.[212] In other words, the amount of Ag added did not produce a transition from CE to MD products.

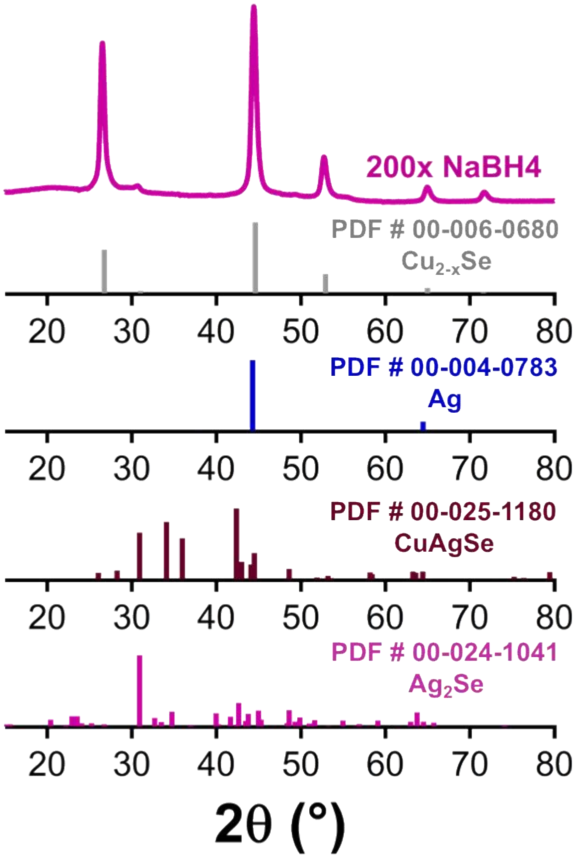

Figure 6.14. Representative PXRD of composite NPs prepared with post-synthetic additions of 200x $NaBH_4$ and $AgNO_3$, matching to references $Cu_{2-x}Se$ (PDF # 00-006-0680), Ag fcc (PDF # 00-004-0783), CuAgSe (PDF # 00-024-1180), and Ag_2Se (PDF # 00-024-1041).

6.3.3 Metal Deposition Outcomes for Au and Pt Addition to $Cu_{2-x}Se$

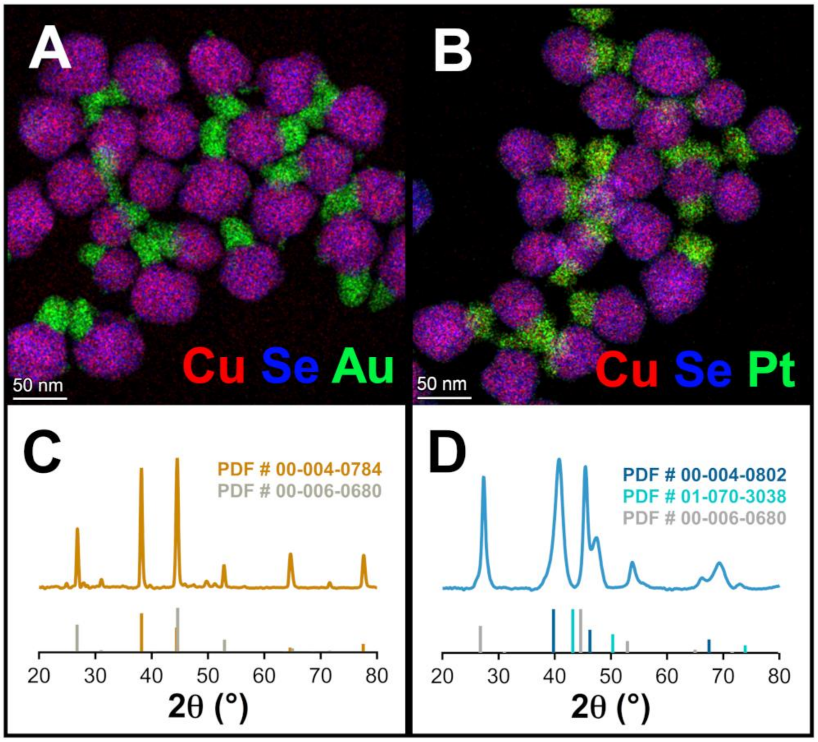

Figure 6.15. Representative STEM-EDS maps and PXRD for composite NPs containing gold (A, C) and platinum (B, D). Cu Kα, Se Lβ, and all secondary metal Lα signals are represented in red, blue, and green respectively. HAADF and individual elemental maps can be found in the Supporting Information. *N.B.* Any difference in contrast between maps should not be taken as quantitative. Included PXRD references are $Cu_{2-x}Se$ (PDF # 00-006-0680, gray) and Au (PDF # 00-004-0784, gold), Pt (PDF #00-004-0802, dark blue), and Cu (PDF # 01-070-3038, light blue). See Figure 6.21 - Figure 6.23 for size distributions and NP population analyses.

In contrast to Hg, Pd, and Ag metal cations, CE products are not observed with post-synthetic addition of Au or Pt precursors. AuSe and $PtSe_2$ lattices both have hexagonal crystal structures, and their corresponding lattice transformation would lead to a 57% and 67% volume contraction from $Cu_{2-x}Se$, respectively. Consistent with what we know from previous reports, a deformation and reconstruction of a relatively rigid Se framework would not be favorable at room temperature.[218-219] Indeed, instead of a CE product, due to the concomitant presence of a reducing agent, both Au and Pt salts heterogeneously nucleate discrete metallic phases on the $Cu_{2-x}Se$ NPs (See **Figure 6.15A** and **Figure 6.16** for Au and **Figure 6.15B** and **Figure 6.18** for Pt).

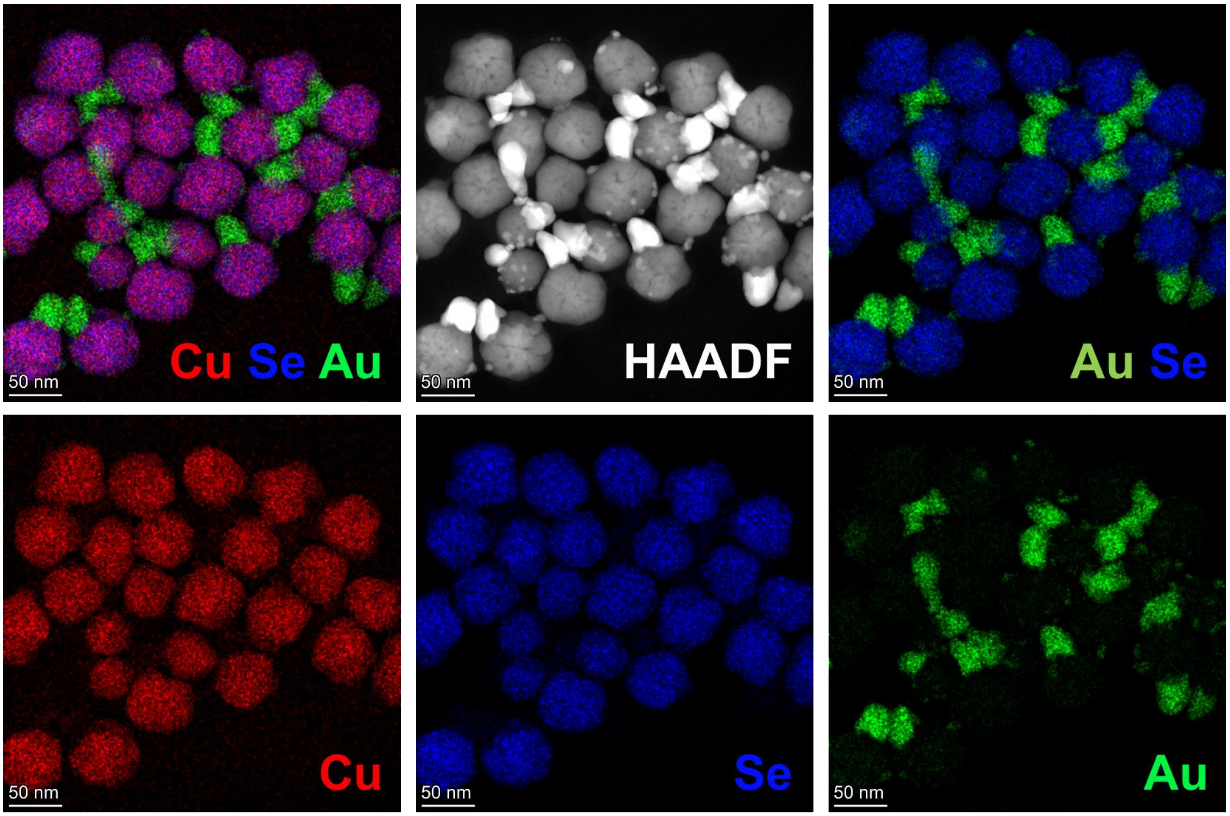

Figure 6.16. Representative STEM-EDS maps and HAADF images of $Cu_{2-x}Se$ NPs after post-synthetic addition of Au, where Cu Kα, Se Lβ, and Au Lα signals are represented in red, blue, and green, respectively.

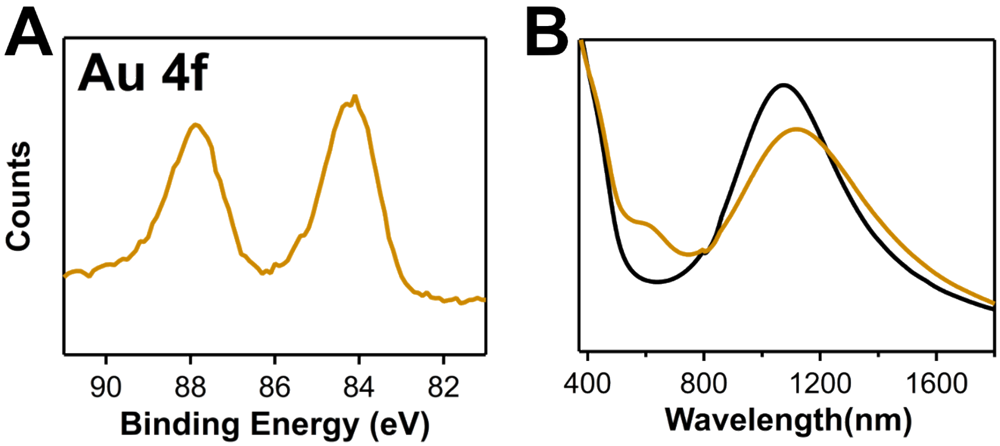

Figure 6.17. Averaged Au4f XPS spectrum (A) and representative extinction spectra of $Cu_{2-x}Se$ starting material (black) and Au-containing composite NPs (gold) in D_2O (B).

We confirm the presence of metallic Au species by PXRD (**Figure 6.16C**), XPS (**Figure 6.17A**), and extinction spectroscopy, by monitoring the presence of a Au LSPR at approximately 600 nm apart from the LSPR of $Cu_{2-x}Se$ near 1100 nm (**Figure 6.17B**).[169, 232-233] Interestingly, the PXRD pattern of Pt-containing products does not match entirely to pure Pt fcc (dark blue vertical lines). Instead, the peaks are broadened and shifted to higher 2θ towards Cu fcc (light blue vertical lines), indicating some degree of alloying between Cu and Pt in the external dendritic domains deposited on $Cu_{2-x}Se$ NPs (**Figure 6.16B**). This composition assignment is supported by STEM-EDS analysis (**Figure 6.19**). A similar observation was reported by Wolf et al., where CuPt alloyed domains were deposited to $Cu_{2-x}Se$.[234] To properly assign the XRD features, we use Vegard's Law to assess the composition of the CuPt alloy of our deposition product and assign the composition to be $CuPt_3$ (See **Section 6.3.3.1** for more details).[235-236] XPS also confirms the presence of a metallic Pt species (**Figure 6.20**).

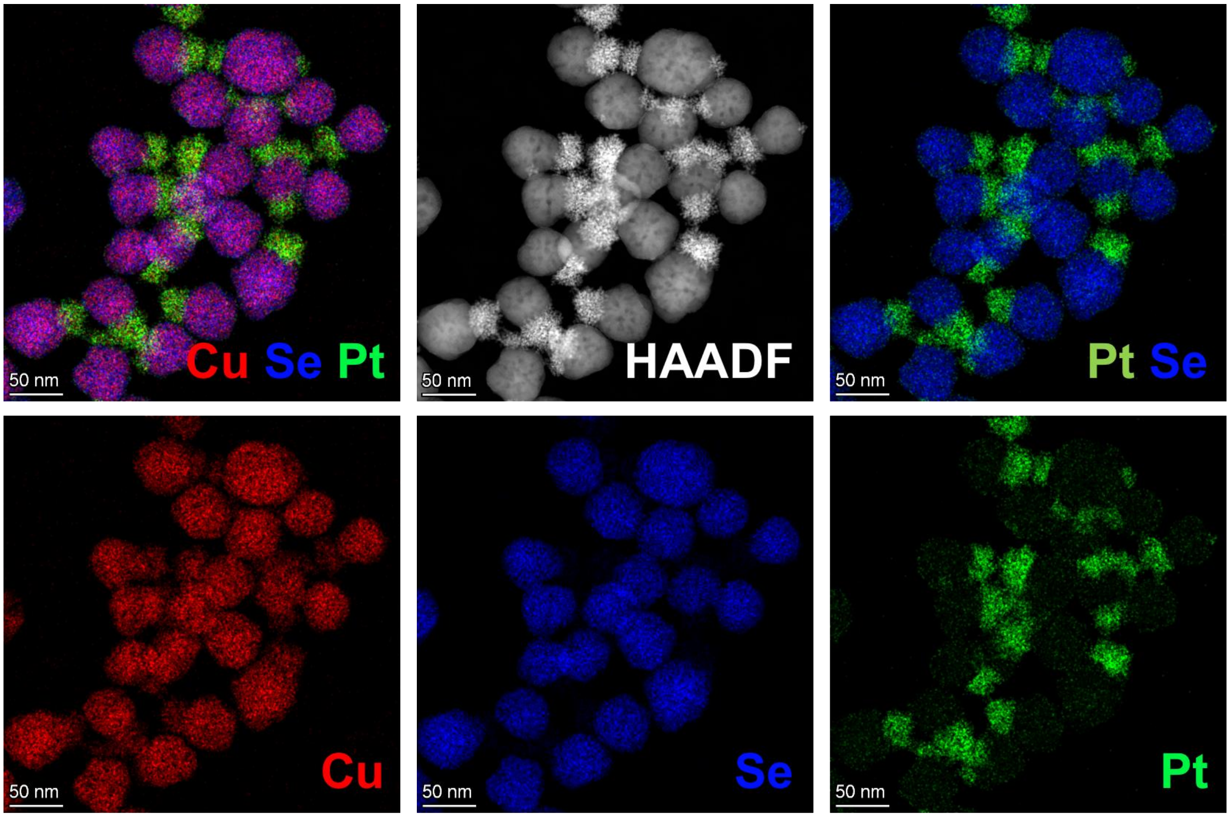

Figure 6.18. Representative STEM-EDS maps and HAADF images of $Cu_{2-x}Se$ NPs after post-synthetic addition of Pt, where Cu Kα, Se Lβ, and Pt Lα signals are represented in red, blue, and green, respectively.

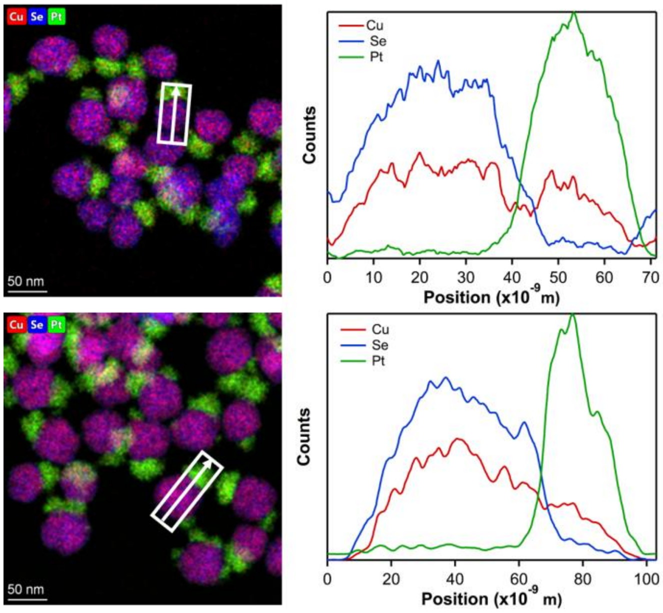

Figure 6.19. Representative STEM-EDS maps and two generated line scans of Pt-containing composite NPs. White box indicates the location used to extract line scan data, with the arrow head indicating the direction.

6.3.3.1 Determination of the Composition of Cu-Pt Alloy using Vegard's Law[235-236]

The lattice parameter of the Cu-Pt alloy (a_{Alloy}) formed on post synthetic modification was determined by using two peaks from the PXRD pattern (**Figure 6.15D**), which corresponded to the said alloy. The peaks at approximately 40° and 47° were chosen for this calculation as they lay matched up as a combination of the peaks from Cu and Pt (fcc structures) referencing (111) and (200) planes. Using the Braggs equation below[237]:

Equation 6.3. Determining Lattice Constants for CuPt Alloy

$$a_{Alloy} = \frac{\lambda\sqrt{h^2 + k^2 + l^2}}{2sin(\theta)}$$

where, λ is the X-ray source (λ= 0.154178 nm), h=k=l=1 for (111) and h=2, and k=l=0 for (200), the average a_{Alloy} was calculated to be 3.83 ± 0.01 nm, where the error represents the standard deviation of six values obtained from three replicates of the sample (getting two values for each replicate using the two aforementioned peaks).

Table 6.4. Lattice Constants of CuPt Alloy Measured Using Various PXRD Peaks Across 3 Experimental Replicates.

Replicate	h	k	l	2θ (°)	a_{Alloy} (nm)
Replicate 1	1	1	1	40.82	3.82
	2	0	0	47.36	3.83
Replicate 2	1	1	1	40.68	3.84
	2	0	0	47.12	3.85
Replicate 3	1	1	1	40.78	3.83
	2	0	0	47.42	3.83

From the averaged a_{Alloy} extracted previously, the composition of the Cu-Pt alloy was determined using Vegard's law in the equation below:

Equation 6.4. Vegard's Law to Determine Cu:Pt

$$a_{Alloy} = xa_{Pt} + (1 - x)a_{Cu}$$

where, a_{alloy} is the lattice constant of the Cu-Pt alloy and x denotes the molar fraction of Pt in the alloy. The x value was determined to be 75%, which we then subsequently assign the composition of the alloy to be $CuPt_3$.

6.3.3.2 Deconvolution of Pt 4f XPS Scan

To determine the oxidation state of the Pt species, XPS Pt4f$_{7/2}$ features also detects the presence of metallic Pt(0) at 71.4 ± 0.1 eV averaged across 4 experimental replicates. Additionally, there is also presence of a shoulder near ~72.5 eV, indicating a presence of an oxidized Pt species (**Figure 6.20**). Similar observations on Pt_3Cu nanopolyhedra have been reported by Sun et al., as well, where the authors attributed the oxidized Pt species observed to dangling bonds of the surface Pt.[238-239] Because the Pt_3Cu domains in our systems may have more Pt atoms on the surface due to their dendritic structures (vide supra, **Figure 6.18**), and consistent with the broadened XRD peaks (**Figure 6.15**) due to smaller crystallite size, we postulate that the dendritic formation leads to the presence of a higher population of surface Pt species as observed by XPS than what has been previously reported in other CuPt alloy NPs.

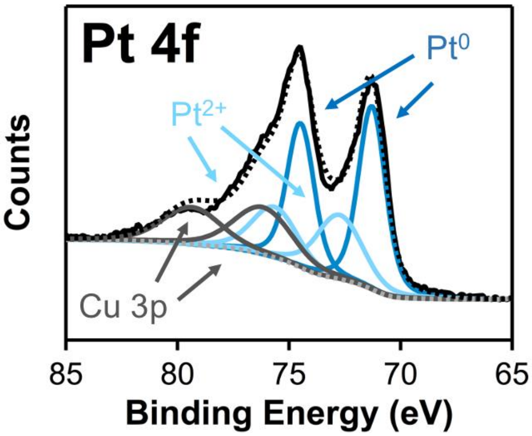

Figure 6.20. Deconvolutions of Pt 4f XPS spectrum of Pt-containing composite NPs, where solid and dotted black lines represent the raw and fitted spectrum, respectively. Fits include Pt^0 in dark blue, Pt^{2+} in light blue, and overlapping Cu3p spectrum in gray, and the background is represented in light grey dotted lines.

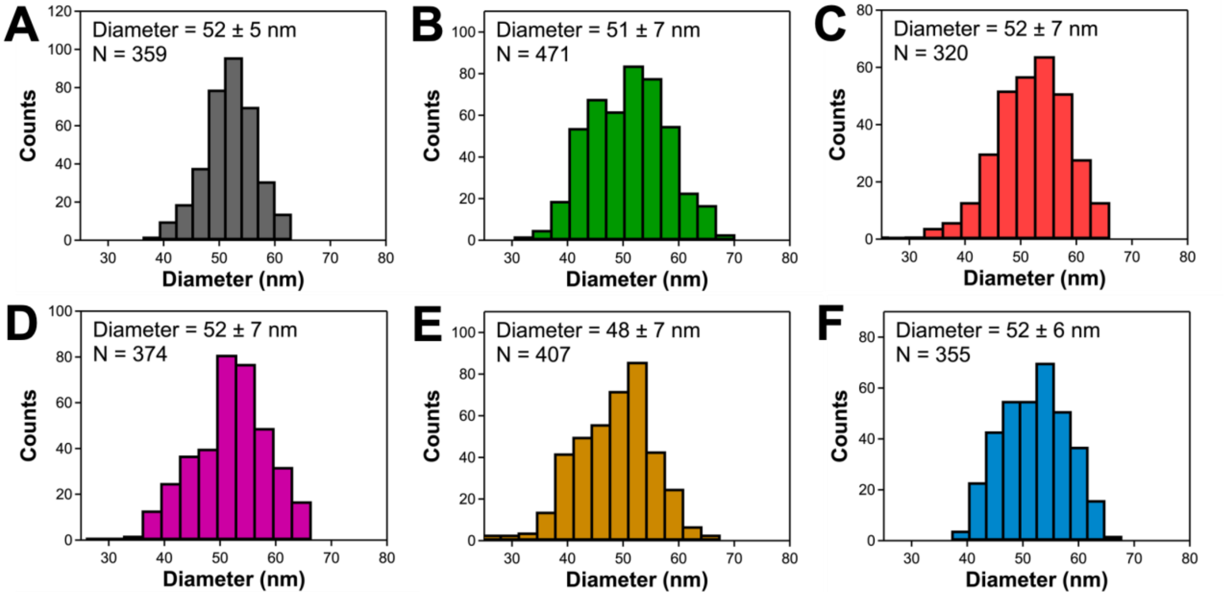

Figure 6.21. TEM-derived size distributions of $Cu_{2-x}Se$ starting material (A) and $Cu_{2-x}Se$-containing domains in products after addition of Hg, Pd, Ag, Au, and Pt salts (B-F), measured over 300 particles across at least 3 experimental replicates.

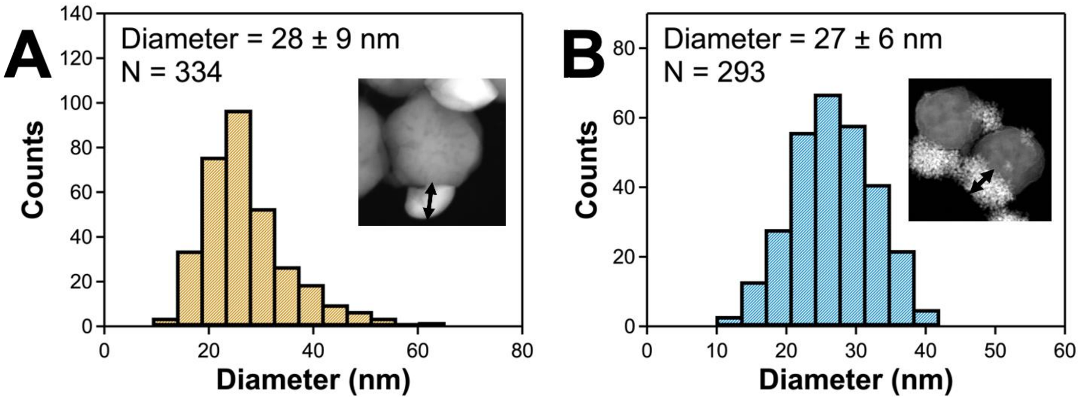

Figure 6.22. TEM-derived size distributions of Au and Pt island domains deposited on $Cu_{2-x}Se$ NPs, where they represent length extending from $Cu_{2-x}Se$ host to the edge of the island domains.

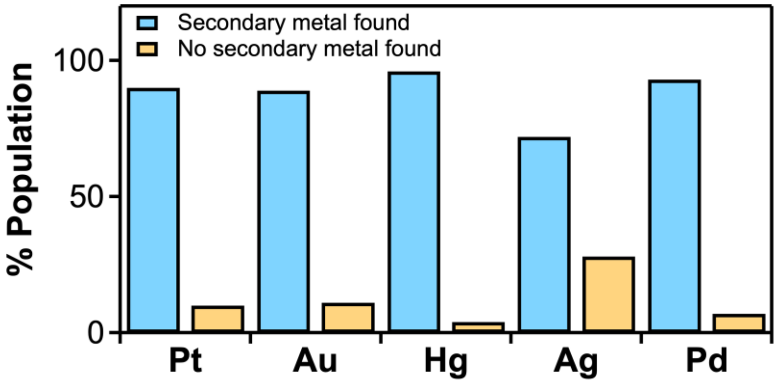

Figure 6.23. Populations of NPs containing the secondary metals added (blue) and without, indicating only "unperturbed" $Cu_{2-x}Se$ (yellow), measured over 300 particles across at least 3 experimental replicates.

6.3.3.3 Metal Deposition Product Not A Function of Phase Segregation Over Time

One could also argue that the formation of Au- and Pt-$Cu_{2-x}Se$ heterostructures are of a function of phase segregation over time, where the Au and Pt elements are originally present within the $Cu_{2-x}Se$ NPs that later migrate outward to achieve a more energetically favorable product. To evaluate this possibility, we performed the post synthetic addition of Au and Pt, and immediately halted the reaction upon metal cation addition by dilution the reaction medium and purifying the products via centrifugation. To confirm that the reaction can be halted by dilution, we performed a control experiment where the reaction media were diluted by 4 times and monitored the reaction via UV-vis-NIR spectroscopy across 12 hours. We did not see an emergence of the Au LSPR until 12 hours later, confirming our assumption (**Figure 6.24A**). By using both TEM and UV-Vis-NIR extinction spectroscopy, we observed the formation of both Au- and Pt-containing heterostructures immediately upon metal additions (**Figure 6.24B**, **Figure 6.24C**, **Figure 6.25**; *N.B.* Pt NPs do not have observable LSPR, hence extinction plots were not used to monitor the reaction[240]). Importantly, these observations confirm that the MD products were not a function of phase segregation that occurs over time to achieve the thermodynamically stable products, but instead are present instantaneously.

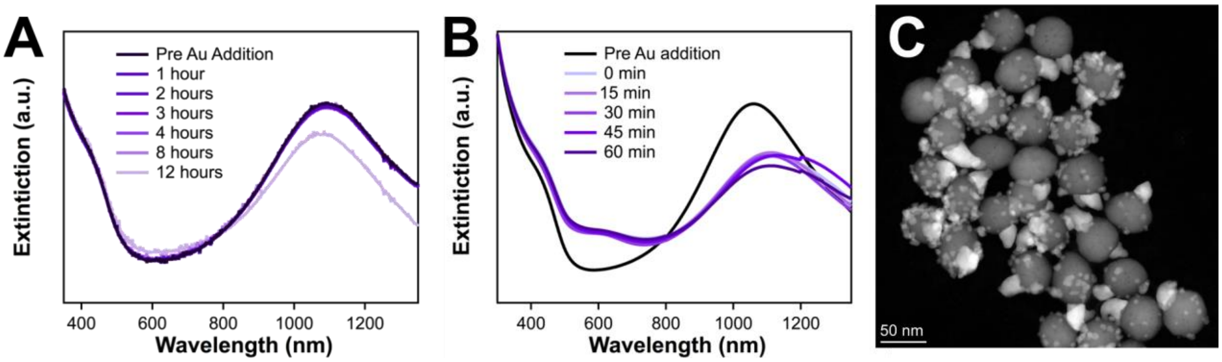

Figure 6.24. Extinction spectra of diluted Au- and $Cu_{2-x}Se$-containing solution measured over 12 hours as a control (A) and aliquots of Au-added to $Cu_{2-x}Se$ NPs purified at times listed (B). Representative HAADF image of Au aliquot arrested immediately upon Au^{3+} addition (t = 0 minutes) (C).

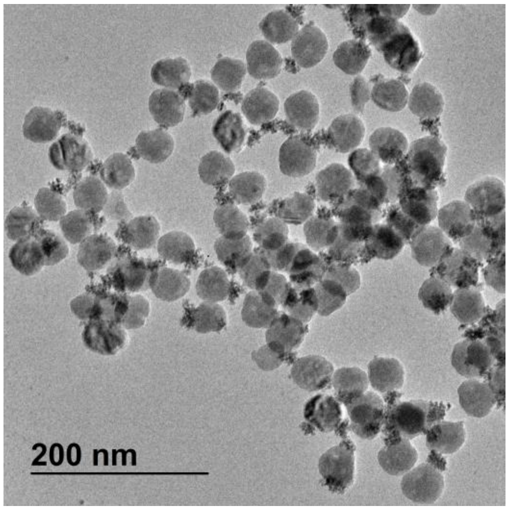

Figure 6.25. Representative BF TEM image of Pt aliquot arrested immediately upon Pt^{2+} addition (t = 0 minutes).

6.4 Conclusion

We have established a straight-forward post-synthetic modification design rule analogous to the Hume-Rothery design rules to prepare metal-semiconductor and semiconductor-semiconductor multicomponent materials using an isotropic crystal lattice substrate. Here, if a lattice retains a symmetry containing mutually orthogonal lattice vectors, CE products are preferred. If the lattice symmetry change extends outside of this family of crystal structures, a MD product is favored under the conditions defined here. Taken together, these results bridge a synthetic knowledge gap between CE and MD reaction pathways using material-specific fundamental properties that are, by definition, independent of environment-sensitive reaction parameters. This connection provides an important step forward for the rational design and implementation of technologically-relevant, earth-abundant composite heterostructures, and points toward the possible discovery of other such directing parameters in nanomaterials syntheses.

Appendix A Statistical Analysis using ANOVA

Single factor analysis of variance (ANOVA) was performed using Microsoft Excel 2017 Analysis ToolPak to determine the statistical significance between the difference in various parameters measured for $Cu_{2-x}Se$ NPs as described in **Chapter 4.0**. This method is used to assess whether multiple populations have the same mean by comparing the variation between the means of multiple samples to the variation within each sample.[241-242] For example, the null hypothesis for this experiment is that NP diameters measured between 3 sample populations are the statistically the same. Here, we use two figures of merit to determine if our sample populations are statistically the same. First, if the p value is larger than a given confidence level, a (in this case, 95%, α = 0.05), then the null hypothesis cannot be rejected. Next, if the value (denoted F) produced by this sample is below a critical value (denoted $F_{critical}$) for a given confidence level ($\alpha = 0.05$), the means of each population are *statistically the same*.

Appendix A.1 Statistical Analyses of $Cu_{2-x}Se$ NP Diameters

The ANOVA derived parameters for $Cu_{2-x}Se$ (x = ~0.6 and ~0.2) for three NP diameters at each stoichiometry (in other words, the results of the ANOVA analysis to see whether the three diameters at each stoichiometry are statistically distinct from one another), each with 5 independent replicates were derived and summarized in the table below:

Table A.1. Statistical Analysis Summary of NP Size as a Function of PVP Concentration for Both $Cu_{2-x}Se$ (x = ~0.6) and (x = ~0.2).

NP diameter as a function of [PVP] used	**$Cu_{2-x}Se$ (x = ~0.6)**	**$Cu_{2-x}Se$ (x = ~0.2)**
p value	< 0.01	< 0.01
F	56.1	247.0
$F_{critical}$	3.885	3.885
Results	**Statistically different**	**Statistically different**

Based on these values, we can reject the null hypothesis and conclude that the NP diameters measured for $Cu_{2-x}Se$ (x = ~0.6) NPs synthesized in 5 mM, 15 mM, and 30 mM 3.5 kDa PVP concentrations are statistically different. Similarly, we can reject the null hypothesis and conclude that the NP diameters measured for $Cu_{2-x}Se$ (x = ~0.2) NPs synthesized in 5 mM, 10 mM, and 15 mM 3.5 kDa PVP concentrations *are statistically different*.

Appendix A.2 Statistical Analyses of $Cu_{2-x}Se$ Carrier Densities

Single factor analysis of variance (ANOVA) was performed using Microsoft Excel 2017 Analysis ToolPak to determine the statistical significance between the difference in carrier densities measured for either $Cu_{2-x}Se$ (x = ~0.6) or $Cu_{2-x}Se$ (x = ~0.2) NPs at three representative sizes as described in **Chapter 4.0**. The ANOVA derived parameters for carrier densities of $Cu_{2-x}Se$ (x = ~0.6 and ~0.2) NPs with 3 representative sizes, each with 5 independent replicates were derived and concluded to be *statistically the same*, summarized in the table below:

Table A.2. Statistical Analysis Summary of NP Carrier Density as a Function of Size for both $Cu_{2-x}Se$ (x = ~0.6) and (x = ~0.2).

Carrier densities as a function of size	**$Cu_{2-x}Se$ (x = ~0.6)**	**$Cu_{2-x}Se$ (x = ~0.2)**
p-value	0.29	0.16
F	1.373	2.106
$F_{critical}$	3.885	3.806
Result	**Statistically the same**	**Statistically the same**

However, comparing the ANOVA derived parameters for carrier densities between $Cu_{2-x}Se$ (x = ~0.6) and $Cu_{2-x}Se$ (x = ~0.2) NPs, we conclude that the carrier densities measured for samples between $Cu_{2-x}Se$ (x = ~0.6) and $Cu_{2-x}Se$ (x = ~0.2) are *statistically different* summarized in the table below:

Table A.3. Statistical Analysis Summary of Carrier Densities as a Function of Cu:Se Ratio for 3 NP Size Ranges.

Carrier density as a function of Cu:Se ratio	**Small**	**Medium**	**Large**
p-value	< 0.01	< 0.01	< 0.01
F	103.02	146.4	385.4
$F_{critical}$	5.318	5.117	5.318
Result	**Statistically different**	**Statistically different**	**Statistically different**

Appendix A.3 Statistical Analyses of $Cu_{2-x}Se$ Molar Extinction Coefficients

Single factor analysis of variance (ANOVA) was performed using Microsoft Excel 2017 Analysis ToolPak (vide supra) to determine the statistical significance between the difference in molar extinction coefficients measured between 3 representative sizes for $Cu_{2-x}Se$ (x = ~0.6) and $Cu_{2-x}Se$ (x = ~0.2) NPs as described in **Chapter 4.0**. The ANOVA derived parameters for molar extinction coefficients of $Cu_{2-x}Se$ (x = ~0.6 and ~0.2) NPs as a function of 3 representative sizes, each with 5 independent replicates were derived and summarized in the table below:

Table A.4. Statistical Analysis Summary for Molar Extinction Coefficients Measured as a Function of NP Size for Both $Cu_{2-x}Se$ (x = ~0.6) and (x = ~0.2).

Molar ext. coeff. as a function of NP size	**$Cu_{2-x}Se$ (x = ~0.6)**	**$Cu_{2-x}Se$ (x = ~0.2)**
p-value	< 0.01	< 0.01
F	128.1	147.3
$F_{critical}$	4.256	4.103
Result	**Statistically different**	**Statistically different**

Based on these values, we conclude that the molar extinction coefficients measured for $Cu_{2-x}Se$ (x = either ~0.6 and ~0.2) between different NP sizes are *statistically different*.

However, comparing the ANOVA derived parameters for molar extinction coefficients between $Cu_{2-x}Se$ (x = ~0.6) and $Cu_{2-x}Se$ (x = ~0.2) NPs, each with 5 independent replicates for each size ranges, were derived and summarized in the table below:

Table A.5. Statistical Analysis Summary for Molar Extinction Coefficients Measured as a Function of Cu:Se Ratio for 3 NP Size Ranges.

Molar ext. coeff. as a function of Cu:Se ratio	**Small**	**Medium**	**Large**
p-value	0.620	0.013	< 0.01
F	0.266	9.402	28.684
$F_{critical}$	5.318	5.117	5.318
Result	**Statistically different**	**Statistically different**	**Statistically the same**

Based on these values, we conclude that the molar extinction coefficients measured for $Cu_{2-x}Se$ (x =~0.6) and (x=~0.2) between different NP sizes are *statistically different*. Therefore, 2 distinct fits were performed on the power functions described in **Sections 4.3.5** and **4.3.6**.

Appendix B Derivation of Extinction Coefficient Dependence on NP Carrier Density

All equations and derivations are acquired from references [1, 49, 55, 60, 95, 103, 107, 111]. The size dependence of the molar extinction coefficients for both $Cu_{2-x}Se$ (x = ~0.6) and (x = ~0.2) can be expressed as follow:

$$Ext_{LSPR}(\omega) = 4\pi R^3 k(\varepsilon_m)^{\frac{1}{2}} Im\left\{\frac{\varepsilon_p(\omega) - \varepsilon_m}{\varepsilon_p(\omega) + 2\varepsilon_m}\right\}$$

where Ext_{LSPR} is the molar extinction coefficients of $Cu_{2-x}Se$ NPs, R is the NP radius, k is the wavevector of the incident light, ε_m is the dielectric constant of the surrounding medium (water), and $\varepsilon_p(\omega)$ is the dielectric functions of $Cu_{2-x}Se$ NPs. The slope (a) of this power function can be summarized as follow:

$$a = 4\pi k(\varepsilon_m)^{\frac{1}{2}} Im\left\{\frac{\varepsilon_p(\omega) - \varepsilon_m}{\varepsilon_p(\omega) + 2\varepsilon_m}\right\}$$

Since every other variable except for $\varepsilon_p(\omega)$ are physical constants, the slopes of the power functions for $Cu_{2-x}Se$ (x = ~0.6) and (x = ~0.2) are proportional to $\varepsilon_p(\omega)$, which is composed of both the real and imaginary parts:

$$\varepsilon_p(\omega) = \varepsilon_1(\omega) + i\varepsilon_2(\omega)$$

where each component can be described as:

$$\varepsilon_1(\omega) = \varepsilon_\infty - \frac{{\omega_p}^2}{({\omega_{LSPR}}^2 + \gamma^2)}$$

and

$$\varepsilon_2(\omega) = \frac{{\omega_p}^2\gamma}{\omega_{LSPR}({\omega_{LSPR}}^2 + \gamma^2)}$$

Here, ε_∞ is the high frequency dielectric constant of $Cu_{2-x}Se$, ω_{LSPR} is the angular frequency of the LSPR peak maximum, γ is the angular frequency of LSPR FWHM, and ω_p is the bulk plasma frequency, which can be expressed as:

$$\omega_p = \sqrt{\frac{Ne^2}{m\varepsilon_0}}$$

where N is the carrier density, e is the charge of an electron, m is the effective mass of the carrier, and ε_0 is the permittivity of free space.

To fulfill the LSPR condition, we set:

$$\varepsilon_1(\omega) = -2\varepsilon_m$$

in $Im\left\{\frac{\varepsilon_p(\omega) - \varepsilon_m}{\varepsilon_p(\omega) + 2\varepsilon_m}\right\}$ and we simplified the term as follows:

$$Im\left\{\frac{\varepsilon_p(\omega) - \varepsilon_m}{\varepsilon_p(\omega) + 2\varepsilon_m}\right\} = Im\left\{\frac{\varepsilon_1(\omega)+i\varepsilon_2(\omega)- \varepsilon_m}{\varepsilon_1(\omega)+i\varepsilon_2(\omega)+ 2\varepsilon_m}\right\}$$

$$= Im\left\{\frac{i\varepsilon_2(\omega)- 3\varepsilon_m}{i\varepsilon_2(\omega)}\right\}$$

$$= Im\left\{\frac{-3i\varepsilon_m-\varepsilon_2(\omega)}{-\varepsilon_2(\omega)}\right\}$$

$$= Im\left\{i\,\frac{3\varepsilon_m}{\varepsilon_2(\omega)} + 1\right\}$$

By only keeping the real term of the imaginary component, we can now express the equation as:

$$Im\left\{\frac{\varepsilon_p(\omega) - \varepsilon_m}{\varepsilon_p(\omega) + 2\varepsilon_m}\right\} = \frac{3\varepsilon_m}{\varepsilon_2(\omega)}$$

which tells us that the slope (a) of the power function is inversely proportional to $\varepsilon_2(\omega)$:

$$Im\left\{\frac{\varepsilon_p(\omega) - \varepsilon_m}{\varepsilon_p(\omega) + 2\varepsilon_m}\right\} \propto \frac{1}{\varepsilon_2(\omega)}$$

To determine the relationship between the carrier density (n) and the slope of the power function (a), we substitute ω_p:

$$\varepsilon_2(\omega) = \frac{\frac{Ne^2}{m\varepsilon_0}\gamma}{\omega_{LSPR}({\omega_{LSPR}}^2 + \gamma^2)}$$

Since $\varepsilon_2(\omega) \propto N$, we can conclude that the slope (a) of the power function is inversely proportional to N:

$$Im\left\{\frac{\varepsilon_p(\omega) - \varepsilon_m}{\varepsilon_p(\omega) + 2\varepsilon_m}\right\} \propto \frac{1}{\varepsilon_2(\omega)} \propto \frac{1}{N}$$

This relationship explains why the slope of the power function of $Cu_{2-x}Se$ (x = ~0.2) is greater than that of $Cu_{2-x}Se$ (x = ~0.6), as the $Cu_{2-x}Se$ (x = ~0.2) system has a lower carrier density, as described in **Section 4.3.6**.

Bibliography

1. Willets, K. A.; Van Duyne, R. P., Localized Surface Plasmon Resonance Spectroscopy and Sensing. *Annu. Rev. Phys. Chem.* **2007,** *58*, 267-297.

2. Brongersma, M. L.; Halas, N. J.; Nordlander, P., Plasmon-Induced Hot Carrier Science and Technology. *Nat. Nanotech.* **2015,** *10*, 25-34.

3. Linic, S.; Christopher, P.; Ingram, D. B., Plasmonic-Metal Nanostructures for Efficient Conversion of Solar to Chemical Energy. *Nat. Mater.* **2011,** *10*, 911-921.

4. Narang, P.; Sundararaman, R.; Atwater, H. A., Plasmonic Hot Carrier Dynamics in Solid-State and Chemical Systems for Energy Conversion. *Nanophotonics* **2016,** *5*, 96-111.

5. Zhang, Y.; He, S.; Guo, W.; Hu, Y.; Huang, J.; Mulcahy, J. R.; Wei, W. D., Surface-Plasmon-Driven Hot Electron Photochemistry. *Chem. Rev.* **2018,** *118*, 2927-2954.

6. Brooks, J. L.; Warkentin, C. L.; Saha, D.; Keller, E. L.; Frontiera, R. R., Toward A Mechanistic Understanding of Plasmon-Mediated Photocatalysis. *Nanophotonics* **2018,** *7*, 1697-1724.

7. Kim, M.; Lin, M.; Son, J.; Xu, H.; Nam, J.-M., Hot-Electron-Mediated Photochemical Reactions: Principles, Recent Advances, and Challenges. *Adv. Opt. Mater.* **2017,** *5*, 1700004-1700025.

8. Freestone, I.; Meeks, N.; Sax, M.; Higgitt, C., The Lycurgus Cup — A Roman Nanotechnology. *Gold Bull.* **2007,** *40*, 270-277.

9. Huang, X.; Jain, P. K.; El-Sayed, I. H.; El-Sayed, M. A., Plasmonic Photothermal Therapy (PPTT) Using Gold Nanoparticles. *Lasers Med. Sci.* **2007,** *23*, 217-228.

10. Mubeen, S.; Lee, J.; Singh, N.; Krämer, S.; Stucky, G. D.; Moskovits, M., An Autonomous Photosynthetic Device in Which All Charge Carriers Derive from Surface Plasmons. *Nat. Nanotech.* **2013,** *8*, 247-251.

11. Osawa, M., Dynamic Processes in Electrochemical Reactions Studied by Surface-Enhanced Infrared Absorption Spectroscopy (SEIRAS). *Bull. Chem. Soc. Jpn.* **1997,** *70*, 2861-2880.

12. Haynes, C. L.; McFarland, A. D.; Duyne, R. P. V., Surface-Enhanced Raman Spectroscopy. *Anal. Chem.* **2005,** *77*, 338 -346.

13. Sharma, B.; Frontiera, R. R.; Henry, A.-I.; Ringe, E.; Van Duyne, R. P., SERS: Materials, Applications, and the Future. *Mater. Today* **2012,** *15*, 16-25.

14. Valley, N.; Greeneltch, N.; Van Duyne, R. P.; Schatz, G. C., A Look at the Origin and Magnitude of the Chemical Contribution to the Enhancement Mechanism of Surface-Enhanced Raman Spectroscopy (SERS): Theory and Experiment. *J. Phys. Chem. Lett.* **2013,** *4*, 2599-2604.

15. Ho, C.-S.; Jean, N.; Hogan, C. A.; Blackmon, L.; Jeffrey, S. S.; Holodniy, M.; Banaei, N.; Saleh, A. A. E.; Ermon, S.; Dionne, J., Rapid identification of pathogenic bacteria using Raman spectroscopy and deep learning. *Nat. Commun.* **2019,** *10*, 4927.

16. Manjavacas, A.; Liu, J. G.; Kulkarni, V.; Nordlander, P., Plasmon-Induced Hot Carriers in Metallic Nanoparticles. *ACS Nano* **2014,** *8*, 7630-7638.

17. Devasia, D.; Das, A.; Mohan, V.; Jain, P. K., Control of Chemical Reaction Pathways by Light–Matter Coupling. *Annu. Rev. Phys. Chem.* **2021**.

18. Brandt, N. C.; Keller, E. L.; Frontiera, R. R., Ultrafast Surface-Enhanced Raman Probing of the Role of Hot Electrons in Plasmon-Driven Chemistry. *J. Phys. Chem. Lett.* **2016,** *7*, 3179-3185.

19. Marimuthu, A.; Zhang, J.; Linic, S., Tuning Selectivity in Propylene Epoxidation by Plasmon Mediated Photo-Switching of Cu Oxidation State. *Science* **2013,** *339*, 1590-1593.

20. Mukherjee, S.; Libisch, F.; Large, N.; Neumann, O.; Brown, L. V.; Cheng, J.; Lassiter, J. B.; Carter, E. A.; Nordlander, P.; Halas, N. J., Hot Electrons Do the Impossible: Plasmon-Induced Dissociation of H_2 on Au. *Nano Lett.* **2013,** *13*, 240-247.

21. Kim, Y.; Wilson, A. J.; Jain, P. K., The Nature of Plasmonically Assisted Hot-Electron Transfer in a Donor–Bridge–Acceptor Complex. *ACS Catal.* **2017,** *7*, 4360-4365.

22. Swearer, D. F.; Zhao, H.; Zhou, L.; Zhang, C.; Robatjazi, H.; Martirez, J. M. P.; Krauter, C. M.; Yazdi, S.; McClain, M. J.; Ringe, E.; Carter, E. A.; Nordlander, P.; Halas, N. J., Heterometallic Antenna−Reactor Complexes for Photocatalysis. *Proc. Natl. Acad. Sci.* **2016,** *113*, 8916-8920.

23. Giannini, V.; Fernández-Domínguez, A. I.; Heck, S. C.; Maier, S. A., Plasmonic Nanoantennas: Fundamentals and Their Use in Controlling the Radiative Properties of Nanoemitters. *Chem. Rev.* **2011,** *111*, 3888-3912.

24. Griffin, S.; Montoni, N. P.; Li, G.; Straney, P. J.; Millstone, J. E.; Masiello, D. J.; Camden, J. P., Imaging Energy Transfer in Pt-Decorated Au Nanoprisms via Electron Energy-Loss Spectroscopy. *J. Phys. Chem. Lett.* **2016,** *7*, 3825-3832.

25. Bora, T.; Dutta, J., Plasmonic Photocatalyst Design: Metal-Semiconductor Junction Affecting Photocatalytic Efficiency. *J. Nanosci. Nanotechnol.* **2019,** *19*, 383-388.

26. Govorov, A. O.; Zhang, H.; Gun'ko, Y. K., Theory of Photoinjection of Hot Plasmonic Carriers from Metal Nanostructures into Semiconductors and Surface Molecules. *J. Phys. Chem. C* **2013,** *117*, 16616-16631.

27. Wu, K.; Chen, J.; McBride, J. R.; Lian, T., Efficient Hot-Electron Transfer by a Plasmon-Induced Interfacial Charge-Transfer Transition. *Science* **2015,** *349*, 632-635.

28. Zhang, Z.; Zhang, C.; Zheng, H.; Xu, H., Plasmon-Driven Catalysis on Molecules and Nanomaterials. *Acc. Chem. Res.* **2019,** *52*, 2506-2515.

29. Boerigter, C.; Aslam, U.; Linic, S., Mechanism of Charge Transfer from Plasmonic Nanostructures to Chemically Attached Materials. *ACS Nano* **2016,** *10*, 6108-6115.

30. Zhao, L.-B.; Zhang, M.; Huang, Y.-F.; Williams, C. T.; Wu, D.-Y.; Ren, B.; Tian, Z.-Q., Theoretical Study of Plasmon-Enhanced Surface Catalytic Coupling Reactions of Aromatic Amines and Nitro Compounds. *J. Phys. Chem. Lett.* **2014,** *5*, 1259-1266.

31. Brooks, J. L.; Frontiera, R. R., Competition between Reaction and Degradation Pathways in Plasmon-Driven Photochemistry. *J. Phys. Chem. C* **2016,** *120*, 20869-20876.

32. Dong, B.; Fang, Y.; Chen, X.; Xu, H.; Sun, M., Substrate-, Wavelength-, and Time-Dependent Plasmon-Assisted Surface Catalysis Reaction of 4-Nitrobenzenethiol Dimerizing to p,p′-Dimercaptoazobenzene on Au, Ag, and Cu Films. *Langmuir* **2011,** *27*, 10677-10682.

33. Keller, E. L.; Frontiera, R. R., Monitoring Charge Density Delocalization upon Plasmon Excitation with Ultrafast Surface-Enhanced Raman Spectroscopy. *ACS Photonics* **2017,** *4*, 1033-1039.

34. Jin, R.; Cao, Y.; Mirkin, C. A.; Kelly, K. L.; Schatz, G. C.; Zheng, J. G., Photoinduced Conversion of Silver Nanospheres to Nanoprisms. *Science* **2001,** *294*, 1901.

35. Thrall, E. S.; Preska Steinberg, A.; Wu, X.; Brus, L. E., The Role of Photon Energy and Semiconductor Substrate in the Plasmon-Mediated Photooxidation of Citrate by Silver Nanoparticles. *J. Phys. Chem. C* **2013,** *117*, 26238-26247.

36. Wu, X.; Thrall, E. S.; Liu, H.; Steigerwald, M.; Brus, L., Plasmon Induced Photovoltage and Charge Separation in Citrate-Stabilized Gold Nanoparticles. *J. Phys. Chem. C* **2010,** *114*, 12896-12899.

37. Sundararaman, R.; Narang, P.; Jermyn, A. S.; Goddard III, W. A.; Atwater, H. A., Theoretical Predictions for Hot-Carrier Generation from Surface Plasmon Decay. *Nat. Commun.* **2014,** *5*, 5788-5796.

38. Kumar, P. V.; Rossi, T. P.; Kuisma, M.; Erhart, P.; Norris, D. J., Direct Hot-Carrier Transfer in Plasmonic Catalysis. *Faraday Discuss.* **2019,** *214*, 189-197.

39. Besteiro, L. V.; Kong, X.-T.; Wang, Z.; Hartland, G.; Govorov, A. O., Understanding Hot-Electron Generation and Plasmon Relaxation in Metal Nanocrystals: Quantum and Classical Mechanisms. *ACS Photonics* **2017,** *4*, 2759-2781.

40. Santiago, E. Y.; Besteiro, L. V.; Kong, X.-T.; Correa-Duarte, M. A.; Wang, Z.; Govorov, A. O., Efficiency of Hot-Electron Generation in Plasmonic Nanocrystals with Complex Shapes: Surface-Induced Scattering, Hot Spots, and Interband Transitions. *ACS Photonics* **2020,** *7*, 2807-2824.

41. Hattori, Y.; Gutiérrez Álvarez, S.; Meng, J.; Zheng, K.; Sá, J., Role of the Metal Oxide Electron Acceptor on Gold–Plasmon Hot-Carrier Dynamics and Its Implication to Photocatalysis and Photovoltaics. *ACS Appl. Nano Mater.* **2021**.

42. Kim, M.; Lee, J.-H.; Nam, J.-M., Plasmonic Photothermal Nanoparticles for Biomedical Applications. *Adv. Sci.* **2019,** *6*, 1900471.

43. Zou, L.; Wang, H.; He, B.; Zeng, L.; Tan, T.; Cao, H.; He, X.; Zhang, Z.; Guo, S.; Li, Y., Current Approaches of Photothermal Therapy in Treating Cancer Metastasis with Nanotherapeutics. *Theranostics* **2016,** *6*, 762-772.

44. Ali, M. R. K.; Wu, Y.; El-Sayed, M. A., Gold-Nanoparticle-Assisted Plasmonic Photothermal Therapy Advances Toward Clinical Application. *J. Phys. Chem. C* **2019,** *123*, 15375-15393.

45. Jain, P. K., Taking the Heat Off of Plasmonic Chemistry. *J. Phys. Chem. C* **2019,** *123*, 24347-24351.

46. Keller, E. L.; Frontiera, R. R., Ultrafast Nanoscale Raman Thermometry Proves Heating Is Not a Primary Mechanism for Plasmon-Driven Photocatalysis. *ACS Nano* **2018,** *12*, 5848-5855.

47. Wang, F.; Li, C.; Chen, H.; Jiang, R.; Sun, L.-D.; Li, Q.; Wang, J.; Yu, J. C.; Yan, C.-H., Plasmonic Harvesting of Light Energy for Suzuki Coupling Reactions. *J. Am. Chem. Soc.* **2013,** *135*, 5588-5601.

48. Swearer, D. F.; Robatjazi, H.; Martirez, J. M. P.; Zhang, M.; Zhou, L.; Carter, E. A.; Nordlander, P.; Halas, N. J., Plasmonic Photocatalysis of Nitrous Oxide into N2 and O2 Using Aluminum–Iridium Antenna–Reactor Nanoparticles. *ACS Nano* **2019,** *13*, 8076-8086.

49. Luther, J. M.; Jain, P. K.; Ewers, T.; Alivisatos, A. P., Localized Surface Plasmon Resonances Arising from Free Carriers in Doped Quantum Dots. *Nat. Mater.* **2011,** *10*, 361-366.

50. Buonsanti, R.; Llordes, A.; Aloni, S.; Helms, B. A.; Milliron, D. J., Tunable Infrared Absorption and Visible Transparency of Colloidal Aluminum-Doped Zinc Oxide Nanocrystals. *Nano Lett.* **2011,** *11*, 4706-4710.

51. Schimpf, A. M.; Gunthardt, C. E.; Rinehart, J. D.; Mayer, J. M.; Gamelin, D. R., Controlling Carrier Densities in Photochemically Reduced Colloidal ZnO Nanocrystals: Size Dependence and Role of the Hole Quencher. *J. Am. Chem. Soc.* **2013,** *135*, 16569-16577.

52. Schimpf, A. M.; Knowles, K. E.; Carroll, G. M.; Gamelin, D. R., Electronic Doping and Redox-Potential Tuning in Colloidal Semiconductor Nanocrystals. *Acc. Chem. Res.* **2015,** *48*, 1929-1937.

53. Agrawal, A.; Johns, R. W.; Milliron, D. J., Control of Localized Surface Plasmon Resonances in Metal Oxide Nanocrystals. *Annu. Rev. Mater. Res.* **2017,** *47*, 1-31.

54. Liu, X.; Swihart, M. T., Heavily-Doped Colloidal Semiconductor and Metal Oxide Nanocrystals: An Emerging New Class of Plasmonic Nanomaterials. *Chem. Soc. Rev.* **2014,** *43*, 3908-3920.

55. Agrawal, A.; Cho, S. H.; Zandi, O.; Ghosh, S.; Johns, R. W.; Milliron, D. J., Localized Surface Plasmon Resonance in Semiconductor Nanocrystals. *Chem. Rev.* **2018,** *118*, 3121-3207.

56. Naik, G. V.; Shalaev, V. M.; Boltasseva, A., Alternative Plasmonic Materials: Beyond Gold and Silver. *Adv. Mater.* **2013,** *25*, 3264-3294.

57. Kriegel, I.; Scotognella, F.; Manna, L., Plasmonic Doped Semiconductor Nanocrystals: Properties, Fabrication, Applications and Perspectives. *Phys. Rep.* **2017,** *674*, 1-52.

58. Faucheaux, J. A.; Stanton, A. L. D.; Jain, P. K., Plasmon Resonances of Semiconductor Nanocrystals: Physical Principles and New Opportunities. *J. Phys. Chem. Lett.* **2014,** *5*, 976-985.

59. Garcia, G.; Buonsanti, R.; Runnerstrom, E. L.; Mendelsberg, R. J.; Llordes, A.; Anders, A.; Richardson, T. J.; Milliron, D. J., Dynamically Modulating the Surface Plasmon Resonance of Doped Semiconductor Nanocrystals. *Nano Lett.* **2011,** *11*, 4415-4420.

60. Mendelsberg, R. J.; Garcia, G.; Li, H.; Manna, L.; Milliron, D. J., Understanding the Plasmon Resonance in Ensembles of Degenerately Doped Semiconductor Nanocrystals. *J. Phys. Chem. C* **2012,** *116*, 12226-12231.

61. Jain, P. K.; Manthiram, K.; Engel, J. H.; White, S. L.; Faucheaux, J. A.; Alivisatos, A. P., Doped Nanocrystals as Plasmonic Probes of Redox Chemistry. *Angew. Chem. Int. Ed.* **2013,** *52*, 13671-13675.

62. Marbella, L. E.; Gan, X. Y.; Kaseman, D. C.; Millstone, J. E., Correlating Carrier Density and Emergent Plasmonic Features in $Cu_{2-x}Se$ Nanoparticles. *Nano Lett.* **2017,** *17*, 2414-2419.

63. Mansour, B. A.; Demian, S. E.; Zayed, H. A., Determination of the Effective Mass for Highly Degenerate Copper Selenide from Reflectivity Measurements. *J. Mater. Sci.: Mater. Electron.* **1992,** *3*, 249-252.

64. Conti III, C. R.; Quiroz-Delfi, G.; Schwarck, J. S.; Chen, B.; Strouse, G. F., Carrier Density, Effective Mass, and Nuclear Relaxation Pathways in Plasmonic Sn:In2O3 Nanocrystals. *J. Phys. Chem. C* **2020,** *124*, 28220-28229.

65. Gibbs, S. L.; Staller, C. M.; Agrawal, A.; Johns, R. W.; Saez Cabezas, C. A.; Milliron, D. J., Intrinsic Optical and Electronic Properties from Quantitative Analysis of Plasmonic Semiconductor Nanocrystal Ensemble Optical Extinction. *J. Phys. Chem. C* **2020,** *124*, 24351-24360.

66. Schimpf, A. M.; Thakkar, N.; Gunthardt, C. E.; Masiello, D. J.; Gamelin, D. R., Charge-Tunable Quantum Plasmons in Colloidal Semiconductor Nanocrystals. *ACS Nano* **2014,** *8*, 1065-1072.

67. Rinehart, J. D.; Schimpf, A. M.; Weaver, A. L.; Cohn, A. W.; Gamelin, D. R., Photochemical Electronic Doping of Colloidal CdSe Nanocrystals. *J. Am. Chem. Soc.* **2013,** *135*, 18782-18785.

68. Schimpf, A. M.; Lounis, S. D.; Runnerstrom, E. L.; Milliron, D. J.; Gamelin, D. R., Redox Chemistries and Plasmon Energies of Photodoped In2O3 and Sn-Doped In2O3 (ITO) Nanocrystals. *J. Am. Chem. Soc.* **2015,** *137*, 518-524.

69. Liu, Z.; Beaulac, R., Nature of the Infrared Transition of Colloidal Indium Nitride Nanocrystals: Nonparabolicity Effects on the Plasmonic Behavior of Doped Semiconductor Nanomaterials. *Chem. Mater.* **2017,** *29*, 7507-7514.

70. Knight, W. D., Nuclear Magnetic Resonance Shift in Metals. *Phys. Rev.* **1949,** *76*, 1259-1260.

71. Korringa, J., Nuclear Magnetic Relaxation and Resonnance Line Shift in Metals. *Physica* **1950,** *16*, 601-610.

72. Tong, Y. Y.; Klink, J. J. V. v. d., Local Metal to Non-Metal Transition on Oxygen-Covered Platinum Particles From195Pt Nuclear Magnetic Resonance. *J. Phys.: Condens. Matter* **1995,** *7*, 2447-2459.

73. Levin, E. M., Effects of Ge Substitution in GeTe by Ag or Sb on the Seebeck Coefficient and Carrier Concentration Derived from 125Te NMR. *Phys. Rev. B* **2016,** *93*, 045209.

74. Levin, E. M.; Cook, B. A.; Ahn, K.; Kanatzidis, M. G.; Schmidt-Rohr, K., Electronic Inhomogeneity and Ag:Sb Imbalance of $Ag(_{1-y})Pb(_{18})Sb(_{1+z})Te(_{20})$ High-Performance Thermoelectrics Elucidated by ^{125}Te and ^{207}Pb NMR. *Phys. Rev. B* **2009,** *80*, 115211-115216.

75. Levin, E. M.; Heremans, J. P.; Kanatzidis, M. G.; Schmidt-Rohr, K., Electronic Inhomogeneity in n- and p-type PbTe Detected by 125Te NMR. *Phys. Rev. B* **2013,** *88*, 115211.

76. Koumoulis, D.; Taylor, R. E.; King, D.; Bouchard, L. S., NMR Study of Native Defects in PbSe. *Phys. Rev. B* **2014,** *90*, 125201.

77. Taylor, R. E.; Alkan, F.; Koumoulis, D.; Lake, M. P.; King, D.; Dybowski, C.; Bouchard, L.-S., A Combined NMR and DFT Study of Narrow Gap Semiconductors: The Case of PbTe. *J. Phys. Chem. C* **2013,** *117*, 8959-8967.

78. Senturia, S. D.; Smith, A. C.; Hewes, C. R.; Hofmann, J. A.; Sagalyn, P. L., Knight Shifts and Band Structure in the Lead-Salt Semiconductors. *Phys. Rev. B* **1970,** *1*, 4045-4057.

79. Marbella, L. E.; Millstone, J. E., NMR Techniques for Noble Metal Nanoparticles. *Chem. Mater.* **2015,** *27*, 2721-2739.

80. Tong, Y. Y.; Wieckowski, A.; Oldfield, E., NMR of Electrocatalysts. *J. Phys. Chem. B* **2002,** *106*, 2434-2446.

81. Levin, E. M.; Cui, J. F.; Schmidt-Rohr, K., Sub-Millisecond 125Te NMR Spin-Lattice Relaxation Times and Large Knight Shifts in Complex Tellurides: Validation of a Quadratic Relation Across the Spectrum. *Solid State Nucl. Magn. Reson.* **2016,** *78*, 40-44.

82. Smith, A. M.; Johnston, K. A.; Crawford, S. E.; Marbella, L. E.; Millstone, J. E., Ligand Density Quantification on Colloidal Inorganic Nanoparticles. *Analyst* **2017,** *142*, 11-29.

83. Love, J. C.; Estroff, L. A.; Kriebel, J. K.; Nuzzo, R. G.; Whitesides, G. M., Self-Assembled Monolayers of Thiolates on Metals as a Form of Nanotechnology. *Chem. Rev.* **2005,** *105*, 1103-1170.

84. Crawford, S. E.; Hartmann, M. J.; Millstone, J. E., Surface Chemistry-Mediated Near-Infrared Emission of Small Coinage Metal Nanoparticles. *Acc. Chem. Res.* **2019,** *52*, 695-703.

85. Johnston, K. A.; Stabryla, L. M.; Gilbertson, L. M.; Millstone, J. E., Emerging Investigator Series: Connecting Concepts of Coinage Metal Stability Across Length Scales. *Envi. Sci: Nano* **2019,** *6*, 2674-2696.

86. Rossi, L. M.; Fiorio, J. L.; Garcia, M. A. S.; Ferraz, C. P., The Role and Fate of Capping Ligands in Colloidally Prepared Metal Nanoparticle Catalysts. *Dalton Trans.* **2018,** *47*, 5889-5915.

87. Straney, P. J.; Diemler, N. A.; Smith, A. M.; Eddinger, Z. E.; Gilliam, M. S.; Millstone, J. E., Ligand-Mediated Deposition of Noble Metals at Nanoparticle Plasmonic Hotspots. *Langmuir* **2018,** *34*, 1084-1091.

88. Hartley, C. L.; Kessler, M. L.; Dempsey, J. L., Molecular-Level Insight into Semiconductor Nanocrystal Surfaces. *J. Am. Chem. Soc.* **2021,** *143*, 1251-1266.

89. De Roo, J.; De Keukeleere, K.; Hens, Z.; Van Driessche, I., From Ligands to Binding Motifs and Beyond; the Enhanced Versatility of Nanocrystal Surfaces. *Dalton Trans.* **2016,** *45*, 13277-13283.

90. Giansante, C., Surface Chemistry Control of Colloidal Quantum Dot Band Gap. *J. Phys. Chem. C* **2018,** *122*, 18110-18116.

91. Gibbs, S. L.; Staller, C. M.; Milliron, D. J., Surface Depletion Layers in Plasmonic Metal Oxide Nanocrystals. *Acc. Chem. Res.* **2019,** *52*, 2516-2524.

92. Lounis, S. D.; Runnerstrom, E. L.; Bergerud, A.; Nordlund, D.; Milliron, D. J., Influence of Dopant Distribution on the Plasmonic Properties of Indium Tin Oxide Nanocrystals. *J. Am. Chem. Soc.* **2014,** *136*, 7110-7116.

93. Crockett, B. M.; Jansons, A. W.; Koskela, K. M.; Johnson, D. W.; Hutchison, J. E., Radial Dopant Placement for Tuning Plasmonic Properties in Metal Oxide Nanocrystals. *ACS Nano* **2017,** *11*, 7719-7728.

94. Tandon, B.; Yadav, A.; Khurana, D.; Reddy, P.; Santra, P. K.; Nag, A., Size-Induced Enhancement of Carrier Density, LSPR Quality Factor, and Carrier Mobility in Cr–Sn Doped In2O3 Nanocrystals. *Chem. Mater.* **2017,** *29*, 9360-9368.

95. Dorfs, D.; Härtling, T.; Miszta, K.; Bigall, N. C.; Kim, M. R.; Genovese, A.; Falqui, A.; Povia, M.; Manna, L., Reversible Tunability of the Near-Infrared Valence Band Plasmon Resonance in $Cu_{2-x}Se$ Nanocrystals. *J. Am. Chem. Soc.* **2011,** *133*, 11175-11180.

96. Kriegel, I.; Jiang, C.; Rodríguez-Fernández, J.; Schaller, R. D.; Talapin, D. V.; da Como, E.; Feldmann, J., Tuning the Excitonic and Plasmonic Properties of Copper Chalcogenide Nanocrystals. *J. Am. Chem. Soc.* **2012,** *134*, 1583-1590.

97. Hartstein, K. H.; Brozek, C. K.; Hinterding, S. O. M.; Gamelin, D. R., Copper-Coupled Electron Transfer in Colloidal Plasmonic Copper-Sulfide Nanocrystals Probed by in Situ Spectroelectrochemistry. *J. Am. Chem. Soc.* **2018,** *140*, 3434-3442.

98. Riha, S. C.; Johnson, D. C.; Prieto, A. L., Cu_2Se Nanoparticles with Tunable Electronic Properties Due to a Controlled Solid-State Phase Transition Driven by Copper Oxidation and Cationic Conduction. *J. Am. Chem. Soc.* **2011,** *133*, 1383-1390.

99. Kaseman, D. C.; Gamble Jarvi, A.; Gan, X. Y.; Saxena, S.; Millstone, J. E., Evolution of Surface Copper(II) Environments in $Cu_{2-x}Se$ Nanoparticles. *Chem. Mater.* **2018,** *30*, 7313-7321.

100. Gan, X. Y.; Keller, E. L.; Warkentin, C. L.; Crawford, S. E.; Frontiera, R. R.; Millstone, J. E., Plasmon-Enhanced Chemical Conversion Using Copper Selenide Nanoparticles. *Nano Lett.* **2019,** *19*, 2384-2388.

101. Gan, X. Y.; Crawford, S. E.; Eikey, E. A.; Sen, R.; Killinger, J. R.; Millstone, J. E., Optoelectronic Impacts of Particle Size in Water-Dispersible Plasmonic Copper Selenide Nanoparticles. *J. Phys. Chem. C* **2020,** *124*, 4747-4754.

102. Link, S.; El-Sayed, M. A., Optical Properties and Ultrafast Dynamics of Metallic Nanocrystals. *Annu. Rev. Phys. Chem.* **2003,** *54*, 331-366.

103. Scotognella, F.; Della Valle, G.; Srimath Kandada, A. R.; Dorfs, D.; Zavelani-Rossi, M.; Conforti, M.; Miszta, K.; Comin, A.; Korobchevskaya, K.; Lanzani, G.; Manna, L.; Tassone, F., Plasmon Dynamics in Colloidal $Cu_{2-x}Se$ Nanocrystals. *Nano Lett.* **2011,** *11*, 4711-4717.

104. Yang, W.; Liu, Y.; McBride, J. R.; Lian, T., Ultrafast and Long-Lived Transient Heating of Surface Adsorbates on Plasmonic Semiconductor Nanocrystals. *Nano Lett.* **2021,** *21*, 453-461.

105. Blemker, M. A.; Gibbs, S. L.; Raulerson, E. K.; Milliron, D. J.; Roberts, S. T., Modulation of the Visible Absorption and Reflection Profiles of ITO Nanocrystal Thin Films by Plasmon Excitation. *ACS Photonics* **2020,** *7*, 1188-1196.

106. Rycenga, M.; Cobley, C. M.; Zeng, J.; Li, W.; Moran, C. H.; Zhang, Q.; Qin, D.; Xia, Y., Controlling the Synthesis and Assembly of Silver Nanostructures for Plasmonic Applications. *Chem. Rev.* **2011,** *111*, 3669-3712.

107. Jain, P. K.; Lee, K. S.; El-Sayed, I. H.; El-Sayed, M. A., Calculated Absorption and Scattering Properties of Gold Nanoparticles of Different Size, Shape, and Composition: Applications in Biological Imaging and Biomedicine. *J. Phys. Chem. B* **2006,** *110*, 7238-7248.

108. Link, S.; El-Sayed, M. A., Spectral Properties and Relaxation Dynamics of Surface Plasmon Electronic Oscillations in Gold and Silver Nanodots and Nanorods. *J. Phys. Chem. B* **1999,** *103*, 8410-8426.

109. Zhang, Q.; Large, N.; Wang, H., Gold Nanoparticles with Tipped Surface Structures as Substrates for Single-Particle Surface-Enhanced Raman Spectroscopy: Concave Nanocubes, Nanotrisoctahedra, and Nanostars. *ACS Appl. Mater. Interfaces* **2014,** *6*, 17255-17267.

110. Kleinman, S. L.; Frontiera, R. R.; Henry, A.-I.; Dieringer, J. A.; Van Duyne, R. P., Creating, Characterizing, and Controlling Chemistry with SERS Hot Spots. *Phys. Chem. Chem. Phys.* **2013,** *15*, 21-36.

111. Staller, C. M.; Gibbs, S. L.; Saez Cabezas, C. A.; Milliron, D. J., Quantitative Analysis of Extinction Coefficients of Tin-Doped Indium Oxide Nanocrystal Ensembles. *Nano Lett.* **2019,** *19*, 8149-8154.

112. Elimelech, O.; Liu, J.; Plonka, A. M.; Frenkel, A. I.; Banin, U., Size Dependence of Doping by a Vacancy Formation Reaction in Copper Sulfide Nanocrystals. *Angew. Chem. Int. Ed.* **2017,** *129*, 10471-10476.

113. Tandon, B.; Ghosh, S.; Milliron, D. J., Dopant Selection Strategy for High-Quality Factor Localized Surface Plasmon Resonance from Doped Metal Oxide Nanocrystals. *Chem. Mater.* **2019,** *31*, 7752-7760.

114. Cui, J.; Li, Y.; Liu, L.; Chen, L.; Xu, J.; Ma, J.; Fang, G.; Zhu, E.; Wu, H.; Zhao, L.; Wang, L.; Huang, Y., Near-Infrared Plasmonic-Enhanced Solar Energy Harvest for Highly Efficient Photocatalytic Reactions. *Nano Lett.* **2015,** *15*, 6295-6301.

115. Cheng, H.; Qian, X.; Kuwahara, Y.; Mori, K.; Yamashita, H., A Plasmonic Molybdenum Oxide Hybrid with Reversible Tunability for Visible-Light-Enhanced Catalytic Reactions. *Adv. Mater.* **2015,** *27*, 4616-4621.

116. Lou, Z.; Gu, Q.; Liao, Y.; Yu, S.; Xue, C., Promoting Pd-Catalyzed Suzuki Coupling Reactions through Near-Infrared Plasmon Excitation of WO3−x Nanowires. *Appl. Catal. B: Envi.* **2016,** *184*, 258-263.

117. Lian, Z.; Sakamoto, M.; Vequizo, J. J. M.; Ranasinghe, C. S. K.; Yamakata, A.; Nagai, T.; Kimoto, K.; Kobayashi, Y.; Tamai, N.; Teranishi, T., Plasmonic p–n Junction for Infrared Light to Chemical Energy Conversion. *J. Am. Chem. Soc.* **2019,** *141*, 2446-2450.

118. Lian, Z.; Sakamoto, M.; Matsunaga, H.; Vequizo, J. J. M.; Yamakata, A.; Haruta, M.; Kurata, H.; Ota, W.; Sato, T.; Teranishi, T., Near Infrared Light Induced Plasmonic Hot Hole Transfer at a Nano-Heterointerface. *Nat. Commun.* **2018,** *9*, 2314-2321.

119. Cai, X.; Zhu, M.; Elbanna, O. A.; Fujitsuka, M.; Kim, S.; Mao, L.; Zhang, J.; Majima, T., Au Nanorod Photosensitized La2Ti2O7 Nanosteps: Successive Surface Heterojunctions Boosting Visible to Near-Infrared Photocatalytic H2 Evolution. *ACS Catal.* **2018,** *8*, 122-131.

120. Sun, M.; Fu, X.; Chen, K.; Wang, H., Dual-Plasmonic Gold@Copper Sulfide Core–Shell Nanoparticles: Phase-Selective Synthesis and Multimodal Photothermal and Photocatalytic Behaviors. *ACS Appl. Mater. Interfaces* **2020,** *12*, 46146-46161.

121. Zhou, D.; Li, X.; Zhou, Q.; Zhu, H., Infrared Driven Hot Electron Generation and Transfer from Non-Noble Metal Plasmonic Nanocrystals. *Nat. Commun.* **2020,** *11*, 2944.

122. Chinen, A. B.; Guan, C. M.; Ferrer, J. R.; Barnaby, S. N.; Merkel, T. J.; Mirkin, C. A., Nanoparticle Probes for the Detection of Cancer Biomarkers, Cells, and Tissues by Fluorescence. *Chem. Rev.* **2015,** *115*, 10530-10574.

123. Neumann, O.; Urban, A. S.; Day, J.; Lal, S.; Nordlander, P.; Halas, N. J., Solar Vapor Generation Enabled by Nanoparticles. *ACS Nano* **2013,** *7*, 42-49.

124. Atwater, H. A.; Polman, A., Plasmonics for Improved Photovoltaic Devices. *Nat. Mater.* **2010,** *9*, 205-213.

125. Boltasseva, A.; Atwater, H. A., Low-Loss Plasmonic Metamaterials. *Science* **2011,** *331*, 290.

126. Knight, M. W.; King, N. S.; Liu, L.; Everitt, H. O.; Nordlander, P.; Halas, N. J., Aluminum for Plasmonics. *ACS Nano* **2014,** *8*, 834-840.

127. Lounis, S. D.; Runnerstrom, E. L.; Llordés, A.; Milliron, D. J., Defect Chemistry and Plasmon Physics of Colloidal Metal Oxide Nanocrystals. *J. Phys. Chem. Lett.* **2014,** *5*, 1564-1574.

128. Zhao, Y.; Pan, H.; Lou, Y.; Qiu, X.; Zhu, J.; Burda, C., Plasmonic Cu2−xS Nanocrystals: Optical and Structural Properties of Copper-Deficient Copper(I) Sulfides. *J. Am. Chem. Soc.* **2009,** *131*, 4253-4261.

129. Polking, M. J.; Jain, P. K.; Bekenstein, Y.; Banin, U.; Millo, O.; Ramesh, R.; Alivisatos, A. P., Controlling Localized Surface Plasmon Resonances in GeTe Nanoparticles Using an Amorphous-to-Crystalline Phase Transition. *Phys. Rev. Lett.* **2013,** *111*, 037401.

130. Kanehara, M.; Koike, H.; Yoshinaga, T.; Teranishi, T., Indium Tin Oxide Nanoparticles with Compositionally Tunable Surface Plasmon Resonance Frequencies in the Near-IR Region. *J. Am. Chem. Soc.* **2009,** *131*, 17736-17737.

131. Ju, L.; Geng, B.; Horng, J.; Girit, C.; Martin, M.; Hao, Z.; Bechtel, H. A.; Liang, X.; Zettl, A.; Shen, Y. R.; Wang, F., Graphene Plasmonics for Tunable Terahertz Metamaterials. *Nat. Nanotech.* **2011,** *6*, 630-634.

132. Langhammer, C.; Schwind, M.; Kasemo, B.; Zorić, I., Localized Surface Plasmon Resonances in Aluminum Nanodisks. *Nano Lett.* **2008,** *8*, 1461-1471.

133. Hsu, S.-W.; On, K.; Tao, A. R., Localized Surface Plasmon Resonances of Anisotropic Semiconductor Nanocrystals. *J. Am. Chem. Soc.* **2011,** *133*, 19072-19075.

134. Yesinowski, J., *Solid State NMR of Inorganic Semiconductors*. Springer-Verlag Berlin Heidelberg: 2012; p 229 -312.

135. Zhang, H.; Kulkarni, V.; Prodan, E.; Nordlander, P.; Govorov, A. O., Theory of Quantum Plasmon Resonances in Doped Semiconductor Nanocrystals. *J. Phys. Chem. C* **2014,** *118*, 16035-16042.

136. Deka, S.; Genovese, A.; Zhang, Y.; Miszta, K.; Bertoni, G.; Krahne, R.; Giannini, C.; Manna, L., Phosphine-Free Synthesis of p-Type Copper(I) Selenide Nanocrystals in Hot Coordinating Solvents. *J. Am. Chem. Soc.* **2010,** *132*, 8912-8914.

137. Shafizade, R. B.; Ivanoa, I. V.; Kazeinets, M. M., Electron Diffraction Study of Phase Transformations of the Compound CuSe. *Thin Solid Films* **1978,** *55*, 211 - 220.

138. Gorbachev, V. V.; Putilin, I. M., Some Parameters of Band Structure in Copper Selenide and Telluride. *Physica Status Solidi (A)* **1973,** *16*, 553-559.

139. Freeman, R.; Kempsell, S. P.; Levitt, M. H., Radiofrequency Pulse Sequences Which Compensate Their Own Imperfections. *J. Magn. Reson.* **2011,** *213*, 247-273.

140. Garba, E. J. D.; Jacobs, R. L., The Electronic Structure of Cu2-xSe. *Physica B+C* **1986,** *138*, 253-260.

141. El Akkad, F.; Mansour, B.; Hendeya, T., Electrical and Thermoelectric Properties of Cu2Se and Cu2S. *Mater. Res. Bull.* **1981,** *16*, 535-539.

142. White, S. L.; Banerjee, P.; Jain, P. K., Liquid-like Cationic Sub-Lattice in Copper Selenide Clusters. *Nat. Commun.* **2017,** *8*, 1-8.

143. Kumar, P.; Singh, K.; Srivastava, O. N., Template Free-Solvothermaly Synthesized Copper Selenide (CuSe, Cu2−xSe, β-Cu2Se and Cu2Se) Hexagonal Nanoplates from Different Precursors at Low Temperature. *J. Cryst. Growth* **2010,** *312*, 2804-2813.

144. Gulay, L.; Daszkiewicz, M.; Strok, O.; Pietraszko, A., Crystal Structure of Cu_2Se. *Chemistry of Metals and Alloys* **2011,** *4*, 200 - 205.

145. Cadars, S.; Smith, B. J.; Epping, J. D.; Acharya, S.; Belman, N.; Golan, Y.; Chmelka, B. F., Atomic Positional Versus Electronic Order in Semiconducting ZnSe Nanoparticles. *Phys. Rev. Lett.* **2009,** *103*, 136802.

146. Abragam, A.; Abragam, A., *The Principles of Nuclear Magnetism*. Clarendon Press: 1961.

147. Babu, P. K.; Lewera, A.; Chung, J. H.; Hunger, R.; Jaegermann, W.; Alonso-Vante, N.; Wieckowski, A.; Oldfield, E., Selenium Becomes Metallic in Ru−Se Fuel Cell Catalysts: An EC-NMR and XPS Investigation. *J. Am. Chem. Soc.* **2007,** *129*, 15140-15141.

148. Carter, G. C.; Bennett, L. H.; Kahan, D. *Metallic Shifts in NMR*; Pergamon Press, 1977.

149. Berrettini, M. G.; Braun, G.; Hu, J. G.; Strouse, G. F., NMR Analysis of Surfaces and Interfaces in 2-nm CdSe. *J. Am. Chem. Soc.* **2004,** *126*, 7063-7070.

150. Selbach, H.; Kanert, O.; Wolf, D., NMR Investigation of the Diffusion and Conduction Properties of the Semiconductor Tellurium. I. Electronc Properties. *Phys. Rev. B* **1979,** *19*, 4435-4443.

151. Lukashev, P.; Lambrecht, W. R. L.; Kotani, T.; van Schilfgaarde, M., Electronic and Crystal Structure of Cu2-xS: Full-Potential Electronic Structure Calculations. *Phys. Rev. B* **2007,** *76*, 195202.

152. Oliveria, M.; McMullan, R. K.; Wuensch, B. J., Single Crystal Neutron Diffraction Analysis of the Cation Distribution in the High-Temperature Phases α-Cu2−xS, α-Cu2−xSe, and α-Ag2Se. *Solid State Ionics* **1988,** *28-30*, 1332-1337.

153. Knight, W.; Kobayashi, S., Knight Shift. John Wiley & Sons: eMagRes, 2007.

154. Shi, M.; Kwon, H. S.; Peng, Z.; Elder, A.; Yang, H., Effects of Surface Chemistry on the Generation of Reactive Oxygen Species by Copper Nanoparticles. *ACS Nano* **2012,** *6*, 2157-2164.

155. Stoll, S.; Schweiger, A., EasySpin, A Comprehensive Software Package for Spectral Simulation and Analysis in EPR. *J. Magn. Reson.* **2006,** *178*, 42-55.

156. Gemperle, C.; Aebli, G.; Schweiger, A.; Ernst, R. R., Phase Cycling in Pulse EPR. *J Magn. Reson.* **1990,** *88*, 241-256.

157. Fauth, J. M.; Schweiger, A.; Braunschweiler, L.; Forrer, J.; Ernst, R. R., Elimination of Unwanted Echoes and Reduction of Dead Time in Three-Pulse eEectron Spin-Echo Spectroscopy. *J Magn. Reson.* **1986,** *66*, 74-85.

158. Kivelson, D.; Neiman, R., ESR Studies on the Bonding in Copper Complexes. *J. Chem. Phys.* **1961,** *35*, 149-155.

159. Delabie, A.; Pierloot, K.; Groothaert Marijke , H.; Schoonheydt Robert , A.; Vanquickenborne Luc , G., The Coordination of Cu(II) in Zeolites − Structure and Spectroscopic Properties. *Eur. J. Inorg. Chem.* **2002,** *2002*, 515-530.

160. Curtis, A. C.; Duff, D. G.; Edwards, P. P.; Jefferson, D. A.; Johnson, B. F. G.; Kirkland, A. I.; Wallace, A. S., Preparation and Structural Characterization of An Unprotected Copper Sol. *J. Phys. Chem.* **1988,** *92*, 2270-2275.

161. Yanase, A.; Komiyama, H., In situ Observation of Oxidation and Reduction of Small Supported Copper Particles using Optical Absorption and X-ray Diffraction. *Surf. Sci.* **1991,** *248*, 11-19.

162. van Wijk, R.; Görts, P. C.; Mens, A. J. M.; Gijzeman, O. L. J.; Habraken, F. H. P. M.; Geus, J. W., XPS/NRA Investigations of Particle Size Effects during the Oxidation of Cu Particles Supported on Oxidised Si (100). *Appl. Surf. Sci.* **1995,** *90*, 261-269.

163. Hambrock, J.; Becker, R.; Birkner, A.; Wei; Fischer, R. A., A Non-Aqueous Organometallic Route to Highly Monodispersed Copper Nanoparticles Using [$Cu(OCH(Me)CH_2NMe_2)_2$]. *Chem. Commun.* **2002,** *0*, 68-69.

164. Wu, S.-H.; Chen, D.-H., Synthesis of High-Concentration Cu Nanoparticles in Aqueous CTAB Solutions. *J. Colloid Interface Sci.* **2004,** *273*, 165-169.

165. Uk Son, S.; Kyu Park, I.; Park, J.; Hyeon, T., Synthesis of Cu_2O Coated Cu Nanoparticles and Their Successful Applications to Ullmann-Type Amination Coupling Reactions of Aryl Chlorides. *Chem. Commun.* **2004,** *0*, 778-779.

166. Peisach, J.; Blumberg, W. E., Structural Implications Derived from the Analysis of Electron Paramagnetic Resonance Spectra of Natural and Artificial Copper Proteins. *Arch. Biochem. Biophys.* **1974,** *165*, 691-708.

167. Singh, R. J.; Punnoose, A.; Mathew, J.; Maurya, B. P.; Umar, M.; Haque, M. I., S=1 and S=2 EPR Signals in Modified CuO and $BaCuO_2$. *Phys. Rev. B* **1994,** *49*, 1346-1349.

168. Würz, R.; Meeder, A.; Fuertes Marrón, D.; Schedel-Niedrig, T.; Knop-Gericke, A.; Lips, K., Native Oxidation of $CuGaSe_2$ Crystals and Thin Films Studied by Electron Paramagnetic Resonance and Photoelectron Spectroscopy. *Phys. Rev. B* **2004,** *70*, 205321-205330.

169. Wolf, A.; Kodanek, T.; Dorfs, D., Tuning the LSPR in Copper Chalcogenide Nanoparticles by Cation Intercalation, Cation Exchange and Metal Growth. *Nanoscale* **2015,** *7*, 19519-19527.

170. Balitskii, O. A.; Sytnyk, M.; Stangl, J.; Primetzhofer, D.; Groiss, H.; Heiss, W., Tuning the Localized Surface Plasmon Resonance in $Cu_{2-x}Se$ Nanocrystals by Postsynthetic Ligand Exchange. *ACS Appl. Mater. Interfaces* **2014,** *6*, 17770-17775.

171. Guler, U.; Shalaev, V. M.; Boltasseva, A., Nanoparticle Plasmonics: Going Practical with Transition Metal Nitrides. *Mater. Today* **2015,** *18*, 227-237.

172. Liu, Y.; Liu, M.; Swihart, M. T., Plasmonic Copper Sulfide-Based Materials: A Brief Introduction to Their Synthesis, Doping, Alloying, and Applications. *J. Phys. Chem. C* **2017,** *121*, 13435-13447.

173. Li, W.; Zamani, R.; Rivera Gil, P.; Pelaz, B.; Ibáñez, M.; Cadavid, D.; Shavel, A.; Alvarez-Puebla, R. A.; Parak, W. J.; Arbiol, J.; Cabot, A., CuTe Nanocrystals: Shape and Size Control, Plasmonic Properties, and Use as SERS Probes and Photothermal Agents. *J. Am. Chem. Soc.* **2013,** *135*, 7098-7101.

174. Ding, X.; Fu, D.; Kuang, Y.; Zou, Y.; Yang, X.; Feng, L.; Sun, X.; Wu, H.; Jiang, J., Seeded Growth of $Cu_{2-x}Se$ Nanocrystals and Their Size-Dependent Phototherapeutic Effect. *ACS Appl. Nano Mater.* **2018,** *1*, 3303-3311.

175. Lie, S. Q.; Wang, D. M.; Gao, M. X.; Huang, C. Z., Controllable Copper Deficiency in $Cu_{2-x}Se$ Nanocrystals with Tunable Localized Surface Plasmon Resonance and Enhanced Chemiluminescence. *Nanoscale* **2014,** *6*, 10289-10296.

176. Rong, F.; Bai, Y.; Chen, T.; Zheng, W., Chemical Synthesis of Cu_2Se Nanoparticles at Room Temperature. *Mater. Res. Bull.* **2012,** *47*, 92-95.

177. Kimling, J.; Maier, M.; Okenve, B.; Kotaidis, V.; Ballot, H.; Plech, A., Turkevich Method for Gold Nanoparticle Synthesis Revisited. *J. Phys. Chem. B* **2006,** *110*, 15700-15707.

178. Frens, G., Controlled Nucleation for the Regulation of the Particle Size in Monodisperse Gold Suspensions. *Nat. Phys. Sci.* **1973,** *241*, 20-22.

179. Liu, Y.; Zhu, D.; Hu, Y.; Swihart, M. T.; Wei, W., Controlled Synthesis of $Cu_{2-x}Se$ Nanoparticles as Near-Infrared Photothermal Agents and Irradiation Wavelength Dependence of Their Photothermal Conversion Efficiency. *Langmuir* **2018,** *34*, 13905-13909.

180. Linic, S.; Aslam, U.; Boerigter, C.; Morabito, M., Photochemical Transformations on Plasmonic Metal Nanoparticles. *Nat. Mater.* **2015,** *14*, 567-576.

181. Stiles, P. L.; Dieringer, J. A.; Shah, N. C.; Duyne, R. P. V., Surface-Enhanced Raman Spectroscopy. *Annu. Rev. Anal. Chem.* **2008,** *1*, 601-626.

182. Szlag, V. M.; Rodriguez, R. S.; He, J.; Hudson-Smith, N.; Kang, H.; Le, N.; Reineke, T. M.; Haynes, C. L., Molecular Affinity Agents for Intrinsic Surface-Enhanced Raman Scattering (SERS) Sensors. *ACS Appl. Mater. Interfaces* **2018,** *10*, 31825-31844.

183. Yu, Y.; Sundaresan, V.; Willets, K. A., Hot Carriers Versus Thermal Effects: Resolving the Enhancement Mechanisms for Plasmon-Mediated Photoelectrochemical Reactions. *J. Phys. Chem. C* **2018,** *122*, 5040-5048.

184. McClain, M. J.; Schlather, A. E.; Ringe, E.; King, N. S.; Liu, L.; Manjavacas, A.; Knight, M. W.; Kumar, I.; Whitmire, K. H.; Everitt, H. O.; Nordlander, P.; Halas, N. J., Aluminum Nanocrystals. *Nano Lett.* **2015,** *15*, 2751-2755.

185. Kim, J.; Agrawal, A.; Krieg, F.; Bergerud, A.; Milliron, D. J., The Interplay of Shape and Crystalline Anisotropies in Plasmonic Semiconductor Nanocrystals. *Nano Lett.* **2016,** *16*, 3879-3884.

186. Ding, X.; Zou, Y.; Ye, F.; Yang, J.; Jiang, J., Pt–CuS Heterodimers by Sulfidation of CuPt Alloy Nanoparticles and Their Selective Catalytic Activity Toward Methanol Oxidation. *J. Mater. Chem. A* **2013,** *1*, 11880-11886.

187. Hanwell, M. D.; Curtis, D. E.; Lonie, D. C.; Vandermeersch, T.; Zurek, E.; Hutchison, G. R., Avogadro: An Advanced Semantic Chemical Editor, Visualization, and Analysis Platform. *J. Cheminformatics* **2012,** *4*, 17-34.

188. Wan, L.-J.; Terashima, M.; Noda, H.; Osawa, M., Molecular Orientation and Ordered Structure of Benzenethiol Adsorbed on Gold(111). *J. Phys. Chem. B* **2000,** *104*, 3563-3569.

189. Rowland, R. S.; Taylor, R., Intermolecular Nonbonded Contact Distances in Organic Crystal Structures: Comparison with Distances Expected from van der Waals Radii. *J. Phys. Chem.* **1996,** *100*, 7384-7391.

190. Sachleben, J. R.; Wooten, E. W.; Emsley, L.; Pines, A.; Colvin, V. L.; Alivisatos, A. P., NMR Studies of the Surface Structure and Dynamics of Semiconductor Nanocrystals. *Chem. Phys. Lett.* **1992,** *198*, 431-436.

191. van Schrojenstein Lantman, E. M.; Deckert-Gaudig, T.; Mank, A. J. G.; Deckert, V.; Weckhuysen, B. M., Catalytic Processes Monitored at the Nanoscale with Tip-Enhanced Raman Spectroscopy. *Nat. Nanotech.* **2012,** *7*, 583-586.

192. Vidal-Iglesias, F. J.; Solla-Gullón, J.; Orts, J. M.; Rodes, A.; Pérez, J. M., Spectroelectrochemical Study of the Photoinduced Catalytic Formation of 4,4′-Dimercaptoazobenzene from 4-Aminobenzenethiol Adsorbed on Nanostructured Copper. *J. Phys. Chem. C* **2015,** *119*, 12312-12324.

193. Choi, H.-K.; Lee, K. S.; Shin, H.-H.; Kim, Z. H., Identification of the First Elementary Step in the Photocatalytic Reduction of Nitrobenzenethiols on a Metallic Surface. *J. Phys. Chem. Lett.* **2016,** *7*, 4099-4104.

194. Hume-Rothery, W.; Mabbott, G. W.; Channel Evans, K. M.; Carpenter, H. C. H., The Freezing Points, Melting Points, and Solid Solubility Limits of the Alloys of Sliver and Copper with the Elements of the B Sub-Groups. *Philos. Trans. Royal Soc. A* **1934,** *233*, 1-97.

195. Alonso, J. A., The Factors Influencing Solid Solubility in Metallic Alloys. *Rev. Latinoam. de Metal. y Mater.* **1985,** *5*, 1-13.

196. Waber, J. T.; Gscheneidner, K.; Larson, A. C.; Prince, M. Y., Prediction of Solid Solubility in Metallic Alloys. *Trans. Metall. Soc. AIME* **1963,** *227*, 717-723.

197. Pei, Z.; Yin, J.; Hawk, J. A.; Alman, D. E.; Gao, M. C., Machine-Learning Informed Prediction of High-Entropy Solid Solution Formation: Beyond the Hume-Rothery Rules. *npj Comput. Mater.* **2020,** *6*, 1-8.

198. Zhang, Y. M.; Yang, S.; Evans, J. R. G., Revisiting Hume-Rothery's Rules with Artificial Neural Networks. *Acta Mater.* **2008,** *56*, 1094-1105.

199. Cui, Z.; Zhang, Z., Ce-Ni Nanoparticles with Shell Structure for Hydrogen Storage. *Nanostruct. Mater.* **1996,** *7*, 355-361.

200. Tabrizi, N. S.; Xu, Q.; van der Pers, N. M.; Lafont, U.; Schmidt-Ott, A., Synthesis of Mixed Metallic Nanoparticles by Spark Discharge. *J. Nanopart. Res.* **2008,** *11*, 1209-1218.

201. Beberwyck, B. J.; Surendranath, Y.; Alivisatos, A. P., Cation Exchange: A Versatile Tool for Nanomaterials Synthesis. *J. Phys. Chem. C* **2013,** *117*, 19759-19770.

202. Aldakov, D.; Lefrançois, A.; Reiss, P., Ternary and Quaternary Metal Chalcogenide Nanocrystals: Synthesis, Properties and Applications. *J. Mater. Chem. C* **2013,** *1*, 3756-3776.

203. McCormick, C. R.; Schaak, R. E., Simultaneous Multication Exchange Pathway to High-Entropy Metal Sulfide Nanoparticles. *J. Am. Chem. Soc.* **2021,** *143*, 1017-1023.

204. Liu, J.; Zhang, J., Nanointerface Chemistry: Lattice-Mismatch-Directed Synthesis and Application of Hybrid Nanocrystals. *Chem. Rev.* **2020,** *120*, 2123-2170.

205. De Trizio, L.; Manna, L., Forging Colloidal Nanostructures via Cation Exchange Reactions. *Chem. Rev.* **2016,** *116*, 10852-10887.

206. Rivest, J. B.; Jain, P. K., Cation Exchange on the Nanoscale: An Emerging Technique for New Material Synthesis, Device Fabrication, and Chemical Sensing. *Chem. Soc. Rev.* **2013,** *42*, 89-96.

207. Fenton, J. L.; Steimle, B. C.; Schaak, R. E., Tunable Intraparticle Frameworks for Creating Complex Heterostructured Nanoparticle Libraries. *Science* **2018,** *360*, 513-517.

208. Banin, U.; Ben-Shahar, Y.; Vinokurov, K., Hybrid Semiconductor–Metal Nanoparticles: From Architecture to Function. *Chem. Mater.* **2014,** *26*, 97-110.

209. Volokh, M.; Mokari, T., Metal/Semiconductor Interfaces in Nanoscale Objects: Synthesis, Emerging Properties and Applications of Hybrid Nanostructures. *Nanoscale Adv.* **2020,** *2*, 930-961.

210. Amirav, L.; Oba, F.; Aloni, S.; Alivisatos, A. P., Modular Synthesis of a Dual Metal–Dual Semiconductor Nano-Heterostructure. *Angew. Chem. Int. Ed.* **2015,** *54*, 7007-7011.

211. Zhou, Y.; Zhao, H.; Ma, D.; Rosei, F., Harnessing the Properties of Colloidal Quantum Dots in Luminescent Solar Concentrators. *Chem. Soc. Rev.* **2018,** *47*, 5866-5890.

212. Eikey, E. A.; Gan, X. Y.; Kaseman, D. C.; Murphey, C. G. E.; Crawford, S. E.; Johnston, K. A.; Yazdi, S.; Millstone, J. E., Efficient Control of Atom Arrangement in Ternary Metal Chalcogenide Nanoparticles Using Precursor Oxidation State. *Chem. Mater.* **2020,** *32*, 1322-1331.

213. Diemler, N., Surface Chemistry Controlled Deposition on Nanoparticle Substrates. 2019.

214. Haynes, W. M.; Lide, D. R.; Bruno, T. J., *CRC Handbook of Chemistry and Physics: A Ready-Reference Book of Chemical and Physical Data*. 92 ed.; CRC Press: Florida, 2011.

215. Gariano, G.; Lesnyak, V.; Brescia, R.; Bertoni, G.; Dang, Z.; Gaspari, R.; De Trizio, L.; Manna, L., Role of the Crystal Structure in Cation Exchange Reactions Involving Colloidal Cu2Se Nanocrystals. *J. Am. Chem. Soc.* **2017,** *139*, 9583-9590.

216. Lesnyak, V.; Brescia, R.; Messina, G. C.; Manna, L., Cu Vacancies Boost Cation Exchange Reactions in Copper Selenide Nanocrystals. *J. Am. Chem. Soc.* **2015,** *137*, 9315-9323.

217. Le, H. K. D.; Xiong, H.; Page, B. A.; Garcia-Herrera, L. F.; McAllister, H. P.; Li, B. C.; Wang, H.; Plass, K. E., Effects of I2 on Cu2–xS Nanoparticles: Enabling Cation Exchange but Complicating Plasmonics. *ACS Mater. Lett.* **2020,** *2*, 140-146.

218. Jain, P. K.; Amirav, L.; Aloni, S.; Alivisatos, A. P., Nanoheterostructure Cation Exchange: Anionic Framework Conservation. *J. Am. Chem. Soc.* **2010,** *132*, 9997-9999.

219. Meir, N.; Martín-García, B.; Moreels, I.; Oron, D., Revisiting the Anion Framework Conservation in Cation Exchange Processes. *Chem. Mater.* **2016,** *28*, 7872-7877.

220. Tu, R.; Xie, Y.; Bertoni, G.; Lak, A.; Gaspari, R.; Rapallo, A.; Cavalli, A.; De Trizio, L.; Manna, L., Influence of the Ion Coordination Number on Cation Exchange Reactions with Copper Telluride Nanocrystals. *J. Am. Chem. Soc.* **2016,** *138*, 7082-7090.

221. Olin, A.; Nolang, B.; Osadchii, E. G.; Ohman, L.-O.; Rosen, E., *Chemical Thermodynamics of Selenium*. Elsevier: 2004; Vol. 7.

222. Chalana, A.; Karri, R.; Mandal, S. C.; Pathak, B.; Roy, G., Chemical Degradation of Mercury Alkyls Mediated by Copper Selenide Nanosheets. *Chem. Asian. J.* **2019,** *14*, 4582-4587.

223. Wang, H.; Xu, S.; Zhao, X.-N.; Zhu, J.-J.; Xin, X.-Q., Sonochemical Synthesis of Size-Controlled Mercury Selenide Nanoparticles. *Mater Sci Eng, B* **2002,** *96*, 60-64.

224. Bouzas-Ramos, D.; Menéndez-Miranda, M.; Costa-Fernández, J. M.; Encinar, J. R.; Sanz-Medel, A., Precise Determination of the Nanoparticle Concentration and Ligand Density of Engineered Water-Soluble HgSe Fluorescent Nanoparticles. *RSC Adv.* **2016,** *6*, 19964-19972.

225. Holade, Y.; Canaff, C.; Poulin, S.; Napporn, T. W.; Servat, K.; Kokoh, K. B., High Impact of the Reducing Agent on Palladium Nanomaterials: New Insights from X-ray Photoelectron Spectroscopy and Oxygen Reduction Reaction. *RSC Adv.* **2016,** *6*, 12627-12637.

226. Xie, Y.; Chen, W.; Bertoni, G.; Kriegel, I.; Xiong, M.; Li, N.; Prato, M.; Riedinger, A.; Sathya, A.; Manna, L., Tuning and Locking the Localized Surface Plasmon Resonances of CuS (Covellite) Nanocrystals by an Amorphous CuPdxS Shell. *Chem. Mater.* **2017,** *29*, 1716-1723.

227. Zhang, L.; Zhao, S.; Li, Y.; Lan, Y.; Han, M.; Dai, Z.; Bao, J., Monoclinic Copper(I) Selenide Nanocrystals and Copper(I) Selenide/Palladium Heterostructures: Synthesis, Characterization, and Surface-Enhanced Raman Scattering Performance. *Eur. J. Inorg. Chem.* **2015,** *2015*, 2229-2236.

228. Chen, Z.; Wang, W.; Zhang, Z.; Fang, X., High-Efficiency Visible-Light-Driven Ag3PO4/AgI Photocatalysts: Z-Scheme Photocatalytic Mechanism for Their Enhanced Photocatalytic Activity. *J. Phys. Chem. C* **2013,** *117*, 19346-19352.

229. Qu, J.; Goubet, N.; Livache, C.; Martinez, B.; Amelot, D.; Gréboval, C.; Chu, A.; Ramade, J.; Cruguel, H.; Ithurria, S.; Silly, M. G.; Lhuillier, E., Intraband Mid-Infrared Transitions in Ag2Se Nanocrystals: Potential and Limitations for Hg-Free Low-Cost Photodetection. *J. Phys. Chem. C* **2018,** *122*, 18161-18167.

230. White, S. L.; Smith, J. G.; Behl, M.; Jain, P. K., Co-operativity in a Nanocrystalline Solid-State Transition. *Nat. Commun.* **2013,** *4*, 2933.

231. Rodrigues, T. S.; Zhao, M.; Yang, T.-H.; Gilroy, K. D.; da Silva, A. G. M.; Camargo, P. H. C.; Xia, Y., Synthesis of Colloidal Metal Nanocrystals: A Comprehensive Review on the Reductants. *Chem. Eur. J.* **2018,** *24*, 16944-16963.

232. Liu, X.; Lee, C.; Law, W.-C.; Zhu, D.; Liu, M.; Jeon, M.; Kim, J.; Prasad, P. N.; Kim, C.; Swihart, M. T., Au–Cu2–xSe Heterodimer Nanoparticles with Broad Localized Surface Plasmon Resonance as Contrast Agents for Deep Tissue Imaging. *Nano Lett.* **2013,** *13*, 4333-4339.

233. Shan, B.; Zhao, Y.; Li, Y.; Wang, H.; Chen, R.; Li, M., High-Quality Dual-Plasmonic Au@Cu2–xSe Nanocrescents with Precise Cu2–xSe Domain Size Control and Tunable Optical Properties in the Second Near-Infrared Biowindow. *Chem. Mater.* **2019,** *31*, 9875-9886.

234. Wolf, A.; Hinrichs, D.; Sann, J.; Miethe, J. F.; Bigall, N. C.; Dorfs, D., Growth of Cu2–xSe–CuPt and Cu1.1S–Pt Hybrid Nanoparticles. *J. Phys. Chem. C* **2016,** *120*, 21925-21931.

235. Fu, G.; Yan, X.; Cui, Z.; Sun, D.; Xu, L.; Tang, Y.; Goodenough, J. B.; Lee, J.-M., Catalytic Activities for Methanol Oxidation on Ultrathin CuPt3 Wavy Nanowires With/Without Smart Polymer. *Chem. Sci.* **2016,** *7*, 5414-5420.

236. Castillo, R.; Dominguez Garcia, E.; Santos, J. L.; Centeno, M. A.; Romero Sarria, F.; Daturi, M.; Odriozola, J. A., Upgrading the PtCu Intermetallic Compounds: The Role of Pt and Cu in the Alloy. *Catal. Today* **2019**.

237. Holder, C. F.; Schaak, R. E., Tutorial on Powder X-Ray Diffraction for Characterizing Nanoscale Materials. *ACS Nano* **2019,** *13*, 7359-7365.

238. Sun, X.; Jiang, K.; Zhang, N.; Guo, S.; Huang, X., Crystalline Control of {111} Bounded Pt3Cu Nanocrystals: Multiply-Twinned Pt3Cu Icosahedra with Enhanced Electrocatalytic Properties. *ACS Nano* **2015,** *9*, 7634-7640.

239. Du, X.; Luo, S.; Du, H.; Tang, M.; Huang, X.; Shen, P. K., Monodisperse and Self-Assembled Pt-Cu Nanoparticles as an Efficient Electrocatalyst For the Methanol Oxidation Reaction. *J. Mater. Chem. A* **2016,** *4*, 1579-1585.

240. Weaver, J. H., Optical Properties of Rh, Pd, Ir, and Pt. *Phys. Rev. B* **1975,** *11*, 1416-1425.

241. Moore, D. S., McCabe, G. P., Craig, B. A., *Introduction to the Practice of Statistics*. Freeman: New York, NY, 2012.

242. Kao, L. S.; Green, C. E., Analysis of Variance: Is There a Difference in Means and What Does It Mean? *J. Surg. Res.* **2008,** *144*, 158-170.